SPECIATION OF ACTINIDES OR THEIR LIGHTER HOMOLOGUES IN AQUATIC ENVIRONMENT

By

Rama Mohana Rao Dumpala
CHEM01201104019

Bhabha Atomic Research Centre
Mumbai - 400085, India

A thesis submitted to the
Board of Studies in Chemical Sciences
in partial fulfillment of requirements
for the Degree of

DOCTOR OF PHILOSOPHY
of
HOMI BHABHA NATIONAL INSTITUTE

August 2017

Homi Bhabha National Institute

Recommendations of the Viva Voce Committee

As members of the Viva Voce Committee, we certify that we have read the dissertation prepared by **Rama Mohana Rao Dumpala** entitled "**Speciation of Actinides or Their Lighter Homologues in Aquatic Environment**" and recommend that it may be accepted as fulfilling the thesis requirement for the award of Degree of Doctor of Philosophy.

Chairman - Dr. S. Kannan		**Date:** 9.1.18
Guide / Convener - Dr. B. S. Tomar		**Date:** 9.1.2018
Technology Advisor- Dr. Neetika Rawat	Neetika Rawat	**Date:** 9. 1. 2018
Examiner - Dr. Kaushik Ghosh	Ghosh	**Date:** 9/1/2018
Member 1- Dr. P. K. Mohapatra		**Date:** 09/1/2018
Member 2- Dr. H. Pal		**Date:** 09-01-2018

Final approval and acceptance of this thesis is contingent upon the candidate's submission of the final copies of the thesis to HBNI.

We hereby certify that we have read this thesis prepared under our direction and recommend that it may be accepted as fulfilling the thesis requirement.

Date: 09-01-2018

Place: Mumbai

Dr. B. S. Tomar

Guide

STATEMENT BY AUTHOR

This dissertation has been submitted in partial fulfillment of requirements for an advanced degree at Homi Bhabha National Institute (HBNI) and is deposited in the Library to be made available to borrowers under rules of the HBNI.

Brief quotations from this dissertation are allowable without special permission, provided that accurate acknowledgement of source is made. Requests for permission for extended quotation from or reproduction of this manuscript in whole or in part may be granted by the Competent Authority of HBNI when in his or her judgment the proposed use of the material is in the interests of scholarship. In all other instances, however, permission must be obtained from the author.

Rama Mohana Rao Dumpala

DECLARATION

I, hereby declare that the investigation presented in the thesis has been carried out by me. The work is original and has not been submitted earlier as a whole or in part for a degree / diploma at this or any other Institution / University.

Rama Mohana Rao Dumpala

List of Publications arising from the thesis

Journal

1. "Thermodynamic study of Eu(III) complexation by pyridine monocarboxylates", **D. Rama Mohana Rao**, Neetika Rawat, R. M. Sawant, D. Manna, T. K. Ghanty, B. S. Tomar, *The Journal of Chemical Thermodynamics*, **2012**, *55*, 67–74.
2. "Complexation of thorium with pyridine monocarboxylates: A thermodynamic study by experiment and theory", **D. Rama Mohana Rao**, Neetika Rawat, D. Manna, R. M . Sawant, T. K. Ghanty, B. S. Tomar, *The Journal of Chemical Thermodynamics*, **2013**, *58*, 432-439.
3. "Protonation of Pyridine Monocarboxylate-N-Oxides – Determination of Thermodynamic, absorbance and Ion Interaction Parameters", **Rama Mohana Rao Dumpala**, Neetika Rawat, B. S. Tomar, *ChemistrySelect,* **2017**, *2,* 820-829**.**
4. "Coordination Modes of Hydroxamates in Neptunium (V) Complexes in Aqueous Solution", **Rama Mohana Rao Dumpala**, Neetika Rawat, Arunasis Bhattacharya and Bhupendra Singh Tomar, *ChemistrySelect,* **2017**, *2,* 2722-2731**.**
5. "Stability, speciation and spectral properties of Np(V) complexes with pyridine monocarboxylates in aqueous solution", **Rama Mohana Rao Dumpala**, Neetika Rawat, B.S. Tomar, *Spectrochimica Acta Part A: Molecular and Biomolecular Spectroscopy,* **2017**, *181,* 13-22.
6. Structural, luminescence, thermodynamic and theoretical studies on mononuclear complexes of Eu(III) with pyridine monocarboxylate-N-oxides in aqueous solution, **Rama Mohana Rao Dumpala**, Neetika Rawat, Anil Boda, Sk. Musharaf Ali, B.S. Tomara, *Spectrochimica Acta Part A: Molecular and Biomolecular Spectroscopy,* **2018**, *190*, 150–163.

7. Thermodynamic Studies Combined with Density Functional Theory Calculation on Complexation of Thorium with Pyridine Monocarboxylate-N-Oxides, **Rama Mohana Rao Dumpala**, Neetika Rawat, Anil Boda, Sk. Musharaf Ali, B. S. Tomar, *J. Chem. Thermodyn.* (Accepted).

8. The solubility of Th(IV) - The effect of pH, Ionic Strength and Colloid Formation, **D. Rama Mohana Rao**, B. K. Nagar, Manjulatha Sahu, V. V. Raut, Neetika Rawat, Naina Raje, S. Jeyakumar, M. K. Saxena, B. S. Tomar, *Env. Sci. Nano* (Under Review).

Conferences/Symposia

1. Speciation of Thorium-Picolinate Complexes and their Stability Constants in 1 M $NaClO_4$ medium, ***D. Rama Mohana Rao***, U.K. Thakur, D.J. Shah, R.S. Sharma, R.M. Sawant and K.L. Ramakumar, 180-181, Vol-1, DAE-BRNS Symposium on Nuclear and Radiochemistry (NUCAR-2011), February 22-26, 2011, GITAM Institute of Science, Visakhapatnam.

2. Speciation of thorium-pyridine carboxylates in 1M NaClO4 medium, **D. Rama Mohana Rao**, Neetika Rawat, R. M. Sawant, B. S. Tomar, pp-243, SESTEC-2012, February 27 – March 01, 2012, SVKM's Mithibai college, Mumbai.

3. Thermodynamics of Complexation of Eu(III) with α-Picolinate, **Dumpala Rama Mohana Rao**, Neetika Rawat, R.M. Sawant, B.S. Tomar, Pitticon Conference and Expo 2012, March 11-15, 2012, Orlando, FL, USA

4. Thermodynamics of complexation of Eu(III) with pyridyl carboxylates, **D. Rama Mohana Rao**, Neetika Rawat, R. M. Sawant, B. S. Tomar, MRS-Y Symposium, April

9 - 13, 2012, Moscone West Convention Center, Marriott Marquis - San Francisco, California, US.

5. A Thermodynamic study of Complexation of Thorium with Pyridine Monocarboxylates by Calorimetry and DFT Calculations, **D. Rama Mohana Rao**, Neetika Rawat, D. Manna, R. M. Sawant, T. K. Ghanty, B.S. Tomar, The eleventh biennial symposium on “Nuclear and Radiochemistry” (NUCAR -2013) at Government Model Science College, R. D. University, Jabalpur, India, February 19-23, 2013, pp 239-240.

6. Thermodynamics of Complexation Benzohydroxamic acid with Np(V) (Np(V)) in Aqueous Medium, ***D. Rama Mohana Rao***, Neetika Rawat, B. S. Tomar, Workshop cum Nineteenth National Symposium on Environment (NSE- 19), M. G. University, Kottayam, Kerala, December 11-13, 2014, pp 181-182.

7. Complexation of Np(V) with pyridine monocarboxylates – A spectrophotometric Study, ***D. Rama Mohana Rao***, Neetika Rawat, R. M. Sawant, B. S. Tomar, DAE-BRNS Symposium on Nuclear and Radiochemistry (NUCAR-2015), February 9-13, 2015, Nabhikiy Urja Bhavan, Anusakthi Nagar, Mumbai pp 222-223.

8. Complexation of Neptunyl(NpO_2^+) ion with Hydroxamic acids in 0.1 M $NaClO_4$ medium, **D. Rama Mohana Rao**, Neetika Rawat, B. S. Tomar, 15th International Conference on the Chemistry and Migration Behaviour of Actinides and Fission Products in the Geosphere, Santa Fe Community Convention Center, Santa Fe, USA, September 13–18, 2015, pp-204.

9. Speciation of Europium in presence of Picolinic acid-n-oxide, **D. Rama Mohana Rao**, B. S. Tomar 7th DAE-BRNS biennial symposium on emerging trends in separation

science and technology (SESTEC 2016), held at Indian Institute of Technology, Guwahati during 17-20 May 2016, PP-155

10. Aqueous phase solubility of thorium - The effect of pH and colloids contribution, DAE-BRNS Symposium on Nuclear and Radiochemistry (NUCAR-2017), KIIT University Bhubaneswar, 6-10 February 2017, ***D. Rama Mohana Rao***, Neetika Rawat, B. S. Tomar

11. Coordination modes of Hydroxamates in Neptunium (V) Complexes in Aqueous Solution, **Rama Mohana Rao Dumpala**, Neetika Rawat, Arunasis Bhattacharya, and Bhupendra Singh Tomar, DAE-BRNS Symposium on Nuclear and Radiochemistry (NUCAR-2017), KIIT University Bhubaneswar, 6-10 February 2017.

12. Effect of Experimental conditions on the colloid formation of aqueous thorium solution, D. Rama Mohana Rao, B. K. Nagar, Manjulatha Sahu, Neetika Rawat, S. Jeyakumar, M. K. Saxena, B. S. Tomar, 16th International Conference on the Chemistry and Migration Behaviour of Actinides and Fission Products in the Geosphere, Barcelona, Spain, September 10–15, 2017.

Rama Mohana Rao Dumpala

Other Publications

1. Determination of lanthanides and yttrium in high purity dysprosium by RP-HPLC using α-hydroxyisobutyric acid as eluent, Pranaw Kumar, P. G. Jaison, D. R. M. Rao, V. M. Telmore, A. Sarkar and Suresh K. Aggarwal, Journal of liquid chromatography and related techniques, volume 36 (2013) 1513-1527.
2. Host-guest interaction of cucurbit[7]uril with para-nitrophenol: A weakly binding inclusion complex, Sabyasachi Patra, Sudip Gorai, D. Rama Mohana Rao, Manoj K Sharma, Sandip K Nayak, Alok K Ray, A. Goswami, Indian Journal of Chemistry Section A, April 201756: 508-512.
3. Redox Speciation of Neptunium with Phenylphosphonic acid (PPA): A comprehensive study to inquest the solution species and its coordination by Electrochemical, Spectroscopic and DFT method, Ashutosh srivatsava, D. Rama Mohana Rao, Neetika Rawat, B. S. Tomar, Dalton Transactions (under review)
4. Study of Complexation of Uranyl with iminodiacetic acid by Potentiometric Method, D. Rama Mohana Rao, R. M. Sawant, B. S. Tomar, The eleventh biennial symposium on “Nuclear and Radiochemistry” (NUCAR -2013) at Government Model Science College, R. D. University, Jabalpur, India, February 19-23, 2013, pp 241-242.
5. Determination of Stability Constants for the Thorium Iminodiacetic acid Complexes, D. Rama Mohana Rao, R. M. Sawant, B.S. Tomar, The fifth international symposium of Asia-Pacific Symposium on Radiochemistry (APSORC 13),22 to 27 September 2013 at Kanazawa, Japan
6. Complexation of Eu(III) with dicarboxylates ligand in binary and ternary complexes, Neetika Rawat, *D. Rama Mohana Rao*, R.M. Sawant, B.S. Tomar, DAE-BRNS Symposium on Emerging Trends in separation science and Technology, SESTEC – 2014, BARC, Mumbai, February 25-28, 2014, pp 251-251.

7. Kinetics of Complexation of Eu(III) by 1,4,7,10-tetraazacyclododecane-1,4,7,10-tetraacetic acid (DOTA) employing time resolved laser induced fluorescence spectroscopy, Poonam Verma, A. S. Kar, D. Rama Mohana Rao, S. Jeyakumar and B. S. Tomar, 7th DAE-BRNS biennial symposium on emerging trends in separation science and technology (SESTEC 2016), held at Indian Institute of Technology, Guwahati during 17-20 May 2016, PP-163
8. Stability and Speciation of Uranyl in presence of Citric acid D. Rama Mohana Rao, B. S. Tomar, 7th DAE-BRNS biennial symposium on emerging trends in separation science and technology (SESTEC 2016), held at Indian Institute of Technology, Guwahati during 17-20 May 2016, PP-183

Rama Mohana Rao Dumpala

Dedicated to My beloved parents

Shri. YARRAYYA DUMPALA

&

Smt. ADILAKSHMI DUMPALA

whose efforts and scarifies are been key to my success all the way.

ACKNOWLEDGEMENTS

I would like to thank the Almighty for everything that I posseess today and tomorrow in my life. Experience is the best teacher, but for me, having you as my teacher is the best experience in my life. I wish to express my sincere gratitude to my guide Prof. B. S. Tomar for his continuous support for my Ph.D study and research, for his patience, motivation, enthusiasm, and immense knowledge. His guidance helped me in all the time of research and writing of this thesis.

I would also like to thank members of the present and previous doctoral committee: Prof. K L. Ramakumar, Dr. S. Kannan, Dr. P. K. Mohapatra, Dr. R. M. Sawant, Dr. H. Pal, for their encouragement and insightful comments during the annual and pre-synopsis review presentations. I am thankful to Dr. Neetika Rawat for her consistent and continuous support since my joining in the institute in enhancing my research abilities to a fruitful conclusion. My sincere thanks are also due to my colleagues and coauthors for many stimulating discussions and their invaluable co-operation during the course of this work. I express my sincere gratitude to all members Complex Chemistry Section, Radioanalytical Chemistry Division for their cooperation and help during this work. I acknowledge the Elsevier Publishers for provoding the copyright permissions for my articles to use in the thesis.

My special thanks are due to my school, Jawahar Navodaya Vidyalaya, Srikakulam, Andhra Pradesh for letting me to nurture myself from human being to social being. I thank my wife and son for their constant love, encouragement and support. Last, but not the least, I would like to thank my parents, who allowed and supported me all the time to show the path of light to achieve the best in my life though they are unable to afford at many times.

Rama Mohana Rao Dumpala

CONTENTS

Synopsis 1

List of Figures 12

List of Tables 21

Chapter 1 Introduction 27

1.1. Indian Nuclear Energy Programme 27

1.2. The Nuclear Fuel Cycle 28

1.3. Challenges in Nuclear Fuel Cycle 29

1.4. The Radioactive Waste 30

- 1.4.1. Exempt Waste (EW) 30
- 1.4.2. Very Short Lived Waste (VSLW) 30
- 1.4.3. Very Low Level Waste (VLLW) 30
- 1.4.4. Low Level Waste (LLW) 30
- 1.4.5. Intermediate Level Waste (ILW) 31
- 1.4.6. High Level Waste (HLW) 31

1.5. Radioactivity in the Environment 31

- 1.5.1. Radionuclides in Aquatic Environment 32
- 1.5.2. Fate of Radionuclides in Aquatic Environment 33
  - 1.5.2.1. Precipitation 34
  - 1.5.2.2. Sorption 35
  - 1.5.2.3. Complexation 35
  - 1.5.2.4. Colloid Formation 36

1.6. Geochemical Models 36

1.7. The Chemistry of Lanthanides and Actinides 38

- 1.7.1. Similarities and Differences Between Lanthanides and Actinides 38

1.7.2. The Oxidation States 39

1.7.3. Hydration of Lanthanides and Actinides 40

1.7.4. Hydrolysis of Lanthanides and Actinides 41

1.8. The Lanthanide and Actinide Complexes in Aquatic Environment 42

1.8.1. Inorganic Complexing Agents 43

1.8.2. Complexation with Natural Organic Matter 44

1.8.3. Anthropogenic Ligands 46

1.9. Actinide Colloids 47

1.10. Thermodynamic Parameters - An Insight to Complexation 48

1.11. Motivation for The Present Work 48

1.12. Scope of The Thesis 53

Chapter 2: Materials, Methodology and Instrumentation 56

2.1. Preparation and Standardization of Solutions 57

2.1.1. Metal ion Solutions 57

2.1.2. Ligand Solutions 58

2.1.3. Auxiliary Solutions 58

2.2. Equilibrium Constants 60

2.3. Activity and Activity Coefficients 61

2.4. Methodology to Determine The Stability Constants 62

2.5. Determination of The Stability Constants 66

2.5.1. Potentiometric Titrations 66

2.5.1.1. pH Electrode 67

2.5.1.2. The Autotitrator 68

2.5.1.3. Determination of Protonation and Stability Constants by Potentiometry 69

2.5.2. Spectrophotometry 71

2.5.2.1. Absorption Spectra of Lanthanides and Actinides in Solution 72

2.5.2.2. Instrumentation for Spectrophotometry 73

2.5.2.3. Determination of Protonation and Stability Constants by UV-VIS-NIR Absorption Spectrophotometry 74

2.5.3. Time Resolved Luminescence Spectroscopy 76

2.5.3.1. Luminescence of Lanthanides and Actinides 77

2.5.3.2. Instrumentation for Time Resolved Luminescence Spectroscopy(TRLS) 79

2.5.3.3. Determination of Stability Constants by Luminescence Spectroscopy 80

2.5.3.4. Determination of Stoichiometry and Mode of Complexation by Luminescence Lifetime Measurements 82

2.6. The Enthalpy and Entropy of Formation of a Complex 83

2.6.1. Isothermal Titration Calorimetry (ITC) 84

2.6.1.1. Instrumentation for ITC 84

2.6.1.2. Determination of Enthalpy of Formation by ITC 86

2.7. Characterization of Colloids 88

2.7.1. Laser Induced Breakdown Detection (LIBD) 89

2.7.1.1. Instrumentation for LIBD 90

2.7.1.2. Methodology to Determine the Size and Concentration of Colloids by LIBD 90

2.7.1.3. Size and Concentration Calibration of LIBD System 91

Chapter 3 Studies on Protonation of Pyridine Monocarboxylates, Their N-Oxides and Hydroxamates 95

3.1. Introduction 95

3.2. Experimental 96

- 3.2.1. Reagents 96
- 3.2.2. Potentiometry 96
- 3.2.3. Calorimetry 97
- 3.2.4. Spectrophotometry 97

3.3. Theoretical Calculations 98

3.4. Results and Discussion 98

- 3.4.1. Protonation of Pyridine Monocarboxylates 98
  - 3.4.1.1. Potentiometry 98
  - 3.4.1.2. Calorimetric Titrations 100
- 3.4.2. Protonation of Pyridine Monocarboxylate-N-Oxides 102
  - 3.4.2.1. Potentiometric Studies 102
  - 3.4.2.2. Calorimetric Titrations 104
  - 3.4.2.3. Ion Interaction Parameters for PCNOs – An SIT approach 108
  - 3.4.2.4. Spectrophotometric Measurements 111
  - 3.4.2.5. Theoretical Calculations 113
  - 3.4.2.6. Comparison with Pyridine Monocarboxylates 118
- 3.4.3. Protonation of Hydroxamates 120
  - 3.4.3.1. Potentiometric Titration 120
  - 3.4.3.2. Spectrophotometric Titration 121
  - 3.4.3.3. Theoretical Calculations 122

3.5. Conclusion 125

Chapter 4 Thermodynamic, Luminescence and DFT Studies on Complexation of Eu(III) by Pyridine Monocarboxylates and Their N-Oxides 126

4.1. Introduction 126

4.2. Experimental 128

- 4.2.1. Reagents 128
- 4.2.2 Potentiometric Titrations 128
- 4. 2.3 Calorimetric Titrations 129
- 4.2.4. Time Resolved Luminescence spectroscopic (TRLS) Measurements 130

4.3. Computational Protocol 130

4.4. Results and Discussion 131

- 4.4.1. Eu(III) Complexation by Pyridine Monocarboxylates 131
  - 4.4.1.1. Potentiometry 131
  - 4.4.1.2. Isothermal Titration Calorimetry 134
  - 4.4.1.3. Time Resolved Luminescence Spectroscopy 137
  - 4.4.1.4. Theoretical Calculations 139
- 4.4.2. Eu(III) Complexation by Pyridine Monocarboxylate-N-oxides 141
  - 4. 4.2.1. Stability, Stoichiometry and Speciation of The Complexes 141
  - 4. 4.2.2. Thermodynamics of Complexation 144
  - 4. 4.2.3. Luminescence Intensities and Lifetime of The Complexes 149
  - 4.4.2.4. Density Functional Theory Calculations 154
    - 4.4.2..4.1. Structural Parameters 154

4.4.2.4.2. Binding Energy and Free Energy of Complexation 159

4.4.2.4.3. Partial Charges of Individual Atoms 161

4.5. Conclusion 164

Chapter 5 Thermodynamic and Density Functional Theory Studies on Complexation of Th(IV) by Pyridine Monocarboxylates and Their N-Oxides 165

5.1. Introduction 165

5.2. Experimental 166

5.2.1. Reagents 166

5.2.2 Potentiometric Titrations 167

5.2.3. Calorimetric Titrations 168

5.3. Computational Protocol 168

5.4. Results and Discussion 169

5.4.1. Complexation of Th(IV) by Pyridine Monocarboxylates 169

5.4.1.1. Potentiometry 169

5.4.1.2. Isothermal Titration Calorimetry 172

5.4.1.3. Theoretical Calculations 175

5.4.1.4. Conclusion 180

5.4.2. Complexation of Thorium with Pyridine Monocarboxylate-N-Oxides 180

5.4.2.1. Potentiometry 180

5.4.2.2. Isothermal Titration Calorimetry 184

5.4.2.3. Theoretical Calculations 187

5.4.2.4. Conclusions 195

Chapter 6 Stability, Speciation and Spectral Properties of Np(V) complexes with Pyridine Monocarboxylates and Hydroxamic acids - Spectrophotometric and Computational Study 197

6.1. Introduction 197

6.2. Experimental 199

- 6.2.1. Reagents 199
- 6.2.2. Spectrophotometric Titrations 200

6.3. Theoretical Calculations 200

6.4. Results and Discussions 202

- 6.4.1. Np(V) Pyridine Monocarboxylates Complexes 202
  - 6.4.1.1. Spectrophotometric Titration 202
  - 6.4.1.2. Linear Free Energy Relationships (LFER) 206
  - 6.4.1.3. Spectral Properties 209
  - 6.4.1.4. Theoretical Calculations 212
- 6.4.2. Np(V) Hydroxamates Complexes 215
  - 6.4.2.1. Structure of $NpO_2(H_2O)_5^+$ 216
  - 6.4.2.2. Complexation of Np(V) with AHA 216
  - 6.4.2.3. Comparison of Np-AHA and Np-BHA 218
  - 6.4.2.4. Coordination Modes of SHA to Np(V) in 1:1:1 Complex 218
  - 6.4.2.5. Comparison of Np-SX and Np-SY Binding Modes 220
  - 6.4.2.6. Linear Free Energy Relationship 220
  - 6.4.2.7. Np-SHA 1:2:2 Complexes 221
  - 6.4.2.8. Np-SHA 1:2:0 Complexes 224

6.5. Conclusions 225

Chapter 7 The Solubility of Th(IV) - The Effect of pH, Ionic Strength and Colloid Formation 227

7.1. Introduction 227

7.2. Experimental 230

7.2.1. Reagents 230

7.2.2. Sample Preparation 230

7.2.3. pH Measurements 231

7.2.4. Ion Chromatography (IC) 231

7.2.5. Inductively Coupled Plasma - Mass Spectrometry (ICP-MS) 231

7.2.6. Dynamic Light Scattering (DLS) 232

7.2.7. Laser Induced Breakdown Detection (LIBD) 232

7.2.8. High Temperature Thermogravimetric Differential Scanning Calorimetry (HT-TG-DSC) 233

7.3. Results and Discussion 233

7.3.1. pH Measurements 233

7.3.2. Fractionation of Soluble Thorium Present in Supernatant Solutions 235

7.3.3. Dynamic Light Scattering Measurements 238

7.3.4. Laser Induced Breakdown Detection (LIBD) 241

7.3.5. Size and Concentrations of Thorium Colloids 241

7.3.6. Fractionation of Soluble Thorium Content 245

7.3.7. Solubility of Thorium Hydrous Oxide [Th(OH)$_4$] 245

7.3.8. Characterization of Thorium (Oxy) Hydroxide Precipitate 247

7.4. Conclusion 252

Summary 254

References 262

SYNOPSIS

The lanthanides and actinides are the key elements in nuclear industry as fuel materials (U, Pu, Th), nuclear poisons (Gd), burn-up monitors (Nd). The nuclear tests, accidental release from nuclear power plants and the low level effluent discharges from nuclear facilities are the major routes by which actinides can enter into environment. Deep geological repositories are one of the proposed methodologies for the immobilization of the high level waste (HLW) generated during the reprocessing of spent nuclear fuel [1]. With the view to access the performance of the deep geological repositories over a long term to retain the long lived actinides and fission products as well as to ensure the containment of the radionuclides in the waste forms, it is important to investigate the migration behavior of these radionuclides in the geosphere [2]. Depending on the prevailing conditions around these nuclides, they can undergo various kinds of interactions like complexation, sorption, precipitation and colloid formations [3]. The complexation of the actinides with ligands that are co-disposed with HLW or the ligands of potential occurrence near the repository conditions is an important pathway for transportation and mobility of these radionuclides from their origin [4]. The anthropogenic ligands may enter the aquatic arena by artificial routes like agro and pharma industries, processing plants, waste water treatment, degradation products of waste confinement barriers or co deposition during decontamination of nuclear equipment. [5-6].

The interaction of actinides with anthropogenic ligands mainly concerned with aliphatic, aromatic carboxylates and aminocarboxylates [7-8] in the literature. The studies on the aqueous complexation of either lanthanides or actinides with pyridine monocarboxylates, its N-oxides and hydroxamates are very limited [9-10]. In the recent years, few studies have been reported on the complexation of Np(V) with picolinic acid, nicotinic acid [11-13]. Most of the literature reports on chemistry of interaction of lanthanides in general and europium in particular with pyridine monocarboxylate-N-oxides (PCNOs) are either with the synthesis of polymers or on coordination networks in solid state to explore their applications in luminescence, catalysis and many other fields [14-16], but the studies in solution are limited [17]. The studies on the interaction of simple hydroxamates with tetra- and pentavalent actinides have been reported in the literature on extraction and reduction of actinides [18-19]. The complexation of Np(V) with HA in aqueous medium has been reported by only one group [20].

The behaviour of actinides in aquatic environment is dependent upon their chemical form viz. ions, polymeric forms or as colloids which in turn may affect their chemical interaction as well as their migration [21]. Thus, the accountability of colloids is always essential to determine the solubility limits accurately which are required as inputs in geochemical model [22]. The presence of colloids can increase the total concentrations of actinides above the equilibrium thermodynamic solubility limits, and thereby increase the mass amount of actinides transportable to the environment [23-25]. Solubility data reported for amorphous Th(IV) precipitates, called either amorphous hydroxides $Th(OH)_4$ (am) or hydrous oxides $ThO_2.xH_2O(am)$, show considerable discrepancies [26-30]. This may be due to the fact that the reported solubilities do not refer to a well-defined solid phase but to hydrated oxyhydroxide $ThO_n(OH)_{4-2n}.xH_2O(am)$ with $0 \leq n \leq 2$ depending on the preparation method, pre-treatment, alteration, and temperature . Furthermore, the presence of colloids can also explain the widely scattered Th(IV) concentrations measured in the various solubility studies [31].

The major findings in the literature that made us to study the complexation of Eu(III), Th(IV) and Np(V) with pyridine monocarboxylates or pyridine monocarboxylate-N-oxides or hydroxamates to determine either thermodynamic parameters and/or coordination modes of complexation are as follows: The log K values differ significantly from one another and the uncertainty in determining the values of formation constants for higher complexes are also high in case of Eu(III)-picolinate complexes. There were no thermodynamic studies reported on complexation for: 1). rare earths with isonicotinate, 2). any of the tetravalent actinides with pyridine monocarboxylates and 3). Eu(III) or Th(IV) with the three isomeric pyridine monocarboxylic acid-N-oxidess in the solution. Most of the studies on complexation of Np(V) with pyridine monocarboxylates are limited to determination of stability constant values only but don't shed any light on the speciation to depict the amount of various stoichiometric complexes formed and their spectral properties during the course of the reaction. No detailed studies to understand the binding modes and the structural changes in terms of bond distances, bond angles, charge densities on individual atoms on coordination with the ligands in Np(V)-HA complexes at molecular level are available in the literature. Further, the systematic study of thermodynamics of complexation of the three pyridine monocarboxylates helps in interpreting the effect of position of the pyridyl nitrogen with respect to carboxylate group on the stability of the complex formed. The effect of ionic strength on protonation constants, the interaction parameters for the deprotonated pyridine monocarboxylic acid-n-oxides have also not been reported in the literature.

Chapter 1: Introduction

The first chapter of the thesis presents the brief outline on the fundamental chemical properties of f-elements covering their electronic configurations, similarities and differences between the lanthanides and actinides, hydration and hydrolysis reactions of the same. The fate of the radionuclides in aquatic environment by various chemical and physical processes like sorption, colloid formation, bio-interactions, precipitations and complexation with various inorganic and organic ligands including the anthropogenic moieties have been discussed in relevance to transportation and migration of these radio nuclides [3]. The three steps namely solubility, aqueous speciation and transportation models of a geochemical code are discussed to explain the process of complete migration of actinides from the source to far field of the repository. The data on colloids formation of actinides and thermodynamic parameters for the complexation process are important inputs during the modelling of migration process using geochemical code [32]. After discussion of the literature on complexation and colloid formation by lanthanides and actinides, the motivation for the work carried out and the scope of thesis are presented at the end of the chapter.

Chapter 2: Experimental Methodologies and Instrumentation

The chapter begins with the procedures for the preparation and standardization of various standard and stock solutions employed in the present investigations [33]. The methodology and instrumentation of autotitrator and spectrophotometer, which are the two main techniques used in the present studies to determine both the protonation and complexation constants, have been described. The instrumentation of time resolved luminescence spectrometer is also given in detail, emphasising the procedure and methodology in utilizing the emission intensity variations and life time in determining the stability constants and number of coordinated water molecules present in the primary hydration sphere of Eu(III) in the complexes respectively. The enthalpy of formation for both protonation of ligand and metal-ligand complexes was determined by isothermal titration calorimetry (ITC). The instrumentation along with the methodology to determine the enthalpy of reactions are also explained in the present chapter. The actinide colloid formation was probed with utilisation of an advanced new technique called laser induced breakdown detection (LIBD). Hence, a detailed discussion on instrumentation, size and concentration calibration procedures were illustrated for better understanding of the technique [34-35].

Chapter 3: Studies on Protonation of Pyridine Monocarboxylates, its N-Oxides and Hydroxamates

The present chapter gives results obtained from the thermodynamic investigations for the protonation of all the three categories of ligands namely pyridine monocarboxylates (PMC), pyridine monocarboxylate-N-oxides (PCNO) and hydroxamates. The discussion on determination of protonation constants of the PCNOs over a range of ionic strength starting from 0.1 M to 3.0 M and to find out the ion interaction parameters and the protonation constants at zero ionic strength (pKa0) by the application of specific ion interaction theory (SIT) was also included in the present chapter. The effect of position of the 'N' (in PMCs) and N-oxide moiety (in PCNOs) with respect to carboxylate group and the side chain (acetyl and phenyl) or additional functionality like ortho hydroxy in salicyl (in hydroxamates) on protonation process are interpreted with the help of thermodynamic parameters. Lastly, the theoretical calculations are carried out to reveal the variations in charge densities on individual atoms for the protonated and deprotonated forms of the three acids for further understanding the trends in experimental data.

Chapter 4: Thermodynamic, Luminescence and DFT Studies on Complexation of Eu(III) by Pyridine Monocarboxylates and its N-Oxides

The present chapter throws light on the determination of thermodynamic parameters for the complexation of Eu(III) with pyridine monocarboxylates and its N-oxides. Though the complexation with nicotinate and its N-oxide is through carboxylate only, very interestingly, the Eu(III) forms innersphere complexes with nicotinate while it forms outersphere complexes with nicotinate-N-oxide. The chapter presents an exclusive discussions on the speciation, thermodynamic and luminescence spectroscopic studies of the Eu(III) complexes. The linear free energy relationships, emission intensity ratios (asymmetric ratio), lifetime relation to coordination of the complexes formed has also been included in this chapter. The change in position of N-oxide has played a key role in deciding the mode of complexation with the metal ion. PANO and IANO favoured the innersphere complexation while NANO favoured an outersphere complexation for ML with a mix of inner-outer sphere complex in ML_2. At the end of the chapter, detailed DFT calculations were added to optimize the geometries of the predicted complexes and to calculate the bond length, bond angles, charges on individual atoms of these optimized geometries. The systematic variation of ligand structure on thermodynamic parameters revealed the role of chelation, charge polarization, hydrogen bonding and hydration on complexation process.

Chapter 5: Thermodynamic and Density Functional Theory Studies on Complexation of Th(IV) by Pyridine Monocarboxylates and its N-Oxides

Th(IV) is a representative of tetravalent actinides such as Pa(IV), U(IV), Np(IV) and Pu(IV). The studies on complexation of Th(IV) with pyridine monocarboxylates and its N-oxides using potentiometry and isothermal titration calorimetry have been described in the present chapter. Th(IV) complexes are relatively more stable than the corresponding Eu(III) complexes which is attributed to higher entropy change due to higher dehydration in case of former complexes. The exothermicity and higher values of formation constants of the picolinates over the other two isomers (nicotinate and isonicotinate) with thorium is due to the extra stability by chelating nature of picolinate. In the case of N-oxide bearing ligands, all the Th-PCNO complexes are endothermic and are entropy driven. The thermodynamic data has been explained on the basis of change in coordination mode due to chelation or change in ligand basicity. The study reveals the significant effect of hetero moiety (N in PMC and N-O in PCNO) on the complexation behaviour. The experimental results were corroborated with the theoretical predictions and were found in good agreement to each other.

Chapter 6: Stability, Speciation and Spectral Properties of Np(V) Complexes with Pyridine Monocarboxylates and Hydroxamic acids - A Spectrophotometric Study Combined with DFT Calculations

The present chapter aimed at determining the stability (log β) of the complexes formed; and the spectral properties of Np(V) complexes with PMCs are discussed in terms of changes in λ_{max} and molal extinction coefficients (ε). Among the three geometrical isomers the picolinate forms strongest complex through five membered chelate formation. In case of nicotinate and isonicotinate, the binding is through carboxylate group but enhanced stability than expected from pKa values of carboxylate groups is attributed to the charge transfers from nonbonding nitrogen. The trend in stability constants and charge polarization in ligand molecules on complexation has been supported by theoretically calculated binding energies and the charges on individual atoms.

The chapter also describes systematic theoretical studies to understand molecular structures and coordination modes of neptunium complexes with three different substituent hydroxamates viz., acetohydroxamate (AHA), benzhydroxamate (BHA) and salicylhydroxamate (SHA) carried out using DFT. The charges on atoms and geometrical parameters like bond angles and bond distances are used to rationalize the energetics of complexation reaction. The results revealed the dominant role of electrostatic interaction in determining the complex stability. In Np-AHA, the acetyl group increases the electron density on donating oxygen atoms compared to phenyl group in BHA, thereby making it more stable. Among the various binding modes of Np-SHA on 1:1:1 complexes, the one involving ortho hydroxyl group and hydroxyl group of hydroxamate moiety is most stable whereas in 1:2:2 complex geometries, steric constraints play the dominant role making the geometry involving hydroxamate moiety only (forming five membered ring) as most stable for the second ligand. The calculated results corroborated the experimentally obtained stability constants.

Chapter 7: The Solubility of Th(IV) - The Effect of pH, Ionic Strength and Colloid Formation

With a view to determine the solubility of Th(IV) in aqueous perchlorate solutions, studies were carried out to evaluate the content of thorium present in the supernatant of equilibrated thorium solution at various hydrogen ion concentrations and ionic strengths. Ion chromatography (IC) technique was used to find out the amount of thorium in ionic state (Th^{4+}) and ICP-MS was employed to determine the total thorium in supernatant. LIBD technique was used to determine the size and concentration of colloid particle formed if any. The present chapter starts with brief introductory lines on the importance and effect of actinide colloids in aquatic environment followed by the necessity of present studies on colloid formation by thorium under different aquatic conditions. The results of pH, IC, ICP-MS, DLS and LIBD measurements on the aged thorium samples was discussed in relation to mechanism of their formation and determination of thorium colloids. The present studies revealed the formation of colloids of range 14-37 nm at concentrations 2 to 385 ppb. The solubility products were found to be lower than the reported values upon taking into consideration the formation of colloids.

Chapter 8: Summary

The results of the studies carried out as a part of this thesis have been summarized in this chapter. The highlights on the outcomes of the Ln / An complexation with various PMCs, PCNOs and HAs and on the studies on colloid contribution under different pH and ionic strengths to thorium solubility were summarised. The trends in the thermodynamic parameters for actinides of different oxidation states and ligands of different functionality have been analysed in the light of their ionic potential (metal ions) and basicity (ligands). The need of experiments to study the complexation and colloid formation under more realistic conditions close to the natural environments was discussed at the end of chapter for future research direction.

References

1. Fergus G.F. Gibb, Waste Management 19 (1999) 207-211.
2. R. C. Ewing, W. Runde, Th. E. Albrecht-Schmitt, MRS Bulletin, 35 (2010) 859-866.
3. R. Silva and H. Nitsche, Radiochimica Acta, 70-71 (1995) 377-396.
4. R. J. Serne, A. R. Felmy, K. J. Cantrell, K. M. Krupka, J. A. Campbell, H. Bolton, Jr., J. K. Fredrickson, NUREG/CR-6124, PNL-8856, Washington (1996) 1-178.
5. M.S. Davis, P.L. Piciulo, B.S. Bowerman, L. Milian, and L. Nicolosi, NUREG/CR-3444, Vol. 2, 1985.
6. N. Evans, T. Heath, SA/ENV-0611. Nirex (2003).
7. U. Casellato, P.A. Vigato, M. Vidali, Coord. Chem. Rev., 26 (1978) 85-159.
8. G.R. Choppin, P. Thakur, J.N. Mathur, Coord. Chem. Rev., 250 (2006) 936-947.
9. T.F. Gritmon, M.P. Geodken, G.R. Choppin, Inorg. Nucl. Chem. 39 (1977) 2021-2023.
10. Y. Fridman, N. Dolgashova, D. Sarbaev, Zh. Neorg, Khim. 18 (1973) 176–181.
11. A. Yusov, A. Bessonov, M.S. Grigor'ev, A.M. Fedoseev, and G. V. Sidorenko, Radiochemistry 55 (2013) 147–154.
12. Nina A. Budantseva, Grigory B. Andreev, Alexander M. Fedoseev, Michail Yu Antipin, Jean-Claude Krupa, Radiochim. Acta 94 (2006) 69–74.
13. Zhicheng Zhang, Yanqiu Yang, Guokui Liu, Shunzhong Luo, Linfeng Rao, RSC Adv. 5 (2015) 75483–75490.
14. A. S. G. Mohamed and A. M. Franz, J. Mol. Struct., 846 (2007) 153-156.
15. Z. He, Z.-M. Wang, C.-H. Yan, Cryst. Engg. Comm., 7 (2005) 143-150.
16. S. Lis, G. Meinrath, Z. Glatty, M. Kubicki, Inorg. Chim. Acta., 363 (2010) 3847-3855.

17. Z. He, E.-Q. Gao, Z.-M. Wang, C.-H. Yan, M. Kurmoo, Inorg. Chem., 44 (2005) 862-874.
18. S. Baghdadi, C. Bouvier-Capely, A. Ritt, A. Peroux, L. Fevrier, F. Rebiere, M. Agarande, G. Cote, Talanta. 144 (2015) 875–882.
19. I. Maya, R. J. Taylor, I. S. Denniss, G. Brown, A. L. Wallwork, N. J. Hill, J. M. Rawson, R. Less, J. Alloy. and Compd. 275–277 (1998) 769–772.
20. H. Moll, M. Glorius, A. Johnsson, M. Sch_fer, H. Budzikiewicz, K. Pedersen, G. Bernhar, Radiochim. Acta 98 (2010) 571–576.
21. J. I. Kim, G. Buckau, R. Klenze, Natural Colloids and Generation of Actinide Pseudocolloids in Groundwater, Springer Netherlands (1987) 289-299.
22. Bruce D. Honeyman, Nature 397 (1999) 23-24.
23. Actinide Nanoparticle Research (Editors: Stepan N. Kalmykov, Melissa A. Denecke), Springer-Verlag Berlin Heidelberg (2011).
24. Bruce D. Honeyman, Colloidal culprits in contamination, Nature 397 (1999) 23–24.
25. Clemens Walther and Melissa A. Denecke, Chem. Rev. 113 (2013) 995−1015.
26. Ryan, J. L.; Rai, D. Inorg. Chem. 26 (1987) 4140-4142.
27. Felmy, A. R.; Rai, D.; Mason, M. J. Radiochim. Acta 55 (1991) 177-185.
28. Rai, D.; Felmy, A. R.; Sterner, S. M.; Moore, D. A.; Mason, M. J.; Novak, C. F. Radiochim. Acta 79 (1997) 239-247.
29. Rai, D.; Moore, D. A.; Oakes, C. S.; Yui, M. Radiochim. Acta 88 (2000) 297-306.
30. Greiling, H.-D.; Lieser, K. H. Radiochim. Acta 35 (1984) 79-89.
31. V. Neck, J. I. Kim, Radiochim. Acta 89 (2001) 1-16.
32. William M. Murphy, Everett L. Shock, Rev. Min. Geochem., 38 (1999) 221-253.
33. Arthur Vogel, A Text-book of Quantitative Inorganic Analysis (1961).

34. Tobias Bundschuh, Tobias U. Wagner and Rainer Köster, Part. Part. Syst. Charact., 22 (2005) 172–180.

35. Tobias Bundschuh, Tobias U. Wagner and Rainer Köster, Part. Part. Syst. Charact., 22 (2005) 181–191.

List of Figures

Figure 1.1: The important stages of nuclear fuel cycle 28

Figure 1.2: Schematic representation of the three classes of ligands (From top to bottom: pyridine monocarboxylates, pyridine monocarboxylate-N-oxides and hydroxamates) 50

Figure 2.1: Schematic diagram of a pH electrode 68

Figure 2.2: Schematic representation of major components Metrohm-905 titrando autotitrator. 69

Figure 2.3: Experimental and fitted potentiometric data for titration of Eu(III) ([Eu(III)] = 4.453 x 10^{-3} M and [HClO4] = 26.44 x 10^{-3} M) with buffered ligand solution ([picolinate] = 0.4989 M and [H] = 0.3328 M) along with speciation data. 71

Figure 2.4: Schematic diagram of JASCO V 530 spectrophotometer (W1 - Halogen lamp, D_2 - Deuterium lamp, S - Slit, F - Filter, G - Grating, BS - Beam splitter, D - Detector, Sam - Sample beam, Ref - Reference beam). (Adopted from [227]) 74

Figure 2.5: The electron energy level diagram of Eu^{3+} ion. 77

Figure 2.6: Block diagram for Time Resolved Luminescence Spectroscopy 80

Figure. 2.7: Cross sectional view of Isothermal Titration Calorimeter (TAM III, Thermometric Sweden) 85

Fig. 2.8: Picture of Isothermal Titration Calorimeter (TAM III, Thermometric Sweden) 85

Figure 2.9: Block diagram with major components of a Laser Induced Breakdown Detection (LIBD) System. 90

Figure 2.10: The plots of BDP Vs. Laser Energy (S-curves) for 30 and 100 nm

polystyrene standards (Insert: Breakdown threshold cut-off plot). 91

Figure 2.11: The plots of BDP Vs. Laser Energy (S-curves) for ultrapure water, (0.1 M and 1.0 M) $NaClO_4$ along with the real samples of thorium which were kept at an initial pH of 5 and 7 for an ageing period of 1080 days. 92

Figure 2.12: The variation in threshold energy with the particle size of standard monodispersed polystyrene nanospheres. 93

Figure 2.13: The variation in breakdown probability with the particle number density (particles/cm^3) of 30 nm standard monodispersed polystyrene nanospheres. 93

Figure 3.1: Integrated calorimetric titration data of protonation of pyridine monocarboxylates (cup solution 2.7 ml of 0.05 M ligand solution) by standard $HClO_4$ (~0.25 M) (□ – picolinic acid, ○ – nicotinic acid, Δ – isonicotinic acid) 101

Figure 3.2: Plot of Δh_{vi} vs n_{avg} for protonation of picolinate 101

Figure 3.3: Plot of Δh_{vi} vs n_{avg} for protonation of nicotinate 101

Figure 3.4: Charges on individual atoms (from left to right) of picolinate, nicotinate and isonicotinate molecules. (Colour variation: pink- nitrogen atom, yellow- carbon atom, blue- hydrogen atom, red- oxygen atom) 102

Figure 3.5: Speciation diagram along with the fitted data for protonation of PANO at T = 298 K and I = 3.0 M $NaClO_4$ (LH is the protonated form whereas L^- is deprotonated form of the base molecule; the calculated pH is deduced from fitting of the data for determination of protonation constant). 103

Figure 3.6: Raw calorimetric data for protonation of isonicotinate-N-oxide 105

Figure 3.7: Integrated calorimetric titration data of protonation of picolinate-N-oxide 105

Figure 3.8: Plot of Δh_{vi} vs. n_{avg} for protonation of nicotinate-N-oxide. 105

Figure 3.9: Variation of pKa with ionic strength without inclusion of any correction terms 110

Figure 3.10: Variation of pKa with ionic strength with inclusion of ion interaction parameters obtained by application of SIT theory 110

Figure 3.11: Absorption spectra of 5 x 10^{-5} M pyridine monocarboxylate-N-oxides on addition of NaOH (10^{-4} M) at T = 298.15 and I = 10^{-4} M $NaClO_4$ (top to bottom PANO, NANO and IANO) 112

Figure 3.12: Charges (Calculated by natural bond orbital analysis) on individual atoms on the deprotonated (left) and protonated (right) forms of pyridine monocarboxylate-N-oxides. (From top to bottom: PANO, NANO, IANO; color code of atoms: grey - carbon, purple - nitrogen, red - oxygen and pink - hydrogen). 115

Figure 3.13: Resonating structures of IANO 117

Figure 3.14: Speciation diagram for protonation of salicylhydroxamate ([SHA] = 0.01 M and [NaOH] = 0.03 M) 120

Figure 3.15: Absorption spectra of hydroxamic acids: from top to bottom - AHA, BHA and SHA ([AHA/BHA / SHA] = 1 x 10^{-4} M and [NaOH] = 4 x 10^{-4} M). 122

Figure 3.16: Charges on the key atoms of AHA (left) and BHA (right). 124

Figure 3.17: Scheme for protonation of SHA 125

Figure 4.1: Experimental and fitted potentiometric data for titration of Eu(III) with picolinate along with speciation data (concentration are given in table 4.1) 131

Figure 4.2: Experimental and fitted potentiometric data of titration of Eu(III) with nicotinate along with speciation data(concentration are given in table 4.1) 132

Figure 4.3: Experimental and fitted potentiometric data for titration of Eu(III) with Isonicotinate along with speciation data (concentration are given in table 4.1) 132

Figure 4.4: Linear Free Energy Relationship for Eu(III) –monocarboxylates (left) and Eu(III) – aminocarboxylates (right). (all the values are taken from the SC database, Academic Software). 134

Figure 4.5: Plot of Δh_{vi} vs n_{avg} for Eu(III)-picolinate complexation. 135

Figure 4.6: Plot of Δh_{vi} vs n_{avg} for Eu(III)-isonicotinate complexation 135

Figure 4.7: Spectroluminescence titration of Eu(III) (Titrand (25 mL): [Eu(III)] = 4.452×10^{-3} M and [$HClO_4$] = 26.44×10^{-3} M) with ligand solution ([picolinate] = 0.4989 M and [H] = 0.3328 M) 137

Figure 4.8: The variation of asymmetric ratio (I_{616}/I_{592}) with volume of picolinate [Eu(III)] = $4.452 \text{ X } 10^{-3}$ M and [$HClO_4$] = $26.44 \text{ X } 10^{-3}$ M) with buffered ligand solution ([Picolinate]= 0.4989 M and [H] = 0.3328 M) 138

Figure 4.9: The variation of luminescence lifetime with the volume of ligand (Left Y-axis: picolinic acid; Right Y-axis: nicotinic and isonicotinic acids) 138

Figure 4.10: Speciation plots for complexation of Eu(III) by PCNOs (top to bottom: PANO, NANO and IANO) at T = 298.15 K and I = 1.0 M $NaClO_4$. 143

Figure 4.11: The calorimetric data for the titration of Eu(III) with PCNOs (From top to bottom: PANO, NANO and IANO) at T = 298.15 K and I = 1.0 M $NaClO_4$. 145

Figure 4.12: Resonance structures of pyridine-N-oxide. 148

Figure 4.13: Resonance structures of PANO. 148

Figure 4.14: Luminescence spectra showing the variation in intensities of ${}^5D_0 \rightarrow {}^7F_J$ (J=0-2) transitions for Eu-PANO complexation. 150

Figure 4.15: The variation in the asymmetric ratio ($^5D_0 \rightarrow {}^7F_2$ / $^5D_0 \rightarrow {}^7F_1$) with the addition of PANO. 151

Figure 4.16: Decay spectra of Eu(III) excited state for different ligand to metal (L/M) ratio. (Top to bottom: Eu-PANO, Eu-NANO and Eu-IANO; (All the concentrations employed in the titration were given in table 4.1). 153

Figure 4.17: Optimized geometries for Eu(III)-PANO complexes at B3LYP/SVP level of theory. (Colour code: Yellow - Eu(III), Red - Oxygen, Blue - Nitrogen, Green - Carbon and White - Hydrogen) 154

Figure 4.18: Optimized geometries for Eu(III)-NANO complexes at B3LYP/SVP level of theory. (Colour code: Yellow - Eu(III), Red - Oxygen, Blue - Nitrogen, Green - Carbon and White - Hydrogen) 157

Figure 4.19: Optimized geometries for Eu(III)-IANO complexes at B3LYP/SVP level of theory. (Colour code: Yellow - Eu(III), Red - Oxygen, Blue - Nitrogen, Green - Carbon and White - Hydrogen) 158

Figure 5.1: Experimental and fitted potentiometric data along with speciation for titration of Th(IV) with buffered ligand solution: a) Th(IV)-Picolinate, b) Th(IV) - nicotinate and c) Th(IV)-isonicotinate (All the metal ligand concentrations are given in table 5.1). 170

Figure 5.2: Linear Free Energy Relationship for Th(IV) – aminocarboxylates (in increasing order of log K_P - picolinic acid, phenylalanine, serine, hydroxyproline, aspargine, valine, proline). (all the values are taken from the SC database, Academic Software) 172

Figure 5.3: Plot of Δh_{vi} vs n_{avg} for complexation of a) Th(IV) - picolinate and b) Th(IV) - isonicotinate (All the metal ligand concentrations are given in table 5.1). 173

Figure 5.4: Speciation diagram for complexation by Th(IV) with PCNOs (a: Th-PANO, b: Th-NANO and c: Th-IANO) in aqueous medium at T = 298 K and I = 1.0 M $NaClO_4$. (All the metal ligand concentrations are given in table 5.1) 183

Figure 5.5: Linear free energy relationship for Th(IV) monocarboxylate complexes (● - increasing order: NANO, IANO, Thenoic acid, ß-chloropropionate, γ-hydroxy butyrate, acetate and propionate; ■ - PANO) (all the values are taken from the SC database, Academic Software) 184

Figure 5.6: Calorimetric plots (h_{vi} vs. n_{avg}) for complexation by Th(IV) with PCNOs (a: Th-PANO, b: Th-NANO and c: Th-IANO) in aqueous medium at T = 298 K and I = 1.0 M $NaClO_4$. (All the metal ligand concentrations are given in table 5.1) 186

Figure 5.7: Optimized geometries for Th(IV)-PANO complexes: a) ML, b) ML_2, c) ML_3 and d) ML_4. 189

Figure 5.8: Optimized geometries for Th(IV)-NANO complexes: a) ML, b) ML_2 and c) ML_3. 189

Figure 5.9: Optimized geometries for Th(IV)-IANO complexes: a) ML, b) ML_2 and c) ML_3. 190

Figure 6.1: Tautomeric forms of acetohydroxamic acid (Left : keto form, Right : Iminol form) 298

Figure 6.2: Absorption spectra of Np(V) picolinate complexation ([Np(V)] = 2.5×10^{-4} M, [pic] = varied from 0.00 to 0.20 M at pH = 4 & T = 298 K in 0.1 M $NaClO_4$ medium; initial volume of Np(V) in cuvette 2.00 mL) 203

Figure 6.3: Absorption spectra of Np(V) nicotinate complexation ([Np(V)] = 2.5×10^{-4} M, [nic] = varied from 0.00 to 0.17 M at pH = 4 & T = 298 K

in 0.1 M $NaClO_4$ medium; initial volume of Np(V) in cuvette 2.00 mL). 203

Figure 6.4: Absorption spectra of Np(V) isonicotinate complexation ([Np(V)] = 2.5 x 10^{-4} M, [isonic] = varied from 0.00 to 0.10 M at pH = 4 & T = 298 K in 0.1 M $NaClO_4$ medium; initial volume of Np(V) in cuvette 2.00 mL). 203

Figure 6.5: Speciation diagram of Np(V) picolinate complexation ([Np(V)] = 2.5 x 10^{-4} M, [pic] = varied from 0.00 to 0.20 M at pH = 4 & T = 298 K in 0.1 M $NaClO_4$ medium; initial volume of Np(V) in cuvette 2.00 mL, ◊ - experimentally measured absorbance values, ▬ calculated absorbance values, □ - Free Np(V), ○ - Np Pic, Δ - Np $(Pic)_2$) 204

Figure 6.6: LFER of Eu(III), Th(IV) and Np(V) complexes with pyridine monocarboxylates (□ - picolinic acid, Δ - isonicotinic acid and ○ - nicotinic acid). 207

Figure 6.7: LFER of Np(V) complexes with carboxylate based ligand (○ Np-monocarboxylate in the increasing order dichloroacetate, chloroacetate, bromoacetate, iodoacetate, benzoate, acetate and phthalate [162], ■ Np-nicotinate and Np-isonicotinate (vs. log K_{P1}), and ▲ Np-nicotinate ♦ isonicotinate and ● Np-picolinate (Vs log K_{P1}+ log K_{P2}). 208

Figure 6.8: Molar absorptivity plots of Np(V)-picolinate complexation. ([Np(V)] = 2.5 × 10^{-4} M, [pic] = varied from 0.00 M to 0.20 M at pH = 4 and T = 298 K in 0.1 M $NaClO_4$ medium; initial volume of Np(V) in cuvette 2.00 mL). 209

Figure 6.9: Molar absorptivity plots of Np(V)-nicotinate complexation. ([Np(V)] = 2.5 × 10^{-4} M, [nic] = varied from 0.00 M to 0.17 M at pH = 4 and T = 298 K in 0.1 M $NaClO_4$ medium; initial volume of Np(V) in cuvette 2.00 mL). 210

Figure 6.10: Molar absorptivity plots of Np(V)-isonicotinate complexation. ([Np(V)] = 2.5×10^{-4} M, [isonic] = varied from 0.00 M to 0.10 M at pH = 4 and T = 298 K in 0.1 M $NaClO_4$ medium; initial volume of Np(V) in cuvette 2.00 mL). 210

Figure 6.11: Charges on individual atoms of (from top to bottom) picolinate, nicotinate and isonicotinate molecules (colour variation: pink-nitrogen atom, yellow-carbon atom, blue-hydrogen atom, red-oxygen atom). 212

Figure 6.12: Charges on individual atoms of Np(V) – picolinate, nicotinate and isonicotinate complexes (colour variation: violet - nitrogen atom, grey - carbon atom, blue -neptunium, pink - hydrogen atom, red- oxygen atom). 212

Figure 6.13: Complexation of Np-AHA and Np-BHA (colour variation: violet - nitrogen atom, grey - carbon atom, blue -neptunium, pink - hydrogen atom, red- oxygen atom). 217

Figure 6.14: Complexation of 1:1:1 complexes of Np-SHA (colour variation: violet - nitrogen atom, grey - carbon atom, blue -neptunium, pink - hydrogen atom, red- oxygen atom). 219

Figure 6.15: Linear free energy relationship between (a) ΔE_P Vs. ΔE_{C1} (left) and (b) Z_{eff} Vs. log K_1 (right) (Dashed line for actinide-SHA complexes). 221

Figure 6.16: Optimized geometries of 1:2:2 complexes of Np-SHA (colour variation: violet - nitrogen atom, grey - carbon atom, blue -neptunium, pink - hydrogen atom, red- oxygen atom). 222

Figure 6.17. Optimized geometry of 1:2:0 complexes of Np-SHA (colour variation: violet - nitrogen atom, grey - carbon atom, blue -neptunium, pink - hydrogen atom, red- oxygen atom). 225

Figure 7.1: Schematic representation for the mechanism of polynucleation of Th(IV) in aqueous perchlorate solutions. 234

Figure 7.2: Typical chromatograms showing Th(IV) peaks for standard (3 µg/mL) and sample (B1) solutions. (Conditions : Column : NS-1, Eluent: 0.5 mM PDCA +0.02M KNO_3 in 5%, MeOH, pH-4, Flow Rate: 1ml/min, Detection: Absorbance at 656 nm, PCR: 4.5×10^{-4} M arsenazo-III) 236

Figure 7.3: Particles size distribution (PSD) graph with two peaks of A2 sample. 240

Figure 7.4: The breakdown probabilities of Th(IV) colloids formed in the thorium perchlorate samples kept at various initial pH and ionic strengths for an equilibration of 1080 days. 242

Figure 7.5: The breakdown threshold (0.01 BDP) energies of Th(IV) colloids formed in the thorium perchlorate samples kept at various initial pH and ionic strengths for an equilibration of 1080 days. 243

Figure 7.6: TG-DSC pattern of $ThO_2.xH_2O + Th(OH)_4$ synthesized by precipitating Th(IV)-perchlorate using NH_4OH 248

Figure 7.7: TG-DSC pattern of precipitates resulted from the equilibrated samples at pH=13 under different ionic strengths (A5, B5, C5 and D5 samples). (Black: Weigh loss and Blue: Heat flow) 249

Figure 7.8: FTIR analysis of precipitates resulted from the equilibrated samples at pH=13 under different ionic strengths. 251

Figure 7.9: XRD patterns of the residues obtained at the end of each peak in thermogram for the aged thorium sample (B-5) along with a freshly prepared $Th(OH)_4$. 252

List of tables

Table 1.1: Oxidation states exhibited by actinide elements (most stable oxidation state are given in bold) 39

Table 2.1: Major hypersensitive transitions of trivalent lanthanide and actinide ions (Restructured from [226]) 73

Table 2.2: The major luminescent excitation, emission peaks and the lifetime of few lanthanide and actinide aqua ions (taken from references [122, 240-247]). 78

Table 3.1: Thermodynamic data for protonation of the pyridine monocarboxylates at 298 K and I = 1.0 M $NaClO_4$. (ΔG_P, ΔH_P, $T\Delta S_P$ are given in kJ/mol) (p.w.= present work) 99

Table 3.2: Protonation constants of pyridine monocarboxylate-N-oxides at various ionic strengths at T = 298 K. [a - studies carried out in 0.1 M $NaClO_4$ and b - ionic strength is not known, p.w - present work]. 104

Table 3.3: Thermodynamic parameters for protonation of pyridine monocarboxylate-N-oxides along with the literature data for simple monocarboxylates and pyridine monocarboxylates at T = 298 K and I = 1.0 M $NaClO_4$. (a - values determined at 0.1 M $NaClO_4$, b - thermodynamic parameters for protonation of carboxylate group only and p.w - present work) 107

Table 3.4: log β^0 and SIT parameters of pyridine monocarboxylate-N-oxides 111

Table 3.5: The prominent peaks (λ_{max} in nm), pKa from absorption measurements and pKa^0 calculated from absorption as well as by potentiometric titrations determined at T = 298 K. (^{a}Spectrophotometry, ^{b}Potentiometry) 113

Table 3.6: Calculated energies for protonated and deprotonated forms of pyridine monocarboxylate-N-oxides and the difference in energy from protonated form to deprotonated form of pyridine monocarboxylate-N-oxides.

(*- The stable conformer having minimum energy were taken). 114

Table 3.7: The bond distances of N-O and C-C (carboxylate carbon and the ring carbon attached to it) in deprotonated and protonated forms of pyridine monocarboxylate-N-oxides. 117

Table 3.8: Protonation constants of HA at T = 298 K and I = 0.1 M.(ΔG is in kJ/mol) 120

Table 3.9: Calculated energy (in eV) for protonation for HA 123

Table 4.1: Concentrations employed for the complex formation studies by Eu(III) with PMCs and PCNOs. Initial Volume of metal solution taken for potentiometric, calorimetric and luminescence studies were 10.00 mL, 2.70 mL and 2.00 mL respectively. 129

Table 4.2: Thermodynamic data for complexation of Eu(III) with pyridine monocarboxylates at 298 K and I = 1.0 M $NaClO_4$. (ΔG, ΔH and TΔS are given in kJ/mol) 132

Table 4.3: Thermodynamic data for complexation of Eu(III) with monocarboxylates at 298 K. (ΔG, ΔH and TΔS are given in kJ/mol) 136

Table 4.4: Calculated complexation energy, metal-ligand bond length and atomic charges for various Eu(III) - pyridine monocarboxylates complexes in solvent phase. 139

Table 4.5: Calculated atomic charges on bonding atoms of the bare pyridine monocarboxylates 141

Table 4.6: Thermodynamic parameters (ΔG, ΔH and ΔS) for the complexation of Eu(III) with PCNOs at T = 298.15 K and I = 1.0M $NaClO_4$. (ΔG, ΔH and TΔS are given in kJ/mol) ^{a} (I = 2.0 M $NaClO_4$) from ref [155] 143

Table 4.7: The lifetime data for the complexation of Eu(III) by PCNOs at different n_{avg} (average number of ligand molecules bound per metal ion). N_{H2O} is

the number of water molecules in the primary coordination sphere). 153

Table 4.8: Average bond distances and bond angles for the optimized geometries of Eu(III) complexes with all the three pyridine monocarboxylate-N-oxides. *within square brackets indicates innersphere nature while outside of it indicates outersphere complexation. 155

Table 4.9: Gas phase and aqueous phase stepwise energetics for the Eu(III)-PCNO complexes (IC - innersphere complex and OC - outersphere complex and ΔE and ΔG are in kJ/mol). 159

Table 4.10: Charges on all atoms of Eu(III)-PCNO complexes in aqueous phase 161

Table 4.11: Charges on bare PCNO molecules in aqueous phase 162

Table 5.1: Titration conditions for the Th(IV) complexation with pyridine monocarboxylates and their N-oxides at I = 1.0 M $NaClO_4$, T=298 K. (Potentiometric titration: cup volume 25 cm^3 for Th(IV)-PMC titrations and 10.00 mL for Th(IV)- PCNO titrations, Calorimetric titration: cup volume 2.7 mL for all complexation studies). 167

Table 5.2: Thermodynamic data for complexation of Th(IV) with pyridine monocarboxylates at 298 K and I = 1.0 M $NaClO_4$. ΔG, ΔH and TΔS are given in kJ/mol. 171

Table 5.3: Calculated metal-ligand bond length Values for various Th(IV)-PMC Complexes (‘OO’ indicates that both the oxygen atoms of the carboxylate group act as donors; ‘ON’ indicates that one oxygen atom of the carboxylate group and the ring nitrogen act as donors) 175

Table 5.4: Calculated atomic charges Values for various Th(IV)- pyridine monocarboxylate Complexes 177

Table 5.5: Calculated atomic charges for the bare pyridine monocarboxylate in

solvent phase. 178

Table 5.6: Calculated Complexation Energy Values for various Th(IV)- pyridine monocarboxylate Complexes. 179

Table 5.7: Thermodynamic parameters for the complexation of Th(IV) with pyridine monocarboxylate-N-oxides in aqueous medium at T = 298 K and I = 1.0 M $NaClO_4$. (All the metal ligand concentrations are given in table 5.1). ΔG, ΔH and TΔS are given in kJ/mol while ΔS is in J/K/mol. 183

Table 5.8: The calculated interaction energy (ΔE), Gibbs free energy of formation (ΔG) (in kJ/mol) and bond lengths (in A^0) between Thorium and the binding atoms of the ligands for all experimentally predicted Th(IV) - PCNO complexes. O (N-O), O (COO) and O (H_2O) represents the oxygen atoms of N-oxide, carboxylate of ligand molecule and water in Th(IV) aqua ion respectively. 191

Table 5.9: The charges on key atoms of all Th(IV)-PCNO complexes. O (N-O), O (COO), N (N-O), O (COO) and O (C-COO) represents the oxygen atoms of N-oxide, carboxylate, nitrogen of N-oxide and carbon atoms of carboxylate and the carbon directly attached to carboxylate carbon of ligand molecule respectively. 193

Table 5.10: The charges on key atoms of bare PCNO molecules. O (N-O), O (COO), N (N-O), O (COO) and O (C-COO) represents the oxygen atoms of N-oxide, carboxylate, nitrogen of N-oxide and carbon atoms of carboxylate and the carbon directly attached to carboxylate carbon of ligand molecule respectively. 194

Table 6.1: Stepwise stability constants (log K), ΔG and maximum percentage of Np(V) pyridine monocarboxylates complexes formed during the

course of reaction along with the reported values. 205

Table 6.2: The λ_{max} with corresponding molar extinction coefficients of the Np(V)-pyridine monocarboxylates complexes ([Np(V)] = 2.5 × 10−4 M, [pic] = varied from 0.00 M to 0.20 M, [nic] = varied from 0.00 M to 0.17 M and [isonic] = varied from 0.00 M to 0.10 M at pH=4 and T= 298 K in 0.1 M NaClO4 medium; initial volume of Np(V) in cuvette 2.00 mL). 211

Table 6.3: Charges on carboxylate oxygen atoms and pyridyl nitrogen of pyridine monocarboxylate anions. 213

Table 6.4: Binding energy, charge on individual atoms and bond distances of Np(V)-pyridine monocarboxylate complexes (1:1 ratio). 213

Table 6.5: Selected bond distances (Å) and bond angles in optimized geometry of Np(V), $NpO_2(H_2O)_5^+$ and 1:1:1 complexes of Np-HA and their interaction energies (ΔE_{C1}) (* Values are average bond distances values) 216

Table 6.6: Charges on Np atom, axial oxygen atoms, NpO_2 moiety and on total ligand atoms in different geometries 219

Table 6.7: Interaction energy for overall complexation (ΔE_{C2}) and stepwise complexation (ΔE_C) for 1:2:2 complexes of Np-SHA 223

Table 6.8: Selected bond distances, d (Å) and bond angles (in degrees) of Np-SHA (1:2:2) complexes 223

Table 7.1: Description of sample labels. (within the parenthesis are the labels assigned for the different ionic strengths and pH of the samples). 230

Table 7.2: The measured pH values of different Th(IV)-perchlorate samples after an equilibration period of ~1000 days. 235

Table 7.3: The amount of thorium present in supernatant determined by IC and ICP-MS. All concentrations are in ppm (µg/mL). 237

Table 7.4: The average diameter (Z_{avg}) along with PDI for the colloids formed in the thorium samples. 239

Table 7.5: Polydisperse colloid particle size distribution for the equilibrated thorium samples measured by DLS method. (PDI: polydispersity index, mean intensity corresponds to mode of the peak and area intensity corresponds to partial area under the peak of the total distribution) 240

Table 7.6: Size (diameter) and concentration (particles per mL and in ppb - ng/mL) of Th(IV) colloids formed by Th(IV) samples under various pH and ionic strengths. 243

Table 7.7: The fractionation of total thorium content present in the supernatants as colloidal and non-colloidal forms (ionic and polymeric form of thorium). 245

Table 7.8: The solubility and solubility products of thorium oxy(hydroxide) at different pH and ionic strengths. 246

Table 7.9: The percentage of weight loss, temperature and the type of thermal event (endo /exo) of the equilibrated samples at pH=13 under different ionic strengths (A5, B5, C5 and D5 samples). 250

Chapter 1

Introduction

Nuclear energy has been identified as one of the clean options and alternative to fossil fuel in many countries in the world, including India. India has a flourishing and largely indigenous nuclear power programme and expects to achieve 25% of electricity from nuclear power by 2050 [1]. Due to limited resources of indigenous uranium, Indian atomic energy program envisages an ambitious plan to harness the energy from fast breeder reactors (II stage) and vast thorium reserves (III stage) [2].

Chemistry plays an important role in all the stages of nuclear fuel cycle viz. mining and milling of Uranium, conversion of yellow cake (ammonium diuranate or magnesium diuranate) into uranium oxide (UO_2), fuel fabrication and its quality control, behavior of the fuel during reactor operation, spent fuel reprocessing and waste management. Inputs from chemistry are also valuable in devising strategies for decontamination of primary heat transport system and moderator system with a view to reduce the man rem and sustain the reactor operation for longer period of time. With the expansion of nuclear energy programs, research and development activities towards advanced fuels, new solvents for reprocessing and innovative waste management philosophies become necessary.

1.1. Indian Nuclear energy Programme

A modest uranium reserve and a large thorium resource in India led to the adoption of the three-stage programme [4]. The first stage is primarily based on the Pressurized Heavy Water Reactors (PHWRs), which use natural uranium dioxide as the fuel and heavy water as both moderator and coolant. A mix of the plutonium from the first stage and natural uranium would initially fuel the second stage. Plutonium fuelled fast reactors, due to their associated high breeding ratio, are the best choice for the second stage. Large-scale utilization of thorium for nuclear power has been envisaged in the third stage wherein a mix of thorium and U-233 fuels the reactors.

1.2. The Nuclear Fuel Cycle

The various activities associated with the production of electricity from nuclear reactors are referred collectively as the nuclear fuel cycle (figure 1.1). It represents the progression of nuclear fuel from creation to disposal [5].

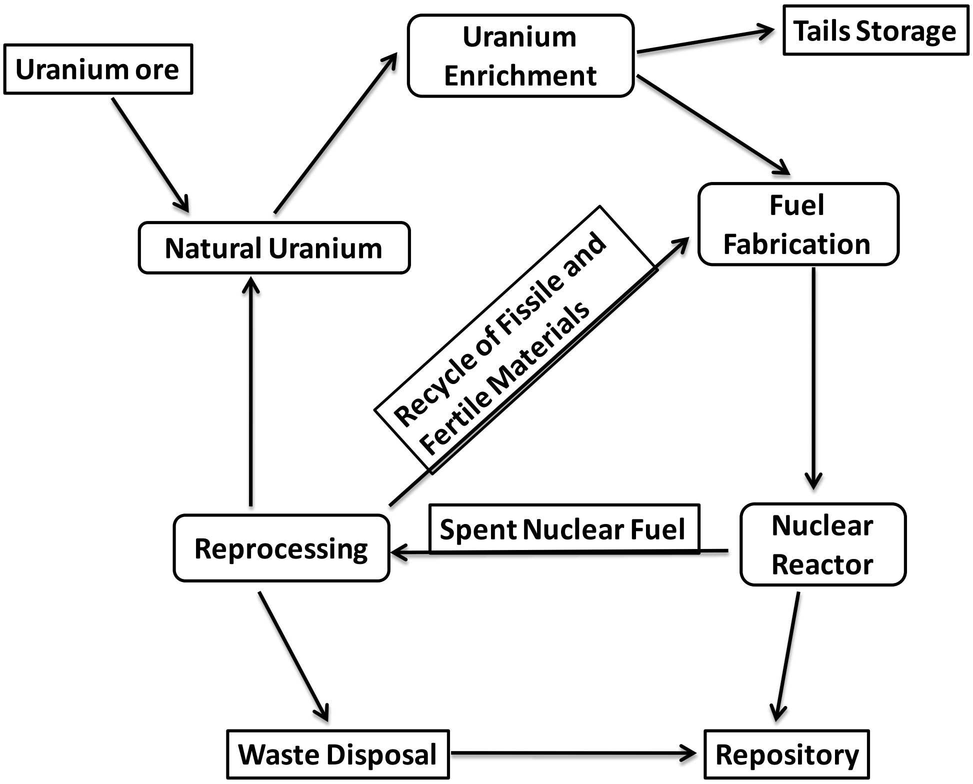

Figure 1.1: The important stages of nuclear fuel cycle

The nuclear fuel cycle typically includes the following stages [6]:

- Mining of uranium and its milling followed by conversion into yellow cake.
- Conversion of yellow cake into UO_2
- Fuel fabrication in suitable form depending upon the reactor type.
- Burning of the fuel in reactors (nuclear power or research)
- Interim storage of spent nuclear fuel

- Reprocessing (or recycling) of spent nuclear fuel to recover the valuable elements such as U, Pu.
- Management of nuclear waste.

1.3. Challenges in Nuclear Fuel Cycle

Subsequent to the irradiation of nuclear fuel in reactor, the spent fuel contains substantial amount of fission products and actinides, making it highly radioactive. In a closed fuel cycle, the spent fuel subjected to reprocessing to cover the valuable U and Pu, leaving the fission products and minor actinides in the high level waste (HLW) [6]. In the once through fuel cycle operation the fuel utilization remains below 1% [7]. The multiple reprocessing and recycling can enhance the fuel utilization by nearly a factor of 60 [8]. The closed fuel cycle results in significant reduction in the radioactive waste burden [9].

Nuclear energy production faces a number of challenges: first and foremost the requirement for continuous enhancement of safety culture (reinforced in particular by the accidents of Three Mile Island, Chernobyl and the more recently at Fukushima Daiichi), the need to adopt technologies and materials so as to make them proliferation resistant and to have a robust radioactive waste disposal and management system [10]. Management of HLW is one of the major challenges being faced by nuclear industry due to its high radiotoxicity. In once through fuel cycle it takes nearly 200,000 years for the radio-toxicity level to come down to that of natural uranium ore. By separating minor actinides from HLW, the radio toxicity of the HLW can be brought down to the level of natural U in a much shorter time scale of about few thousand years [11], which is a challenging task. Recently separation of Minor Actinides (MA) from HLW has been demonstrated on a pilot plant scale [12]. The separated minor actinides can be transmuted in accelerator driven subcritical (ADS) reactor so as to convert them into short-lived radionuclides.

1.4. The Radioactive Waste

The International Atomic Energy Agency (IAEA) defines Radioactive waste as "any material that contains or is contaminated by radionuclides at concentrations or radioactivity levels greater than the exempted quantities established by the competent authorities and for which no use is foreseen" [13]. Classification schemes for radioactive waste are based on different factors, such as safety or regulatory related aspects or process engineering demands. As per IAEA safety and protection guidelines [14], there are six classes of waste forms

1.4.1. Exempt Waste (EW): Waste that meets the criteria for clearance, exemption or exclusion from regulatory control for radiation protection purposes.

1.4.2. Very Short Lived Waste (VSLW): Waste that can be cleared from regulatory control according to arrangements approved by the regulatory body, after storing (to a low decay) for a limited period of up to a few years. This includes waste containing primarily radionuclides with very short half-lives often used for research and medical purposes.

1.4.3. Very Low Level Waste (VLLW): Waste that does not necessarily meet the criteria of EW, but that does not need a high level of containment and isolation and, therefore, is suitable for disposal in near surface landfill type facilities with limited regulatory control. Such landfill type facilities may also contain other hazardous waste. Typical waste in this class includes soil and rubble with low levels of activity concentration. Concentrations of longer lived radionuclides in VLLW are generally very limited.

1.4.4. Low Level Waste (LLW): Waste that is above clearance levels, but with limited amounts of long-lived radionuclides. Such waste requires robust isolation and containment for periods of up to a few hundred years and is suitable for disposal in engineered near surface facilities. This class covers a very broad range of waste. LLW may include shortlived radionuclides at higher levels of activity concentration, and also longlived radionuclides, but only at relatively low levels of activity concentration.

1.4.5. Intermediate Level Waste (ILW): Waste requiring a greater degree of containment and isolation than that provided by near surface disposal, owing to its content, and long lived radionuclides, ILW may contain long-lived radionuclides, in particular, alpha emitting radionuclides that will not decay to a level of activity concentration acceptable for near surface disposal during the time for which institutional controls can be relied upon. Therefore, waste in this class requires disposal at greater depths, of the order of tens of meters to a few hundred meters.

1.4.6. High Level Waste (HLW): Waste with levels of activity concentration high enough to generate significant quantities of heat by the radioactive decay process or waste with large amounts of long lived radionuclides that need to be considered in the design of a disposal facility for such waste. Disposal in deep, stable geological formations usually several hundred meters or more below the surface is the generally recognized option for disposal of HLW. The management of HLW comprises a comprehensive longterm strategy, involving solidification, interim storage, reprocessing, partitioning, packaging and the ultimate disposal in a deep geological repository [15].

1.5. Radioactivity in the Environment

The major sources of radionuclides into the environment can be either of natural or artificial origin. We are surrounded by naturally occurring radioactive elements in the geosphere, and are showred with cosmic rays entering the earth's atmosphere from outer space. We receive internal exposure from radioactive elements, which get into our bodies through food, water, and air. In addition, natural radioactive elements (^{40}K, and ^{14}C) are also present in our body [16].

The major radioactive contamination to the environment has coccurred by nuclear events, such as testing of nuclear weapons, nuclear reactor accidents, and re-entry of satellites into earth's atmosphere [17]. In addition, small quantities of radioactive materials may get into the environment through nuclear fuel cycle activities, viz., mining and milling, fuel fabrication, reactor operation and reprocessing of spent fuel and waste management [18]. Lelieveld et al. has described all the major nuclear accidents in different parts of the world along with the risk assessments for the same [19]. The beginning of the atomic age marked the onset of nuclear weapons testing, which is responsible for the radioactive contamination of a large number of sites worldwide [20].

1.5.1. Radionuclides in Aquatic Environment

The aquatic environment has received the greatest input of radionuclides from the atmospheric testing of nuclear weapons, though very low level of acceptable discharges from nuclear facilities may also add a small fraction to this inventory [21]. Santschi et al has given a detailed report on the concentration, residence times in marine waters, half lives of all the major radionuclides present in the different water bodies like oceans, rivers, estuaries etc. [22-23]. Actinides may get released to the environment at different stages of the nuclear fuel cycle, primarily through improper disposal of mill tailings and effluents, low-level discharges from enrichment and reprocessing plants [24].

MAYAK production association in former USSR and Hanford site in US are the two best examples for release of high level radioactivity in aquatic environments. Through a series of accidents and spills, the Russian nuclear facility at Mayak contaminated more than 15,000 km² with highly radioactive waste. Three significant contamination events have occurred at Mayak: direct releases of radionuclides to the Techa river, an explosion in a high-level radioactive waste tank in 1957 (Kyshtym) and dispersal of radionuclides from the dried out bed of Lake Karachay in 1967. Between 1949 and 1956, 100 Peta-Becquerel (Peta = 10^{15})

of radioactive discharge, containing strontium-90, cesium-137, plutonium, and uranium was released into the Techa river system [25]. At the Hanford Site, the U.S. produced most of its weapons grade plutonium during the Cold War. Although the facility was decommissioned in 1988, it remains the most radioactively contaminated site in the Western Hemisphere. The radioactive releases from Hanford had contaminated air, groundwater, soil and the Columbia River. Fallout had spread more than 200 radioactive isotopes over Oregon, Idaho, California, Montana and Canada [26]. Most recently, the radioactive emissions from the Fukushima nuclear disaster into the Pacific Ocean have been estimated at 78 P Bq [27].

Actinides and long-lived fission products are the major contributors to the radionuclide inventory in the aquatic environments. During the ractor operation, Pu isotopes, ^{241}Am, ^{237}Np and ^{244,245}Cm isotopes undergo neutron capture followed by β-decays. In addition, underground repositories of radioactive wastes and the soils contaminated with radionuclides may be sources of radionuclide inventory in aquatic environment.

1.5.2. Fate of Radionuclides in Aquatic Environment

Release and migration of radionuclides from nuclear wastes strongly depend on their chemical composition and on the speciation of the released radionuclides [28]. The aquatic behavior of radionuclides play the central role as water is one of the prime agents for distribution of elements on earth and hence to the living world. Consequently, aquatic ecosystems greatly affect the fate of radionuclides [22] along with the soils and sediments which may fix the radionuclides depending upn their chemical properties [29].

Among all the radioactive nuclides, actinides are of major concern in aquatic environments owing to their complex chemical behavior and the possibility of transportation and migration to faraway places from the place of origin [30-31]. Although minor in abundance in earth’s crust (U, 2−4ppm; Th, 10−15 ppm) and in seawater (U, 0.003 ppm; Th, 0.0007 ppm), lighter actinides (Th, Pa, U, Np, Pu, Am, and Cm) are important environmental contaminants associated with anthropogenic activities [24]. Actinide ions in waters are often not in a state of thermodynamic equilibrium and their solubility and migration behavior is related to the form in which they are introduced into the aquatic system. Chemical speciation, oxidation state, redox reactions, and sorption characteristics are necessary in predicting solubility of the different actinides, their migration behaviors and their potential effects on marine biota [32].

In order to predict release and transport rates, as well as design cleanup and containment methods, it is essential to understand the chemical reactions that the radionuclides will undergo in prevailing environmental conditions. The actinides in aquatic environments undergo a wide range of complex geochemical processes such as sorption, dissolution, hydrolysis, colloid formation, precipitation, redox equilibration, radiolysis, complexation by humic substances and other potential ligands. Of all these mechanisms, four important processes for consideration of actinide transportation and migration in aquatic systems are precipitation, sorption, complexation, and colloid formation [33].

1.5.2.1. Precipitation

The aqueous concentrations of actinides in aquatic environments are controlled by the dissolution and precipitation of discrete mineral phases. Contaminant uptake by organisms as well as its transport in natural systems typically occurs through the solution phase, wherein the thermodynamic solubility of contaminant-bearing minerals can directly influence the chemical reactivity, transport, and ecotoxicity of their constituent ions. Precipitation of a solid phase will have a retarding effect on their release and transport rates, and thus is considered to be one of the key processes for the immobilization of radionuclides in the environment. Hydroxide, carbonate, sulfate, phosphate and fluoride ions present in aquatic environments form insoluble compounds with actinides, which has been corroborated by solubility and speciation experiments with actinides in different oxidation states such as U(VI), Np(V), Pu(IV) and Am(III) in various aquifers [34].

1.5.2.2. Sorption

Actinide in aquifers can attach themselves reversibly or irreversibly onto rock or mineral surfaces, which tends to retard migration. The mobility of released radionuclides is strongly dependent on the sorption and desorption processes occurring at mineral surfaces. An insight into the sorption mechanisms is of paramount importance for any predictive modeling of radionuclide migration, and the bioavailability of radionuclides in the natural environment [35-36]. Actinide sorption is influenced by ionic interaction of cations with sorption sites as well as by steric effects. At neutral and basic pH, actinides interact with hydroxyl groups of polysilicic acid, and hydrated iron oxides as well as with surface hydroxyl groups of colloidal materials [32]. The chemical form of the actinides and their sorption, are highly dependent on the composition of the aqueous system with respect to pH, redox potential, and concentration of anions like carbonate, phosphate, fluoride, and organic acids. Depending on geochemical conditions and the type of mineral, reactions other than sorption, such as surface induced redox reactions and actinide incorporation into the solid matrix, are also possible [37].

1.5.2.3. Complexation

Fundamental understanding of the complexation of actinides in solution is of great importance in the development of efficient separation processes as well as the environmental management of nuclear wastes. Complexation increases the amount of radionuclide in solution and tends to increase the release of radionuclides and hence the migration rates. The inorganic ligands in ground water responsible for the complexation of the actinides are the same as discussed under precipitation. Besides inorganic ligands, humic acids (HA), organic macromolecules like fulvic acids, and pyoverdins are also ubiquitous in aquatic environments, and play important role in the migration of actinide. In addition, certain organic ligands used in separation of actindies and decontamination of contaminated components in nuclear industry may also get into the nearby aquatic streams and can complex the actinide ions, thereby significantly influencing their migration in aquatic environment [38].

1.5.2.4. Colloid Formation

Actinide ions can sorb on groundwater colloids generating pseudo colloids or can undergo extensive hydrolysis resulting in polynuclear species to form intrinsic or Eigen colloids. Colloid formation can, depending on the nature of the colloid and the solution conditions, enhance or retard migration of the radionuclide. Therefore, failure to account for the colloid migration as a potential vehicle for actinides can lead to serious underestimates of the distances that actinides can migrate. For example, at Los Alamos National Laboratory, plutonium and americium detected in monitoring wells > 1 mile from a liquid waste outfall were characterized by ultrafiltration as being bound on colloids of 25-450 nm in diameter. For these reasons, much attention has been focused recently on the role of colloids in facilitating actinide migration in the geosphere [39].

1.6. Geochemical Models

The movement and fate of radionuclides in aquatic environment is determined by two parameters: the maximum solubility of a particular radionuclide in the relevant solutions and the distribution of the particular radionuclide between the solid and liquid phases that they encounter on their migration path [40]. The geochemical model includes three sub-models: solubility model, aqueous speciation model and transport model [41].

Solubility Model: Percolating water penetrates into repository waste packages and dissolves some of the actinides. The dissolved actinides undergo re-precipitation and re-dissolution through the canisters and form a series of complex alteration phases or secondary minerals.

Aqueous Speciation Model: Some of these phases finally leave the waste packages and then enter the unsaturated zone.

Transport Model: During the migration through the UZ, the dissolved actinides species undergo a series of chemical reactions, such as hydrolysis reaction, and reaction with other complexing anion viz. carbonate over a range of pH values.

A wide range of literature is available on the many aspects related to speciation and migration of radionuclides in the geosphere. These include the data on solubility, hydrolysis, complexation, sorption, and the influence of colloids and humic substances on the transport of radionuclides. In addition, extensive literature exists on the application of new analytical spectroscopic techniques for detection and determination of speciation in aquatic systems (particularly for actinides) [42].

As discussed above, complexation of actinides with inorganic and organic ligands present in aquatic system plays a key role in their transportation and migration from the source [43]. The primary factor determining the mobility of actinides (An) in the environment is their oxidation state, which can have a wide range of values depending on environmental redox condition [24]. Apart from the natural radioactivity series, the most significant long-lived radionuclides present in HLW (for example technetium, neptunium, iodine, plutonium, americium and curium) are not normally present in measurable concentrations in relevant natural geological systems. The actinides, such as, ^{237}Np and ^{239}Pu, do exist naturally but only in very small quantities [44]. Therefore, in order to study the behavior of these critical long-lived radionuclides, suitable chemical analogues are required which exhibit similar physico-chemical properties. The trivalent lanthanides (Eu^{3+} or Nd^{3+}), tetravalent thorium (Th^{4+}), pentavalent neptunium (Np(V)) and hexavalent uranium (UO_2^{2+}) are used as chemical analogues for the actinides in +3, +4, +5 and +6 oxidation states respectively [45].

1.7. The Chemistry of Lanthanides and Actinides

The lanthanides and actinides have partially filled f orbital. The lanthanides (the fourteen elements following lanthanum, represented as ‘Ln’) are known as the rare earths and are characterized by the filling up of the 4f energy levels, which are not usually involved in bonding. These highly electropositive elements have a common oxidation state of +3 and generally resemble each other in their chemical and physical properties. They have a generic symbol “Ln”. The symbol “An” is used while referring to any of the actinide series elements. The actinides (the 14 elements following Actinium, represented as ‘An’) are the elements occupying the final row of the periodic table, that in which the 5f shell is filled. The group is also known as heavier elements or inner series transition elements following actinium [46]. All actinide series elements are radioactive in nature, they release large amount of energy on radioactive decay. These elements are used in nuclear reactors and nuclear weapons. Uranium and thorium have diverse applications, whereas americium is used in ionization chambers of modern smoke detectors. The lanthanides and actinides are the key elements in nuclear industry as fuel materials (U, Pu, Th), nuclear poisons (Gd), burn-up monitors (Nd) [47].

1.7.1. Similarities and Differences Between Lanthanides and Actinides

Though both the series of elements Ln and An, have similar electronic configuration namely filling of (n-2) f orbital, the different degree of shielding and radial distribution of 4f and 5f orbitals manifest in small differences in their chemical properties. In addition, the higher relativistic effects and poor shielding of 5f orbitals in actinides compared to that in lanthanides results in difference in the relative energies of (n-2)f and (n-1)d orbitals which in turn affects the stability of oxidation states particularly among the early actinides. Both the groups are highly electropositive and very reactive in nature. With increase in atomic number there is a decrease in atomic and ionic size (lanthanide / actinide contraction) for a particular oxidation state. Both show magnetic properties [48].

1.7.2. The Oxidation States

Lanthanide ions show +3 as the most stable oxidation state owing the non-participation of the 4f orbitals in bonding. However there are exceptions such as Eu and Yb, which also show +2 oxidation state due to extra stability of half filled (f^7) and completely filled (f^{14}) orbitals respectively. In addition Ce also shows +4 oxidation state due to extra stability of unfilled (f^0) orbitals [49].

Table 1.1: Oxidation states exhibited by actinide elements (most stable oxidation state are given in bold)

89	**90**	**91**	**92**	**93**	**94**	**95**	**96**	**97**	**98**	**99**	**100**	**101**	**102**	**103**
Ac	**Th**	**Pa**	**U**	**Np**	**Pu**	**Am**	**Cm**	**Bk**	**Cf**	**Es**	**Fm**	**Md**	**No**	**Lr**
						2		2				2	2	
3	3	3	3	3	3	**3**	**3**	**3**	**3**	**3**	**3**	**3**	**3**	**3**
	4	4	4	4	**4**	4	4	4						
		5	5	**5**	5	5								
			6	6	6	6								
				7	7									

In the actinides, the f shell does not start to fill until Pa and the 5f shell is destabilized by differential screening due to relativistic effects, which explains in part its greater availability for bonding, and the existence of high oxidation states in the early actinides, wherein the 5f orbital is higher in energy compared to 6d. As the electron are being filled in 5f it gets stabilized and becomes lower in energy than 6d, the cross over point being at Am (table 1.1) [50]. Consequently the 5f orbitals are able to participate in the bonding of early actinide, thereby showing variable oxidation states in early actinides. Beyond Am the 5f orbital gets sufficiently stabilized and hence is unable to participate in bonding thus explaining the common oxidation state (+3) of transplutonium elements, which behave chemically similar to Ln^{3+}. However, due to extra stability of half filled (f^7) and completely filled (f^{14}) orbitals, Bk and No show +4 and +2 oxidation state respectively.

Among the early actinides, the most stabile oxidation state corresponds to $5f^0$ configuration namely Ac(III), Th(IV), Pc(V) and U(VI). Beyond uranium, the most stable oxidation state is lower than that corresponding f^0 viz. Np(V) and Pu(IV) with higher oxidation states getting stabilized under alkaline conditions. An(III) and An(IV) exist in water as aqua-cations, An^{3+} and An^{4+}, An(V) and An(VI) form actinyl-cations, AnO_2^+ and AnO_2^{2+}, with protactinium(V) being an exception [43]. However, there is wide variability in the stability of a particular oxidation state across the actinide series and for some actinides several oxidation states can coexist in the same solution. This is most evident for plutonium owing to small differences in the redox potentials of Pu(III), Pu(IV), Pu(V), and Pu(VI) over a range of pH values [51].

1.7.3. Hydration of Lanthanides and Actinides

Solvation and complexation reactions of lanthanide and actinide ions are dominated primarily by strong ion-dipole interactions. Therefore, the number of donor groups (ligands) in the primary coordination sphere are the result of the subtle interplay between steric and electrostatic factors [52]. The hydration of Ln^{3+} has been mainly investigated by neutron diffraction [53], X-ray diffraction [54] and extend X-ray absorption spectroscopy [55] and by computational calculations [56]. Ln^{3+} ions in aqueous non-complexing media exist predominantly as unhydrolyzed aqua ions below pH of about 5 or 6. The ionic radius of Ln^{3+} decreases from La^{3+} to Lu^{3+} due to the lanthanide contraction, with the corresponding increase in ionic potential. This causes an increase in the ion-dipole forces that affect hydration [57]. However, owing to decrease in the ionic radii of Ln^{3+} with atomic number, the hydration number decrease from 9 (La-Pm) to 8 (Tb-Lu) with the intermediate elements (Sm-Gd) showing, non-integral hydration numbers [48].

The trivalent cations of both the An^{3+} and Ln^{3+} series have similar cationic radii, and a similar decrease in hydration number from nine to eight is observed for the trivalent actinide elements between Am^{3+} and Es^{3+}, which span the same range of cationic radii as Pm^{3+}–Dy^{3+} [58]. The coordination numbers for the Th^{4+} – Bk^{4+} aqua ions are between eight and thirteen, indicating large uncertainties in their determination [59]. In the case of actinyl cations, ‘yl’ oxygen atoms occupy the axial position and hence the water molecules can bind only through equatorial plane. Accordingly the hydration number n = 5 is the most stable for actinyl cations [60].

1.7.4. Hydrolysis of Lanthanides and Actinides

The high ionic potential of Ln and An ions result in hydrolysis reactions of type,

$$M(H_2O)_n^{m+} ==> M(H_2O)_{n-1}(OH)^{(m-1)+} + H^+ \qquad (1.1)$$

The driving force for this hydrolysis reaction is to decrease the ionic potential and is favored at higher metal ion concentration and lower H^+. Soluble hydrolysis products are particularly important in natural water systems in which trace concentrations of metal ions are present. The low cation concentrations and relatively wide range of pH conditions over which oxo and hydroxo complexes can be present can significantly affect the chemical behavior of these metals [61]. Actually, less than 2% of the total Ln^{3+} may be transformed into hydrolysis products before the formation of a solid phase, at pH values close to 7 [62]. The hydrolysis of trivalent lanthanides occurs near neutral conditions and depends on the metal ion concentration, pH, temperature and ionic strength [63] and can form mono, di, tri, tetra and polynuclear hydrolysis products. The complete data on stability constants and formation of various lanthanide hydroxides under different experimental conditions are available in literature [63-65].

The degree of cation hydrolysis is principally determined by the cation charge to radius ratio (ionic potential) and is sensitive to solution conditions including the presence or absence of other dissolved species and their concentrations, temperature, and pH. In dilute solutions, there can be an entire series of hydrolysis products spanning the monohydroxo- to the fully hydrolyzed $[M(H2O)_m(OH)_n]$ moiety and can include equilibriums that result in the simultaneous presence of two or more such species [59]. Hydrolysis reactions occur for actinides in weakly acidic to alkaline solutions in all oxidation states and often compete with other complexation reactions in neutral and basic solutions. Hydrolysis of the pentavalent actinides occurs for pH > 8. The strength of hydrolysis follows the order: $An^{4+} > AnO_2^{2+} > An^{3+} > AnO_2^{+}$ [66]. This behavior follows directly from the effective charges of the ion, which is 4, 3.3, 3 and 2.2 for tetravalent, hexavalent, trivalent and pentavalent respectively [67].

Tetravalent actinides have very strong tendency to hydrolyze even in acidic solutions (pH > 2). Moreover, An^{4+} cations of elements from protactinium through americium can undergo redox reactions relatively easily if the pH is not very low or in the absence of a strong complexant [66]. The hydrolysis of Th^{4+} involves extensive formation of polynuclear complexes. A number of hydrolyzed species, $Th_m(OH)_n$, denoted by (n,m), are observed in solution, including monomeric (1,1), (2,1), (3,1) and (4,1); dimeric (1,2), (2,2), (3,2), (4,2) and (7,2); trimeric (3,3), (5,3) and (6,3); tetrameric (8,4) and (12,4), and hexameric (14,6) and (15,6) species [68].

1.8. The Lanthanide and Actinide Complexes in Aquatic Environment

Natural water contains a large number of metal ions as well as anions, mostly in trace concentrations. Complexation increases the actinide solubility as opposed to the hydrolysis reaction [69]. The complexation strength is a measure of how effectively a ligand can compete with water in the coordination sphere of an actinide ion. The lanthanide and actinide ions are hard Lewis acids, and metal-ligand bonds are predominantly ionic [70].

The complexation of lanthanide and actinide ions by different types of ligands has been the focus of much research, in the past many decades, from the point of view of separating individual actinide elements from each other or from other elements in the nuclear fuel cycle, as well as understanding their environmental chemistry. A number of inorganic and organic ligands that can form complexes with the actinide ions in solution may be present in ground waters. Determination of the thermodynamic quantities is of prime importance in understanding the basic chemistry behind the complexation reactions such as the feasibility, stability, the enthalpy and entropy of formation. These data also help in predicting the migration behavior of the radionuclides in aquatic environment as the complexation increases the amount of the actinide in solution and thus tends to increase their release and migrations rates [71].

1.8.1. Inorganic Complexing Agents

The common anions in ground waters are hydroxide, carbonate, sulphate, phosphate, fluoride, chloride, nitrate and silicate [72]. Many authors have reported the thermodynamics and structural studies on complexation of lanthanides as well as actinides with above anions [73-77]. The reaction involving the cation, anion and water can be best explained by Eigen and Tamm, in which there are three major steps to depict the complete formation of an ion pair (complex) in the solution [78]. These include (i) the formation of ion pair of hydrated cation and anion (ii) formation of single hydration sphere and (iii) removal of hydrated water molecule to form the inner sphere complex. Eigen and Tamm suggested that the conversion from hydrated sphere contact complex (diffusion of cation and anion to each other's hydration spheres) to inner sphere complex is the slowest step during the entire complexation reaction (ligand bonding to metal in its primary coordination sphere). The entire scheme of Eigen Tamm mechanism can be correlated with the below relation.

$$M(H_2O)_x + L(H_2O)_y \rightarrow M(H_2O)_x L(H_2O)_y \rightarrow M(H_2O)_n L \rightarrow ML \rightarrow ML(H_2O)_f \quad (1.2)$$

The relative tendency of a ligand to form inner sphere compared to outer sphere is proportional to its position in spectrochemical series relative to water (the basicity of the ligand). Choppin and group extensively investigated the inner vs. outer sphere complexation for f-elements with a number of inorganic and organic ligands [79-82] and stated that the ligands whose acids have pKa < 2 form outer sphere complexes predominantly while those having pKa > 2 form inner sphere complexes with lanthanide ions.

For a given ligand, the stability of the actinide complexes decreases in the order $An^{4+} > AnO_2^{2+} > An^{3+} > AnO_2^{+}$. The strength of the monohalogeno complexes decreases in the order $Cl^- > Br^- > I^-$ and they form outer sphere complexes [83-84]. In general, the tendency of actinide ions to form complexes with univalent or bivalent inorganic ligands follows the trends $OH^- > F^- > NO_3^- > Cl^- >>> ClO_4^-$ and $CO_3^{2-} > SO_3^{2-} > SO_4^{2-}$ [66, 85]. Thermodynamic parameters for the formation of the inorganic anion complexes of actinides in various oxidation states vary in the order U > Np > Pu for penta and hexavalent actinides [86], Th < U < Np ~ Pu for tetravalent actinides, and Am < Cm < Bk < Cf for trivalent actinides [87].

1.8.2. Complexation with Natural Organic Matter

Dissolved organic matter (DOM) plays an important role in aquatic ecosystems. In many freshwaters and coastal waters, the major source of DOM is the degradation of terrestrial plant matter, which is dissolved and transported through river systems and estuaries to the marine environment. Exudation by aquatic plants and their degradation are also important sources of DOM in natural waters. DOM is a heterogeneous mixture of aliphatic and aromatic polymers and its composition varies in time and space depending on proximity to sources and exposure to degradation processes [88]. Organic ligands, from simple carboxylic acids to more complex fulvic and humic acids are present at variable concentrations in most natural waters [89]. For example, in oil-field brines, acetic acid concentrations can approach thousands of parts per million [90] whereas surface and shallow ground-waters typically contain di- and tricarboxylic acids at concentrations of ∼10−100 ppm and a high proportion of humic acids [91]. Dissolved humic substances (HS) (humic and fulvic acids) exist in surface waters and ground waters in concentrations ranging from less than 1 mg (TOC)/L to more than 100 mg(TOC)/L. (TOC = Total Organic Carbon) [92]. The formation of water-soluble complexes of humic substances with metal ions is of particular interest because complexing can increase concentrations of these ions in natural waters far above that expected based on the solubility of the inorganic species [93].

Several reports exist in literature on the interaction of lanthanides with fulvic and humic acids, involving determination of the stability, binding sites and effect of environmental conditions [94-98]. The lanthanide complexation with humic and fulvic acids display a lanthanide contraction effect, a gradual increase in log K from La to Lu by 2–3 orders of magnitude. Humic substances show polyelectrolyte effects which causes log K to increase with increasing pH and decreasing ionic strength [99]. This has been explained in terms of four different types of metal binding sites on the humic substance (HS), having different binding constant [100-101].

Most of the studies on actinide interaction with fulvic and humic substances were aimed to investigate their behavior towards the formation of pseudo colloids and/or to know the modes of binding by different models [102-108]. Actinides in all the oxidation states III, IV, V and VI can form more stable complexes with humic and fulvic acids, than hydroxide and carbonate complexes, particularly at low metal ion concentration. Therefore, they compete with inorganic ligands for actinide ions even when present in low concentration.

The presence of humic acid complexes would significantly reduce the sorption of actinides on geologic media. This does not, however, necessarily lead to a potentially enhanced mobility under environmental conditions, since humic and fulvic acids carrying trace metals also would be strongly bound to mineral surface e.g. sediments and clays [109].

1.8.3. Anthropogenic Ligands

The anthropogenic ligands are basically organic moieties which enter the aquatic arena by artificial routes like agro and pharma industries, processing plants, waste water treatment, degradation products of waste confinement barriers or co deposition during decontamination of nuclear equipment. Large number of aminocarboxylates like picolinic acid, iminodiacetic acid, EDTA, isosaccharinic acids were found near waste storage facilities in deterministic quantities [110-115]. In addition, humic substances formed by the degradation of plants and animals constitute a heterogeneous group of compounds with complexing tendency due to the presence of carboxylic, hydroxy and phenolic groups [116]. Therefore, different carboxylates including amino, polyamino poly carboxylates, hydroxy carboxylates, amino acids can used as model compounds to understand the complexing nature of humic substances with lanthanides and actinides. Thus, anthropogenic ligands can be considered as organic functional moieties, which are either introduced into the environment by manmade activities or used as model compounds to understand the nature of interactions by radionuclides with HS.

Large number of reports are available in literature on the thermodynamic parameters and the coordination modes in the complexes of lanthanides or actinides with various aliphatic and aromatic carboxylates, aminoacids, polycarboxylates and polyamino polycarboxylates [115-126]. Pyridine monocarboxylates, pyridine monocarboxylate-N-oxides and simple hydroxamic acids like aceto, benzo and salicylhydroxamic acids are widely used in nuclear industry for decontamination or for reprocessing of the spent nuclear fuel. In addition they are also used as valuable raw materials in agro and pharma industries [127-131]. Thus, a large amount of these molecules are co-disposed along with the waste into aquifer systems, resulting in their significant presence in the aquatic environments. Hence, these ligands form a small but important group of anthropogenic ligands owing to their strong complexation tendency, which plays a key role in the transportation, and migration of the radionuclides.

1.9. Actinide Colloids

Once actinide ions are introduced into groundwater, two kinds of colloids can be distinguished: (1) real colloids, which are produced by aggregation of hydrolyzed actinide ions through oxo or hydroxyl bridge formation, and (2) pseudo colloids, which are generated by sorption of actinide ions on real colloids or on aquatic colloids [132-133]. The hydrolysis reaction, through splitting up the proton from hydrated water molecules, is the primary chemical process of actinide ions in aquatic systems of near neutral pH. The process proceeds to polynucleation, depending on the effective charge of actinide aquoions, and then to formation of colloidal species through oxo or hydroxyl bridging. The relative tendency to generate real colloids of actinide ions follows their hydrolysis properties. The real-colloid generation is unambiguously observed for tetravalent actinide ions, less clearly for trivalent and hexavalent actinide ions [134].

Actinide containing particles exhibit great variability in size, activity, composition, and structure, depending on their source, mode of formation, and history [135-136]. The colloids act as a third phase and, depending upon their surface charge and size, can enhance or retard the migration of the actinides in the geosphere [137]. Therefore, failure to account for the colloid migration as a potential vehicle for actinides can lead to serious underestimates of the distances that actinides can migrate [138]. Walther and Denecke have reviewed the literature on the source, formation and interaction of colloids as well as their role in the migration of actinides recently [139].

1.10 Thermodynamic Parameters - An Insight to Complexation

Modeling the behavior of actinides under environmental conditions is very challenging as it requires accurate information about thermodynamic parameters for complexes formed by interaction actinides with potential ligands that can regulate the environmental transport of metal ions through formation of complexes. For instance, in multi-component systems, such as natural waters, the stability constants of all the known complexes and the concentrations of each component are used to predict the resultant species. It is often difficult to measure the chemical activities of actinide ions, ligands, and complexes, and hence concentrations are used commonly in place of activities for calculation of stability constants. Such apparent stability constants are valid for only a limited range of conditions due to their dependence on the ionic strength of the solution. These values also help in predicting the migration behavior of the radionuclides in aquatic environment. The enthalpy and entropy of complex formation reflect the disruption of the solvent structure as well as the combination of the ions. The elimination of water molecules from both the metal cation and the ligand anion in the complexation results in an endothermic enthalpy change, which is compensated for by a positive entropy contribution. Thus, the determination of the thermodynamic quantities , such as, stability, enthalpy and entropy of formation is of prime importance in understanding the basic chemistry behind the complexation reactions. These data also serve as valuable inputs in the geochemical models used to predict speciation and migration of radionuclides in geosphere.

1.11. Motivation for The Present Work

Mixtures of decontamination reagents such as EDTA (ethylene diaminetetraacetic acid), NTA (nitrilotriacetic acid) and picolinic acid are used for in decontamination in nuclear industry [110]. Nicotinic acid, also known as vitamin B-3, is one of the B-complex vitamins that support the metabolism of natural compounds needed for good health [140] and prohibits the penetration of Np and Pu into living organisms [141]. Isonicotinic acid and its derivatives are chiefly used in manufacturing pharmaceuticals [142] and agrochemicals [143].The natural occurrence of N-oxides in plant/animal tissues, and microorganisms has posed interesting problems as to the biochemistry and function of these compounds in biological systems [144]. Through feed wastes or from wastewater treatment plants, N-oxides might enter soils, sediments, and aquatic environments as contaminants [145]. Formo- and acetohydroxamic acid are used as reducing and stripping agents for neptunium in modified PUREX and UREX solvent-extraction processes currently under development for future spent fuel reprocessing [146]. Thus, a large amount of these molecules are either co-disposed along with the waste or released as effluents into aquifer systems, resulting in their significance presence in the aquatic environment. In this context, the interaction of actinides with pyridine monocarboxylates, its N-oxides and hydroxamates (Figure 1.2) in aquatic environment is quite prominent. Hence, the studies on complexation of actinides with pyridine monocarboxylates and their derivatives would be very informative to know the fate of these contaminants in the aquatic environments. Thus, it is important to study the interaction of actinides with pyridine monocarboxylates, its N-oxides and hydroxamates (Figure 1.2).

Pyridine Monocarboxylic acids

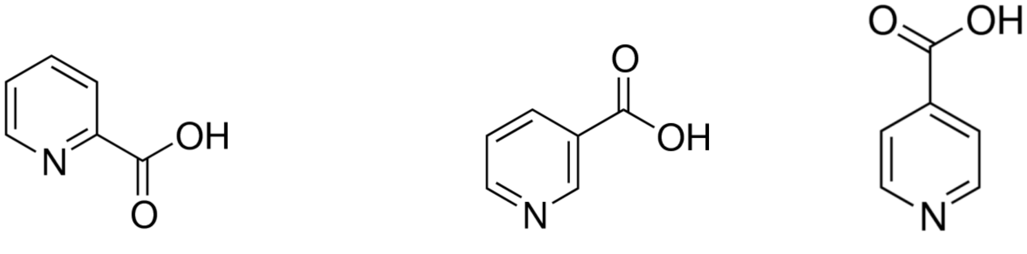

From left to right: Picolinic acid, Nicotinic acid and Isonicotinic acid.

Pyridine Monocarboxylic acid N-oxides

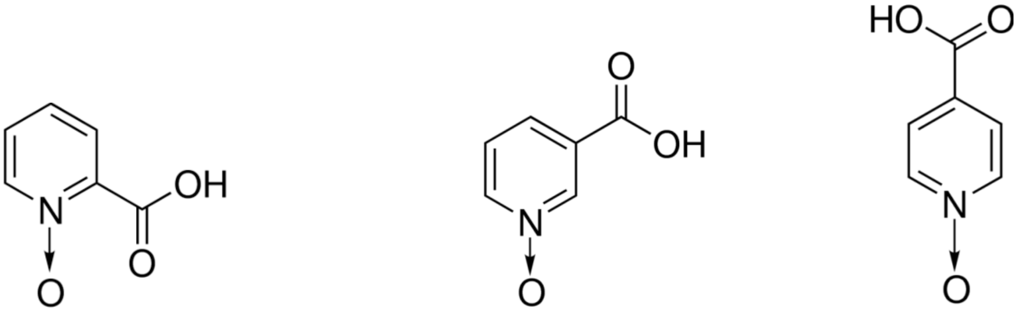

From left to right: Picolinic acid-n-oxide (PANO), Nicotinic acid-n-oxide (NANO), Isonicotinic acid (IANO)

Hydroxamic acids

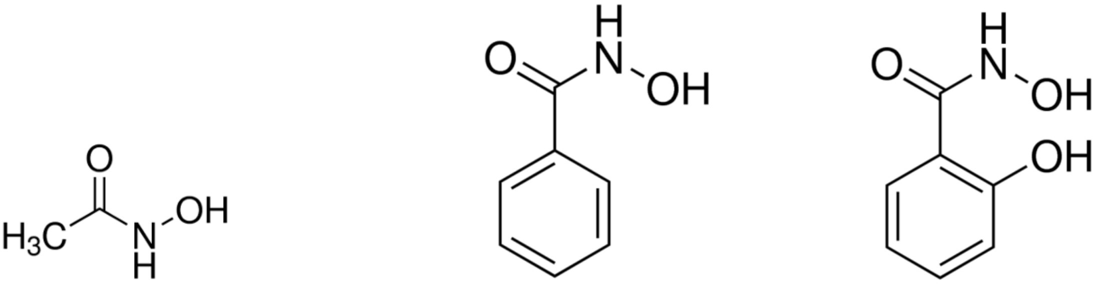

From left to right: Acetohydroxamic acid (AHA), Benzhydroxamic acid (BHA) and Salicylhydroxamic acid (SHA).

Figure 1.2: Schematic representation of the three classes of ligands (From top to bottom: pyridine monocarboxylates, pyridine monocarboxylate-N-oxides and hydroxamates).

The literature reports on interaction of actinides with anthropogenic ligands are mainly concerned with aliphatic, aromatic carboxylates and aminocarboxylates [147-153]. The studies on the aqueous complexation of either lanthanides or actinides with pyridine monocarboxylates, its N-oxides and hydroxamates are very limited. Most of the thermodynamic studies on complexation of pyridine monocarboxylic acids in solution are concerned with transition metals. A large number of crystallographic and spectroscopic studies on lanthanides pyridine carboxylates and their derivatives were done to explore their luminescence properties for various applications, and there are only few studies on the thermodynamics of complexation of rare earths with pyridine monocarboxylates [154-158]. In the recent years, few studies have been reported on the complexation of neptunium with picolinic acid, and nicotinic acid [159-165].

Most of the literature reports on chemistry of interaction of lanthanides in general and europium in particular with pyridine monocarboxylate-N-oxides (PCNOs) are related to the synthesis of polymers or on coordination networks in solid state to explore their applications in luminescence, catalysis and many other fields [166-170], but the studies related to chemistry in solution are limited [155, 171]. Many studies have reported the solid-state characterization of uranyl and thorium complexes with different aromatic-N-oxides [172-174]. Interaction of simple hydroxamates with tetra- and pentavalent actinides has been studied with a view to understand their extraction and reduction [175-181]. The only studies towards determination of stability constant involve complexation of U(VI) complexes by BHA, SHA and benzoic acid [182] and that of Np(V) by HA [183] in aqueous medium. A detailed literature survey on actinide complexation by pyridine monocarboxylates and their derivatives revealed that, (i) The log K values differ significantly from one another and the uncertainty in determining the values of formation constants for higher complexes are also high in case of Eu(III)-picolinate and nicotinate complexes. (ii) To the best of our knowledge no studies were reported the thermodynamic quantities of complexation of rare earths with isonicotinate in solution. (iii) Further, there are no thermodynamic studies on the complexation of any of the tetravalent actinides with pyridine monocarboxylates in the solution, although a few thermo gravimetric and crystallographic studies were reported on the complexes of pyridine carboxylates and its derivatives with thorium [184-187]. (iv) Most of the studies on complexation of Np(V) with pyridine monocarboxylates are limited to determination of stability constant values only but don't shed any light on the speciation plots to depict the amount of various stoichiometric complexes formed and their spectral properties during the course of the reaction. (v) Only the protonation constants of the three-pyridine monocarboxylate-N-oxides were found in literature [188-189] but no other thermodynamic parameters for the protonation of any of the three-pyridine monocarboxylate-N-oxides have been reported. (vi) The effect of ionic strength on protonation constants, the interaction parameters for the deprotonated pyridine monocarboxylic acid-n-oxides has also not been reported in the literature. (vii) There were no thermodynamic studies on aqueous phase complexation of Eu(III) / Th(IV) with all the three isomeric pyridine monocarboxylic acid-N-oxides.

With this in view a systematic study of the complexation of Eu(III)/Th(IV)/Np(V) with pyridine monocarboxylates or pyridine monocarboxylate-N-oxides or hydroxamates has been carried out to determine either thermodynamic parameters and/or coordination modes of complexation. Further, a systematic study of thermodynamics of complexation of the three-pyridinemonocarboxylates has also been carried out to investigate the effect of position of the pyridyl nitrogen with respect to carboxylate group on the stability of the complex.

Another important area of research in actinide speciation, which has attracted considerable interest in the recent times, is the role of colloids in the migration of actinides in geosphere. The presence of actinide colloids provides an important pathway for enhancing the migration of radionuclides, which can be of significance in the performance assessment of a geologic repository for high-level nuclear waste [135-138]. The migration behavior of colloids in groundwater can be very different from both soluble species and precipitates. The presence of colloids can increase the total concentrations of actinides above the equilibrium thermodynamic solubility limits, and thereby increase the mass amount of actinides transportable to the environment. Solubility data reported for amorphous Th(IV) precipitates, called either amorphous hydroxides $Th(OH)_4$ (am) or hydrous oxides $ThO_2.xH_2O(am)$, show considerable discrepancies [190-194]. This may be due to the fact that the reported solubility do not refer to a well-defined solid phase but to hydrated oxyhydroxide $ThO_n(OH)_{4-2n}.xH_2O(am)$ with $0 \leq n \leq 2$ depending on the preparation method, pre-treatment, alteration, and temperature. Furthermore, the presence of colloids can also explain the widely scattered Th(IV) concentrations measured in the various solubility studies [195].

With this in view the solubility of thorium in aqueous solutions under the varying conditions of pH, ionic strength and centrifugation rate at long ageing periods was studied. For this purpose various experimental techniques, viz., dynamic light scattering (DLS), laser induced breakdown detection (LIBD), ion chromatography (IC) and inductively coupled plasma mass spectrometry (ICP-MS) were used.

1.12. Scope of The Thesis

The complexation and colloid formation are inevitable processes that play a key role in the transportation and migration of radionuclides. The thermodynamic data on complexation and contribution of colloids in solubility limits are crucial parameters for any cleanup or decontamination strategies and for geochemical modeling for safety assessment of a deep geological repository. Anthropogenic ligands, though not present as such in environment, could become a matter of concern for nuclear waste management methodologies, due to their co-deposition with the waste and release from the industries. Most of the anthropogenic ligands are the organic moieties with one or more dissociable protons, which occurs on complexation with various metal ions present in the aqueous medium. Thus, the protonation/deprotonation process is always a part of complexation reaction that needs to be taken care for the thermodynamic studies on complexation process.

The present thesis has mainly three categories of investigations: (a) The protonation studies of the ligands, (b) The complexation of metal ions with the ligands and (c) The contribution of colloids in determining the solubility of thorium in aqueous perchlorate solutions.

(a) There are two protonation sites in pyridine monocarboxylates and their N-oxides, one at carboxylate oxygen and the other at nitrogen in the pyridine ring or the oxygen of N-O moiety in case of N-oxides. The protonation constants revealed the presence of mono-protonated (protonated carboxylate group) as well as di-protonated pyridine monocarboxylate (protonated carboxylate and nitrogen atom). The protonation of nitrogen atoms in pyridyl monocarboxylates is found to be highly exothermic whereas enthalpy of protonation of carboxylate is nearly zero. The protonation of carboxylate groups is mainly driven by entropy whereas protonation of pyridyl nitrogen atoms are driven by entropy as well as enthalpy. In case of pyridine monocarboxylate-N-oxides, the pKa determined by Potentiometry follow the order: PANO > IANO > NANO at all ionic strengths. The calorimetric results revealed entropy driven protonation of PANO while the other two have minor contribution to enthalpy. The hydroxamate group has three potential donor atoms: the carbonyl oxygen, the nitrogen and oxygen of the -NHOH group (Figure 1.2). Hydroxamates behave generally as bidentate ligand, coordinating metal ions by means of carbonyl and deprotonated hydroxyl group oxygen atoms, leading to the formation of stable five membered rings. The analysis of potentiometric data indicated the presence of monoprotonated species for AHA and BHA, wth mono- and di- protonated species for SHA.

(b) The thermodynamic parameters (log K, ΔG, ΔH and ΔS) for complexation of Eu(III)/Th(IV) with pyridine monocarboxylates and their corresponding N-oxides have been studied by potentiometry and calorimetry. Time resolved luminescence spectroscopy (TRLS) of Eu(III) was employed to reveal the stoichiometry of the complexes as well as to determine their log K. Life time measurements by TRLS, for the decay of $^5D_0$ state of Eu(III) also used to reveal the mode of complexation (inner vs. outersphere) in Eu(III) complexation with pyridine monocarboxylate-N-oxides. The log β values, speciation and spectral properties of Np(V) complexes with pyridine monocarboxylates viz. picolinate, nicotinate and isonicotinate, have been studied using spectrophotometry. The role of substitution in hydroxamate on complexation was investigated by carrying out DFT calculations on Np-AHA, Np-BHA and Np-SHA complexes. The charges on atoms and geometrical parameters like bond angles and bond distances are used to rationalize the energetic of complexation reaction. The experimental observations on the stability and binding mode of the complexes are corroborated by theoretical calculations using the TURBOMOLE software. The results obtained by experiments were interpreted using those calculated theoretically for the complexes for various geometries.

(c) Speciation of thorium in aqueous phases, is greatly influenced by pH to the hydrolysis, which is also dependent on metal ion concentration. There has also been evidence that thorium may form polymeric chains attaching on the colloid particle instead of only sorbing at the host rock surface site. These polymer chains may increase the amount of metal that may be associated to the colloid, therefore transporting higher quantities outside of the source. In the present study, the effect of pH, ionic strength and centrifugation rate on solubility of thorium and its fractionation to ionic and colloids form as been studied. The presence of colloids of size 14-37 nm at very high concentrations (10^{10}-10^{12} particles per mL) were found to be formed under the experimental conditions and has a significant effect on the solubility of thorium in aqueous perchlorate solutions.

Chapter 2

Materials, Methodology and Instrumentation

In the present chapter, the details of the methodologies employed to study the complexation and speciation of actinides and lanthanides in aqueous systems have been described along with the instrumentation. The methodologies include, (i) potentiometric titration of ligand solution with acid and/or base to determine the protonation constants as well as the titration of the metal ion solution with the ligand solution to determine the stability constant of the complex, (ii) UV-visible spectrophotometric measurements of the metal ion solution with addition of ligand solution, (iii) time resolved luminescence spectroscopy of metal ions solutions with varying ligand to metal ratio, (iv) isothermal titration calorimetry of metal ligand systems for determination of enthalpy of complexation, (v) fitting of the titration data with the help of nonlinear least square based programmes, viz., Hyperquad, (vi) density functional theory (DFT) based calculation of structures and energies of the complexes and laser induced breakdown detection (LIBD) for determination of size and concentration of aquatic colloids.

The aqueous speciation studies, namely, complexation and colloid formation under different aquatic conditions, need the preparation and standardization of a number of metal ion solutions (Eu, Th, Np), ligand solutions (pyridine monocarboxylates, its N-oxides, hydroxamates), standard solutions (NaOH, $HClO_4$, $NaClO_4$) and reagent solutions (buffers, indicators). The thermodynamic parameters are greatly affected by the accuracy in concentration of the solutions used to study the protonation or complexation process. For a complete thermodynamic study, there are three key factors that always play an essential role: (i) the preparation and standardization of all the solutions employed for the study; (ii) the instrumentation and methodology employed for the determinations; and (iii) the methods for data analysis which give a final value for the thermodynamic parameter.

2.1. Preparation and Standardization of Solutions

All the solutions employed during the course of present study can be categorized into three groups.

1. Metal ion solutions
2. Ligand Solutions
3. Auxiliary Solutions

Metal ion stock solutions are maintained at high acidity to avoid the hydrolysis, particularly in case of actinides in higher oxidation states. Auxiliary solutions are essential to maintain the experimental conditions, viz., ionic strength ($NaClO_4$) or for preparation and standardization of metal ion and ligand solutions (acids, bases, buffers and indicators).

2.1.1. Metal Ion Solutions

The work carried out as a part of present thesis involves the complexation studies with europium, thorium and neptunium in aqueous solutions.

Eu(III) Stock Solution: Eu(III) stock solution was prepared by dissolving A.R. grade Eu_2O_3 in concentrated nitric acid. This was converted into perchlorate by evaporating to dryness and dissolving the residue in concentrated $HClO_4$. The solution was evaporated to dryness thrice and finally the residue was dissolved in 0.01 M $HClO_4$. The Eu(III) concentration in the stock solution was determined by EDTA titration using xylenol orange as an indicator [196].

Th(IV) Stock Solution: $Th(NO_3)_4.4H_2O$ was dissolved in water and $Th(OH)_4$ (s) was precipitated by adding NaOH. The precipitate was centrifuged, washed with water and re-dissolved with an excess of $HClO_4$. The precipitation and dissolution were repeated three times. The Th(IV) concentration in the stock solution was determined by EDTA titration using xylenol orange as an indicator [196].

Np(V) Stock Solution: Np-237 stock solution in our laboratory was used for the present studies. It was purified from Pa-233 and other cations using anion exchange (Dowex 1X4) resin in nitrate form [197]. The acidity of the Np stock solution was adjusted to 7.5 M (HNO_3) for loading on the anion exchange resin (Dowex 1X4). To this solution, ferrous sulphamate and hydrazine solutions were added to ensure that all Np(VI) and Np(V) is reduced to Np(IV). This feed solution was loaded on the column and after three column volume washings of the resin with 7.5 M HNO3, the solution was eluted with 0.35 M HNO3 to collect the purified Np solution. The purity of neptunium was checked by alpha spectrometry. The concentration of purified neptunium was estimated by alpha spectrometry and by measuring the absorbance at 981 nm by UV-VIS-NIR spectrophotometry [198].

2.1.2. Ligand Solutions

The three types of ligands used in the present study include**, (i)** Alfa Aesar, A.R. grade picolinic acid (pyridine-2-carboxylic acid) (99%), nicotinic acid (pyridine-3-carboxylic acid) (99%), isonicotinic acid (pyridine-4-carboxylic acid) (99%), (ii) A.R. grade (Sigma Aldrich) picolinic acid-N-oxide (PANO or pyridine-2-carboxylic acid-N-oxide) (97%), nicotinic acid-N-oxide (NANO or pyridine-3-carboxylic acid-N-oxide) (98%), isonicotinic acid-N-oxide (IANO or pyridine-4-carboxylic acid-N-oxide) (99%), and (iii) A.R. grade (Sigma Aldrich) acetohydroxamic acid (AHAH) (98%), benzhydroxamic acid (BHAH) (99%) and salicylhydroxamic acid (SHAH) (99%). The ligand solution for complexation titration were prepared by dissolving appropriate amounts in milliQ (18 Mohm.cm) water and addition of required amounts of standardized NaOH for half neutralization.

2.1.3. Auxiliary Solutions

Carbonate free NaOH was used for the electrode calibration. Potassium hydrogen phthalate as a primary standard has been used to standardize the NaOH. The ionic strength in all the solutions was adjusted by using $NaClO_4$. Acetate buffer was used to adjust the pH of europium solution to determine its concentration by EDTA titration with xylenol orange as indicator. For all acid-base standardization, phenolphthalein was used as an indicator solution. Zn(II) solution is used as primary standard solution for the standardization of EDTA solution. MilliQ water was (Millipore, resistivity =18 M Ohm.cm) was used for preparing all aqueous solutions.

Potassium Hydrogen Phthalate and Zinc Solution: A known amount of potassium hydrogen phthalate / zinc metal was dissolved in ultrapure water to prepare the corresponding solution of required strength.

Phenolphthalein Indicator Solution: 0.5 g of phenolphthalein is dissolved in 100 mL solution consisting of 50 mL ethanol and 50 mL water.

Xylenol Orange Indicator Solution: 0.1 g of xylenol orange is dissolved in 100 mL of high pure water and filtered if necessary.

NaOH Solution: A known amount of Suprapure (> 99.99 % purity) sodium hydroxide (pellets) was dissolved in appropriate amount of milliQ water. Thorough washing was done to remove the carbonate impurity present on pellets. The addition of $Ba(OH)_2$ to NaOH solution removes carbonate as $BaCO_3$ in precipitate form and the supernatant after filtration can be taken as such for the stock solution. The concentration of NaOH is determined by titrating against potassium hydrogen phthalate wherein phenolphthalein was used as an indicator.

$HClO_4$ Solution: Supra-pure (70 %) perchloric acid was diluted in milliQ water to prepare the $HClO_4$ working solutions. The standardization was done by titrating against NaOH with phenolphthalein as indicator.

EDTA Solution: Required amount of disodium salt of EDTA was dissolved in milliQ water and the solution was standardized by titrating against Zn(II) solution. Eriochrome Black T (EBT) was used as indicator and the change in colour of EDTA solution from light red to light sky blue is the indication of end point.

2.2. Equilibrium Constants

The formation constant (K_f) of a complex, which is also called the stability constant, is defined as the equilibrium constant of the following complexation reaction,

$$x\,M \quad + \quad y\,L \quad <=> \quad M_xL_y \tag{2.1}$$

$$K_f = \frac{[M_xL_y]}{[M]^x[L]^y} \tag{2.2}$$

where M is a metal ion, L is a ligand, and x and y are coefficients. The stability constants could be represented in two ways: stepwise and overall. For a complex formation with stoichiometry ML_4, the reaction schemes could be in two ways

$$M \quad + \quad L \quad <=> \quad ML \tag{2.3}$$

$$ML \quad + \quad L \quad <=> \quad ML_2 \tag{2.4}$$

$$ML_2 \quad + \quad L \quad <=> \quad ML_3 \tag{2.5}$$

$$ML_3 \quad + \quad L \quad <=> \quad ML_4 \tag{2.6}$$

or the complexation scheme can also be shown in a single reaction as

$$M \quad + \quad 4\,L \quad <=> \quad ML_4 \tag{2.7}$$

The reactions 2.3 to 2.6 represent the stepwise formation of the complex ML_4 with their equilibrium constant known as step wise stability constants (K_i), while equation 2.7 represents the formation of ML_4 in one step, with its equilibrium constant called as cumulative stability constant (β_i). The stepwise stability constants for all the reactions leading to the formation of complex ML_4 can be represented as follows

$$K_1 = \frac{[ML]}{[M][L]} \qquad K_2 = \frac{[ML_2]}{[ML][L]} \quad K_3 = \frac{[ML_3]}{[ML_2][L]} \quad K_4 = \frac{[ML_4]}{[ML_3][L]} \tag{2.8}$$

Similarly, the overall stability constants for the successive addition of ligand to metal for formation of all the four complexes are

$$\beta_1 = \frac{[ML]}{[M][L]} \quad \beta_2 = \frac{[ML_2]}{[M][L]^2} \quad \beta_3 = \frac{[ML_3]}{[M][L]^3} \quad \beta_4 = \frac{[ML_4]}{[M][L]^4} \tag{2.9}$$

from equations 2.8 and 2.9, the relation between overall or cumulative stability constants and stepwise stability constants is deduced as

$$\beta_N = K_1 \text{ x } K_2 \text{ x } K_3 \text{ x } .... \text{ x } K_N \qquad (2.10)$$

or in terms of logarithmic values

$$\log \beta_N = \log K_1 + \log K_2 + \log K_3 + ... + \log K_N \qquad (2.11)$$

2.3. Activity and Activity Coefficients

The thermodynamic equilibrium constant is defined as the ratio of activities of products to that of the reactants. For infinitely dilute solutions, the activities can be equated with the concentrations. However, in practice, the experiments are carried out at finite concentrations and hence the measured equilibrium constants need to be corrected for the finite concentration of solutes. For this purpose, the conditional equilibrium constants are determined at a constant value of ionic strength and the ionic strength dependent data are extrapolated to zero ionic strength to determine the thermodynamic stability constant. The ionic strength (I) of a solution is a measure of the concentration of ions in that solution.

$$I = \Sigma C_i \text{ x } Z_i^2 \qquad (2.12)$$

where C_i and Z_i are the concentration and charge of the species 'i' respectively. The thermodynamic activities (a_i) of aqueous solute species are usually defined on the basis of molalities. Thus, the concentrations (C_i) in equation 2.12 are expressed in molality while γ_i, represents the molal activity coefficients.

Ionic solutions depart strongly from ideality due to the long-range electrostatic interactions between the reacting species and with the solvent. Deviations from ideality are accommodated by modifying the concentration by an activity coefficient [199]. Concentration can be related to activity using the activity coefficient as,

$$a_i = \gamma_i \text{ x } C_i \qquad (2.13)$$

where a_i is the activity, γ_i is the activity coefficient and C_i is the concentration of the species 'i' in the solution.

2.4. Methodology to Determine The Stability Constants

Determination of stability constant of a complex requires the determination of the concentration of the complex, as well as the concentration of free metal ion and free ligand. These three quantities are related to each other through the equation of stability constant 2.9 as well as the mass balance equations. For the formation of a complex of stoichiometry ML_4, shown by equation 2.7, the mass balance equations can be written as

$$[M]_T = [M]_F + [M]_C \qquad (2.14)$$

and

$$[M]_C = [ML] + [ML_2] + [ML_3] + [ML_4] \qquad (2.15)$$

where the subscripts T, F and C correspond to total, free and complex. From the expressions of overall stability constants for these successive complexes as shown by equation 2.9, the complexed metal concentration can be written as,

$$[M]_C = \beta_1 [M]_F [L]_F + \beta_2 [M]_F [L]_F^2 + \beta_3 [M]_F [L]_F^3 + \beta_4 [M]_F [L]_F^4 \qquad (2.16)$$

Substituting the value of $[M]_C$ from equation 2.15 in equation 2.16,

$$[M]_T = [M]_F + \beta_1 [M]_F [L]_F + \beta_2 [M]_F [L]_F^2 + \beta_3 [M]_F [L]_F^3 + \beta_4 [M]_F [L]_F^4 \qquad (2.17)$$

$$[M]_T = [M]_F (1 + \beta_1 [L]_F + \beta_2 [L]_F^2 + \beta_3 [L]_F^3 + \beta_4 [L]_F^4) \qquad (2.18)$$

$$[M]_T = [M]_F (1 + \Sigma \beta_i [L]_F^i) \text{ where } i = 1\text{-}4. \qquad (2.19)$$

Similarly, the mass balance equation for the total ligand concentration are

$$[L]_T = [L]_F + [L]_C \qquad (2.20)$$

and

$$[L]_C = [ML] + [ML_2] + [ML_3] + [ML_4] \qquad (2.21)$$

From the expressions of overall stability constants for these successive complexes as shown by equation 2.9, the complexed ligand concentration can be written as,

$$[L]_C = \beta_1 [M]_F [L]_F + 2 \beta_2 [M]_F [L]_F^2 + 3 \beta_3 [M]_F [L]_F^3 + 4 \beta_4 [M]_F [L]_F^4 \qquad (2.22)$$

Substituting the value of $[M]_C$ from equation 2.22 in equation 2.20,

$$[L]_T = [L]_F + \beta_1 [M]_F [L]_F + 2 \beta_2 [M]_F [L]_F{}^2 + 3 \beta_3 [M]_F [L]_F{}^3 + 4 \beta_4 [M]_F [L]_F{}^4 \tag{2.23}$$

$$[L]_T = [L]_F + [M]_F (1 + \beta_1 [L]_F + 2 \beta_2 [L]_F{}^2 + 3 \beta_3 [L]_F{}^3 + 4 \beta_4 [L]_F{}^4) \tag{2.24}$$

$$[L]_T = [L]_F + [M]_F (1 + \Sigma\, i\, \beta_i [L]_F{}^i) \text{ where } i = 1\text{-}4. \tag{2.25}$$

The complexation of metal ions with ligands having dissociable protons is always accompanied by protonation and deprotonation process. Thus, the mass balance equation for total hydrogen ion concentrations are necessary to solve the equations to calculate the protonation constants. The mass balance equation for total hydrogen ion concentration for a diprotonated ligand can be given as

$$[H]_T = [H]_F + [H]_C \tag{2.26}$$

and

$$[H]_C = [HL] + [H_2L] \tag{2.27}$$

$$[H]_C = \beta_{P1} [H]_F [L]_F + 2 \beta_{P2} [L]_F [H]_F{}^2 \tag{2.28}$$

where β_{P1} and β_{P2} are overall protonation constants for mono and di protonated ligand respectively. Substituting the value of $[H]_C$ from equation 2.28 in equation 2.26,

$$[H]_T = [H]_F + \beta_{P1} [H]_F [L]_F + 2 \beta_{P2} [L]_F [H]_F{}^2 \tag{2.29}$$

$$[H]_T = [H]_F + [L]_F (1 + \beta_{P1} [H]_F + 2 \beta_{P2} [H]_F{}^2) \tag{2.30}$$

$$[H]_T = [H]_F + [L]_F (1 + \Sigma\, i\, \beta_i [H]_F{}^i) \text{ where } i = 1\text{-}2. \tag{2.31}$$

Parameters like cell constant (E_0) and slope S are related to the stability constants through free ligand or metal ion concentration using Nernst equation by the expression

$$E = E_0 \pm S \log [L/M] \tag{2.32}$$

Bjerrum introduced a function called "Degree of formation or ligand number (n)" which is the average number of ligand bound per metal ion present in whatever form [200].

$$n = \frac{[Complexed\ ligand]}{[Total\ metal]} \tag{2.33}$$

By replacing above expression with the values of $[L]_C$ and $[M]_T$, we get

$$n = \frac{[L]_C}{[M]_T} \tag{2.34}$$

Putting equations 2.24 and 2.17 in 2.34,

$$n = \frac{\beta 1\,[\mathrm{M}]_F\,[\mathrm{L}]_F + 2\,\beta_2\,[\mathrm{M}]_F\,[\mathrm{L}]_F^2 + 3\,\beta_3\,[\mathrm{M}]_F\,[\mathrm{L}]_F^3 + 4\,\beta_4\,[\mathrm{M}]_F\,[\mathrm{L}]_F^4}{[\mathrm{M}]_F + \beta 1\,[\mathrm{M}]_F\,[\mathrm{L}]_F + \beta_2\,[\mathrm{M}]_F\,[\mathrm{L}]_F^2 + \beta_3\,[\mathrm{M}]_F\,[\mathrm{L}]_F^3 + \beta_4\,[\mathrm{M}]_F\,[\mathrm{L}]_F^4} \tag{2.35}$$

$$n = \frac{[\mathrm{M}]_F(\beta 1\,[\mathrm{L}]_F + 2\,\beta_2\,[\mathrm{L}]_F^2 + 3\,\beta_3\,[\mathrm{L}]_F^3 + 4\,\beta_4\,[\mathrm{L}]_F^4)}{[\mathrm{M}]_F(1 + \beta 1\,[\mathrm{L}]_F + \beta_2\,[\mathrm{L}]_F^2 + \beta_3\,[\mathrm{L}]_F^3 + \beta_4\,[\mathrm{L}]_F^4)} \tag{2.36}$$

$$n = \frac{\sum_{i=1}^{4} i\,\beta_i\,[L]_F^i}{\sum_{i=0}^{4} \beta_i\,[L]_F^i} \tag{2.37}$$

when i = 0, $\beta_0 = 1$ and the expression in denominator for i = 0 represents the free metal ion concentration.

Similar function can be determined for protonation of ligand: the mean number of protons bound per noncomplex bound ligand molecule (n_A) at different pH value is given as

$$n_A = \frac{\sum_{i=1}^{2} i\,\beta_i\,[H]_F^i}{\sum_{i=0}^{2} \beta_i\,[H]_F^i} \tag{2.38}$$

When n_A versus pH is plotted, the values of pK_1 and pK_2 are equated to the values of pH, at which the values of n_A =1.5 and 0.5, respectively.

The stability constants can be obtained from pH measurements by construction of the formation curve of the system as a plot of n vs. pL (= - log [L]) and by solving the formation function of the system given by equation 2.37.

Similar to formation function, Leden [201] and Fronaeus [202] also defined two different functions given by F([A]) and X(A) respectively by the expressions

$$\mathrm{F([A])} = \frac{\text{Total Metal} - \text{Free Metal}}{\text{Free Metal} * \text{Free Ligand}} \tag{2.39}$$

$$\mathrm{F([A])} = \frac{\mathrm{M_T - M_F}}{\mathrm{M_F * L_F}} \tag{2.40}$$

$$\mathrm{F([A])} = \frac{\beta 1\,[\mathrm{M}]_F\,[\mathrm{L}]_F + \beta_2\,[\mathrm{M}]_F\,[\mathrm{L}]_F^2 + \beta_3\,[\mathrm{M}]_F\,[\mathrm{L}]_F^3 + \beta_4\,[\mathrm{M}]_F\,[\mathrm{L}]_F^4}{[\mathrm{M}]_F * [\mathrm{L}]_F} \tag{2.41}$$

$$F([A]) = \sum_{i=1}^{4} \beta_i\,[L]_F^{i-1} \tag{2.42}$$

$$\mathrm{X(A)} = \frac{\text{Total Metal}}{\text{Free Metal}} \tag{2.43}$$

$$\mathrm{X(A)} = \frac{\mathrm{M_T}}{\mathrm{M_F}} \tag{2.44}$$

$$\mathrm{X(A)} = \frac{[\mathrm{M}]_\mathrm{F} + \beta 1\,[\mathrm{M}]_\mathrm{F}\,[\mathrm{L}]_\mathrm{F} + \beta_2\,[\mathrm{M}]_\mathrm{F}\,[\mathrm{L}]_\mathrm{F}^2 + \beta_3\,[\mathrm{M}]_\mathrm{F}\,[\mathrm{L}]_\mathrm{F}^3 + \beta_4\,[\mathrm{M}]_\mathrm{F}\,[\mathrm{L}]_\mathrm{F}^4}{[\mathrm{M}]_\mathrm{F}} \tag{2.45}$$

$$X(A) = 1 + \textstyle\sum_{i=1}^{4} \beta_i\,[L]_F^i \tag{2.46}$$

Irving and Rossotti have discussed different methods for obtaining the stability constants from the formation curve such as method of least squares, successive approximation method, solution of simultaneous equations, interpolation of half n values, interpolation of various n values, use of the midpoint slope, Schwarzenbach's graphical method [203]. All these methods are based on: solution of the formation function, graphical representation of the data, the use of numerical integration of curve fitting procedure. The method of least square is the most reliable and accurate as it makes use of all the experimental data and avoids subjective smoothening of the data accidental to plotting the best straight line [203]. Graphical methods are very simple and could be used quite satisfactorily for systems with not more than 1:2 complexes. However, for higher stoichiometry and in case of polynuclear complex formations and if the ratio of successive complex stability constants is less than 1000, the method predicts erroneous results [204-206].

Digital computers have been increasingly used for computing stability constants and many programmes are now available, which are generally based on the non-linear Gauss-Newton least-squares method [207]. The most commonly used programs were reviewed by many authors time to time [208-210]. The strategies employed in the calculations were: separate refinement of the protonation constants, which were then given fixed values in the calculation of the complexation constants; simultaneous refinement of both the protonation and complexation constants; separate refinement of the data from each titration; comparison of the results of the calculations based on data with and without the points for which the pH was greater than 9 [211].

2.5. Determination of The Stability Constants

Stability constants of metal ligand complexes can be determined by potentiometry, voltammetric methods (polarography and anodic stripping voltammetry), competitive equilibria, ion chromatography, solvent extraction, spectrophotometric and luminescence methods, and nuclear magnetic resonance spectroscopy [212-215]. The most widely used technique for the measurement of metal complex stability constants is based on potentiometric titrations of a ligand in the absence and presence of metal ions [211]. In the present work potentiometry, spectrophotometry, emission spectroscopy, solvent extraction and ion-exchange methods have been used to determine the protonation constants of the ligands as well as stability constants of their complexes with lanthanides and actinides.

2.5.1. Potentiometric Titrations

Potentiometry is based on the measurement of the potential of an electrode system (e.g. electrochemical cell) in the absence of current flow. In potentiometry the measuring setup always consists of two electrodes: the measuring electrode, also known as the indicator electrode, and the reference electrode. The potential of one electrode - the working or indicator electrode - responds to the analyte’s activity, and the other electrode - the counter or reference electrode - has a known, fixed potential. Potential on an electrode depends on the ions present in the solution and their concentration. The dependence of potential between electrodes from concentration of ions is expressed by Nernst equation [216].

$$E = E_0 - \frac{R * T}{n * F} \ln a \qquad (2.47)$$

where E - Electrode potential

E_0 - Standard potential of the electrode

R - Universal gas constant (8.314 J/K/mol)

F - Faraday constant (96485 C/mol)

T - Temperature in kelvin

n - Charge of the ion or number of electrons participating in the reaction

a - Activity of the ions.

Substituting the values of R, F and T = 298 K in equation 2.47, the simplified form would be

$$E = E_0 \pm \frac{0.059}{n} \ln a \qquad (2.48)$$

2.5.1.1. pH Electrode

pH is defined as the negative logarithm of the hydrogen ion activity (a_H):

$$\mathrm{pH} = -\log_{10} a_H \qquad (2.49)$$

The most convenient and accurate way of determining pH is by using a glass electrode. The pH electrode depends on ion exchange in the hydrated layers formed on the glass electrode surface. Glass consists of a silicate network amongst which are metal ions coordinated to oxygen atom, and it is the metal ions that exchange with H^+. The glass electrode acts like a battery whose voltage depends on the H^+ activity of the solution in which it is immersed. A glass pH electrode consists of an inert glass tube with a pH sensitive glass tip, either hemispherical (bulb) or flat in shape, blown onto it. The tip contains a fill solution with a known pH, and it is the influence of this solution on the inside of the glass tip versus the influence of the process solution on the outside that gives rise to its potential. Ideally, the pH electrode will have a slope (response) of -59.16 mV/pH. The potential (E) due to H^+ is given by the equation:

$$E = E_o + 2.303 \frac{RT}{F} \log \frac{H_i^+}{H_o^+} \qquad (2.50)$$

where H^+_i and H^+_o are the molar concentrations of H^+ inside and outside the glass electrode respectively.

$$E = E_o + 0.059 \log \frac{H_i^+}{H_o^+} \qquad (2.51)$$

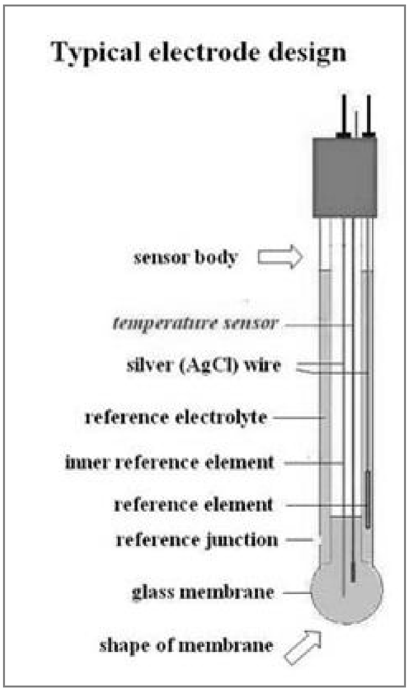

Figure 2.1: Schematic diagram of a pH electrode

2.5.1.2. The Autotitrator

Autotitrator allows the automation of all operations involved in titration: titrant addition, monitoring of the reaction (signal acquisition), recognition of the endpoint, data storage, calculation and results storage. In the present studies, the potentiometric titrations were carried out using Metrohm (Model 905 Titrando) autotitrator (figure 2.2). The titrando is the heart of the modular titrando system. Operation is carried out by a computer with a corresponding software. It is provided with measuring interfaces like a potentiometric electrode (pH, metal or ion-selective electrode), an iconnect (measuring interface for electrodes with integrated data chip, so-called iTrodes), a temperature sensor (Pt1000 or NTC) depending on the model version. Dosino is a burette unit mounted on the top of the titrant reservoir. The Dosino units of 10 and 20 mL were used. The titrant is added to the reaction vessel through dosing tube containing anti diffusion tip which prevent outside liquid from diffusing inwards. Titrant is added by the movement of the software controlled piston. The transparent housing of the dosino helps in visual monitoring of the piston movement and hence the presence of air bubbles in the cylinder can be observed. The reaction vessel is placed on a stirrer which provides variable stirring speed and is also controlled by computer.

Figure 2.2: Schematic representation of major components Metrohm-905 titrando autotitrator.

2.5.1.3. Determination of Protonation and Stability Constants by Potentiometry

All the potentiometric titrations were carried out with Metrohm autotitrator (model no 905 Titrando). Prior to potentiometric titrations, the inner filling solution of electrode was replaced by 1.0 M $NaClO_4$ to avoid the clogging of frit due to formation of insoluble $KClO_4$. The Decarbonated NaOH was standardized by titrating with known amount of potassium hydrogen phthalate (primary standard). Strong acid (0.05 M $HClO_4$) - strong base (0.1 M NaOH) titration was done to calibrate the electrode. Glee software [217] was utilized for determination of electrode standard parameters like E_0, slope and carbonate impurity. The emf of the electrode was recorded as a function of the volume of the base and the emf vs. pH showed a linear plot representing Eqs. 2.52 and 2.53 for acidic and basic region, respectively.

$$E = E_o + 2.303 \frac{RT}{F} log\,[H^+] + \gamma_H [H^+] \quad (2.52)$$

$$E = E_o + 2.303 \frac{RT}{F} log\,k_w - 2.303 \frac{RT}{F} log\,[OH^-] + \gamma_{OH} [OH^-] \quad (2.53)$$

The ligand solution (10 mL of 0.05 M) was titrated against 0.1 M standardized NaOH and the pH at each addition of NaOH was recorded to analyze the data by Hyperquad software [218] to determine the protonation constants of all the ligands. As the acid-base titrations are instantaneous, the time between two successive points was kept around one minute which showed a drift of < 0.01 mV or < 0.001 pH units. Titration of the metal ion solution with the standard alkali (~0.1 M NaOH) was employed to determine the proton concentration in the metal ion solution by Gran’s method [219]. Metal solution (25 mL) was taken in the beaker and was titrated against the nearly half neutralized ligand solutions to determine the formation constants of the complexes in solution. The data was considered up to the point of first appearance of turbidity in the titrand solution in case of complexation tending towards precipitation. The software Hyperquad [218] was used to analyze the potentiometric data to determine the stability constants of the individual complexes. For this purpose, several chemically possible species including the hydrolysis products of the metal ion were submitted as input to Hyperquad [218]. However, the software program consistently converged with the best model containing a specific set of metal complex species only along with the estimated stability constant values (Figure 2.3). Other species were ignored or rejected during the refinement process. All the titrations were done in duplicate and were carried out at a temperature of 298 K and the ionic strength was adjusted by $NaClO_4$. For all the calculations the ionic product of water (pKw) was taken as 13.77.

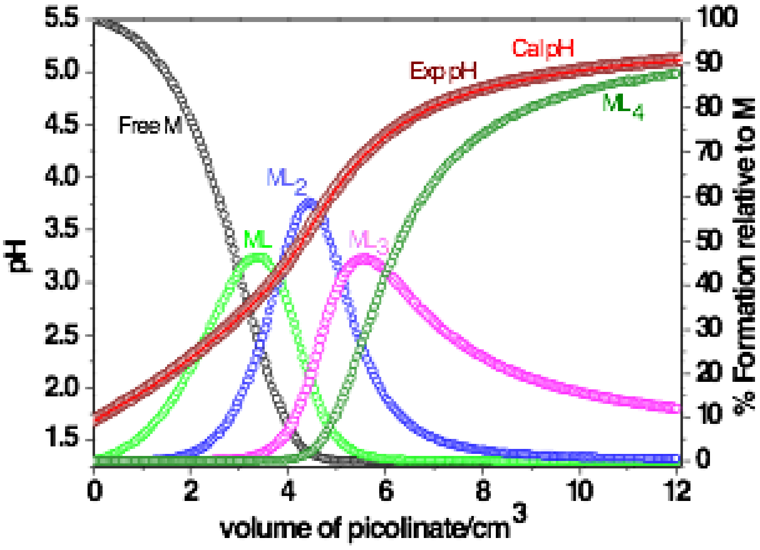

Figure 2.3: Experimental and fitted potentiometric data for titration of Eu(III) ([Eu(III)] = 4.453 x 10^{-3} M and [$HClO_4$] = 26.44 x 10^{-3} M) with buffered ligand solution ([picolinate] = 0.4989 M and [H] = 0.3328 M) along with speciation data.

2.5.2. Spectrophotometry

Metal ions, ligands or their complexes may absorb the incident light photons and get excited from ground state to higher electronic state. The degree of absorption depends upon the extent to which the transition is allowed. Electronic transitions occur with the photons having wavelength in the range of 190-900 nm, that is, UV to near IR region. Absorption of incident photons by a chemical species follows Beer Lambert's law,

$$A = \log (I_0/I) = \varepsilon \times C \times L \qquad (2.54)$$

where A is the absorbance, I_0 and I are the incident and transmitted light intensity, ε is the molar extinction/absorption coefficient, C is the molar concentration of the absorbing species and L is the path length. As can be seen from the equation, there is a linear relationship between absorbance and absorber concentration, which makes UV-Vis spectroscopy especially attractive for making quantitative measurements [220-221]. Molar absorption coefficient (ε) is independent of concentration and path length, whereas absorption depends upon both. If the values of ε and λ_{max} (wavelength at which maximum absorption occurs) are known, the concentration of its solution can be calculated.

2.5.2.1. Absorption Spectra of Lanthanides and Actinides in Solution

The f-electrons of lanthanides and actinides yield two types of transitions, namely, f-f and f-d transitions. The observed spectral transitions of the lanthanide and actinide ions are f-f transitions (table 2.1). The intensity of f-f transitions is weak, as these transitions are Laporte forbidden. Relaxation of this selection rule is very less effective than that of d-d transitions owing to weak crystal field interaction [222]. The actinide f-f absorption bands are generally an order of magnitude greater in intensity than those of the lanthanides. The absorption spectra of the di- and tetravalent lanthanide and certain actinide ions exhibit broad-band transitions arising from f-d or ligand-metal charge-transfer mechanisms. These "allowed" transitions result in high molar absorptivities, several orders of magnitude greater than those of the f-f transitions, and are strongly affected by the surrounding chemical environment [223].

The presence of internal 4f electron transition spectra in the accessible spectral region for most of the lanthanides and the sensitivity of these transitions toward the immediate coordination environment makes quantitative absorption spectrophotometry a powerful tool in the investigation of lanthanide coordination chemistry, especially in aqueous solutions. Intra 4f-4f transition spectra provide information on the effective outer and inner sphere coordination, the extent of the metal 4f orbital involvement in the immediate coordination environment, lability of the ligands coordinated to the metal, and the structural nature of the complexes in solution [224].

The absorption bands that show abnormal variations in intensity and fine structure are known as “hypersensitive”. These variations are attributed to the action of an inhomogeneous electromagnetic field from the surrounding chemical environment. The intensities of normally weak quadrupole transitions increase as a result of the inhomogeneous field. The hypersensitive lines are strongly affected by changes in the symmetry of the field on the lanthanide and actinide ion [225].

Table 2.1: Major hypersensitive transitions of trivalent lanthanide and actinide ions (Restructured from [226])

Lanthanide	**Transition**	**λ_{max} (nm)**
Pr^{3+}	${}^3P_2 \leftarrow {}^3H_4$, ${}^1D_2 \leftarrow {}^3H_4$	444.0, 593.8
Nd^{3+}	${}^4G_{5/2}$, ${}^2G_{7/2} \leftarrow {}^4H_{9/2}$, ${}^4G_{7/2} \leftarrow {}^4H_{9/2}$	578.0, 521.9
Sm^{3+}	${}^6P_{7/2}$, ${}^6F_{9/2}$, ${}^4D_{1/2} \leftarrow {}^6H_{5/2}$	376.0
Eu^{3+}	${}^5D_2 \leftarrow {}^7F_0$	465.1
Dy^{3+}	${}^4G_{11/2} \leftarrow {}^6H_{15/2}$, ${}^6I_{15/2} \leftarrow {}^6H_{15/2}$	427.3, 457.5
Ho^{3+}	${}^5G_6 \leftarrow {}^5I_8$, ${}^3H_6 \leftarrow {}^5I_8$	452.4, 361.0
Er^{3+}	${}^2H_{11/2} \leftarrow {}^4I_{15/2}$, ${}^4G_{11/2} \leftarrow {}^4I_{15/2}$	520.0, 378.0
Tm^{3+}	${}^3H_4 \leftarrow {}^3H_6$, ${}^1G_4 \leftarrow {}^3H_6$	793.4, 469.0
Actinide	**Transition**	**λ_{max} (nm)**
U^{3+}	${}^4F_{5/2} \leftarrow {}^4I_{9/2}$, ${}^4G_{5/2} \leftarrow {}^4I_{9/2}$	1052.6, 900.9
Np^{3+}	$(J = 2) \leftarrow {}^5I_4$, $2 \leftarrow J = 4$	1315.8, 854.7
Pu^{3+}	${}^6F_{3/2} \leftarrow {}^6H_{5/2}$, ${}^6F_{1/2} \leftarrow {}^6H_{5/2}$	1470.6, 1408.4
Am^{3+}	${}^7F_2 \leftarrow {}^7F_0$, ${}^5G_2 \leftarrow {}^7F_0$	1886.8, 476.2
Bk^{3+}	${}^7F_5 \leftarrow {}^7F_6$	2000
Cf^{3+}	${}^6F_{11/2} \leftarrow {}^6H_{15/2}$, ${}^6H_{13/2} \leftarrow {}^6H_{15/2}$	1538.5, 1250

2.5.2.2. Instrumentation for Spectrophotometry

All the spectrophotometric measurements done in the present thesis work were carried out using a JASCO V530 model spectrophotometer. The V-530 is designed to measure the absorbance of a sample in the wavelengths range 190 to 1100 nm. The light sources used in the V-530 are a deuterium (D_2) lamp (190 to 350 nm) for the UV region and a halogen (WI) lamp (340 to 1100 nm) for the VIS/NIR region. The schematic of a double beam spectrophotometer is given in figure 2.4.

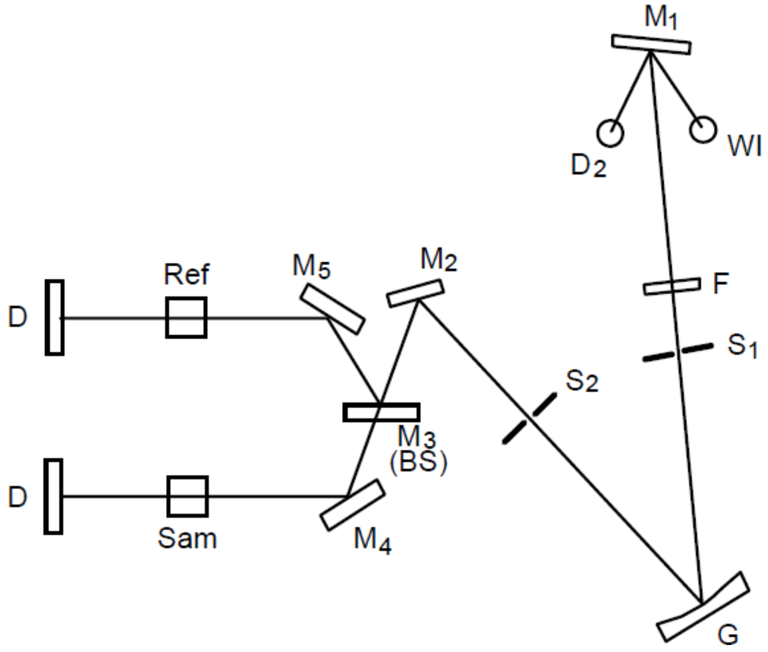

Figure 2.4: Schematic diagram of JASCO V 530 spectrophotometer (W1 - Halogen lamp, D_2 - Deuterium lamp, S - Slit, F - Filter, G - Grating, BS - Beam splitter, D - Detector, Sam - Sample beam, Ref - Reference beam). (Adopted from [227])

2.5.2.3. Determination of Protonation and Stability Constants by UV-VIS-NIR Absorption Spectrophotometry

The conjugated and aromatic organic molecules usually have very high molar extinction coefficients facilitating determination of their thermodynamic parameters for protonation reactions employing very low concentrations and hence at lower ionic strengths. The ease of carrying out measurements at very low ionic strengths further enables the application of simplest theories of ionization like Debye-Huckel and Debye Huckel limiting law to calculate the pKa values at infinite dilution or at zero ionic strength (pKa_0). In 5.00 mL quartz cuvette containing 2.00 mL of ligand solution, NaOH solution was added in increments of 10-50 μL for protonation studies. The absorption spectra were recorded over 190-400 nm with an interval of 1.0 nm. All the titrations were carried out at a temperature 298 K and ionic strength of 10^{-4} M adjusted by $NaClO_4$. The spectroscopic data was analyzed using Hyperquad software [218] to determine the species present and their fraction along with the respective protonation constants for all the ligands.

The ligand solutions were added in steps (10 to 50 μL) to a known volume (2.00 mL) of metal solution to determine the stability constants of the complexes. An equilibration time of 5 min between the successive additions showed a stable absorbance curve for each point of titration and the absorption spectra were recorded for each addition of ligand over the wavelength range from 900 to 1100 nm (in case of Np) with a wavelength interval of 0.1 nm. All the titrations were carried out at a temperature 298 K and 0.1 M $NaClO_4$. The spectroscopic data was analyzed using Hyperquad software [217] to determine the species present and their percentage of formation along with the respective log β values for all the Np(V) complexes formed during the course of reaction. Further the molar absorptivity of the complexes formed was derived from the deconvolution of the respective absorption spectra of all the Np(V) complexes.

The formation constant of a complex can be calculated by taking known amounts of a metal and a ligand; and measuring the optical densities of the metal, ligand & metal-ligand mixture separately. The composition of the complex can be determined by Job's method of continuous variation, method of mole ratio, method of slope ratio, method of isosbestic point [228-233]. The absorbance, of the solution in which the complexes of stoichiometry ML_i (i= 1-4) are present simultaneously, is an additive contribution of the absorbance of all individual species present in the solution at that point of time.

$$A_T = A_M + A_{ML} + A_{ML_2} + A_{ML_3} + A_{ML_4} \tag{2.55}$$

$$A_T = \varepsilon_M c_M l + \varepsilon_{ML} c_{ML} l + \varepsilon_{ML_2} c_{ML_2} l + \varepsilon_{ML_3} c_{ML_3} l + \varepsilon_{ML_4} c_{ML_4} l \tag{2.56}$$

$$A_T = l \sum_{i=0}^{4} \varepsilon_{ML_i} c_{ML_i} \tag{2.57}$$

where ε_{MLi} - Molar absorption coefficient of species 'ML_i'

C_{MLi}- Concentration of species 'ML_i'

l - Path length of the cell

The addition of each increment of ligand solution to metal solution results in an equation of the form 2.57 for all the wavelengths. This results in a matrix of the form A (N, λ) where N is the number of titration point and λ is the wavelength of consideration to solve the equation 2.57. The solution of this matrix in combination with mass balance equations are used to determine the molar absorption coefficients and stability constants of the species formed during the course of titration.

2.5.3. Time Resolved Luminescence Spectroscopy

Absorption of incident light photons by a molecule leaves it in an excited state, which may de-excite by different pathways, such as, light emission (luminescence) and non-radiative de-excitation. The luminescence can be in the form of fluorescence or phosphorescence depending upon the degree to which the transition is allowed. A typical electronic states diagram of Eu^{3+} ion is shown in figure 2.5. For any metal ion, there is a unique wavelength (excitation wavelength) at which the ground state is excited to the excited state, which undergoes light emission. Further, the emission wavelength is also unique characteristic of the particular metal ion. Different excited states of metal ions show unique luminescence decay life times. Thus measurement of excitation spectrum, emission spectrum and life time data offer triple resolution in the techniques, called time resolved luminescence spectroscopy (TRLS).

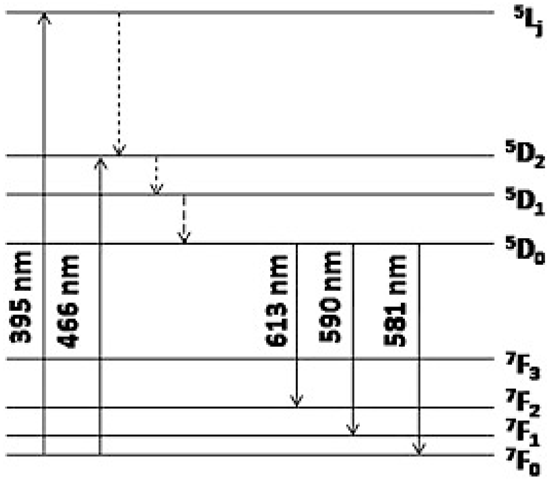

Figure 2.5: The electron energy level diagram of Eu(III) ion.

2.5.3.1. Luminescence of Lanthanides and Actinides

Luminescence spectroscopy has proven to be a powerful tool in the speciation analysis of actinides and lanthanides. Based on the spectroscopic properties, a wealth of information on the species of these ions present in the sample can be obtained. From the point of view of luminescence in aqueous solutions lanthanides(III) can be divided into three groups. The first one consists of elements in the middle of the lanthanide series, Sm, Eu, Gd, Tb and Dy, which exhibit the strongest luminescence. The elements in the second group, comprising Pr, Nd, Ho, Er and Tm give low luminescence intensities. Ce, Yb and Lu, which make up the third group, give no luminescence in the visible or ultraviolet part of the spectrum [234]. Luminescent transitions of actinide ions in solution have been studied on Am(III), Cm(III), Bk(III), Cf(III), Es(III) and U(VI). The excitation, emission wavelengths along with life time of principle excited state for luminescent lanthanides and actinides was shown in table 2.2. Some spectroscopic speciation methods of these elements based on their luminescence properties using laser-induced luminescence were developed and made it possible to perform the direct analysis of their hydration numbers or ligand coordination states. In the series of the lower actinides the luminescence properties of U(VI), Am(III) and Cm(III) are well known and often used for speciation studies connected with coordination chemistry [235-238]. The luminescence properties of Pr(IV) and U(IV) have been reported recently [239-240]. Little work has been performed on the luminescence spectroscopy of americium. This may be due to the short luminescence lifetime of this cation in aqueous solution [241]. While the f-f transitions are generally insensitive to the ligand environment field surrounding the metal ion, some transitions show intensity variations which depend on the chemical environment. These are referred to as hypersensitive transitions and generally follow the selection rules $|\Delta J| \leq 2$ and $|\Delta L| \leq 2$. These transitions can be used to probe the coordination structure of the metal ion [122].

Table 2.2: The major luminescent excitation, emission peaks and the lifetime of few lanthanide and actinide aqua ions (taken from references [122, 240-247]).

Metal ion	**$\lambda_{excitation}$ (nm)**	**$\lambda_{emission}$ (nm)**	**Lifetime (τ in μs)**
Sm^{3+}	402	594	2.3
Eu^{3+}	395	616	110
Gd^{3+}	274	310	2300
Tb^{3+}	351	543	400
Dy^{3+}	350	479	2.4
Cm^{3+}	396	593.2	65
Am^{3+}	503	691	0.0232
UO^{2+}	266	510	1.9
U^{4+}	245	320, 336, 410	< 0.020
Pa^{4+}	278	464	0.0183

Several lanthanides (Sm, Eu, Gd, Tb, Dy) and actinides (U and Cm) have characteristic long lived luminescence, that is strongly influenced by the coordination of ligands. Luminescence decay rates are caused by radiative and non-radiative processes, the latter being due mainly to energy transfer from the excited state to ligand vibrators, e.g. OH vibration of coordinated H_2O molecules. Luminescence lifetime measurements were used to obtain information about the composition of the first coordination sphere of luminescent lanthanide or actinide ion. Horrocks (for Eu^{3+}) and later Kimura and Choppin (for Cm^{3+}) obtained a linear correlation between the decay rate (life time) and the number of H_2O molecules in the first coordination sphere around the metal ion [242-243]. In addition, the time dependence of the luminescence emission contains information about the kinetics of the complex formation reactions. If the rate of ligand exchange is high compared to that of luminescence decay of the different excited species, we expect to observe an average lifetime of the species and a mono-exponential decay. If the ligand exchange rate is lower than that of luminescence decay, we expect a bi-exponential decay [244].

2.5.3.2. Instrumentation for Time Resolved Luminescence Spectroscopy (TRLS)

All luminescence instruments contain three basic components: source of light, sample holder and detector. The excitation and emission wavelengths are selected by filters which allow measurements to be made at any pair of fixed wavelengths. In the present studies, all the steady state (emission spectra) measurements and the time resolved (lifetime) measurements were carried out on an Edinburgh F-900 unit equipped with M 300 monochromators. A Xenon flash lamp with frequency range of 10–100 Hz was used as the excitation source. The monochromatic light from the source falls on the 1 cm thick quartz cell and the luminescence light emitted at 90^0 is monitored by an array of diode detectors cooled to 247 K by Peltier cooling method. The luminescence decay spectra were collected in a 2048 channel analyzer with a time calibration of 1 μs per channel. The data were fitted into multiexponential function to obtain the lifetime of the excited state. The Luminescence Lifetime is based on the technique of Time Correlated Single Photon Counting (TCSPC).

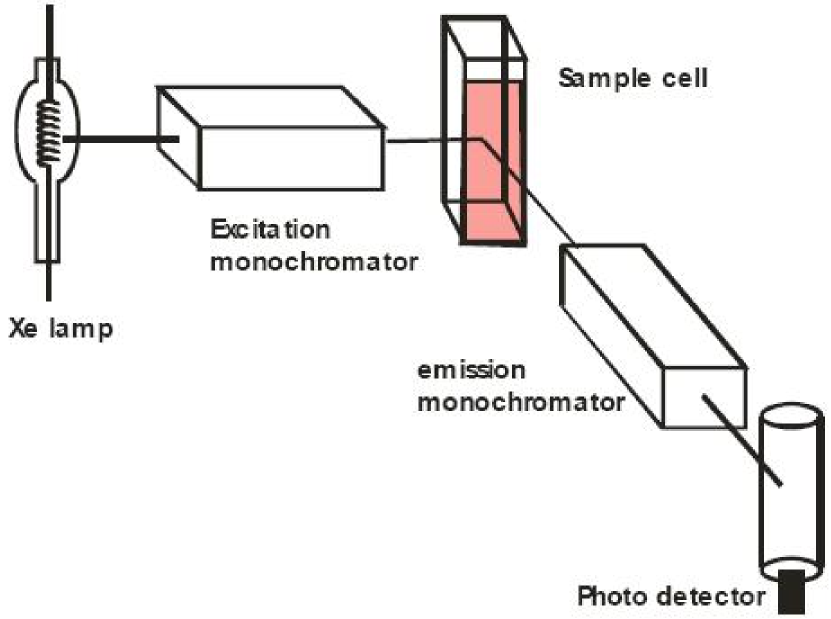

Figure 2.6: Block diagram for Time Resolved Luminescence Spectroscopy

2.5.3.3. Determination of Stability Constants by Luminescence Spectroscopy

The main aim of the TRLS measurements was to obtain stability constant from emission spectra and to determine the number of water molecules in the primary coordination sphere of the Eu(III) complex by life time measurements, which in turn, provides information about the nature and number of ligand anions complexed to the central metal ion. The excitation wavelength was selected at 396 nm, while the emission spectra were recorded in the wavelength range of 560–640 nm. The monochromatic light from the source falls on the 1 cm thick quartz cell and the luminescence light emitted at 90^0 is monitored by an array of diode detectors cooled to 247 K by Peltier cooling method.

The luminescence emission and decay data in the case of Eu(III) complexes were measured as a function of the volume of titrant. The spectra have been normalized to the intensity of 592 nm peak. The 616 nm peak corresponds to hypersensitive transition ($^5D_0 \rightarrow {}^7F_2$) and its intensity with respect to 592 nm peak ($^5D_0 \rightarrow {}^7F_1$) increases with complexation owing to its electric dipole nature. The ratio of intensities of 616 nm to 592 nm peaks, known as the asymmetric ratio (AR) is a measure of formation of the complex. The emission intensity of a luminescent species (F) is proportional to the intensity of the excitation beam that is absorbed ($I_0 - I$) by the sample.

$$F = K\,(I_0 - I) \tag{2.58}$$

where I_0 = Intensity of incident radiation

I = Intensity of transmitted radiation

The constant 'K' depends upon the quantum efficiency of the luminescence process. Using the Beer's law,

$$\frac{I}{I_0} = e^{-\varepsilon Cl} \tag{2.59}$$

Thus,

$$F = K\,I_0\,(1 - e^{-\varepsilon Cl}) \tag{2.60}$$

Applying Taylor's expansion on $e^{-\varepsilon cl}$,

$$e^{-\varepsilon Cl} = 1 - \varepsilon cl + \frac{(\varepsilon Cl)^2}{2!} - \frac{(\varepsilon Cl)^3}{3!} + \frac{(\varepsilon Cl)^4}{4!} \ldots\ldots\ldots\ldots \tag{2.61}$$

For $\varepsilon Cl < 0.05$, the subsequent terms in above equation can be neglected compared to 1 and hence

$$F = K\,I_0\,\varepsilon\,C\,l \tag{2.62}$$

Thus for low concentrations, (absorbance < 0.05) the luminescence intensity varies linearly with concentration. For large C, such that $A > 0.05$, the higher order terms become important and the linearity is lost. The overall measured luminescence intensity (F) is equal to the sum of the luminescence from the free metal (I_F) and the complexed metal (I_C). The methodology to determine the stability constants of the complexes formed during the course of reaction is similar to that in absorption spectrophotometry (section 2.5.2.3).

2.5.3.4. Determination of Stoichiometry and Mode of Complexation by Luminescence Lifetime Measurements

Luminescence spectra and lifetimes are very sensitive to the first solvation sphere of the Eu(III) ion and they can be used to study the kind of interaction of Eu(III) ion with different anions and the stoichiometry of the corresponding complex in case of innersphere complex formation. The method for the determination of the number of coordination water molecules is based on observations that the OH oscillators (vibrations) of coordinated H_2O molecules can efficiently non-radiatively depopulate the $^5D_0$ excited state of Eu(III), whereas the OD oscillators of coordinated D_2O molecules are much less efficient for non-radiative relaxation of the $^5D_0$ level [248–253]. Horrocks and Sudnick derived an empirical formula between the luminescence decay rates of a series of crystalline Eu(III) complexes, separately synthesized in H_2O and D_2O, and for the number of coordinated water molecules (known from single crystal X-ray diffraction studies) [242, 254] .

$$N_{H_2O} = 1.05\left(\frac{1}{\tau_{H_2O}} - \frac{1}{\tau_{D_2O}}\right) \qquad (2.63)$$

where N_{H2O} is the number of water molecules present in the primary hydration sphere of Eu(III) ion and τ is the life time of the complex formed. The estimation has an error of ± 0.5 water molecules

Barthelemy and Choppin developed a formula that can be use to determine the q value, using only the lifetime of the $^5D_0$ state in water [255].

$$N_{H_2O} = 1.05 * \frac{1}{\tau_{H_2O}} - 0.70 \qquad (2.64)$$

Considering the presence of nine water molecules in the primary coordination sphere of aqua ion, the number of water molecules removed (n_{H2O}) by the complexation of a ligand can be calculated by

$$n_{H_2O} = 9 - N_{H_2O} \qquad (2.65)$$

The value of n_{H2O} is a direct indication of the stoichiometry, denticity (chelation) and the mode of (inner sphere or outer sphere) complexation. A ligand capable of removing the water molecule from primary hydration sphere of aqua Eu(III) ion will form an inner sphere complex while a ligand unable to remove water molecule forms an outer sphere complex. Further, a monodentate ligand will expel one water molecule from the primary hydration shell of Eu(III) (in case of inner sphere complex formation) whereas a multidentate ligand can remove more than two depending on the number of donor atoms present and the size (bulkiness) of ligand. From the denticity of the ligand and the number of water molecules still present in the primary coordination sphere of Eu(III), the stoichiometry of the complex can be determined.

2.6. The Enthalpy and Entropy of Formation of a Complex

Two important thermodynamic parameters that are directly measured by experiments are the stability constant (K) and the enthalpy of complexation (ΔH). Other parameters, including Gibbs free energy (ΔG) and entropy (ΔS) are derived from the stability constant and enthalpy of complexation as follows.

$$\Delta G = -2.303\ R \times T \times \ln K \qquad (2.66)$$

$$\Delta G = \Delta H - T\Delta S \qquad (2.67)$$

Thus

$$\Delta S = (\Delta H - \Delta G) / T \qquad (2.68)$$

The enthalpy of complexation is resultant of the energy released in bond formation (ΔH_b) and the energy required for dehydration (ΔH_h) of the metal ion and the ligand. Depending upon the dominance of former or the latter energy, the reaction will be either exothermic or endothermic in nature. Enthalpy of complexation can be calculated from the temperature dependent stability constants by Van't Hoff equation

$$\frac{d \ln K}{dT} = \frac{\Delta H}{RT^2} \qquad (2.69)$$

The enthalpy of complexation can also be directly measured using titration calorimetry. Provided that the magnitudes of equilibrium constant (K) and enthalpy (ΔH) of a reaction are within certain ranges, calorimetric titrations can be applied to simultaneous determination of the equilibrium constant and enthalpy [148].

2.6.1. Isothermal Titration Calorimetry (ITC)

Isothermal titration calorimetry (ITC) is a technique used to study the thermodynamics of a chemical or physical processes, and is considered as the gold standard. It measures the energetics (heat released or absorbed) of a chemical reaction at constant temperature. In this case, reaction is triggered by changing the chemical composition of the sample by titration of a required reactant. The heat associated with the reaction is the direct thermodynamic observable (related to both the enthalpy and extent of reaction). The foundation of this technique is based on the measurement of heat, q. Because of the relationship between the change in enthalpy and the change in internal energy (ΔE) of a system, the heat (q) absorbed or released is equal to ΔH when the system is at constant pressure (P)

$$\Delta H = \Delta E + P\Delta V \tag{2.70}$$

$$\Delta E = q + w = q - P\Delta V \tag{2.71}$$

$$\Delta H = q_p - P\Delta V + P\Delta V = q_p \tag{2.72}$$

where ΔV = change in volume

w = work

2.6.1.1. Instrumentation for ITC

A typical ITC instrument consists of a reference cell and a reaction cell, both made of an inert highly conductive metal. The cells are located in an adiabatic jacket and are connected by a thermoelectric device (TED) or Peltier device that is sensitive to relative changes in the cells’ temperatures and is connected to a feedback power supply. The temperature difference between the reference and the sample cell is measured and calibrated to a power level displayed in μW. This “feedback” power is used to maintain constant temperature and is sometimes referred to as the differential power (DP) or cell feedback power (CFB). When a constant power is supplied to the sample cell heater, and the thermocouples detect a difference in temperature (ΔT) between the two cells, power is reduced or increased to the sample cell feedback heater proportionally to ΔT, thereby returning to the equilibrium state [256].

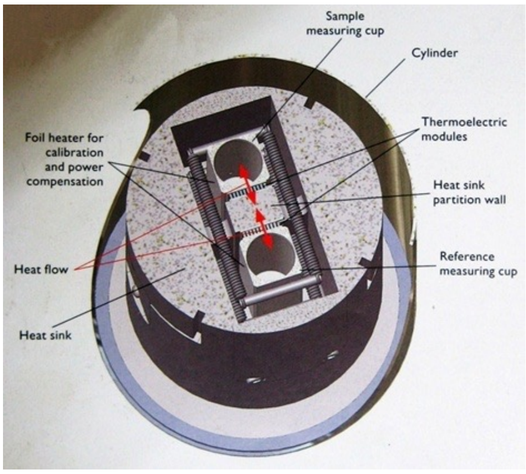

Fig. 2.7: Cross sectional view of Isothermal Titration Calorimeter(TAM III, Thermometric Sweden)

Fig. 2.8: Picture of Isothermal Titration Calorimeter(TAM III, Thermometric Sweden)

An isothermal titration calorimeter (Nanocalorimeter TAM-III, Thermometric AB, Sweden) was used to carry out all the calorimetric experiments. It is a twin thermopile heat conduction type calorimeter and differential power signal measured is dynamically corrected for the thermal inertia of the system. The titration assembly consists of 4 ml reaction vessel and a reference vessel. The heat capacity of reaction vessel and reference vessel is balanced by keeping the same volume of solutions in both sides in order to minimize the short-term noise. The titrant is delivered in the reaction vessel through a stainless steel injection needle (length 1 m and internal diameter $1.5 * 10^{-4}$ m) connected to the Hamilton syringe containing the titrant. The syringe is driven by Lund Syringe pump. The temperature of the bath was maintained at 298.0000 (±0.0001) K. The instrument was calibrated electrically and the performance of the instrument was tested by measuring log K and DH for the reaction between $BaCl_2$ and 18C6 in water

2.6.1.2. Determination of Enthalpy of Formation by ITC

The interaction of metal ion with acidic ligands like carboxylates, is accompanied by deprotonation of ligand. Thus, thermodynamic parameters for ligand protonation are required during analysis of calorimetric data. The enthalpy of protonation (ΔH_P) of ligand can be obtained by either titrating the protonated ligand solution with base or by titrating deprotonated ligand anion with acid solution. In the present study, the later procedure was employed to determine the enthalpy of formation of protonated species of ligands. All the titrations were carried out in 1.0 M $NaClO_4$ ionic medium at 298 K temperature.

The heat released in protonation titration comprises of two components, namely, the heat of protonation reaction and that due to dilution of titrant, which was determined in a separate calorimetric titration of the blank electrolyte solution (I = 1.0 M $NaClO_4$) with the titrant solution used in protonation experiment. At each step of titration, the reaction heat (Q_i^P) solely of protonation, was calculated using the equation

$$Q_i^P = Q_i^T - Q_i^D \tag{2.73}$$

Where Q_i^D - the heat change during dilution titration

Q_i^T - the sum of heat changes due to both the protonation and dilution

The heat change during the formation of protonated ligand is related to ΔH_P (enthalpy of protonation) and ΔH_n (enthalpy of neutralization) by following relation

$$Q_i^P = \Delta H_{P1}\left(v_i^{HL} - v_{i-1}^{HL}\right) + \left(\Delta H_{P1} + \Delta H_{P2}\right)\left(v_i^{H_2L} - v_{i-1}^{H_2L}\right) + \Delta H_n\,\Delta v_{H_2O} \tag{2.74}$$

where v_i^X - the number of moles of species 'X' in the cup after ith injection which were calculated using Hyperquad Simulation and Speciation software (HySS 2006) [257] by the following relation

$$v_i^X = V_i^X[X]_i \tag{2.75}$$

V_i^X and $[X]_i$ are respectively the total volume of solution and concentration of the species 'X' in the cup after ith injection. ΔH_{P1} and ΔH_{P2} are calculated by nonlinear least square fitting of Q_i^P data using equation (2.74).

For the calorimetric titration of complexation studies, the metal ion solution at the desired pH and ionic strength was taken in the reaction vessel and was titrated with the ligand solution. The heat released due to complexation only (Q_i^C) at any injection i can be given by

$$Q_i^C = Q_i^T - Q_i^D - Q_i^P \tag{2.76}$$

where Q_i^T is the heat released in titration of ligand with metal atom and Q_i^D is the heat released due to dilution and Q_i^P is the heat of protonation of the ligand. Using Hess's law of constant heat summation, the enthalpy of formation for each complex (for example: the formation of ML_4) can be related to Q_i^C by the relation

$$Q_i^C = \Delta H_{ML}\left(v_{i+1}^{ML} - v_i^{ML}\right) + \left(\Delta H_{ML} + \Delta H_{ML_2}\right)\left(v_{i+1}^{ML_2} - v_i^{ML_2}\right) + \left(\Delta H_{ML} + \Delta H_{ML_2} + \Delta H_{ML_3}\right)\left(v_{i+1}^{ML_3} - v_i^{ML_3}\right) + \left(\Delta H_{ML} + \Delta H_{ML_2} + \Delta H_{ML_3} + \Delta H_{ML_4}\right)\left(v_{i+1}^{ML_4} - v_i^{ML_4}\right) \tag{2.77}$$

In the above equation, ΔH_{MLi} is the enthalpy of formation for the complex ML_i and v_i^{MLi} is the number of moles present at ith injection for the complex ML_i obtained from

Hyperquad Speciation Simulation (Hyss) program [257] by providing the stability constants of the complexes obtained from potentiometry data as inputs. The non linear least square fitting of the equation 2.77 gives the enthalpy of formation of all the complexes formed during the course of reaction.

The calorimetric data can also be presented in the form of heat per mol of ligand (h_{vi}) vs. n_{avg} from which ΔH_{MLi} can be calculated graphically, where h_{vi} is calculated by using the following equation.

$$h_{vi} = \frac{\sum_i^n Q_i^C}{n_M} \quad (2.78)$$

where n_M is the moles of metal ion present in the reaction system and n_{avg} is the average number of ligand atoms bound per metal ion. From such graphs, the enthalpy of formation can directly be obtained as h_{vi} at n_{avg} = 1, 2, 3 and 4 corresponds to the enthalpy of formation of the complexes ML, ML_2, ML_3 and ML_4 respectively. The entropy of formation (ΔS) of the complexes was calculated from the log K and ΔH for the formation of complexes using equation 2.68.

2.7. Characterization of Colloids

The number density and the size distribution of colloids in environmentally relevant low concentrations, as well as the elemental composition of these nano particles are essential information for the prediction of solubility data [258]. Methods commonly used for speciation and quantification of colloids are scanning electron microscopy (SEM), transmission electron microscopy (TEM), photon correlation spectroscopy (PCS), secondary X-ray spectroscopy (SXS), auger spectroscopy, electron energy loss spectroscopy (EELS), mass spectrometry, X-ray-based methods (including scattering, absorption, emission, (spectro) microscopy), etc. [139]. Ultra filtration, ultra centrifugation, and dialysis are commonly used as supporting methods. Because of obvious difficulties involved in sample preparation, speciation by SEM or TEM may produce fictitious results, i.e., alteration of original states by aggregation of particles and/or deformation through dehydration. Although PCS is a suitable method for characterizing mono dispersed spherical particles of relatively large sizes, it is inadequate for aquatic colloids [134]. Laser-induced Breakdown Detection (LIBD) enables the concentration and size of aquatic nano-particles (colloids), in the range of 10-1000 nm and from about 1 ng/L up to few mg/L. Such particles, which are frequently encountered in aquatic systems, cannot be detected using methods based on laser light scattering, and even if detection is possible, then only at a comparably low level of accuracy [259]. In the present studies, laser induced breakdown detection (LIBD) technique was employed for the determination of both the size and concentration of colloids formed by thorium at various pH and ionic strengths in perchlorate media.

2.7.1. Laser Induced Breakdown Detection (LIBD)

The method of LIBD uses a high-energy pulsed laser beam to selectively generate a plasma (dielectric breakdown) on particles and provides information on both the mean particle size and concentration in aqueous samples. The method is practically non-invasive, owing to minimal sample preparation and online measurement. The technique is based on the generation of a dielectric breakdown in the focus region of a pulsed laser beam. When the local pulse energy density is high enough and as the particle crosses the beam section in the focal area, the light-matter interaction breaks the atomic links by a multi photon process and creates plasma. As the threshold energy (irradiance) to incite breakdown for solid is lower than for liquid or gas, the breakdown can be generated selectively on particles dispersed in solution at suitable pulse energy [260].

2.7.1.1. Instrumentation for LIBD

A typical LIBD setup comprises a stable pulsed nanosecond laser, viz., a frequency doubled Nd:YAG laser emitting at 532 nm. The energy of the pulses is adjusted automatically with the help of a variable attenuator and recorded by an energy detector. The laser beam is focused into a sample cell (Quartz) by a set of AR coated optical lenses (typical beam diameter at focus is < 10 μm). The sample cell is secured in a fixed position with respect to the beam focus. A beam dump system is usually placed after the cell to block the unabsorbed beam. The plasma events are detected in the cell by acoustic method where an acoustic sensor (piezoelectric transducer) is connected to the sample cell and the plasma is detected by the acoustic wave emitted during the plasma expansion into the liquid. The system is calibrated using standards (e.g., latex) of known size and concentrations to determine the size and concentration of colloids in the unknown sample [261].

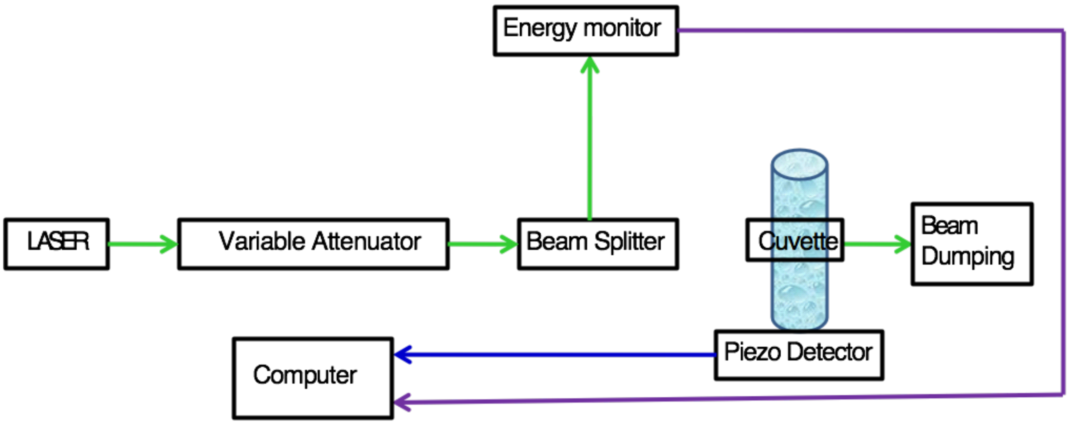

Figure 2.9: Block diagram with major components of a Laser Induced Breakdown Detection (LIBD) System.

2.7.1.2. Methodology to Determine The Size and Concentration of Colloids by LIBD

The laser energy is scanned from zero to the plasma threshold of ultrapure water with optimized energy incremental steps. For each step, a fixed number of laser pulses (typically between 500 to 2000) at 100 Hz repetition rate bombarded. The number of induced plasma events are recorded by a high speed acquisition card, each plasma event corresponding to a breakdown in the liquid. For each pulse energy, a Break Down Probability (BDP) value is calculated using the following equation.

$$BDP = \frac{Number\ of\ plasma\ events}{number\ of\ laser\ pulses} \qquad (2.79)$$

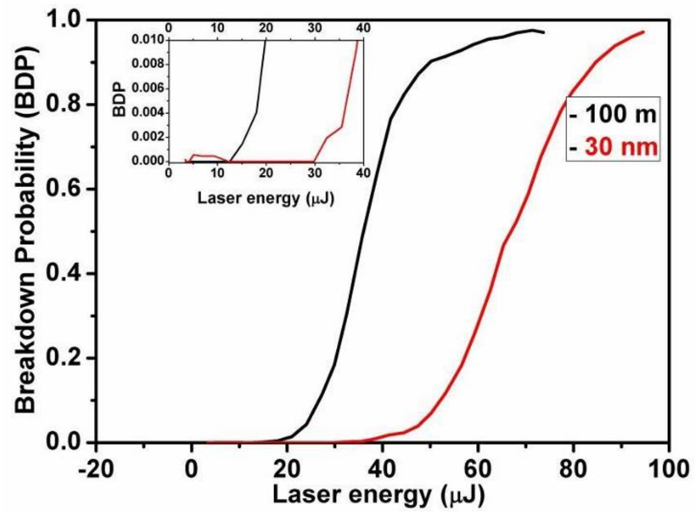

Figure 2.10: The plots of BDP Vs. Laser Energy (S-curves) for 30 and 100 nm polystyrene standards (Insert: Breakdown threshold cut-off plot).

BDP depends on several parameters: the laser beam fluence, the size and the concentration of the nanoparticles, and varies from 0 (no breakdown) to 1 (100% of breakdown). The plot of BDP versus pulse energy follows a typical S shape (Figure 2.10), which is characterized by two parameters: laser energy threshold and its slope. The breakdown threshold depends on the particle size: bigger the particle size, the lower the threshold. The slope of the S curve is related to the colloidal concentration: the higher the particle concentration, the higher the slope. Fitting the S curve with calibration data allows to determine the size distribution and the absolute concentration of the colloid traces in the solution [259].

2.7.1.3. Size and Concentration Calibration of LIBD System

The breakdown threshold of a material is the power density at which its dielectric property collapses and a plasma is generated. The laser pulse energy released is recorded under constant optical and experimental conditions, that is, focal length of the lens, wavelength of the laser light, laser pulse duration, etc. The beam is aligned precisely by optical inspection with a laser beam profiler. The laser pulse energy is adjusted to a constant value, at which the highest signal-to-background ratio is attained for the colloid detection.

Such operational energy is selected by comparing the breakdown probability of 'ultrapure water' with that of colloid dispersion as a function of the laser pulse energy (Figure 2.11). A calibration of the colloid mass concentration, or number density, is made by measuring the breakdown probability for different particle size as a function of the laser pulse energy (Figure 2.12 and 2.13). Various commercially available monodispersive particle standards may be applied for the calibration of the LIBD instrumentation. In particular, polystyrene standards, available in various sizes, have been found to be suitable. In this work, monodispersed polystyrene reference colloids (Duke Scientific) were used for standard calibration, with mean diameters of (20 ± 2) nm, (30 ± 1) nm, (40 ± 1) nm, (60 ± 4) nm, (81 ± 3) nm, (102 ± 3) nm, (203 ± 5) nm, (400 ± 9) nm, (707 ± 9) nm.

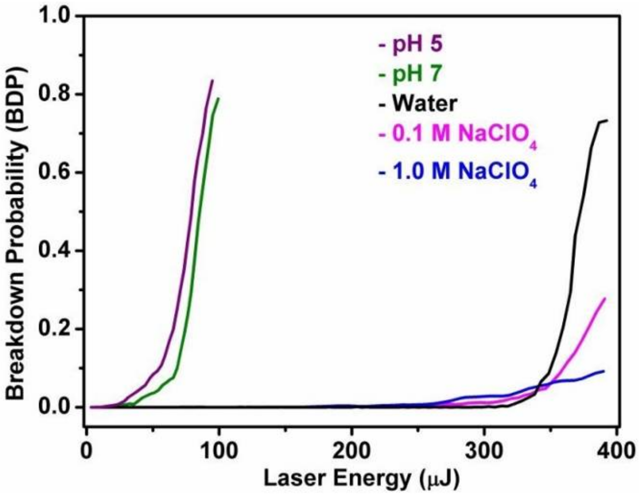

Figure 2.11: The plots of BDP Vs. Laser Energy (S-curves) for ultrapure water, (0.1 M and 1.0 M) $NaClO_4$ along with the real samples of thorium which were kept at an initial pH of 5 and 7 for an ageing period of 1080 days.

By adjusting the laser pulse energy to a value where the breakdown probability of pure water reaches zero, a breakdown event can be selectively induced by colloids. The breakdown probability of polystyrene reference particles is measured as a function of the laser pulse energy. The laser energy required to reach the breakdown threshold decreases with increasing the particle concentration as well as with increasing the particle diameter.

With decreasing the particle diameter, a higher particle number density is needed to give the same breakdown probability. Varying the concentrations of the particles influences the slope of the energy curves, but not the point at which these curves start to rise (breakdown threshold). The energy values may vary slightly, depending on the optical parameters chosen. Consequently, any change of system parameters is likely to require a new calibration. The position of the curves relative to each other, however, does not change.

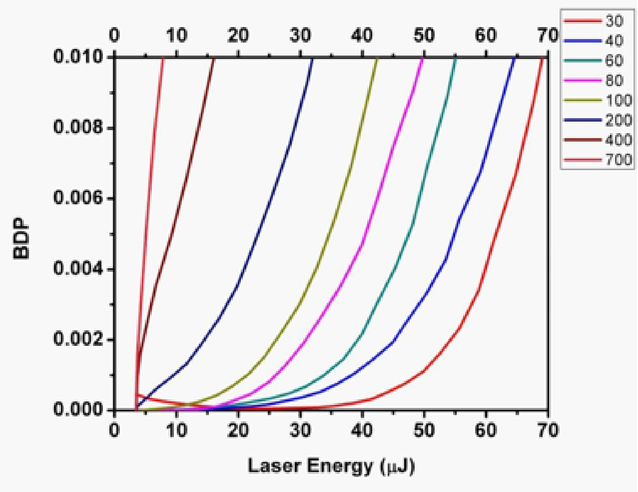

Figure 2.12: The variation in threshold energy with the particle size of standard monodispersed polystyrene nanospheres.

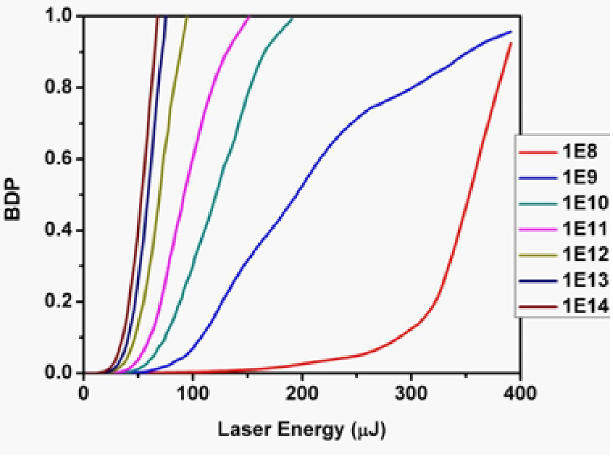

Figure 2.13: The variation in breakdown probability with the particle number density (particles/cm^3) of 30 nm standard monodispersed polystyrene nanospheres.

In conclusion, the thermodynamic parameters (log K, ΔG, ΔH and ΔS) for complexation of have been studied by potentiometry, UV-VIS-NIR absorption spectrophotometry, calorimetry and Time resolved fluorescence spectroscopy (TRFS) while the colloid formation by thorium in perchlorate media were investigated by Laser Induced Breakdown detection (LIBD) method.

Chapter 3

Studies on Protonation of Pyridine Monocarboxylates, Their N-Oxides and Hydroxamates

3.1. Introduction

As discussed in the chapter-1, actinides and long lived fission products may get into the geosphere through various modes, such as, accidental release from the operating nuclear facilities, underground nuclear tests conducted in the past, and in future, probably from the mobilized waste forms buried in deep geological repositories. The migration of these released radionuclides in the geosphere might be further accelerated by their complexation with the complexing ligands present in the aquatic systems, either naturally or of anthropogenic origin. Pyridine monocarboxylates, their N-oxides and the hydroxamates have a significant availability in the geological media and are potential anthropogenic carriers for the radionuclide migration in aqueous media (detailed in chapter 1 under sections 1.8.3 and 1.11). Interactions of the complexing agents with radionuclides and the host environment, and their response to changes in the physicochemical conditions make their role far from simple to elucidate [262]. Determination of the thermodynamic quantities of complexation, such as stability, enthalpy and entropy of formation of various kinds of species that may probably form during the course of reaction is of prime importance in understanding the basic interactions in the complexation reactions. In the case of complexation of metal ion with acidic ligands like carboxylates, the complexation process is accompanied by deprotonation of ligand. Thus, thermodynamic parameters for ligand protonation are required during analysis of thermodynamic data of complexation.

The equilibrium process involving charged species or charge separation deviates largely from ideality due to long range Coulombic interactions. All concentration equilibrium constants thus need to be corrected for this non ideality. Measurements at varying ionic strengths and extrapolation to zero ionic strength is the straightforward way to correct for non-ideality. Ionic strength can have quite a dramatic effect on the pK_a of an acid or base, and consequently on the fraction deprotonated or protonated, even though the stoichiometric concentration remains the same [263].

The determination of thermodynamic stability constants of the metal ligand complexes, by techniques, such as, spectrophotometry, potentiometry, etc, required the knowledge of protonation constants of the complexing anions. As these data are not available in the literature, systematic studies on protonation of the complexing anions were carried out by potentiometry and calorimetry before undertaking the metal complexation by these ligands. Further, the three classes of ligands have a systematic variation in position of hetero atom (pyridine monocarboxylic acids and its N-oxides) or change of substituent moiety (hydroxamic acids) which helps in interpreting the role of substitution on protonation thermodynamics.

3.2. Experimental

3.2.1. Reagents

A.R. grade pyridine monocarboxylic acids (picolinic acid, nicotinic acid, isonicotinic acid) (99 %) procured from Alfa Aesar, pyridine Monocarboxylic acid-N-oxides (PANO (97%), NANO (98%), IANO (99%)) and hydroxamic acids (AHAH (98%), BHAH (99%) and SHAH (99%)) procured from Sigma Aldrich were used as such without any further purification. Decarbonated NaOH was used for electrode calibration and for titration of these acids for determination of protonation constants. NaOH was standardized by titrating with potassium hydrogen phthalate as primary standard.

3.2.2. Potentiometry

The potentiometric titration, to determine the protonation constants of all the acids were carried out, using an autotitrator Metrohm (Model no. 716 DMS Titrino) at 298 K. All the titrations were carried out in duplicate. The details of pH meter and potentiometric titration methodology are given in chapter-2. Glee software was used to obtain the values of E^0, slope and carbonate impurity in alkali [216]. For all the potentiometric titrations to study the protonation, 10 mL of pure ligand solution (0.05 M) was taken in the beaker and was titrated against the standard NaOH solution (0.1 M). The potentiometric titration data were analyzed using the computer program Hyperquad [217] to obtain the protonation constants of all the three classes of ligands. For all the calculations the ionic product of water (pK_W) was taken as 13.77.

3.2.3. Calorimetry

The calorimetric experiments were conducted with an isothermal titration calorimeter system (Nanocalorimeter TAM-III, Thermometric AB, Sweden). The details of instrumentation, methodology to obtain enthalpy of protonation from calorimetric data were given in the previous chapter (sections 2.6.1.1 and 2.6.1.2). The enthalpy of protonation of ligand was obtained by either titrating protonated ligand solution with base or titrating deprotonated ligand anion with acid solution. Calorimetric titration of the partially deprotonated ligand solutions with standard $HClO_4$ was carried out to determine the enthalpy of protonation of the ligands. All the titrations were carried out in 1.0 M $NaClO_4$ ionic medium at 298 K temperature.

3.2.4. Spectrophotometry

All the spectrophotometric measurements were carried out using a JASCO V530 model spectrophotometer. 2.00 cm^3 of ligand solution was titrated with standard (0.1 M) NaOH solution in increments of 10-50 µL. The absorption spectra were recorded over the wavelength range from 190-400 nm with an interval of 1.0 nm. All the titrations were carried out at a temperature 298 K and ionic strength of 10^{-4} M adjusted by $NaClO_4$. The spectroscopic data was analyzed using Hyperquad software [218] to determine the species present and their fraction along with the respective protonation constants.

3.3. Theoretical Calculations

All the calculations were carried out using TURBOMOLE program package [264]. Gas phase geometries of all the three ligands and their protonated forms were optimized at the GGA level of density functional theory (DFT). Becke's exchange functional [265] in conjunction with Perdew's correlation functional (BP86) [266] were used with generalized gradient approximation (GGA). The geometries were optimized using def-SV(P) basis set whereas energy and charge calculations were carried out using def2-TZVP basis set. The charges on individual atoms were calculated by natural atomic orbitals and natural bond orbital analysis. In order to compare charge by another method, the charges were also calculated using Mulliken populated charge analysis.

3.4. Results and Discussion

3.4.1. Protonation of Pyridine Monocarboxylates

3.4.1.1. Potentiometry

There are two kinds of proton binding sites in pyridine monocarboxylates; one at the carboxylate oxygen and the other at the pyridyl nitrogen in the ring. The potentiometric titrations were carried out at two different ionic strengths (0.1 and 1.0 M $NaClO_4$). The protonation constants (log K_{P1} and log K_{P2}) for the three pyridine monocarboxylates obtained from potentiometric titration are given in table 3.1 along with the corresponding literature data. The more basic nature of pyridyl nitrogen of picolinic acid (log Kp_1) compared to other two isomers can be attributed to formation of intra molecular hydrogen bond between proton attached to carboxylate anion and pyridyl nitrogen. In case of nicotinate and isonicotinate there is no possibility of intramolecular hydrogen bonding owing to the far away position of nitrogen in the pyridyl ring from carboxylate group.

Table 3.1: Thermodynamic data for protonation of the pyridine monocarboxylates at 298 K and I = 1.0 M $NaClO_4$. (ΔG_P, ΔH_P, $T\Delta S_P$ are given in kJ/mol)

Reaction	**log K_P**	**ΔG_P**	**ΔH_P**	**$T\Delta S_P$**	**I (M)**	**Ref.**
Picolinic acid (Pyridine-2-carboxylic acid)						
$H^+ + L^- \rightarrow$	5.75 ± 0.02	-32.8	-10.4 ± 0.4	22.4	1.0	p.w
HL	5.80	-33.1			1.0	[267]
	5.38 ± 0.02	-30.7	-13.9 ± 0.6	16.8	1.0	[165]
	5.20 ± 0.02	-29.7			0.1	p.w
	5.22	-29.8			0.1	[268]
$H^+ + HL \rightarrow$	1.23 ± 0.04	-07.0	~0	07.0	1.0	p.w
H_2L^+	1.36	-07.8			1.0	[267]
	1.07 ± 0.03	-06.1			0.1	p.w
	1.03	-05.8			0.1	[268]
Nicotinic acid (Pyridine-3-carboxylic acid)						
$H^+ + L^- \rightarrow$	4.86 ± 0.02	-27.7	-14.9 ± 0.1	12.8	1.0	p.w
HL	4.72	-26.9			1.0	[269]
	4.62 ± 0.03					
	4.69	-26.4			0.1	p.w
		-26.8			0.1	[269]
$H^+ + HL \rightarrow$	2.08 ± 0.03	-11.8	-3.2 ± 0.6	8.7	1.0	p.w
H_2L^+	1.99	-11.4			1.0	[268]
	2.24 ± 0.09	-12.8			0.1	p.w
	2.33	-13.3			0.1	[269]
Isonicotinic acid (Pyridine-4-carboxylic acid)						
$H^+ + L^- \rightarrow$	4.94 ± 0.02	-28.2	-16.6 ± 0.3	11.6	1.0	p.w
HL	4.96	-28.3			1.0	[270]
	4.74 ± 0.02	-27.1			0.1	p.w
	4.88	-27.6			0.1	[269]

$H^+ + HL \rightarrow$	1.93 ± 0.04	-11.0	-1.1 ± 0.4	9.9	1.0	p.w
H_2L^+	1.75	-10.0			1.0	[270]
	1.84 ± 0.07	-10.5			0.1	p.w
	1.76	-10.0			0.1	[269]

(p.w.=present work)

3.4.1.2. Calorimetric Titrations

The enthalpy of protonation (ΔH_P) was determined by calorimetric titration. The graph of Q_i^P vs. volume of the titrant (ligand solution) for all the three pyridine monocarboxylic acids is given in figure 3.1. ΔH_{P1} and ΔH_{P2} were calculated by nonlinear least square fitting of Q_i^P data using equation 2.77 (in section 2.6.1.2). The calorimetric data can also be presented in the form of heat per mol of ligand (h_{vi}) vs n_{avg} (average number of protons bound per ligand), from which the enthalpy of protonation can be derived directly from the plot. Figure 3.2 and 3.3 shows the plot of h_{vi} vs n_{avg} for picolinate and nicotinate protonation respectively. The protonation of nitrogen atoms in pyridyl monocarboxylates was found to be highly exothermic whereas enthalpy of protonation of carboxylate is nearly zero. The protonation of carboxylate groups are mainly driven by entropy whereas that of pyridyl nitrogen atoms are driven by entropy as well as enthalpy. The less dehydration energy required for nitrogen makes the enthalpy of protonation negative and is determined by electron density on nitrogen atom.

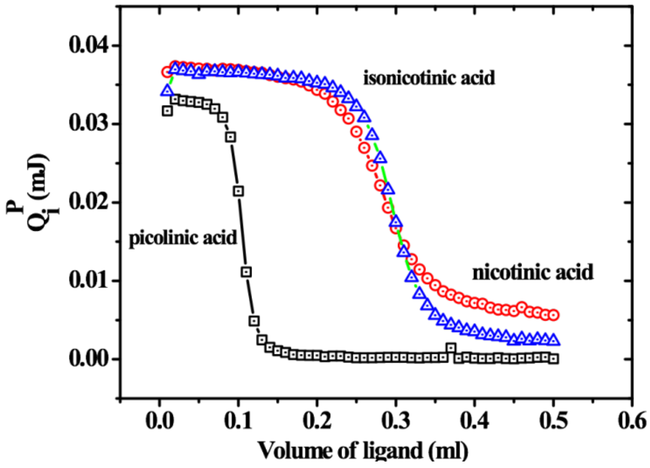

Figure 3.1: Integrated calorimetric titration data of protonation of pyridine monocarboxylates (cup solution 2.7 ml of 0.05 M ligand solution) by standard $HClO_4$ (~0.25 M) (□ – picolinic acid, ○ – nicotinic acid, Δ – isonicotinic acid)

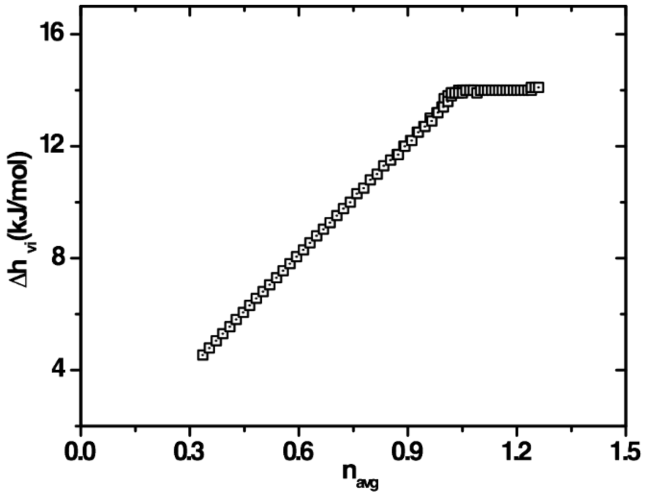

Figure 3.2: Plot of Δh_{vi} vs n_{avg} for protonation of picolinate

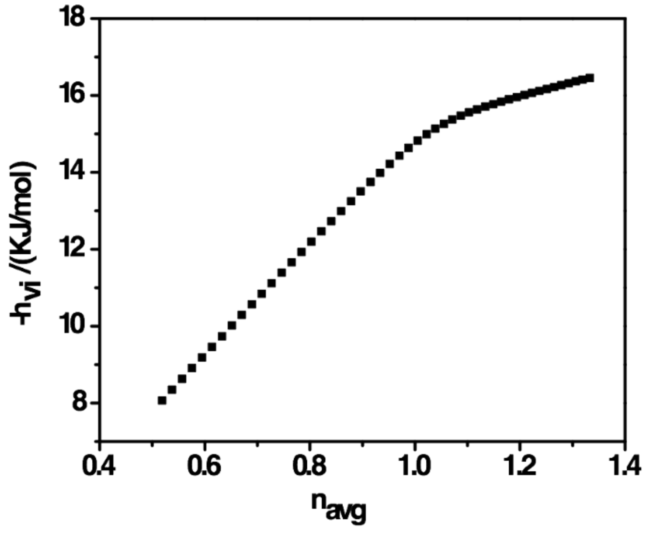

Figure 3.3: Plot of Δh_{vi} vs n_{avg} for protonation of nicotinate

The enthalpy of protonation of nitrogen in pyridyl carboxylates have been found to be in line with theoretically calculated electron density. The lower electron density on pyridyl nitrogen of picolinate compared to isonicotinate and nicotinate (Figure 3.4) can be explained by effective delocalization of electron density by resonance as well as negative inductive (-I) effect. The similar theoretically calculated electron density on pyridyl nitrogen is reflected in similar thermodynamic parameters for protonation of nicotinate and isonicotinate.

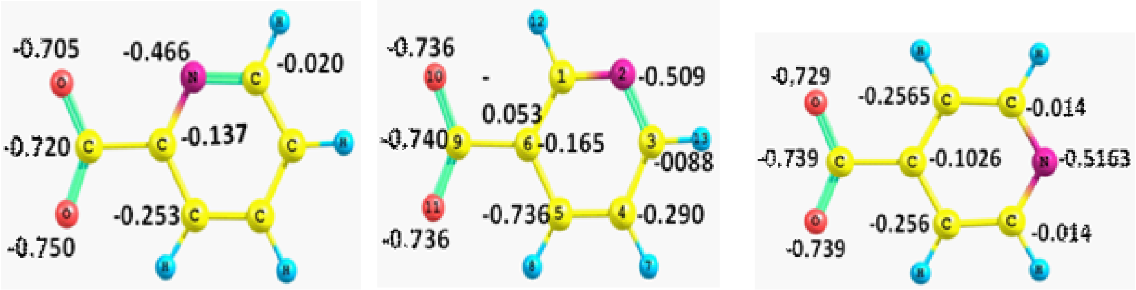

Figure 3.4: Charges on individual atoms (from left to right) of picolinate, nicotinate and isonicotinate molecules. (Colour variation: pink- nitrogen atom, yellow- carbon atom, blue- hydrogen atom, red- oxygen atom)

3.4.2. Protonation of Pyridine Monocarboxylate-N-Oxides

Zon et al. studied the reduction mechanism of pyridine monocarboxylate and its N-oxides at mercury electrode and reported the dissociation constants of both the N-oxide and carboxylate group while Angulo et al. studied the same in basic solutions [271-272]. The protonation constants of the three pyridine monocarboxylate-N-oxides are available in literature [187-188]. To the best of our knowledge no other thermodynamic parameters for the protonation of any of the three pyridine monocarboxylate-N-oxides has been reported. The effect of ionic strength on protonation constants, the interaction parameters for the deprotonated pyridine monocarboxylic acid-n-oxides have also not been reported in the literature.

3.4.2.1. Potentiometric Studies

The potentiometric data analysis showed the formation of only monoprotonated (protonated carboxylate group) pyridine monocarboxylate N-oxide. Speciation of PANO on progress of titration along with the fitted experimental and calculated pH is shown in figure 3.5. The speciation diagram depicts the percentage of formation of protonated and deprotonated form with respect to total ligand along with the change in hydrogen activity (pH) at all points of titration.

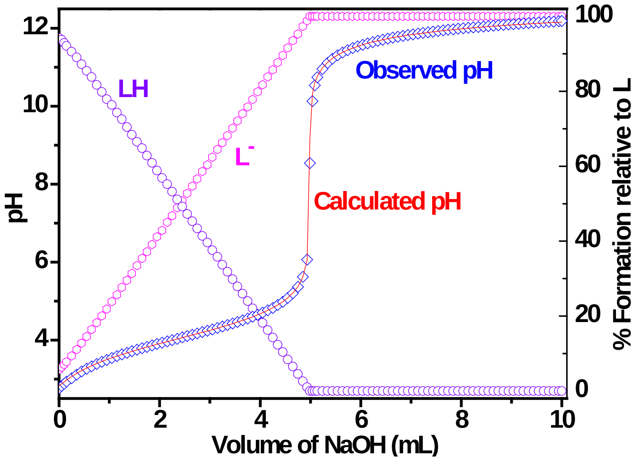

Figure 3.5: Speciation diagram along with the fitted data for protonation of PANO at $T = 298$ K and I = 3.0 M $NaClO_4$ (LH is the protonated form whereas L^- is deprotonated form of the base molecule; the calculated pH is deduced from fitting of the data for determination of protonation constant).

The protonation constants (pKa) for the three pyridine monocarboxylate-N-oxides obtained from potentiometric titration at various ionic strengths along with the data available in the literature are given in table 3.2. From the table, it can be seen that at all ionic strengths, the protonation constants follow the order PANO > IANO > NANO. PANO, being the ortho isomer, facilitates binding of proton to the oxygen atom of N-oxide through intra molecular hydrogen bonding. The higher protonation constants of PANO among all the three can be attributed due to the stabilization of protonated form by intra molecular hydrogen bonding interactions. In case of other two, the N-oxide group being far away from the carboxylate oxygen, the intra molecular hydrogen is ruled out there by resulting in lower protonation constants than PANO. IANO, the para isomer, being in a favorable position with regard to electron movement in the ring can pull more electron density from the non-bonding N-oxide oxygen atom to bonding carboxylate oxygen atom resulting in its higher log K than NANO, a meta isomer having carboxylate group at unfavorable position for electron movement.

Table 3.2: Protonation constants of pyridine monocarboxylate-N-oxides at various ionic strengths at T = 298 K. [a - studies carried out in 0.1 M $NaClO_4$ and b - ionic strength is not known, p.w - present work].

I (molarity)	I (molality)	pKa(PANO)	pKa(NANO)	pKa(IANO)	Reference
0.100	0.101	3.35± 0.01	2.52± 0.01	2.64 ± 0.01	p.w
0.500	0.513	3.37 ± 0.01	2.49 ± 0.01	2.63± 0.01	p.w
1.000	1.051	3.47± 0.01	2.56± 0.01	2.74± 0.01	p.w
2.000	2.212	3.76± 0.01	2.61± 0.03	2.89± 0.01	p.w
3.000	3.503	4.05± 0.01	2.87± 0.01	3.10± 0.01	p.w
		3.63 ± 0.06	2.63 ± 0.08		[187][a]
			2.63	2.90	[188][b]

3.4.2.2. Calorimetric Titrations

The data obtained from a calorimetric titration are shown in three different plots: the raw calorimetric data (figure 3.6) which gives the change in power with time; the cumulative heat against the volume of titrant added (figure 3.7), and h_{vi} vs. n_{avg} (figure 3.8)

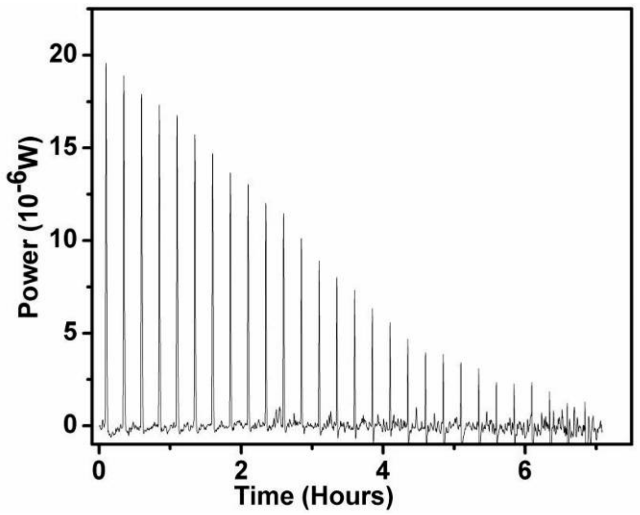

Figure 3.6: Raw calorimetric data for protonation of isonicotinate-N-oxide

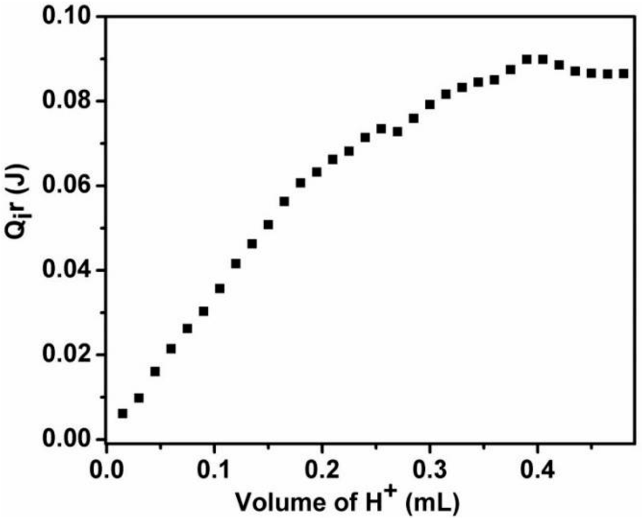

Figure 3.7: Integrated calorimetric titration data of protonation of picolinate-N-oxide

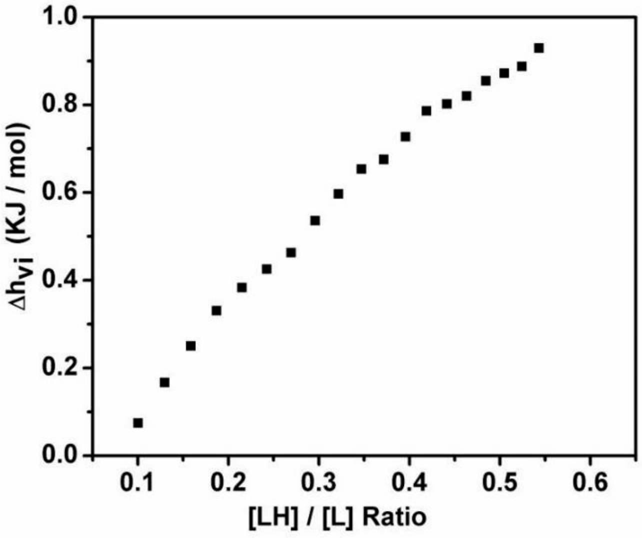

Figure 3.8: Plot of Δh_{vi} vs. n_{avg} for protonation of nicotinate-N-oxide.

The enthalpy for the protonation (ΔH_P) along with all the other thermodynamic parameters for the three pyridine monocarboxylate-N-oxides are given in table 3.3. The thermodynamic parameters for the protonation of some simple monocarboxylates and the pyridine monocarboxylates were also given in the same table for comparison. It can be seen that the protonation of PANO is endothermic in nature while that for IANO and NANO are exothermic in nature. The enthalpy of protonation is resultant of the energy released in bond formation in the protonated form and the energy required for dehydration of the proton and the anion. Depending upon the dominance of former or the latter energy, the reaction will be governed by enthalpy or entropy.

The various factors which affect the above two opposing forces include (a) repulsive interaction between two negative charges (oxygen of carboxylate and of N-oxide group). The protonation of such charged group make the process enthalpically favorable. (b) formation of intra molecular hydrogen bonding either in anion or acid form. (c) conformational changes involved on protonation. (d) dehydration of the reacting species (anion and proton) and the hydration of protonated form [273]. The conformational effects on protonation are negligible as the carboxylate is attached to a rigid pyridine ring in all the three acids. Despite of the enthalpically favorable first two factors (a and b) in PANO, ΔH_P is positive which indicates the dominant role of dehydration in determining ΔH_P. The high dehydration of PANO compared to NANO and IANO is also reflected in its ΔS_P values.

The dehydration and hydration process involves the perturbation of complete solvation shell around the two negative charges and solvation of the protonated form. The hydration shell around the carboxylate molecules include the water molecules interacting with ionic end through electrostatic interaction and with hydrophobic end through hydrophobic interaction. Molecular dynamic study of small dicarboxylates by Minofar et al revealed the dominant role of hydrophilic interactions leading to encompassing of the complete molecule by hydration shell [274]. The same effect of hydration has also been observed in small dicarboxylates like oxalate and malonate having endothermic ΔH_P of 4.013 ± 0.02 and 1.81 ± 0.05 kJ/mole respectively [275]. The other carboxylate ligand having similar structure, like phthalate and salicylate, also have endothermic ΔH_P, 4.1 and 2.25 kJ mol^{-1}respectively [276-277]. This further supports the dominant effect of hydration on ΔH_P. The similar hydration can be expected for PANO leading to endothermic ΔH_P. In case of NANO and IANO, due to larger distance between two negative charges, this effect is nullified. The hydration of protonated species also play a vital role in determining the entropy of protonation. In case of NANO and IANO, the protonated species have negatively charged oxygen atom of N-oxide away from the bound carboxylate which have higher ordering effect on water molecules reflecting in lower ΔH_P and ΔS_P values. On the contrary, intra-molecular hydrogen bonding decreases the interaction of water molecules with protonated PANO leading to more positive ΔH_P and ΔS_P. In case of NANO and IANO, the protonation is similar to that of the simple monocarboxylates like acetate, formate, etc. (table 3.3) for which ΔH_p is around 0 to 2 kJ/mol.

Table 3.3: Thermodynamic parameters for protonation of pyridine monocarboxylate-N-oxides along with the literature data for simple monocarboxylates and pyridine monocarboxylates at T = 298 K and I = 1.0 M $NaClO_4$. (a - values determined at 0.1 M $NaClO_4$, b - thermodynamic parameters for protonation of carboxylate group only and p.w - present work)

Carboxylate	***pKa***	**ΔG_P (KJ mol^{-1})**	**ΔH_P (KJ mol^{-1})**	**ΔS_P (J mol^{-1} K^{-1})**	**Ref**
Simple Monocarboxylates					
Formate	3.54	-20.2	-1.28	63.5	[278]
Acetate	4.62	-26.4	-1.68	82.8	[278]
Propionate	4.71	-26.9	-1.08	86.6	[278]
Benzoate ^{a}	3.99	-22.8	-0.87	74.0	[279]
Pyridine Monocarboxylates					
Picolinic acid	1.23	-7.02	~0	23.48	[280]
Nicotinic acid	2.08	-11.87	-3.2	29.18	[280]
Isonicotinic acid	1.93	-11.02	-1.1	33.20	[280]
Pyridine Monocarboxylate-N-oxides					

Picolinic acid-N-oxide (PANO)	3.472 ± 0.007	-19.82	6.76 ± 0.31	89.15	p.w
Nicotinic acid-N-oxide (NANO)	2.563 ± 0.003	-14.63	-1.83 ± 0.08	42.94	p.w
Isonicotinic acid-N-oxide (IANO)	2.744 ± 0.004	-15.66	-0.40 ± 0.02	51.20	p.w

3.4.2.3. Ion Interaction Parameters for PCNOs – An SIT approach

As the above measurements of enthalpy were carried out at finite ionic strength, the system will deviate from ideality due to strong electrostatic interactions between the ions present in the solution. At higher ionic strengths, non Coulombic interactions will add additional deviations from ideality, which can be addressed by determining the activity coefficient that correlates the activity with the concentration of the reactant. There are numerous methods for estimating activity coefficients of aqueous species in electrolyte solutions. The simplest models like Debye Huckel theory and Davies equations, which account for electrostatic interactions between ions of opposite charge, can be used for estimation of activity coefficients at ionic strengths less than 0.03 and 0.1 mol/kg respectively, that too for the case of 1:1 ionic systems. The short range non electrostatic interactions predominating at higher concentrations can be taken care by the adding extra terms to Debye Huckel expression. More elaborate models like the Pitzer equations extend the range of application to concentrated salt solutions but a large number of empirical parameters need to be assigned which must be obtained from experimental data. The Brønstedt-Guggenheim-Scatchard specific ion-interaction theory (SIT) [281] takes an intermediate position in that it requires only a minimum number of empirical parameters but it is commonly considered to be restricted to ionic strengths below about 3.5 mol kg^{-1}.

There are two basic assumptions in the SIT theory based on which the ion interaction parameters ε(i, k) are calculated. (I) According to the SIT model, the activity coefficient (γ_i) of an ion of charge Z_i in a solution of ionic strength (I_m) is given by an additional linear term to Debye Huckel term,

$$\log \gamma_i = -Z_i \frac{A\sqrt{I_m}}{1+aB\sqrt{I_m}} + \sum_k \varepsilon\,(i,k)\, m_k \qquad (3.1)$$

where the first term on right side of (3.1) is the Debye Huckel term to account for all electrostatic interactions and ε(i, k) is the specific ion interaction coefficient between ions i and k (zero for ions of the same charge and sign). The second term on the right side of equation (3.1) accounts for the all short-range non-electrostatic interactions between the charged particles. With this SIT model for activity coefficients, the relation between concentration protonation constants (pK_a) and thermodynamic protonation constants (pK_a^0) of a reaction in an ionic medium of molality m is given by

$$pK_a - \Delta Z^2 \frac{A\sqrt{I_m}}{1+aB\sqrt{I_m}} = pK_a^0 - \Delta\varepsilon\, I_m \qquad (3.2)$$

$$\Delta Z^2 = \Delta Z_{HL}^2 - \Delta Z_{H^+}^2 - \Delta Z_{L^-}^2 \qquad (3.3)$$

$$\Delta\varepsilon = \varepsilon_{HL} - \varepsilon_{H^+} - \varepsilon_{L^-} \qquad (3.4)$$

The second assumption of SIT theory is that the linear correction term in the activity coefficient ε (i, k) is assumed to be zero for uncharged species or for ions of the same charge, thereby implying that ε(i, k) for the neutral molecule is zero. In case of mono-protonated ligands, as in case of the pyridine monocarboxylate-N-oxides, ε_{HL} is zero. Using the literature data for the ion interaction (SIT) parameter ($\varepsilon_H{}^+$) of proton in the medium under study, it is possible to calculate the ε values for the deprotonated pyridine monocarboxylic acid-N-oxides provided the Δε is known. In the present study, the pKa of all the three-pyridine monocarboxylate-N-oxides were determined at five different ionic strengths to determine their ε values. The variation of pKa with the increase in ionic strength is given in table 3.2 and is plotted in figure 3.9. The correlation coefficients (R^2) in figure 3.9 show a deviation from linearity of protonation constants with the ionic strength.

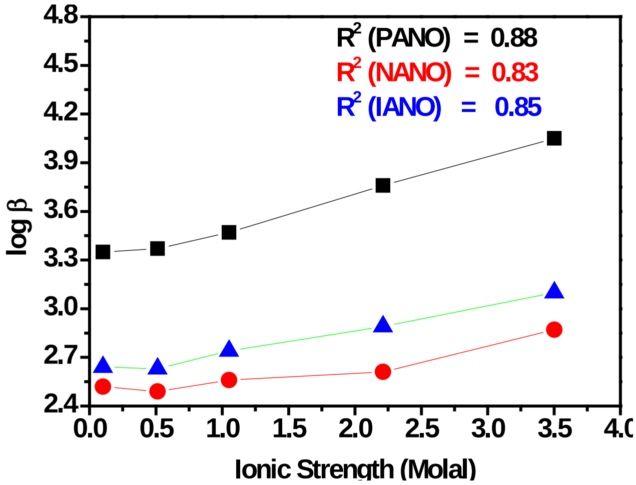

Figure 3.9: Variation of pKa with ionic strength without inclusion of any correction terms

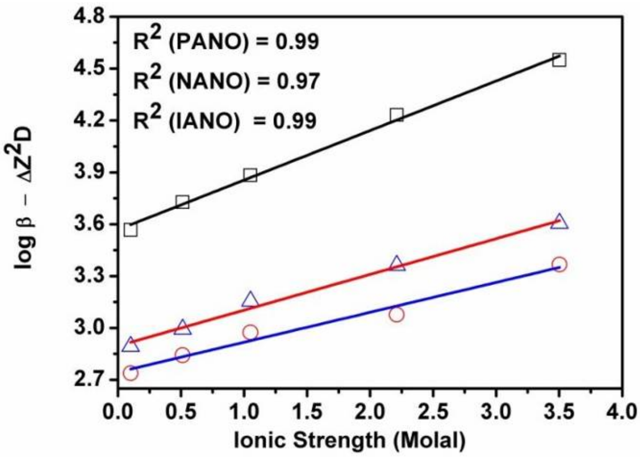

Figure 3.10: Variation of pKa with ionic strength with inclusion of ion interaction parameters obtained by application of SIT theory

Considering the deviations due to electrostatic interactions (by Debye Huckel term D) and non-electrostatic interactions (by SIT parameter ε(i, k)), the plot of log β – ΔZ^2D with I becomes linear (Figure 3.10), thereby supporting the application of SIT theory in the I_m range studied in the present work. The linear plots shown in figure 3.10 can be characterized by the slope and the intercept which give the values of Δε and pK_a^0 respectively for each of the three pyridine monocarboxylate-N-oxides. Once the Δε for the protonation reaction is known and using the ε (H^+, ClO_4^-) from literature [282] it is possible to calculate the ion interaction parameters (ε) for the pyridine monocarboxylate-N-oxides using the equation 3.4. The ε values of all the three pyridine monocarboxylate-N-oxides along with the respective pK_a^0 values are given in the table 3.4.

Table 3.4: log β^0 and SIT parameters of pyridine monocarboxylate-N-oxides

Ligand	**pKa^0**	**Δ ε**	**ε Cation**	**ε Anion**
PANO	3.568± 0.021	0.287± 0.011	0.300	-0.013
NANO	2.745 ± 0.030	0.173± 0.016	0.300	-0.127
IANO	2.896 ± 0.021	0.207± 0.010	0.300	-0.093

3.4.2.4. Spectrophotometric Measurements

The conjugated and aromatic organic molecules usually have very high molar extinction coefficients facilitating determination of the thermodynamic parameters for their protonation reactions employing very low concentrations and hence at lower ionic strengths. The ease of carrying out measurements at very low ionic strengths further enables the application of simplest theories of ionization like Debye-Huckel and Debye Huckel limiting law to calculate the pK_a values at infinite dilution or at zero ionic strength (pKa^0). In the present study, 2 mL of 5 x 10^{-5} M pyridine monocarboxylic acid-N-oxide solution was titrated against 10^{-4} M NaOH and the absorbance was monitored over the wavelength range 190-400 nm for each addition of titrant. All the titrations were done in duplicate and the ionic strength was maintained at 10^{-4} M using $NaClO_4$ as background electrolyte. The variation in absorbance of pyridine monocarboxylic acid-N-oxides on addition of NaOH is shown in figure 3.11. The absorbance at all the wavelengths decreases on adding the base for all the three pyridine monocarboxylic acid-N-oxides.

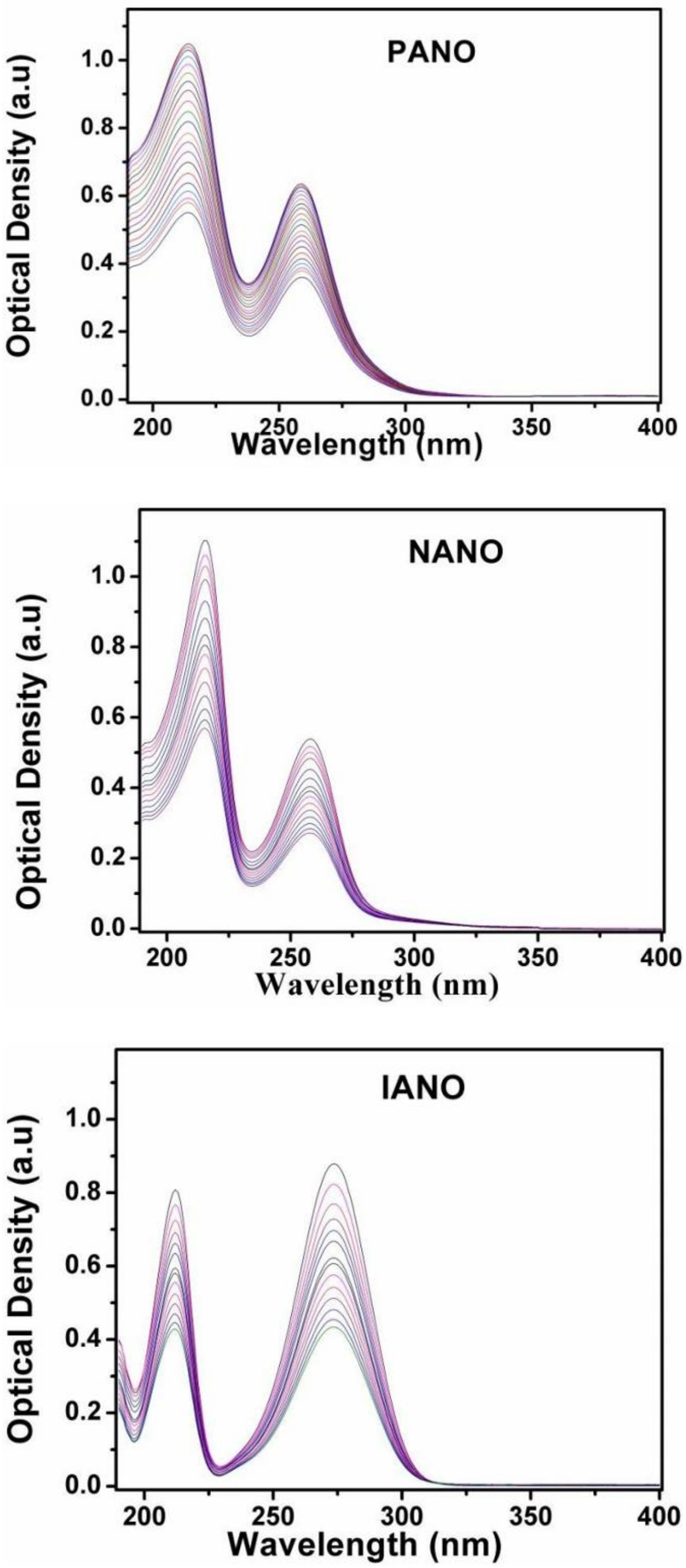

Figure 3.11: Absorption spectra of 5 x 10^{-5} M pyridine monocarboxylate-N-oxides on addition of NaOH (10^{-4} M) at T = 298 K and I = 10^{-4} M $NaClO_4$ (top to bottom PANO, NANO and IANO)

The absorbance data was analyzed using Hyperquad program [217] to determine the *pKa* values of all the three pyridine monocarboxylate-N-oxides, which are shown in table 3.5 along with the calculated pKa^0 values determined by employing Debye Huckel theory. The pKa^0 values determined from potentiometric data employing specific ion interaction theory are also given in the same table and are in good agreement with those determined by spectrophotometric measurements.

Table 3.5: The prominent peaks (λ_{max} in nm), *pKa* from absorption measurements and pKa^0 calculated from absorption as well as by potentiometric titrations determined at T = 298 K.

Ligand	**Peak 1**	**Peak 2**	**Spect. (I = 10^{-4} M)**	**Spect. (I = 0 M)[a]**	**Pot. (I = 0 M)[b]**
PANO	212	252	3.55 ± 0.01	3.58	3.57 ± 0.02
NANO	220	258	2.63 ± 0.01	2.66	2.74 ± 0.03
IANO	214	274	2.901 ± 0.01	2.93	2.90 ± 0.02

[a]Spectrophotometry, [b]Potentiometry

3.4.2.5. Theoretical Calculations

Most of the quantum chemical calculations reported in the literature have focused on evaluation of intra molecular hydrogen bonding, vibrational spectra and proton dynamics of picolinic acid-N-oxide [283-290]. Studies on Nicotinic acid N-oxide (NANO) [291-292] and isonicotinic acid-N-oxide [293] have been carried out using UV, NMR, IR and Raman spectra of their monomers and oligomers. The energies of different conformers of NANO were calculated by Atac et al.[292], while that for IANO were calculated by Karaca et al [293]. The dipole moments and the overall charge densities on all the three pyridine monocarboxylic acid-N-oxides have been reported by Stefan Lis et al [187]. But the detailed charge calculations on each atom and energies of the pyridine monocarboxylate-N-oxide and its protonated form have not been carried out in detail in literature. The energies for the protonated and deprotonated forms for the optimized conformers of the three pyridine monocarboxylic acid N-oxides along with literature reported values are given in the table 3.6.

Table 3.6: Calculated energies for protonated and deprotonated forms of pyridine monocarboxylate-N-oxides and the difference in energy from protonated form to deprotonated form of pyridine monocarboxylate-N-oxides.

Energy → **Ligand ↓**	***E* (L^-) (in Hartree)**	***E* (LH) (in Hartree)**	**Δ*E* (LH - L^-) (in Hartree)**	**Δ*E* (LH - L^-) (in kJ mol^{-1})**	**Ref.**
PANO	-508.670	-512.240	-3.570	-9374.184	p.w
NANO	-511.714	-512.249	-0.535	-1403.720	p.w
		-512.161			[286]*
IANO	-511.716	-512.254	-0.5374910	-1411.183	p.w
		-512.164			[287]*

*- The stable conformer having minimum energy were taken.

From table 3.6, it can be observed that the difference in energy (Δ*E*) between protonated to deprotonated form of the pyridine monocarboxylate-N-oxide is highest for PANO and lowest for NANO, which is also reflected in *pKa* values as well (order of pK_a : PANO > IANO > NANO from table 3.2). The difference in Δ*E* for PANO to NANO and PANO to IANO are -7970 and -7963 kJ mol^{-1} respectively while the same from IANO to NANO is only -7.46 kJ mol^{-1}. The larger difference in case of PANO can be attributed to extra affinity for proton through intra molecular hydrogen bonding. The small variation of ΔE between NANO and IANO reflects similar kind of affinity for proton by carboxylate as in case of simple monocarboxylates.

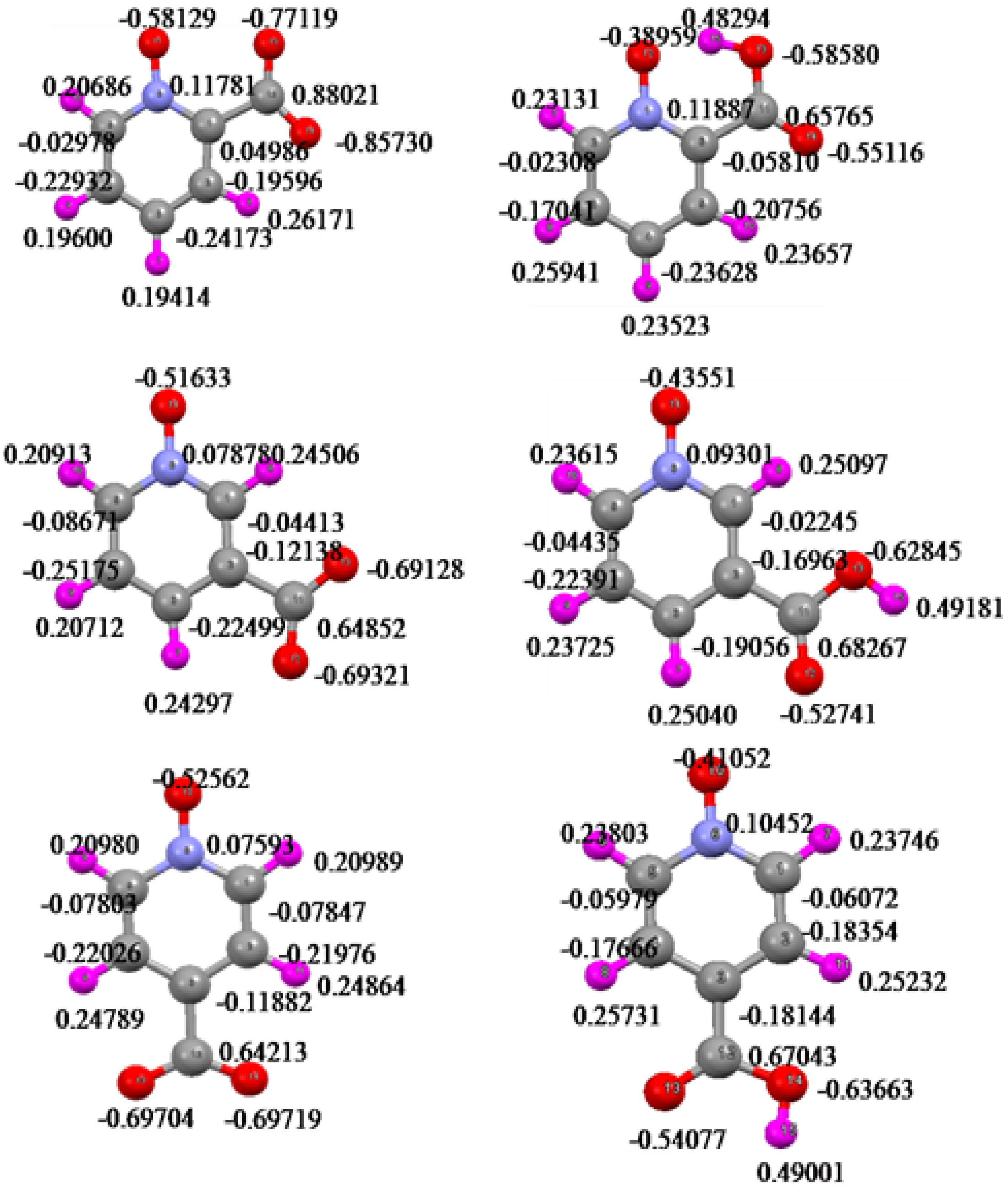

Figure 3.12: Charges (Calculated by natural bond orbital analysis) on individual atoms on the deprotonated (left) and protonated (right) forms of pyridine monocarboxylate-N-oxides. (From top to bottom: PANO, NANO, IANO; color code of atoms: grey - carbon, purple - nitrogen, red - oxygen and pink - hydrogen).

The detailed calculation of charge on every individual atom of the deprotonated and protonated forms of all the three pyridine monocarboxylate-N-oxides further gives an insight into the effect of each individual atom on protonation. The charges on all individual atoms for both protonated and deprotonated forms are shown schematically in figure 3.12. From the charges on atoms before and after protonation, the conclusions can be drawn using the following four major fragmentations. (i) The oxygen and nitrogen of N-oxide moiety, (ii) The carbon and two oxygen atoms of the carboxylate group, (iii) The ring carbon atoms, (iv) The hydrogen atoms attached to the ring carbon atoms.

Upon protonation, the positive charge on the nitrogen atom increased while the negative charge on oxygen atom decreased for N-oxide moiety in case of all the three-pyridine monocarboxylate-N-oxides. The change in charge densities on these atoms is more pronounced for PANO and IANO than that for NANO (figure 3.12). This can be attributed to the redistribution of positive charge gained on protonation over the N-oxide group. The ortho and para positions being at activated positions (Figure 3.13), the changes are more pronounced at these positions than that in NANO where the N-oxide is at deactivating meta position. The electronic charge on all the carbon atoms of the ring became less negative on protonation except for the carbon atom directly attached to carboxylate group in all the three-pyridine monocarboxylate-N-oxides. The increase in negative charge on ring carbon bound to carboxylate on protonation is typical of charge polarization. Similar observation on carboxylate ligand on binding to metal ions has been reported in the literature [293]. The higher negative charge on binding oxygen atoms of carboxylate in IANO (-0.69719 e) and total charge on complete carboxylate group (-0.75210 e) compared to that on NANO, can be explained by higher charge transfer from para position compared to meta. This results in higher electrostatic interaction of IANO for proton compared to NANO. In addition to the above observation, in case of IANO, there is also decrease in the positive charge on carbon atoms at para positions to carboxylate and ortho position to N-oxide group which is due to the combined effect of both the deactivating groups, namely N-oxide and carboxylate group on these positions at a time on protonation. The charge on all the hydrogen atoms is more positive on protonated form than that in case of deprotonated form in all the three pyridine monocarboxylate-N-oxides.

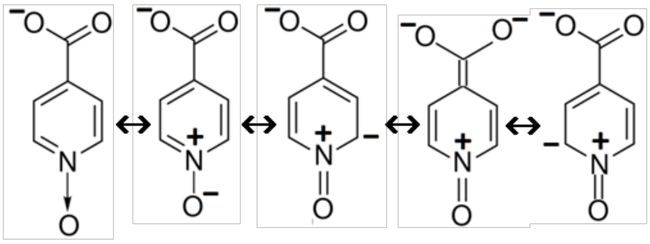

Figure 3.13: Resonating structures of IANO

Table 3.7: The bond distances of N-O and C-C (carboxylate carbon and the ring carbon attached to it) in deprotonated and protonated forms of pyridine monocarboxylate-N-oxides.

Molecule	**Deprotonated form**		**Protonated form**	
	d_{N-O} (A^0)	**d_{C-C} (A^0)**	**d_{N-O} (A^0)**	**d_{C-C} (A^0)**
PANO	1.260	1.595	1.293	1.524
NANO	1.279	1.574	1.264	1.499
IANO	1.281	1.560	1.261	1.484

Table 3.7 gives the N-O bond distance (d_{N-O}) and the bond distance between carboxylate carbon and the ring carbon attached to it (d_{C-C}). Both the bond distances have been found to decrease on protonation of the respective carboxylate group except for d_{N-O} of PANO. From the resonance structures of IANO (figure 3.14), it can be observed that the negative charge on oxygen of N-oxide can move towards the ortho and para positions as in case of PANO and IANO.

In case of IANO, the lone pair of electrons interacts with the pi-electron of the ring leading to positive charge on nitrogen atom and movement of negative charge towards the carbon attached to carboxylate group. This movement of electron density from oxygen atom of N-oxide group to carboxylate group leads to increased double bond character in N-O and

C-$C_{carboxylate}$ bonds. Thus, protonation of IANO leads to decrease in $d_{N\text{-}O}$ and $d_{C\text{-}C}$. The protonation of carboxylate stabilizes this resonance form by reducing electron repulsion in carboxylate group. However in case of protonation of PANO, the structure having negative charge on oxygen atom is stabilized by intra molecular hydrogen bonding from the ortho carboxylate group, thereby favoring the single bond character of N-O bond. Further, the intra molecular hydrogen bonding leads to increased transfer of charge from the ring to the protonated carboxylate group, thereby shortening of $d_{C\text{-}C}$.

3.4.2.6. Comparison with Pyridine Monocarboxylates

There are two protonation sites in pyridine monocarboxylates and their N-oxides, one at carboxylate oxygen and the other at nitrogen in the pyridine ring or the oxygen of N-O moiety in case of N-oxides. In the present section the thermodynamic parameters for the protonation of carboxylate oxygen in pyridine monocarboxylates and their N-oxides is discussed. The thermodynamic parameters for simple monocarboxylates and pyridine monocarboxylates available in the literature along with that for protonation of pyridine monocarboxylate-N-oxides determined in the present study are given in table 3.3. The protonation of pyridine monocarboxylate-N-oxides can be differentiated from that of carboxylate group of pyridine monocarboxylate by the following points. (i) The carboxylate group in pyridine carboxylate is more acidic (lower pK_a values) than that in corresponding isomer in pyridine monocarboxylate-N-oxides (higher pK_a values), (ii) the contribution of entropy term in free energy of protonation is much higher for pyridine monocarboxylate-N-oxides than that for respective pyridine monocarboxylates. (iii) Among the isomers, the increasing order of acidity of carboxylate group in case of pyridine carboxylate follows the order, ortho > para > meta isomers whereas in case of pyridine monocarboxylate-n-oxides the order is reversed, that is, meta > para > ortho isomer.

The above mentioned major differences can be explained on the basis of structural variation caused by the N-O group on the corresponding carboxylates. The *log Kp* for protonation of nitrogen atom in picolinic acid, nicotinic acid and isonicotinic acid are 5.75, 4.86 and 4.94 respectively. At lower pH values (< 5), the nitrogen atom in pyridine monocarboxylic acids present in protonated form (NH^+). The protonated nitrogen acts as a strong electron withdrawing group, which pulls the electron density at carboxylate group, thereby making pyridine monocarboxylates more acidic than simple benzoic acid (*pKa* = 4.03). The higher affinity of proton for carboxylate in pyridine monocarboxylate-N-oxide compared to pyridine monocarboxylates can be attributed to higher electron withdrawing effect of protonated nitrogen atom compared to N-oxide group. In case of picolinic acid, ortho isomer, the intramolecular hydrogen bonding forms between the protonated nitrogen and deprotonated carboxylate oxygen atom that stabilizes the deprotonated form and hence making it the most acidic among all the three pyridine monocarboxylates. In case of PANO, intra molecular hydrogen bonding is formed between the protonated carboxylate group and oxygen of N-oxide group thereby stabilizing the protonated form and making it least acidic among its other isomers. Due to presence of intra molecular hydrogen bonding in protonated PANO and deprotonated picolinic acid, these molecules have lower hydration compared to the corresponding meta and para isomers. The lower hydration of protonated form of PANO leads to its high entropy of protonation (ΔS_P) whereas the similar argument for deprotonated picolinic acid leads to its lowest ΔS_P values among the corresponding series of carboxylates. However, in general, the high ΔS_P for pyridine monocarboxylate-N-oxides can be attributed to their higher basicity compared to corresponding pyridine monocarboxylate, which results in the higher dehydration energy of the N-oxides during protonation.

3.4.3. Protonation of Hydroxamates

3.4.3.1. Potentiometric Titration

The analysis of potentiometric data by Hyperquad [217] indicated the presence of monoprotonated species for AHA and BHA as against mono- and di- protonated species for SHA. The speciation diagram indicating the presence of the monoprotonated SHA (LH^-) and diprotonated SHA (LH_2) is given in figure 3.14. The protonation constants obtained from potentiometric titrations are given in table 3.8.

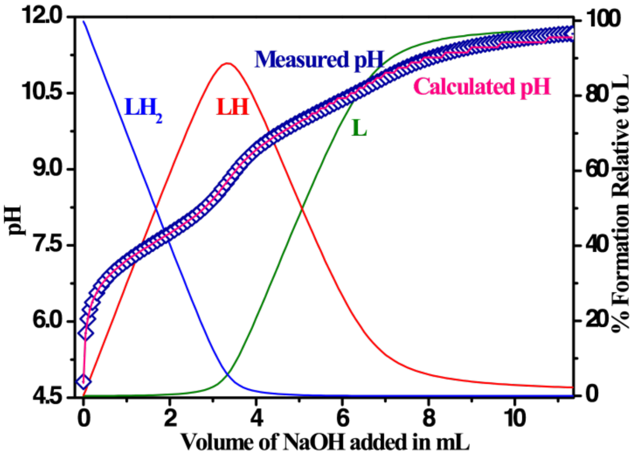

Figure 3.14: Speciation diagram for protonation of salicylhydroxamate ([SHA] = 0.01 M and [NaOH] = 0.03 M)

Table 3.8: Protonation constants of HA at T = 298 K and I = 0.1 M. (ΔG is in kJ / mol)

HA	log β_{HL}	ΔG_{HL}	log β_{H2L} (logK_{P2})	ΔG_{H2L}	Technique / Ref
AHA	9.36 ± 0.03	-23.20	-	-	Pot.
	9.27 ± 0.04	-22.99			Spec.
	9.23	-22.88			[294]
BHA	8.87 ± 0.04	-21.99	-	-	Pot.
	8.69 ± 0.06	-21.54			Spec.
	8.43	-20.90			[295]
SHA	9.95 ± 0.02	-24.66	17.53 ± 0.03 (7.58± 0.04)	-43.45	Pot.
	9.68 ± 0.02	-23.99	17.19 ± 0.05 (7.51± 0.04)	-42.61	Spec.
	9.25	-22.93	17.25	-42.76	[296]

3.4.3.2. Spectrophotometric Titration

High molar extinction coefficients of hydroxamic acids (HAH) enable spectrophotometry to be used as a convenient method to reveal the speciation and spectral properties of various HAH and their deprotonated species. The HAH solutions were titrated against a standardized NaOH and the absorption spectra were recorded over the wavelength range of 190 to 350 nm. The AHAH and BHAH have prominent absorption peaks at 196 and 227 nm respectively whereas SHAH has three peaks at 202, 236 and 295 nm (figure 3.15). In the case of AHAH and BHAH, the intensity of these peaks were found to gradually decrease with addition of standardized NaOH to HAH solution and isosbestic points appeared at 213 and 272 nm respectively. The presence of isosbestic point suggests the formation of only one species during the titration which corroborates the Hyperquad [217] analysis of potentiometric as well as spectrophotometric data suggesting deprotonation of only one proton in AHAH and BHAH. In the case of SHAH, a gradual decrease in peak intensities was observed instead of isosbestic point (figure 3.15). The protonation constant for all the three ligands by spectrophotometric titrations and potentiometric titrations are given in Table 3.9. Details of the analysis of spectrophotometric titration data to obtain the protonation constants of the ligand are given in previous chapter (Section 2.5.2.3).

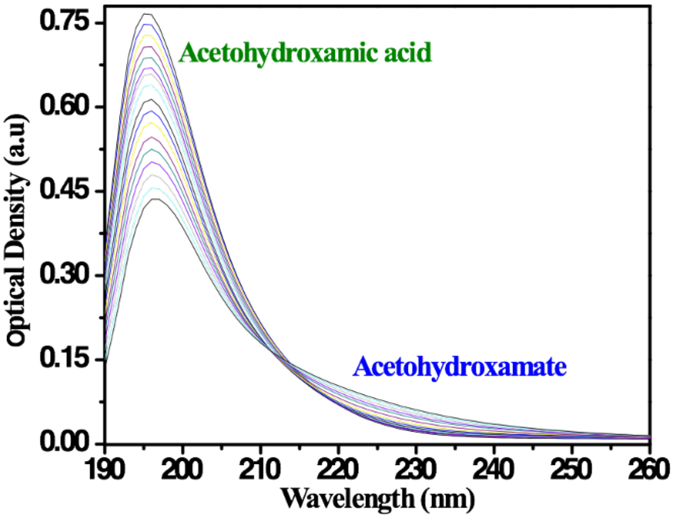

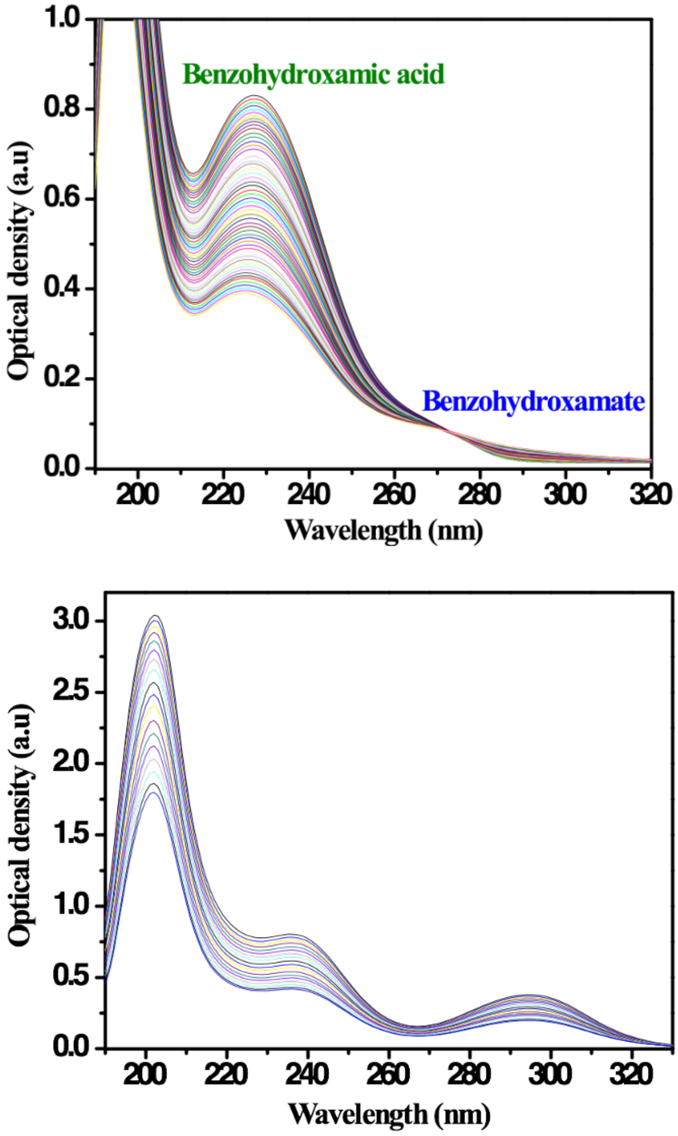

Figure 3.15: Absorption spectra of hydroxamic acids: from top to bottom - AHA, BHA and SHA ([AHA / BHA / SHA] = 1 x 10^{-4} M and [NaOH] = 4 x 10^{-4} M).

3.4.3.3. Theoretical Calculations

HAs have two probable deprotonation sites (NH and OH) which can be expressed by following reactions.

$$\text{RCONHOH} \leftrightarrow \text{RCONHO}^- + \text{H}^+ \qquad (3.5)$$

$$\text{RCONHOH} \leftrightarrow \text{RCON}^-\text{OH} + \text{H}^+ \qquad (3.6)$$

Several studies have been reported in the literature on experiments and theoretical calculations on protonation of HA. However, the deprotonation site of HA has not been identified conclusively. Investigations by Exner and Kakac using IR and UV point towards protonation of nitrogen atom in HA [297] which is in agreement with the ^{17}O NMR, FT-IR, and N vs. O alkylation experiments [295], but is contrary to the oxygen atom protonation shown in other studies [298-301]. Recently, number of authors have pointed out coexistence of both the protonated species, with one form being preferred over the other depending on the medium and substituents on HA [302]. Boulet et al. carried out DFT calculations to obtain energy of deprotonation (ΔE_P) in gas phase as well as in water as solvation medium [303]. The authors revealed that ΔE_P for deprotonation of NH in gas phase is lower than that of OH whereas the trend was opposite in solvated medium. Thus, deprotonation of HA occurs first at OH, as the calculated pKa of NH indicate that its deprotonation is highly improbable in aqueous medium.

Among the three HAs, the log K_P, which is a measure of basicity, follows the order, SHA > AHA > BHA (table 3.8). DFT calculations were carried out for protonation of all the three HAs. The structure of protonated and deprotonated HA given by equation 3.7 were optimized and the energy and charge on atoms in optimized structure were calculated.

$$L^{-n} \quad + \quad H^{+} \quad \leftrightarrow \quad LH^{-(n-1)} \qquad (3.7)$$

The energy of protonation (ΔE_P) were calculated as

$$\Delta E_P = E_{LH}^{-(n-1)} - E_L^{-n} - E_H^{+} \qquad (3.8)$$

where E_X is the calculated energy for species 'X' (X = L^{-n}, H^+, $LH^{-(n-1)}$). The calculated energies for protonation reaction of three acids are given in table 3.9.

Table 3.9: Calculated energy (in eV) for protonation for HA

	$\mathbf{E_L^{-n}}$	$\mathbf{E_{LH}^{-(n-1)}}$	$\mathbf{E_{LH2}^{-(n-2)}}$	$\mathbf{\Delta E_{P1}}$	$\mathbf{\Delta E_{P2}}$
AHA	-7711.727	-7727.751	0	-16.024	0
BHA	-12922.610	-12937.974	0	-15.364	0
SHA	-14948.172	-14966.502	-14981.406	-18.330	-14.903

The trend in proton binding energy of hydroxamate ligand ($-\Delta E_{P1}$), SHA > AHA> BHA, is in good agreement with the experimental log K_{P1} (table 3.8). The charges on the protonating site are also useful to understand their affinity for proton. The electron density on oxygen atom of -NHO^- group in AHA (-0.755 e) is higher than that in BHA (-0.652) (figure 3.16) which explains the higher log K_P of AHA compared to that of BHA. This can be attributed to positive inductive effect of acetyl group in AHA and negative inductive effect of phenyl group in BHA. Figure 3.17 shows stepwise protonation of SHA^{2-}. The first protonation decreases the negative charge on the atoms thereby reducing the electronic repulsion in the dianion. The trend, $|-\Delta E_{P1}| > |-\Delta E_{P2}|$ is in agreement with log K_{P1} > log K_{P2} (log β_{H2L}- log β_{HL}). The effect of hydroxyl group on protonation of SHA^{2-}can be understood by comparing protonation of –NHO^-in BHA ($-\Delta E_{P1}$ = -15.363984eV) and SHA ($-\Delta E_{P2}$= -14.903329 eV) (table 2).The negative charge on –NHO^- group is higher in case of BHA^- (-0.655e) compared to that in case of SHA-H^- (-0.598e) (figure 3.17). Thus, decrease in electron density on –NHO^- oxygen atom in SHA-H^- due to presence of ortho hydroxyl group leads to decrease in its basicity and thereby its protonation constant.

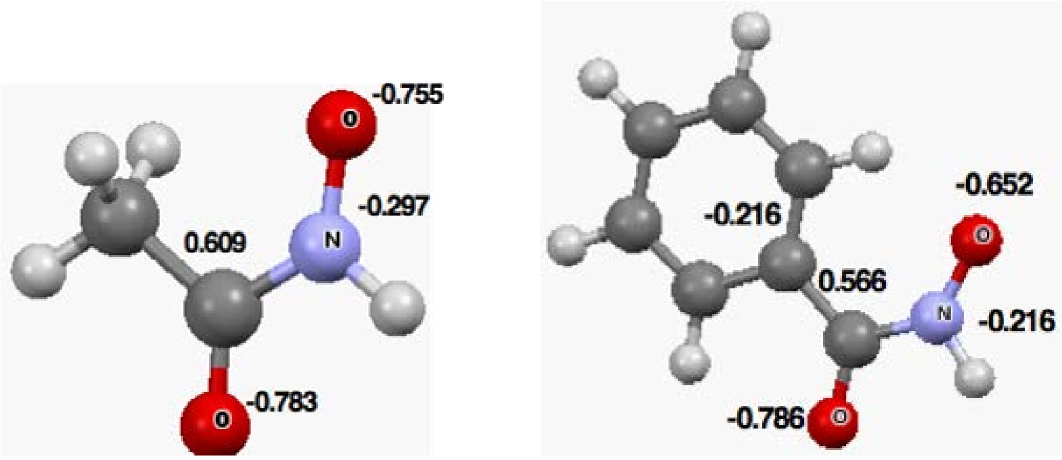

Figure 3.16: Charges on the key atoms of AHA (left) and BHA (right).

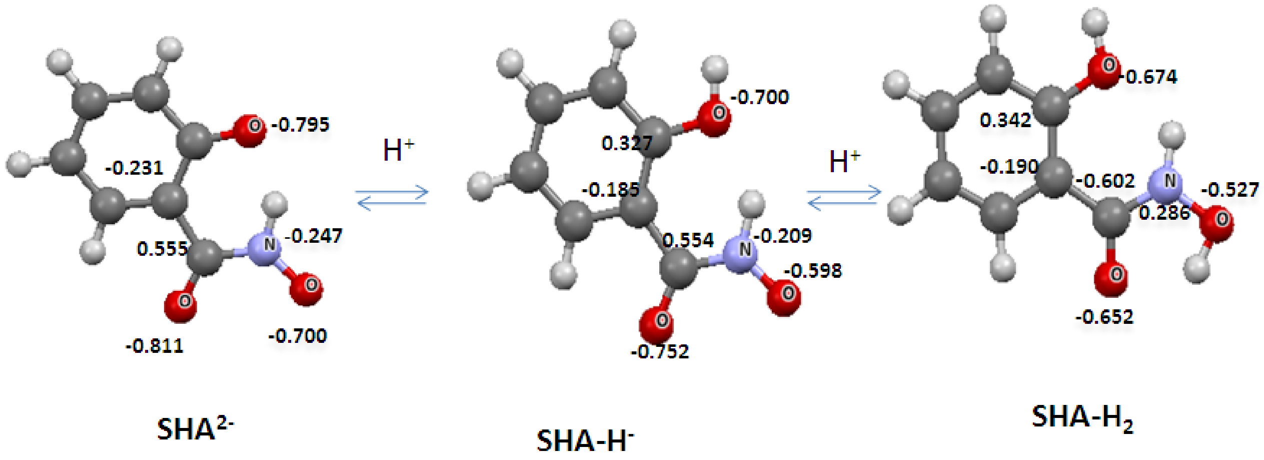

Figure 3.17: Scheme for protonation of SHA

3.5. Conclusion

The protonation constants for the ligands having possibility of intramolecular hydrogen bond formation (Picolinate, PANO and SHA) are relatively higher among the respective class of ligands. Further, between the remaining two ligands of a particular class, the one having positive inductive effect (acetyl compared to benzyl) or at favorable position of charge polarization (isonicotinate/IANO compared to nicotinate/NANO) have higher log K_P than the other. The enthalpy of formation is negative or positive depending on the stability of either deprotonated form (as in case of picolinate) or protonated form (as in case of PANO) of a ligand wherein intra molecular hydrogen bond formation is feasible. The nature of hetero moiety (N in pyridine monocarboxylates and N-O in its N-oxides) has a dramatic effect on the protonation thermodynamics. Though the position is same for the corresponding class of ligands, the thermodynamic parameters (log K_P, ΔH) follow the opposite trend in that particular class of ligands. Further, the extent of dehydration during the deprotonation process also plays a key role in governing the exothermic or endothermic nature of the process. Density functional theory calculations to derive the charge on individual atoms in the bare ligands are in line with the experimental observation on the protonation constants of the ligands.

Chapter 4

Thermodynamic, Luminescence and DFT Studies on Complexation of Eu(III) by Pyridine Monocarboxylates and Their N-Oxides

4.1. Introduction

The natural occurrence of pyridine based carboxylates and their N-oxides in plant and animal tissues, microorganisms has posed interesting problems as to the biochemistry and function of these compounds in biological systems [144]. Through feed wastes or from wastewater treatment plants, N-oxides may enter the soils, sediments, and aquatic environments as emerging contaminants [145]. Thus, the interaction of these N-oxide moieties with various metal ions present in aquatic environments is of interest from the point of view of their migration in the aquatic environments. In the present chapter the complexation of Eu(III) (analogues of trivalent actinides) by various pyridine monocarboxylates and their N-oxides has been studied by isothermal titration calorimetry, time resolved luminescence spectroscopy and density functional theory.

Most of the thermodynamic studies on complexation of pyridine monocarboxylic acids (PMCs) in solution are concerned with transition metals [304-309]. A large number of crystallographic and spectroscopic studies on lanthanides pyridine carboxylates and their derivatives have been carried out to explore their luminescence properties for various applications [310-319], and there are only few studies on the thermodynamics of complexation of rare earths with picolinate [154-157] and nicotinate [158]. But the log K values differ significantly from one another with large uncertainty in the values of formation constants for higher complexes. To the best of our knowledge no studies were reported the thermodynamic quantities of complexation of rare earths with isonicotinate in solution.

Pyridine monocarboxylic acid-N-oxides (PCNOs) have an extra oxygen atom as donor than nitrogen compared to corresponding PMCs and the studies on their complexation with lanthanides are limited [320-326]. The flexible N-oxide functionalization of pyridine monocarboxylic acid-N-oxides enhances their ability to coordinate and/or hydrogen bonding resulting in different characteristics of lanthanide PCNO complexes as compared with the corresponding lanthanide PMC complexes [327]. Most of the literature reports on chemistry of interaction of lanthanides in general and europium in particular with PCNOs related to either the synthesis of polymers or coordination networks in solid state to explore their applications in luminescence, catalysis and many other fields [165-169]. Stefan and et al studied the structure and spectroscopy of lanthanide(III) complexes with picolinic acid N-oxide in solution and in the solid state but the studies in solution are limited to identification of the number of different stoichiometric complexes [170], with no information on the speciation, thermodynamic and coordination behaviour of the complexation. Yoneda et al determined only the stability constants of ML and ML_2 lanthanide picolinate-N-oxide complexes but the stability constants values for higher stoichiometry and other thermodynamic parameters including for ML and ML_2 were not determined [155]. The polymeric structures of europium with nicotinic acid-N-oxide and isonicotinic acid-N-oxide were synthesized and characterized by J. G. Mao et al. [327] and Lijuan Zhang et al. [328] but no studies on aqueous complexation were reported.

The present study was aimed at determining the stability, speciation, stoichiometry, thermodynamic and luminescence properties of the europium complexes with the three structurally isomeric pyridine monocarboxylates and its N-oxides at 298 K temperature in 1.0 M $NaClO_4$ medium. Potentiometry and luminescence spectroscopy were used to determine the stability constants and hence the speciation diagrams of the complexation. Isothermal titration calorimetry was used to determine the heats of formation of the complexes, which, along with stability constant data, were used for determination of entropy of formation of the complexes. The fluorescence lifetime of the $^5D_0$ state of Eu(III) was used to reveal the number of water molecules left in primary hydration sphere and hence the stoichiometry of the complexes. The thermodynamic parameters (ΔH and ΔS) along with variation in luminescence lifetime of $^5D_0$ state of Eu(III) of the complexes was used to find out the mode of complexation (inner vs. outer sphere complexation) for Eu-PCNO complexes. The systematic study on thermodynamics of complexation for the three PMCs/PCNOs helps in interpreting the effect of position on the pyridyl nitrogen or N-oxide with respect to carboxylate group on the stability of the complex formed. Theoretical calculations were also carried out to determine the energies for most probable structures and the bond distances, bond angles and charges on individual atoms for all the complexes to corroborate experimental determinations.

4.2. Experimental

4.2.1. Reagents

Eu(III) stock solution was prepared by dissolving A.R. grade Eu_2O_3 in concentrated nitric acid. This was converted into perchlorate by evaporating to dryness and dissolving the residue in concentrated perchloric acid. The solution was evaporated to dryness thrice and finally the residue was dissolved in 0.01 M $HClO_4$. The Eu(III) concentration in the stock solution was determined by EDTA titration using xylenol orange as an indicator. All the chemicals of A.R. grade (99%) procured from Sigma Aldrich were used. For determination of the stability constants of the complexes, ligand solutions were prepared by adding known amount of standardized NaOH.

4.2.2 Potentiometric Titrations

Standardized Eu(III) solution (0.002 M) was titrated with half neutralized ligand solution and the data was analyzed using Hyperquad [217] to determine the stability constants of Eu(III) - pyridine monocarboxylate and its N-oxide complexes. The methodology to determine the stability constants from the potentiometric data was given chapter 2 (section 2.5.1.3). The detailed concentrations of metal and ligand solution are given in table 4.1.

Table 4.1: Concentrations employed for the complexation by Eu(III) with PMCs and PCNOs. Initial Volume of metal solution taken for potentiometric, calorimetric and luminescence studies were 10.00 mL, 2.70 mL and 2.00 mL respectively.

Complex	**Cup Solution**		**Titrant Solution**	
	C_M /10^{-3} M	**C_H /M**	**C_L /M**	**C_H /M**
Eu(III) - picolinate	2.672	0.0192	0.4989	0.3328
	4.453	0.0264	0.4989	0.3328
Eu(III) - nicotinate	2.672	0.0192	0.4991	0.2359
	4.453	0.0264	0.4991	0.2359
Eu(III) - isonicotinate	2.672	0.0192	0.1934	0.0980
	4.453	0.0264	0.1934	0.0980
Eu(III) - PANO	2.000	0.008	0.2	0.1
Eu(III) - NANO/IANO	2.000	0.008	0.1	0.05

4. 2.3 Calorimetric Titrations

The calorimetric experiments were conducted with an isothermal titration calorimeter system (TAM-III, Thermometric AB, Sweden). The details of the instrumentation was given in section 2.6.1.1. For the calorimetric titration of Eu(III) with the PMCs and PCNOs, the metal ion solution at the desired pH and ionic strength was taken in the reaction vessel and was titrated with the ligand solution (Table 4.1). The heat of dilution of titrant was determined in a separate calorimetric titration of the blank electrolyte solution (I = 1.0 M $NaClO_4$) with the titrant solution. The dilution corrected calorimetric titration data were analyzed to obtain the enthalpy changes in the reaction (detailed in section 2.6.1.2).

4.2.4. Time Resolved Luminescence Spectroscopic (TRLS) Measurements

The main aim of the TRLS measurements was to obtain stability constant from emission spectra and to determine the number of water molecules in the primary coordination sphere of the Eu(III) complex by lifetime measurements which, in turn, provides information about the nature and number of ligand anions complexed to the central metal ion. The details of the instrument are given in chapter 2 (under section 2.5.3.2). The excitation wavelength was selected at 396 nm, while the emission spectra were recorded in the wavelength range of 560–640 nm with a data interval of 1 nm. The data were fitted into single-exponential function to obtain the lifetime of the excited state, $^5D_0$, of Eu(III).

4.3. Computational Protocol

The structure of PMCs, PCNOs and their complexes with Eu(III) ion were optimized without imposing any symmetry restriction using B3LYP functional [264,329] with split valence plus polarization (SVP) basis set as implemented in Turbomole package [330]. Effective core potential was used for Eu(III) ion, that is, def-ecp with core 28 for Eu atoms [331]. The use of B3LYP/SVP level of theory has been reported in literature by many authors for actinide-lanthanide complexes [332-335]. The optimization of the complexes with Eu(III) ion was performed using septet spin state for Eu atom. The total energies were calculated with B3LYP functional [264,329] using triple zeta valence plus polarization (TZVP) basis set as practiced earlier [332-335] . The present calculations neglect spin-orbit interactions which will be less effective in ligand field complexes with 4f shells of Eu [336]. All the complexes studied here show real vibrational frequencies, confirming the minimum energy structures on the potential energy surfaces. Additionally, the $\langle S^2 \rangle$ values are very close to the $S(S+1)$ ideal values which indicates that all the structures exhibit negligible spin contamination [337-338]. The changes in enthalpy (ΔH), and Gibbs free energy (ΔG) were obtained by frequency calculations including thermal corrections and zero-point energy with the B3LYP/TZVP/RECP level of theory in the gas phase (298.15 K, 0.1MPa). The aqueous solvent effects in the energetic were incorporated using conductor like screening model (COSMO) approach [339-340]. The default COSMO radii were used for all elements except Eu (1.90Å) [341]. The dielectric constant, ε of water was taken as 78.4. The gas phase optimized geometries were used for the single point energy calculation in COSMO phase [342].

4.4. Results and Discussion

4.4.1. Eu(III) Complexation by Pyridine Monocarboxylates

4.4.1.1. Potentiometry

Figures 4.1-4.3 show the potentiometric titration data for complexation of Eu(III) with picolinic acid, nicotinic acid and isonicotinic acid along with fitted data and speciation diagram obtained by Hyperquad 2006 respectively. The potentiometric results reveal formation of four complexes, ML_i (i= 1-4) in case of picolinate but only ML (1:1 type) complexes in case of nicotinate and isonicotinate. The log K_i values obtained are given in table 4.2.

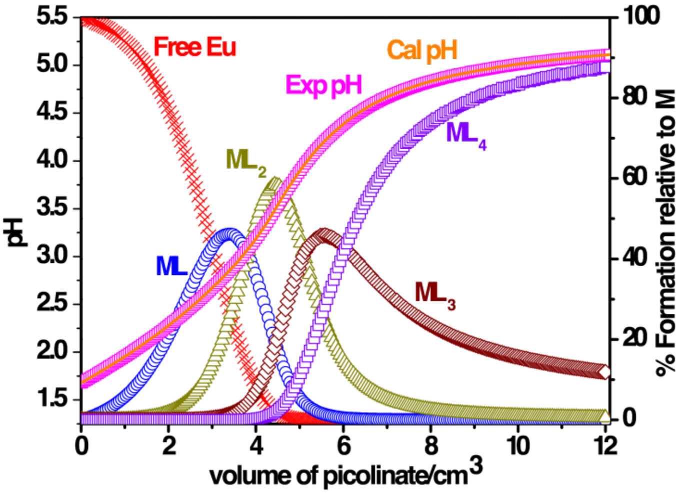

Figure 4.1: Experimental and fitted potentiometric data for titration of Eu(III) with picolinate along with speciation data. (concentration are given in table 4.1)

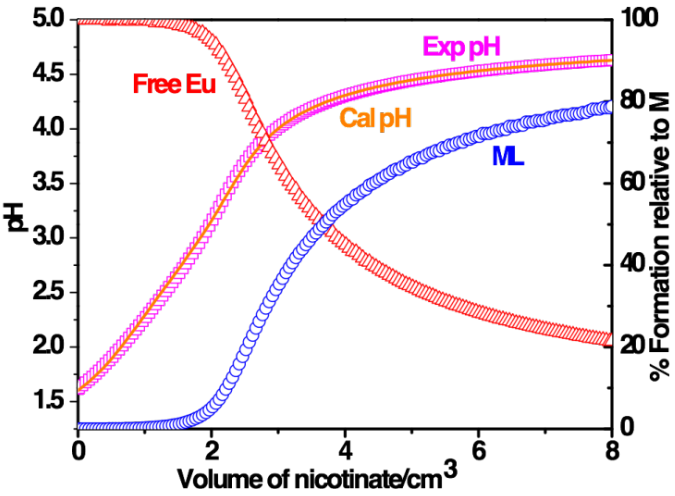

Figure 4.2: Experimental and fitted potentiometric data of titration of Eu(III) with nicotinate along with speciation data (concentration are given in table 4.1).

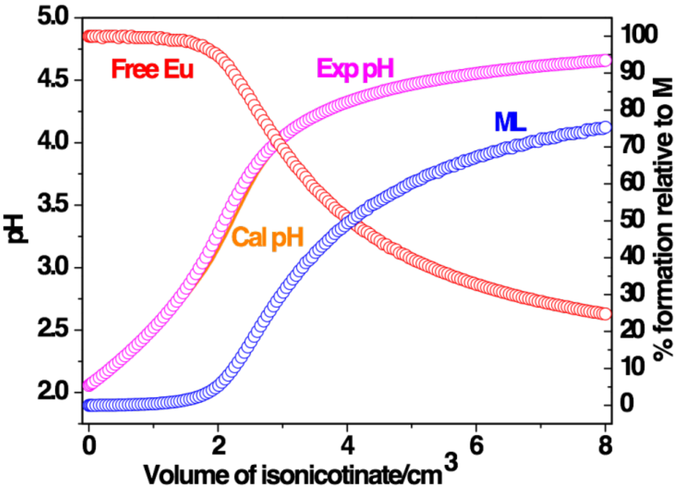

Figure 4.3: Experimental and fitted potentiometric data for titration of Eu(III) with isonicotinate along with speciation data. (concentration are given in table 4.1)

Table 4.2: Thermodynamic data for complexation of Eu(III) with pyridine monocarboxylates at 298 K and I = 1.0 M $NaClO_4$. (ΔG, ΔH and TΔS are given in kJ/mol)

Reaction	**log K_{MLi}**	**ΔG_{MLi}**	**ΔH_{MLi}**	**$T\Delta S_{MLi}$**	**Method**
			Eu(III)-Picolinate Complexes		
ML	4.38 ± 0.10	-25.0	-12.3 ± 0.3	12.7	Pot.
	4.27 ± 0.13				TRFS

ML_2	3.85 ± 0.12	-22.0	-11.2 ± 0.2	10.8	Pot.
	3.94 ± 0.15				TRFS
ML_3	2.93 ± 0.12	-16.7	-10.3 ± 0.7	6.4	Pot.
	3.00 ± 0.16				TRFS
ML_4	2.42 ± 0.18	-13.8	-9.4 ± 0.5	4.4	Pot.
	2.24 ± 0.25				TRFS
Eu(III)-Nicotinate Complexes					
$Eu^{3+} + L^- \rightarrow EuL^{2+}$	1.93 ± 0.04	-11.0	9.0 ± 0.6	20.0	Pot.
	2.02 ± 0.04				TRFS
Eu(III)-Isonicotinate Complexes					
$Eu^{3+} + L^- \rightarrow EuL^{2+}$	2.28 ± 0.12	-13.0	5.5 ± 0.3	18.5	Pot.
	2.20 ± 0.08				TRFS

According to linear free energy relationship (LFER) which is based on the electrostatic binding between the metal ion and the complexing anion, the log K_{ML} varies linearly with log K_P; however the data for Eu(III)-picolinate are well above that predicted from the correlation when compared with monodentate ligands and fall in line on comparison with similar kind of bidentate ligands (figure 4.4) indicating the chelate formation via pyridyl nitrogen atom. Log K_{ML} for Eu(III)-nicotinate and Eu(III)-isonicotinate are higher than that expected on the basis of log K_{P1} or log K_{P2}. However, log K_{ML} for Eu(III)-nicotinate and Eu(III)-isonicotinate fall in line with LFER when plotted with log K_{P1} + log K_{P2}, which indicates the participation of electron density from both groups.

The higher stability of Eu(III) complexes with nicotinate and isonicotinate compared to the predictions of LFER, can be explained by charge polarization from pyridyl nitrogen to carboxylate group on complexation with Eu(III). The electron density on carboxylate with protonated nitrogen (log K_{P2}) is low enough to form stable complex and hence MLH complexes are not observed under the experimental conditions. The absence of MLH species further confirms the deprotonation of nitrogen atom and charge polarization during complexation. The higher value of log K_P of isonicotinate than nicotinate is also reflected in stability constants of the complexes.

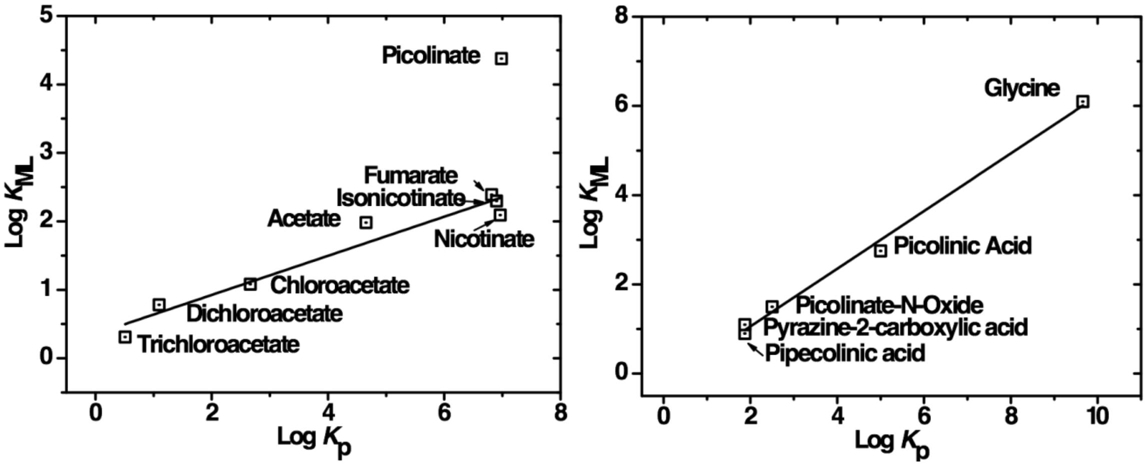

Figure 4.4: Linear Free Energy Relationship for Eu(III) –monocarboxylates (left) and Eu(III) – aminocarboxylates (right). (all the values are taken from the SC database, Academic Software).

4.4.1.2. Isothermal Titration Calorimetry

Figure 4.5 and 4.6 show the data presented in the form of h_{vi} vs n_{avg} for complexation of Eu(III) with picolinate and isonicotinate respectively. Similar plots were obtained for nicotinate system. The ΔH_C for different complexes are given in table 4.2. ΔH_C is the resultant of enthalpy change during metal-ligand bond formation (ΔH_{M-L}) and metal-water bond breaking (dehydration of hydrated metal ion ΔH_{M-H2O}).

$$\Delta H_C = \Delta H_{M-L} - \Delta H_{M-H_2O} \tag{4.1}$$

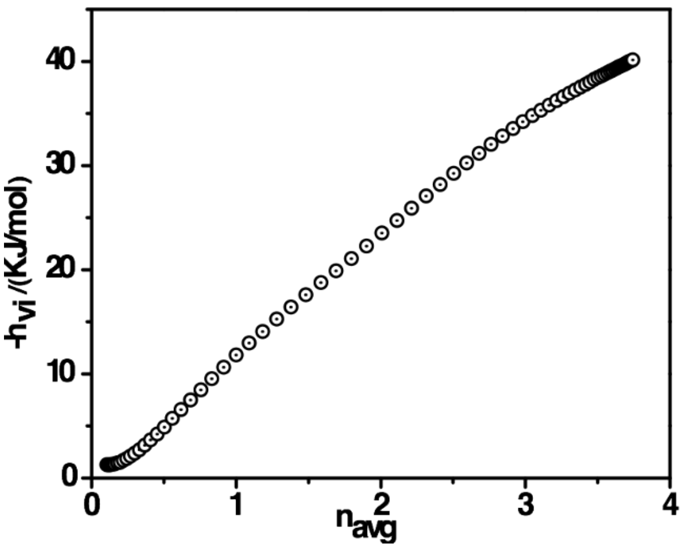

Figure 4.5: Plot of Δh_{vi} vs n_{avg} for Eu(III)-picolinate complexation.

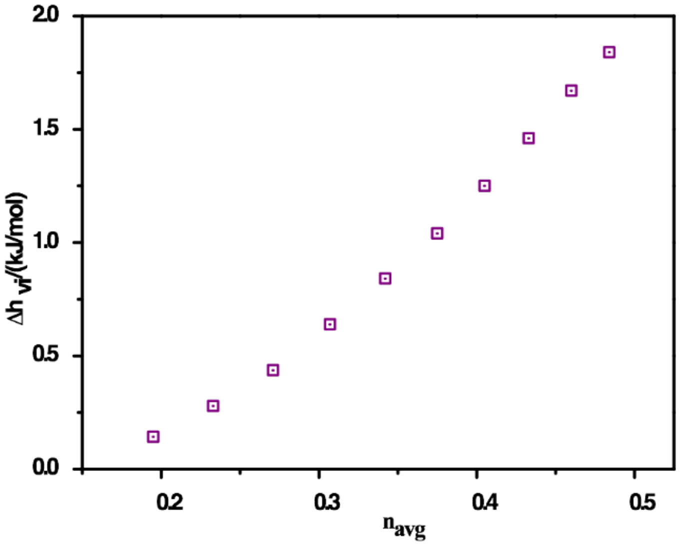

Figure 4.6: Plot of Δh_{vi} vs n_{avg} for Eu(III)-isonicotinate complexation.

The complexation of Eu(III) with simple carboxylates is endothermic in nature and is entropy driven. This is typical of hard acid hard base behaviour where both the metal ion and ligand are highly hydrated. The energy required for dehydrating the metal ion and ligand is more than that released in metal-ligand bond formation thus making the overall reaction endothermic. The water molecules released during complexation increase the entropy of complexation. However, the participation of other functional groups like hydroxyl and amino groups increases Eu(III) ligand interaction making the reaction exothermic. For instance, ΔH_C for Eu(III) complexation with alpha hydroxy isobutyrate, glycolate and glycine are - 4.0, - 2.1

and - 13 kJ/mol respectively. More negative value in the case of Eu(III)-glycine can be attributed to higher basicity of 'N' compared to 'O'. In case of Eu(III)-picolinate complexes, the metal ion binds with the ligand through both carboxylic oxygen and nitrogen atom and thus forms chelate complexes. Therefore, higher exothermicity of Eu(III)-picolinate indicates the role of nitrogen atom as well as rigid structure of ligand which favors the complexation process. The complexation of Eu(III) with picolinate was found to be highly exothermic, the exothermicity decreasing with successive complexation. The decreasing magnitude of ΔH_C on successive complexation is the result of decreased metal ligand interaction due to reduced charge on metal ion and limited availability of coordination space around the metal ion to facilitate further ligand participation.

In the case of nicotinate and isonicotinate, as there is no possibility of chelation via pyridyl nitrogen due to far away position of the nitrogen from the oxygen, the complexation is found to be endothermic and entropy driven. This indicates that the complexation is similar to that in case of carboxylates (table 4.3) in which the metal ion binds through carboxylate. The difference in endothermicity between the complexes of nicotinate and isonicotinate is indicative of a much higher charge transfer from nitrogen to carboxylate oxygen in case of isonicotinate than that in case of nicotinate, which is corroborated by theoretical calculations to be discussed in section 4.4.1.4.

Table 4.3: Thermodynamic data for complexation of Eu(III) with monocarboxylates at 298 K. (ΔG, ΔH and $T\Delta S$ are given in kJ/mol)

Ligand	**log K_{ML}**	**ΔG_{ML}**	**ΔH_{ML}**	**$T\Delta S_{ML}$**	**Reference**
Acetate	1.97 ± 0.05	-11.20	6.2 ± 0.8	17.4	[343]
Benzoate	2.16 ± 0.04	-12.33	7.9 ± 0.6	20.3	[124]
Nicotinate	1.93 ± 0.04	-11.01	9.0 ± 0.6	20.0	Present work
Isonicotinat	2.28 ± 0.12	-13.01	5.5 ± 0.3	18.5	Present work

e

4.4.1.3. Time Resolved Luminescence Spectroscopy

Figure 4.7 shows some of the normalized (with respect to 592 nm) fluorescence emission spectra of Eu(III)-picolinate system recorded during the fluorimetric titration of Eu(III) with picolinate at various L/M ratio. The asymmetric ratio (AR), that is, ratio of the intensity of 616 nm with respect to 592 nm peak increases with L/M (figure 4.8), indicating the successive formation of Eu(III)-picolinate complexes.

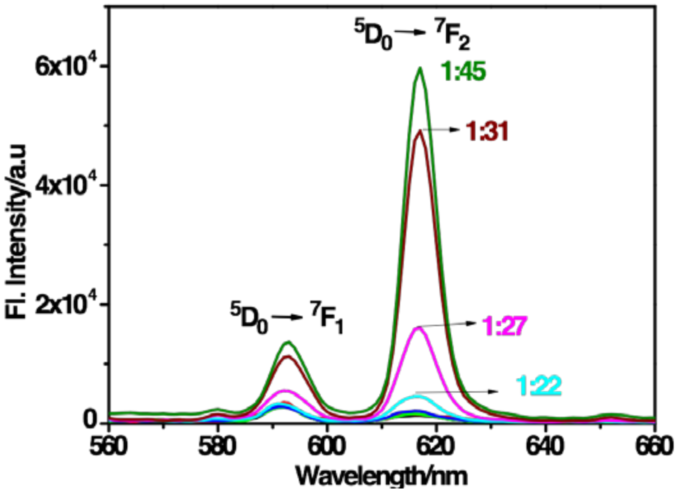

Figure 4.7: Spectroluminescence titration of Eu(III) (Titrand (25 mL): [Eu(III)] = 4.452 x 10^{-3} M and [$HClO_4$] = 26.44 x 10^{-3} M) with ligand solution ([picolinate]= 0.4989 M and [H] = 0.3328 M)

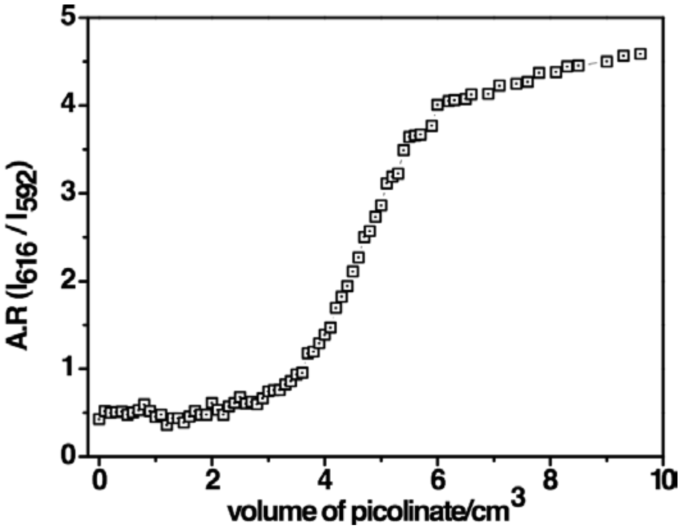

Figure 4.8: The variation of asymmetric ratio (I_{616}/I_{592}) with volume of picolinate [Eu(III)] = 4.452×10^{-3} M and [$HClO_4$] = 26.44×10^{-3} M) with buffered ligand solution ([picolinate]= 0.4989 M and [H] = 0.3328 M)

Luminescence spectra and lifetimes are very sensitive to the first solvation sphere of the Eu^{3+} ion and hence can be used to study the kind of interaction between Eu(III) ion and different anions. The coordinated water molecules around Eu(III) act as quenchers as they provide non-radiative pathways for deexcitation of $^5D_0$ state through their vibronic levels. The life time of the excited state ($^5D_0$) of Eu(III) is related to the number of water molecules present in the primary coordination sphere of metal ion (refer to chapter-2) and provide a direct method to know the mode (inner or outer sphere) of complexation process [241-242].

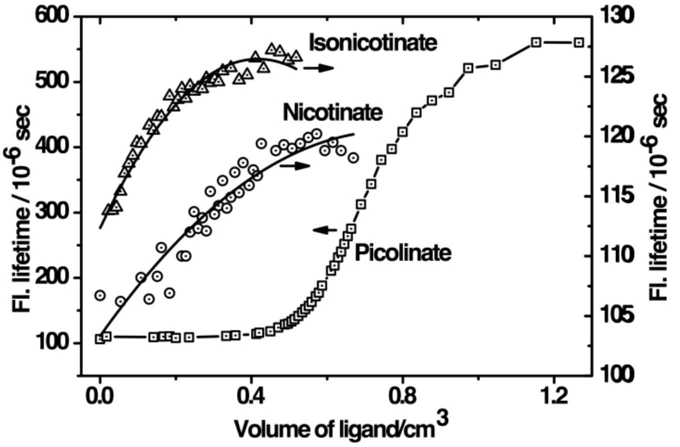

Figure 4.9: The variation of luminescence lifetime with the volume of ligand (Left Y-axis: Eu(III)-picolinate complexation; Right Y-axis: Eu(III)-nicotinate/isonicotinate complexation)

Figure 4.9 shows the plot of the luminescence decay lifetime for Eu(III)-pyridine monocarboxylate systems. The single lifetime obtained during the titration indicates the fast exchange of ligand between free and complexed metal ion. The lifetime increases with volume of titrant as more and more complex is formed and finally attains a constant value at 560 µs which corresponds to formation of ~100 % ML_4. Only one water molecule is present in ML_4 indicating expulsion of two water molecules on complexation by each picolinate anion. Thus, in all the complexes ML_i (i=1 to 4) picolinate acts as bidentate ligand. The lifetime of Eu(III) nicotinate and Eu(III) isonicotinate were saturated at 120 µs (n_{avg} = 0.7) and 127 µs (n_{avg}= 1.19) respectively indicating the monodentate nature of the complexes through carboxylate oxygen (acetate life time is133 µs) .

4.4.1.4. Theoretical Calculations

Stability parameter (complexation energy), geometrical parameter (bond lengths) and the charge distribution values (table 4.4) were calculated for all the aqueous complexes using natural population analysis scheme in TURBOMOLE. Following equation has been used for the calculation of the complexation energy (ΔE_s) of the various complexes considered in the present work.

$$M^{3+}\,(aq) + n\,L^{-}(aq) \rightarrow [ML_n]^{n-3}\,(aq) \qquad (4.1)$$

$$\Delta E_s = E(ML_n)^{n-3} - n*E(L^-) - E(M^{3+}) \qquad (4.2)$$

where $E(ML_n)^{n-3}$, $E(L^-)$ and $E(M^{3+})$ denote the energy of the complex, ligand and the metal ion, respectively. Here ‘n’ denotes the number of ligands considered in complex, $(ML_n)^{n-3}$. The complexation energy and bond lengths calculated for different geometries are listed in the table 4.4. In case of picolinate, ML, ML_2 and ML_3 complexes are found to be more stable with both nitrogen and oxygen as donors instead of two oxygens in solvent phase. This can be explained in terms of the formation of 5-membered chelating complexes when the nitrogen and one of the oxygen centers are involved in binding, instead of 4-membered chelates with two oxygen donors.

Table 4.4: Calculated complexation energy, metal-ligand bond length and atomic charge values for various Eu(III) - pyridine monocarboxylates complexes in solvent phase.

	ΔE_s /eV	**d_{Eu-O}**	**$d_{Eu-N)}$**	**q_{EU}**	**q_O**	**q_N**
			Eu(III)-Picolinate Complexes			
ML (OO)	-2.81	2.379	-	2.454		

ML (ON)	-2.90	2.243	2.531	2.209	-0.793, -0.499	-0.607
ML2 (ON)$_2$	-4.55	2.272	2.533	1.843	-0.801	-0.598
ML21 (ON)(OO)	-4.12	2.255, 2.275	2.521	2.447		
ML22 (OO)$_2$	-4.13	2.380	-	2.278		
ML3 (ON)$_3$	-5.71	2.270	2.609	1.881	-0.780, -0.627	-0.569
ML31 (ON)$_2$(OO)	-5.68	2.278, 2.418	2.599	2.412		
ML32 (ON)(OO)$_2$	-5.55	2.281, 2.424	2.580	2.291		
ML33 (OO)$_3$	-4.99	2.383	-	1.918		
Eu(III)-Nicotinate Complexes						
ML (OO)	-2.63	2.383	-		-0.773	-0.339
ML (N)	-2.51	-	2.461			
ML2 (OO)$_2$	-3.90	2.375	-		-0.717	-0.493
ML3 (OO)$_3$	-3.97	2.380	-		-0.718	-0.507
Eu(III)-Isonicotinate Complexes						
ML (OO)	-2.23	2.312	-		-0.943	-0.071
ML (N)	-2.02	-	2.514			
ML2 (OO)$_2$	-3.86	2.380	-		-0.725	-0.478
ML3 (OO)$_3$	-3.89	2.384	-		-0.708	-0.496

In the case of Eu-Nicotinate and Eu-Isonicotinate systems, the complexation energies for all the three complexes (ML, ML_2 and ML_3) are lower than the respective complexation energies with Eu-Picolinate complexes, which could be due to the proximity of the N and O donor centers in Eu-Picolinate. However, there is a significant change in charge on each atom in the complex, compared to that in bare ligand (table 4.5).

Table 4.5: Calculated atomic charges on bonding atoms of the bare ligands

Ligand	q_O	$q_{N)}$
Picolinate	-0.773	-0.512
Nicotinate	-0.773	-0.528
Isonicotinate	-0.768	-0.526

In case of Eu(III)-picolinate complexes, there is a reduction in the charge on carboxylate oxygen and an increase in the charge on nitrogen compared to the free ligand case. Further the enhanced charge on nitrogen facilitates the stronger electrostatic interaction which can be attributed to the stronger binding in these complexes by chelation through pyridyl nitrogen atom. From the table 4.5, it can be clearly observed that reduction of charge density on pyridyl nitrogen is more in case of isonicotinate (-0.526 to -0.088) compared to nicotinate (-0.528 to -0.339), indicating higher charge transferred from nitrogen to carboxylate in case of isonicotinate than that in nicotinate. This is understandable, as the meta position is deactivating (nicotinate) while para position is an activating site (isonicotinate). The higher charge transfer in isonicotinate faciliates closure approach of carboxylate to the metal ion than in nicotinate, which is well reflected in the values of bond lengths (table 4.4) and also a greater decrease in the charge on central atom in the 1:1 complexes of these ligands with Eu(III). This is also evident from the higher stability constant and lower endothermic ΔH_{ML} values of isonicotinate complex than nicotinate complex.

4.4.2. Eu(III) Complexation by Pyridine Monocarboxylate-N-oxides

4. 4.2.1. Stability, Stoichiometry and Speciation of The Complexes

The addition of half neutralized ligand to fixed volume of metal and monitoring the change in hydrogen activity was employed to determine the stability constants and speciation diagrams of europium pyridine monocarboxylate-N-oxide complexes using Hyperquad programming [217]. The speciation diagrams (figure 4.10) show that europium forms ML_i (i = 1-4) complexes with PANO, while it forms only ML and ML_2 kind of complexes with NANO and IANO. The stability constants for complexes of Eu(III) with all PCNOs are given in table 4.6.

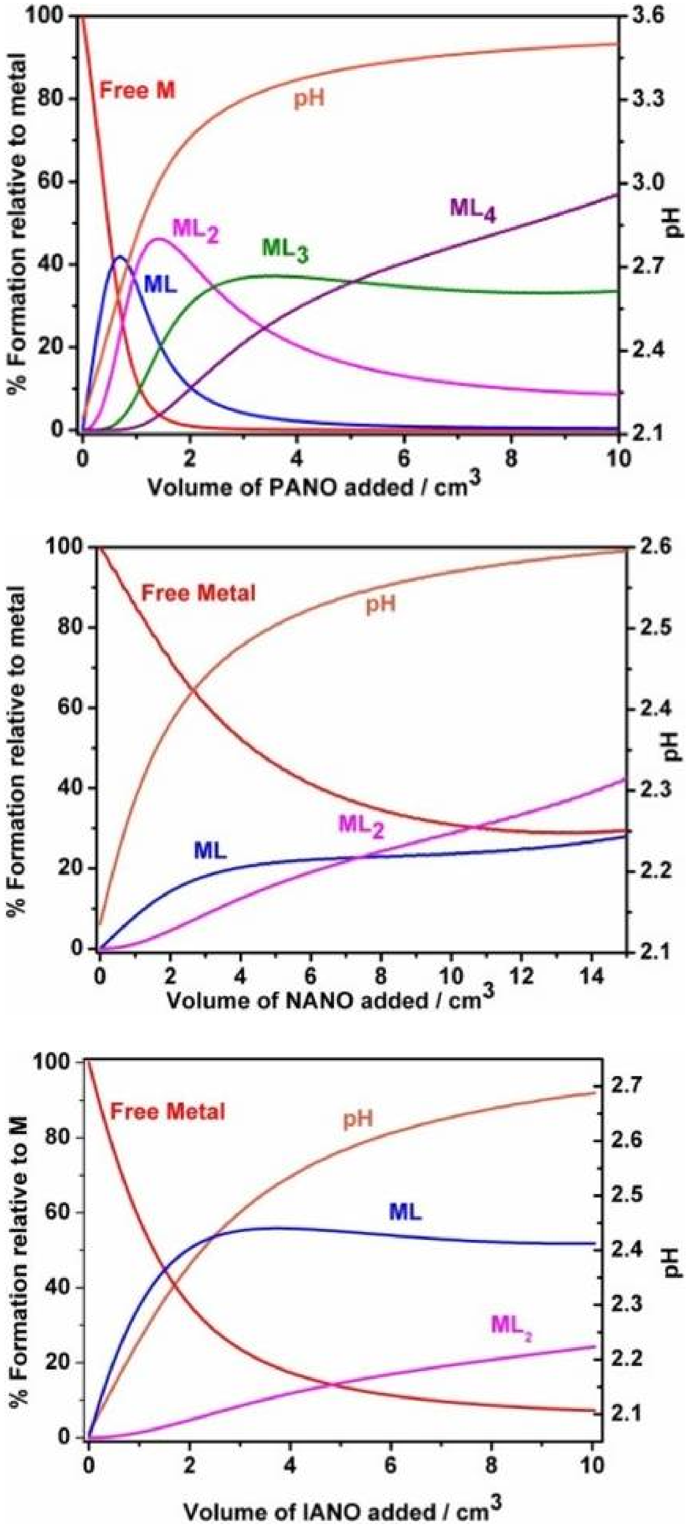

Figure 4.10: Speciation plots for complexation of Eu(III) by PCNOs (top to bottom: PANO, NANO and IANO) at T = 298.15 K and I = 1.0 M $NaClO_4$. (The concentrations employed for the titrations are given in table 4.1)

Table 4.6: Thermodynamic parameters (ΔG, ΔH and ΔS) for the complexation of Eu(III) with PCNOs at T = 298.15 K and I = 1.0M $NaClO_4$. (ΔG, ΔH and TΔS are given in kJ/mol)

Complex	**log K**	**-ΔG**	**ΔH**	**TΔS**	**ΔS**
	Eu(III) - Picolinic acid-N-oxide (PANO) Complexation				
ML	3.03 ± 0.02 2.94 ± 0.05[a]	17.29 ± 0.10	2.12 ± 0.02	19.42 ± 0.12	65.1 ± 0.4
ML_2	2.61 ± 0.01 2.29 ± 0.08[a]	14.90 ± 0.06	1.55 ± 0.01	16.45 ± 0.07	55.2 ± 0.2
ML_3	1.90 ± 0.02	10.85 ± 0.08	0.79 ± 0.03	11.64 ± 0.11	39.0 ± 0.4
ML_4	1.53 ± 0.01	08.73 ± 0.06	0.30 ± 0.02	09.03 ± 0.08	30.3 ± 0.3
	Eu(III) - Nicotinic acid-N-oxide (NANO) Complexation				
ML	1.51 ± 0.01	08.62 ± 0.04	-4.04 ± 0.02	4.57 ± 0.06	15.3 ± 0.2
ML_2	1.70 ± 0.01	09.70 ± 0.02			
	Eu(III) - Isonicotinic acid-N-oxide (IANO) Complexation				
ML	2.51 ± 0.01	14.34 ± 0.05	7.80 ± 0.09	22.14 ± 0.14	74.2 ± 0.5
ML_2	1.33 ± 0.02	09.09 ± 0.04			

[a] (I = 2.0 M $NaClO_4$) from ref [155]

The following observations can be made from the stability constants Eu(III) - PCNO complexes (table 4.6). (i) The log K for Eu-PANO complexes is considerably higher than respective Eu-NANO and Eu-IANO complexes. (ii) Among Eu-NANO and Eu-IANO complexes, the latter forms stronger complexes than former with log K being comparable to that of ML_2 of Eu-PANO complex, (iii) The log K for successive complexation decreases (i.e. log $K_1 >$ log $K_2 >$ log K_3) in general but the log K_2 for Eu-NANO complex is higher than its log K_1. The log K_2 for Eu-NANO was also found to be higher than log K_2 for Eu-IANO, which is reverse of the order for log K_1. The higher log K of Eu-PANO complexes is due to the formation of six membered chelate involving the oxygen of N-oxide and the oxygen of carboxylate group, which is not possible in NANO and IANO due to lack of favorable configuration.

The higher log K_1 of Eu-IANO than Eu-NANO can be explained by drawing the possible resonance forms of IANO (figure 3.14). During complexation the resonance form IV of IANO is more stabilized which acts like a dianion and thus forms stronger complexes than simple carboxylates. The abnormality in trend of log K_1 and log K_2 for Eu-NANO can be attributed to change in complexation process from outer sphere complex in ML to a mix of outer and inner sphere or completely inner sphere complex in case of ML_2. Harmon et al., also observed similar trend in case of Am(III) thiocynate complexes for which log K_3 is higher than log K_2 and was attributed to the transition from outer to innersphere complexation during the formation of ML_3 from ML_2 [344-345].

4. 4.2.2. Thermodynamics of Complexation

The enthalpy of complex formation (ΔH_C) can be directly obtained from the plots of h_{vi} vs. n_{avg} (Figure 4.11) as h_{vi} at $n_{avg} = 1, 2, 3$ corresponds to the enthalpy of formation of the complexes ML, ML_2 and ML_3 respectively. The entropy of formation (ΔS_C) of the complexes was calculated from the log K and ΔH_C for the formation of complexes using equation 4.3.

$$\Delta G = -2.303\ R * T * \ln K = \Delta H_C - T\Delta S_C \qquad (4.3)$$

The thermodynamic parameters (log K, ΔG, ΔH and ΔS) for the formation of all the Eu(III) - PCNO complexes are given in table 4.6.

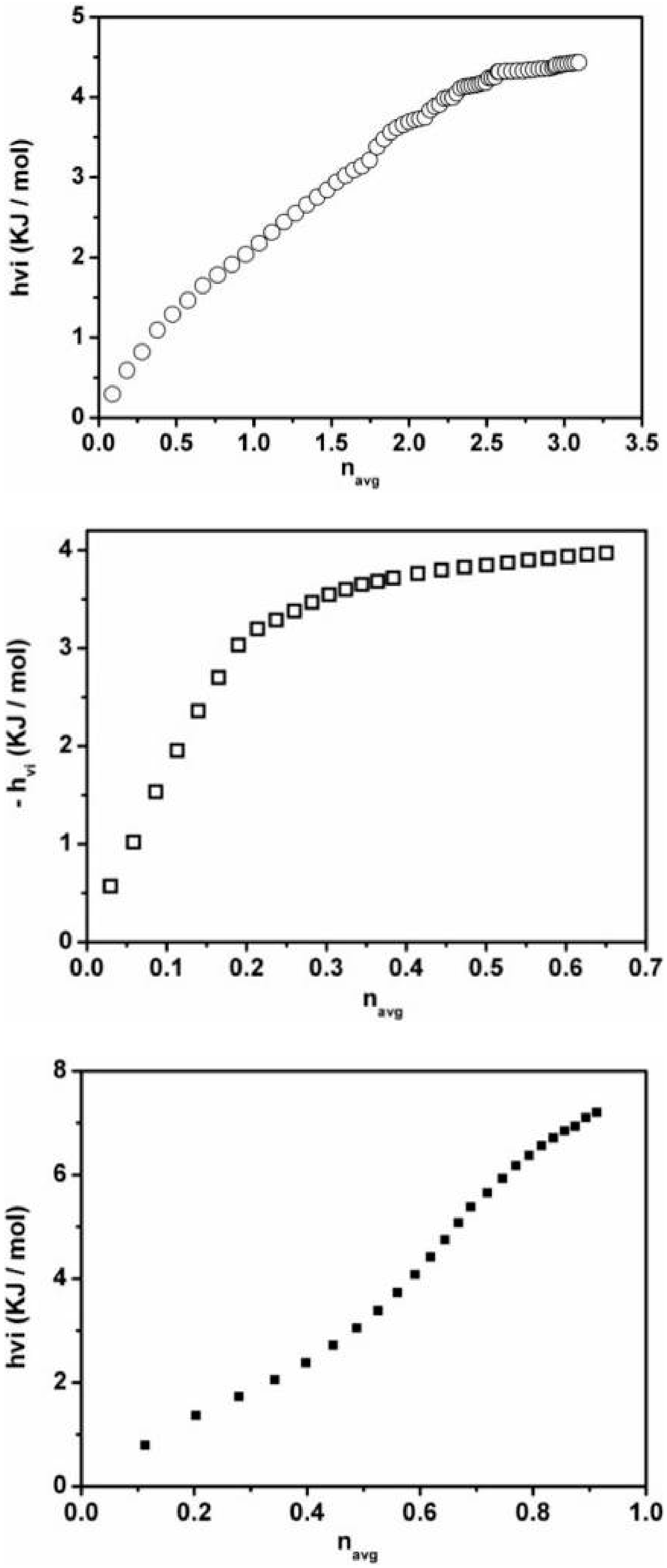

Figure 4.11: The calorimetric data for the titration of Eu(III) with PCNOs (From top to bottom: PANO, NANO and IANO) at T = 298.15 K and I = 1.0 M $NaClO_4$. (The concentrations are given in table 4.1).

The ΔH_C for Eu(III) complexes with PANO and IANO are positive (endothermic) while for NANO, the same is negative (exothermic). The variation in the ΔH_C with respect to change in the position of carboxylate group to N-oxide moiety can be explained on the basis of Eigen Tamm mechanism, in which there are four major states to depict the complete formation of an ion pair (complex) in the solution [78], viz, the approach of completely hydrated reactants towards each other to come in direct contact followed by merge of bothe the hydration spheres (of metal and ligand ions) to single hydration sphere and the complex and finally direct contact of metal and ligand. Eigen and Tamm suggested that the conversion from hydrated sphere contact complex (diffusion of cation and anion to each other's hydration spheres) to direct contact complex involves the energy requirement for the removal of hydration spheres and is the slowest step during the entire complex formation procedure (ligand bonding to metal in its primary coordination sphere). The entire scheme of Eigen Tamm mechanism can be correlated with the following relation.

$$M(H_2O)_x + L(H_2O)_y \rightarrow M(H_2O)_x L(H_2O)_y \rightarrow M(H_2O)_n L \rightarrow ML \rightarrow ML(H_2O)_f \qquad (4.4)$$

where the subscripts x and y are the number of water molecules attached to bare metal and ligand representing their respective primary hydration spheres, n is the number of water molecules in the diffused hydration sphere complex and $0 < n < x+y$ depending on the ability of ligand to replace the water molecule in primary coordination sphere and on the stoichiometry of the resulting complex, f is the number of water molecules in the hydrated complex after ML inner-sphere complex formation. The mechanism consists of a gradual substitution of the solvent molecules in the different coordination shells of the metal ions, involving various effects such as ion-dipole interaction, dipole-dipole interaction, field stabilization of the ligands and stereo specific effects.

The lanthanides being hard acids and having high ionic potentials are generally heavily hydrated in aqueous medium. For a ligand to bind with the metal ion, this hydration sphere along with its own hydration sphere has to be broken out to form a complex if the ligand is to occupy in the primary coordination shell (as in case of inner-sphere complexation). Thus the complexation of lanthanides with carboxylates are considered to be endothermic in nature and follows Eigen Tamm mechanism. The complexation of Eu(III) with PANO and IANO falls in the similar lines forming inner-sphere complexes and results in positive enthalpy of formation. The outer-sphere complexation of Eu(III) by NANO (also supported by luminescence life time results) doesn't require energy to break the hydration sphere of metal, and the ligand is attached to metal while its primary hydration sphere is intact with the metal. Hence these complexation processes favor the formation of ion pairs that leads to release of energy making the overall process exothermic in nature.

Two important and interesting observations are noteworthy from the data of ΔH_C (table 4.6): (i) Though the bonding moiety (carboxylate) is same in both Eu-NANO and Eu-IANO complexes, the former is exothermic and outer-sphere while the other is endothermic and inner-sphere. (ii) Between Eu-PANO and Eu-IANO complexes, the latter is more endothermic and more entropically favorable (higher positive ΔS) than the former. Both the observations can be explained by looking at the resonance structure of pyridine-N-oxide (figure 4.12). The charge polarization in canonical structures of pyridine-N-oxide (figure 4.12) takes place only at ortho (2-position) and para (4-position) to N-oxide group. Thus the ortho and para isomers can withdraw more electron density from N-oxide group to binding carboxylate at these positions resulting in higher basicity of the ligand and enabling replacement of water molecule form inner-sphere complexes.

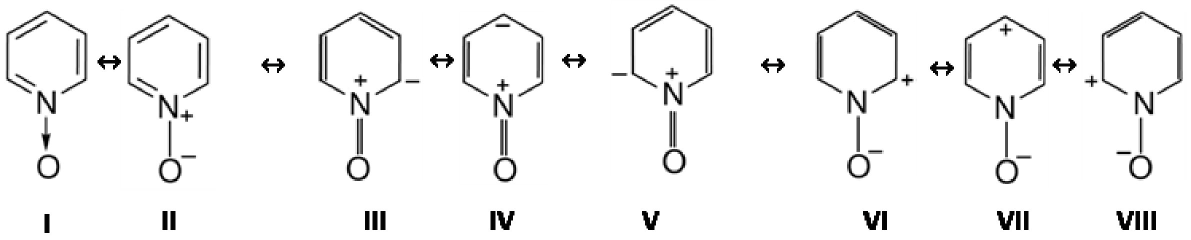

Figure 4.12: Resonance structures of pyridine-N-oxide.

The additional chelation possibility in Eu-PANO complexes further enhances their stability. In case of Eu-NANO complexes, neither the chelation nor the ligand basicity favors the removal of water molecule from coordination sphere of metal ion leading to outer-sphere complexation. Comparison of resonance structures of PANO (figure 4.13) and IANO (figure 3.14) can help in understanding higher endothermicity of Eu-IANO complexation than Eu-PANO complexation. The binding atoms in ligand are oxygen of N-oxide and oxygen of carboxylate in Eu-PANO complexes while in case of Eu-IANO complexes both the oxygen atoms of carboxylate are binding.

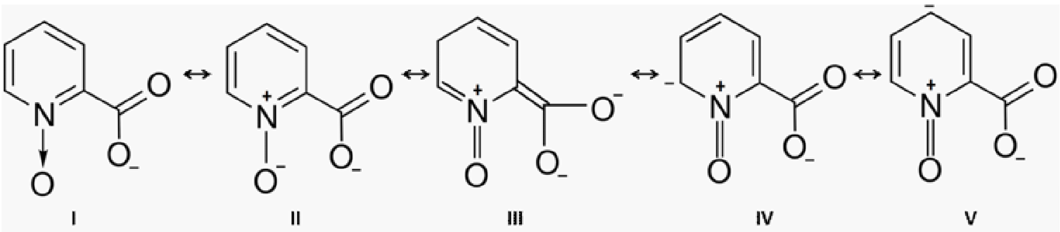

Figure 4.13: Resonance structures of PANO.

The resonance structure II of PANO (figure 4.13) bearing a negative charge on oxygen of N-oxide and oxygen of carboxylate is more favored during the complexation in which europium forms six membered chelate complexes with PANO. The oxygen atom in N-oxide moiety is coordinately bonded to nitrogen while the oxygen of carboxylate is covalently bonded to carbon atom. The coordinate bonds are commonly considered to be comparable to, but weaker than covalent bonds as the entire bonding electrons comes from one atom (from nitrogen in case of N-oxide) [346]. In PANO, the oxygen of N-oxide is more like neutral due to proximity of positive charge on nitrogen and hence the extent of hydration around this atom would be relatively low compared to carboxylate oxygen where it behaves more like an anion. In case of IANO, during complexation, the resonance structure IV (figure 3.14) bearing negative charge on the both oxygen atoms of carboxylate acts like a dianion and heavily hydrated resulting in more endothermicity and higher ΔS of the Eu-IANO complexes compared to Eu-PANO complexes.

Molecular dynamic studies have shown that for dianion separated by two aliphatic carbon atoms, the hydrophobic interactions dominate the solvation process and encompass the whole molecule [274]. However the solvation of dianion (as in case of oxalate) having less space between two anions was lower where only six water molecules are around the dianion [347]. Similarly, the number of water molecules that can encompass the PANO is smaller than IANO in which both the negative charges of the molecule can accommodate more number of water molecules. Therefore the complexation leads to higher dehydration in IANO than PANO and hence both ΔH and ΔS are more positive for Eu-IANO complexes than the corresponding Eu-PANO complexes. This indicates the key role of hydration of a ligand on thermodynamic parameters during its complexation with metal ion.

4. 4.2.3. Luminescence Intensities and Lifetime of The Complexes

In the present study, the luminescence emission spectra and lifetime for the decay of europium excited state ($^5D_0$) are measured for all the three Eu(III)-PCNO complexes in titration mode (details in experimental section). The intensities of three important emission peaks $^5D_0 \rightarrow {}^7F_0$, $^5D_0 \rightarrow {}^7F_1$ and $^5D_0 \rightarrow {}^7F_2$ (hypersensitive transition) on complexation of Eu(III) with PANO (addition of ligand solution to fixed concentration of europium solution) is shown in figure 4.14 which clearly shows the appearance of peak at 580 nm, decrease in intensity of $^5D_0 \rightarrow {}^7F_1$ transition and an increase in intensity of $^5D_0 \rightarrow {}^7F_2$ transition with the increased addition of ligand to metal solution. $^5D_0 \rightarrow {}^7F_0$ transition is strictly forbidden according to Judd-Ofelt theory (a 0-0 transition is forbidden by ΔJ selection rule) [348]. Although $^5D_0 \rightarrow {}^7F_0$ emission is generally observed to be relatively weak, its intensity is quite sensitive to the ligand environment. The observation of $^5D_0 \rightarrow {}^7F_0$ transition is an indication that the Eu^{3+} ion occupies a site with C_{nv}, C_n or C_s symmetry [349, 122]. This transitions appears when the highly symmetric (D_{3h}) $Eu(H_2O)_9$ is gradually converted to a more asymmetric ML_i (i=1-4) complex. The appearance of this transition further indicates that the symmetry is being reduced on complexation leading to the possibility of J-mixing and thus facilitating the transition [122].

The $^5D_0 \rightarrow {}^7F_1$ transition is a magnetic dipole transition and is mostly independent of Eu^{3+} environment. Even in low-symmetry systems the $^5D_0 \rightarrow {}^7F_1$ transition retains its magnetic dipole character, and its radiative transition probability is not much affected by the ligand environment. The invariance in intensity of $^5D_0 \rightarrow {}^7F_1$ transition is applicable only to the total integrated intensity but not to individual intensities of the crystal field components. The total intensity can be influenced by the J-mixing. The intensity of this transition will be highest among all other transitions of Eu^{3+} ion when it is present in centrosymmetric environment as in case of $Eu(H_2O)_9$ [350]. Both $^5D_0 \rightarrow {}^7F_0$ and $^5D_0 \rightarrow {}^7F_1$ transitions show very little variations in intensity and mostly provide qualitative information like the changes in centre of inversion and symmetry of Eu(III) aqua ion on complexation.

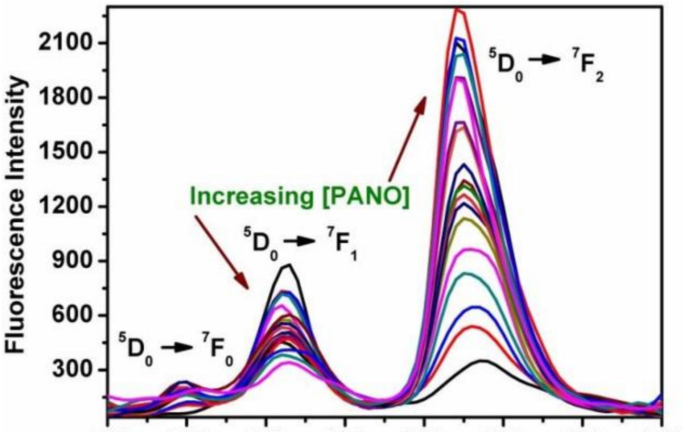

Figure 4.14: Luminescence spectra showing the variation in intensities of $^5D_0 \rightarrow {}^7F_J$ (J=0-2) transitions for Eu-PANOcomplexation.

The hypersensitive $^5D_0 \rightarrow {}^7F_2$ transition, on the other hand, is predominantly electric dipole in character, and the radiative transition probabilities are very sensitive to the ligand field around Eu(III) ion. The high intensity of $^5D_0 \rightarrow {}^7F_2$ transition or the ratio of intensities $^5D_0 \rightarrow {}^7F_2$ / $^5D_0 \rightarrow {}^7F_1$ are often attributed to the asymmetry caused by ligand complexation with metal though other factors like the polarizability, chelation ability of ligand also play an important role [351]. The complexation of ligand to primary coordination sphere of metal ion can also be related to this ratio (figure 4.15). The progress of complexation on addition of more ligand will change the coordination environment around the Eu(III) aqua ion by replacing the water molecules with ligands leading the formation of higher stoichiometric complexes.

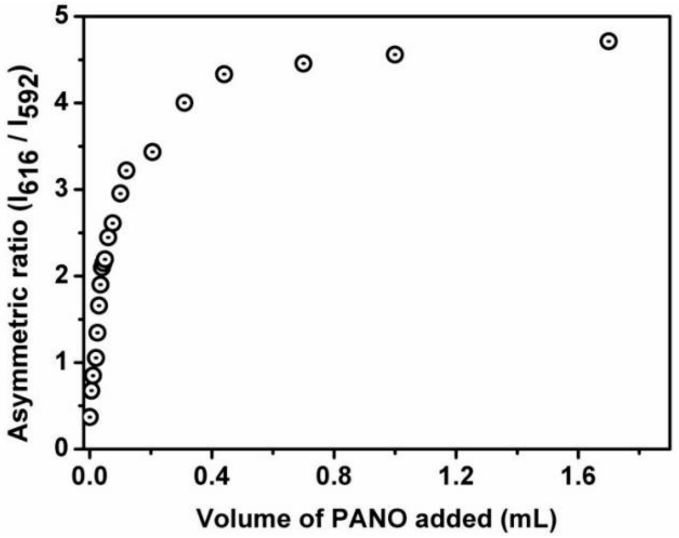

Figure 4.15: The variation in the asymmetric ratio ($^5D_0 \rightarrow {}^7F_2$ / $^5D_0 \rightarrow {}^7F_1$) with the addition of PANO.

The decay profiles of excited $^5D_0$ state of Eu(III) on addition of increasing volumes of the ligand are shown in figure 4.16 and the lifetime (τ) values for the same are given in table 4.7. The table also shows the number of water molecules present in the primary coordination sphere (N_{H2O}) of Eu(III) ion for different n_{avg} (average number of ligands bound per metal ion). The lifetime data for the complexation of Eu(III) by PANO show an increasing trend of the lifetime with a corresponding decrease in the number of water molecules present in the primary hydration sphere indicating an inner sphere complexation process. Further, at the end of titration, for an n_{avg} value of 3.12, there are only three water molecules in the primary hydration sphere of Eu(III) confirming the removal of six water molecules and hence bidentate coordination by each PANO ligand.

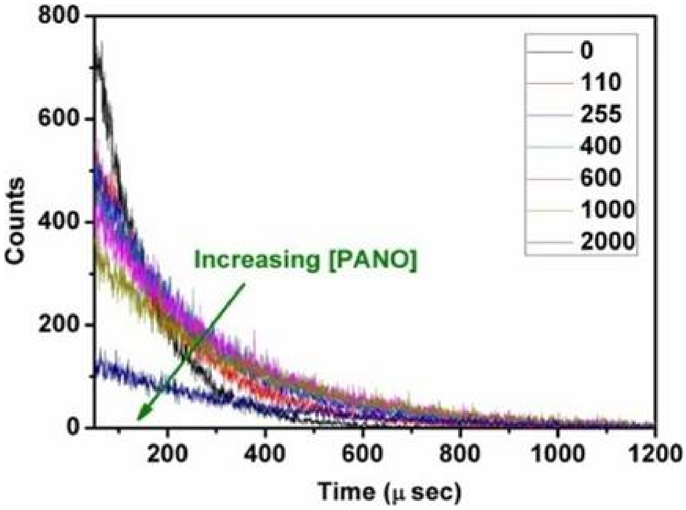

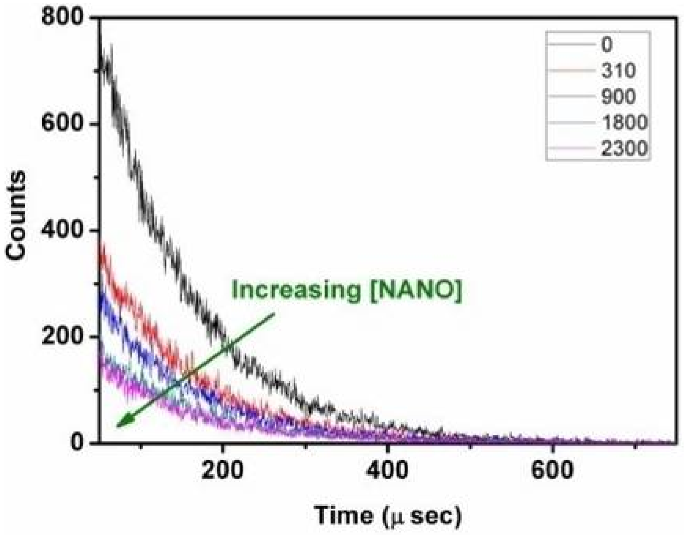

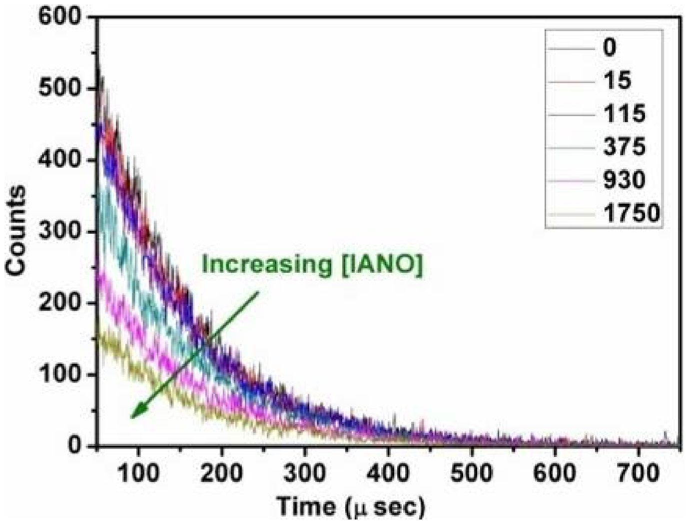

Figure 4.16: Decay spectra of Eu(III) excited state for different ligand to metal (L/M) ratio. (Top to bottom: Eu(III)-PANO, Eu-NANO and Eu-IANO; (All the concentrations employed in the titration were given in table 4.1).

The similar observation for complexation of Eu(III) by IANO indicates an innersphere complexation with removal of one water molecule on formation of 1:1 complex. The lifetime data of Eu(III)-NANO complexation shows no removal of water molecule (considering an error of 0.5 water molecules) after the formation of 1:1 complex (n_{avg} = 1.04 in the table 4.7). But the life time data has a systematic increase with increase in the n_{avg} value indicating a possibility of transition from outer-sphere to inner-sphere complexation at higher stoichiometric ratios (larger n_{avg} values).

Table 4.7: The lifetime data for the complexation of Eu(III) by PCNOs at different n_{avg} (average number of ligand molecules bound per metal ion). N_{H2O} is the number of water molecules in the primary coordination sphere).

Eu-PANO			**Eu-NANO**			**Eu-IANO**		
n_{avg}	**τ (μ sec)**	**N_{H2O}**	**n_{avg}**	**τ (μ sec)**	**N_{H2O}**	**n_{avg}**	**τ (μ sec)**	**N_{H2O}**
0	109.5	9.15	**0**	109.0	9.19	**0**	109.9	9.11
0.63	171.7	5.67	**0.30**	109.0	9.19	**0.04**	111.5	8.98
1.63	214.7	4.45	**0.62**	109.7	9.13	**0.25**	115.3	8.67
2.15	246.7	3.82	**0.66**	112.3	8.91	**0.60**	119.8	8.32
2.47	269.7	3.45	**1.04**	114.4	8.74	**0.86**	124.5	7.99
2.72	291.6	3.16				**1.03**	129.3	7.68
3.12	313.4	2.91						

4.4.2.4. Density Functional Theory Calculations

4.4.2..4.1. Structural Parameters

The optimized geometries for the complexes of Eu(III) ion with PANO are shown in figure 4.17 and the calculated structural parameters like bond distances and the bond angles for the binding atoms are tabulated in table 4.8. Four inner sphere complexes (ML_i; i=1-4) of Eu(III) ion with PANO, namely $[Eu(PANO)(H_2O)_7]^{2+}$, $[Eu(PANO)_2(H_2O)_5]^{+}$, $[Eu(PANO)_3(H_2O)_3]$and $[Eu(PANO)_4(H_2O)]^{-}$ as per the experimental observation were considered for the theoretical studies while all the possible inner and outer sphere complexes of Eu(III) ion with NANO and IANO were considered for the same.

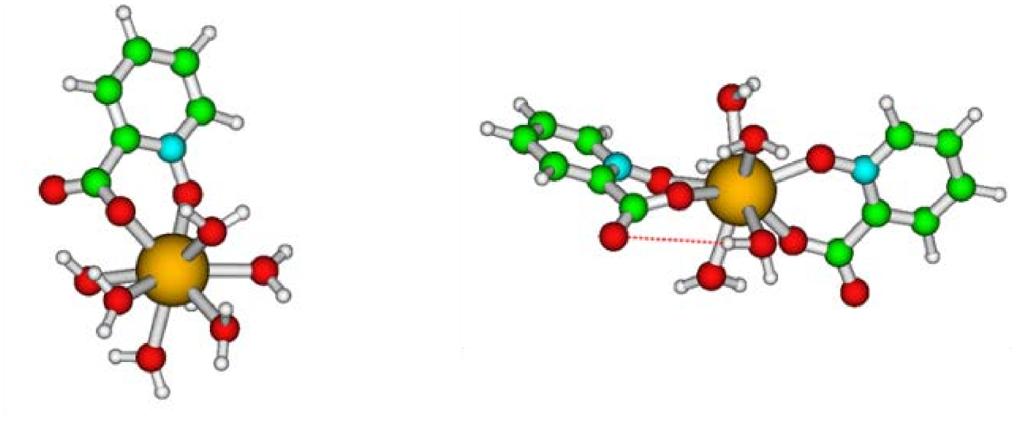

$[Eu(PANO)(H_2O)_7]^{2+}$ $[Eu(PANO)_2(H_2O)_5]^{+}$

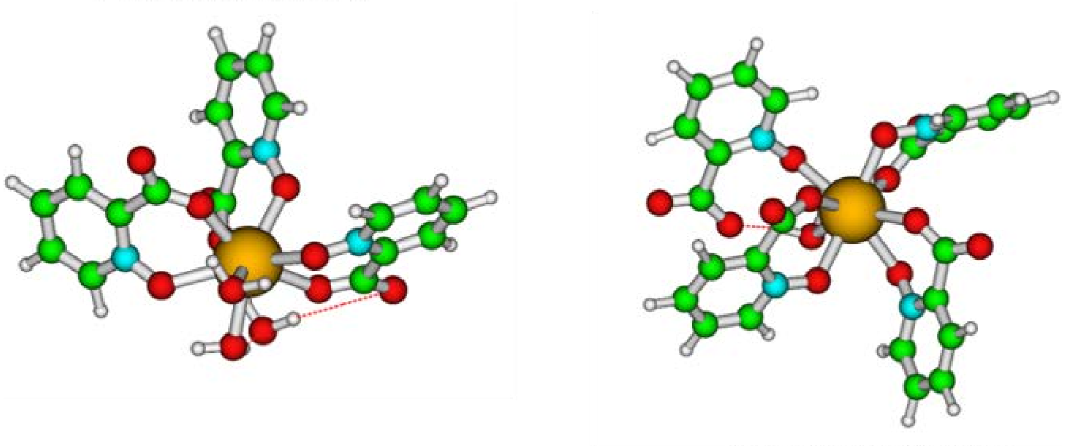

$Eu(PANO)_3(H_2O)_3$ $[Eu(PANO)_4(H_2O)]^{-}$

Figure 4.17: Optimized geometries for Eu(III)-PANO complexes at B3LYP/SVP level of theory. (Colour code: Yellow - Eu(III), Red - Oxygen, Blue - Nitrogen, Green - Carbon and White - Hydrogen)

From the Table 4.8, it can be seen that the average Eu-O (of H_2O) bond distance is 2.500 Å in case of $[Eu(H_2O)_9]^{3+}$ and on complexation with PANO, the same increases with increase in L/M. Further, among the bonding atoms, the bond distance between Eu-O (of N-O) and Eu-O (of COO) also increases with increase in L/M, which can be attributed to the steric hinderance and lower probability of interaction on successive complexation process to achieve higher L/M ratio. The bond angles (∟O-Eu-O) also follow descending order from ML to ML_4. The steric strain around the metal atom constrains the bond angles to freeze further on attaining higher stoichiometry of the complex. The elongation of Eu-O (O of H_2O) bond on complexation is the lowest for Eu-PANO complexes among all the three Eu-PCNO complexes. This can be explained on the basis of formation of inter molecular hydrogen bonding. The inter molecular hydrogen bonding between the unbound oxygen of carboxylate with the hydrogen atom of water molecule still present in primary coordination sphere of Eu ion. In the case of other two complexes, such intramolecular hydrogen bonding is not possible due to involvement of both the oxygen atoms in binding to metal ion during the complex formation.

Table 4.8: Average bond distances and bond angles for the optimized geometries of Eu(III) complexes with all the three pyridine monocarboxylate-N-oxides.

Complex	**$d_{Eu\text{-}O\ (N\text{-}O)}$ (A^0)**	**$d_{Eu\text{-}O\ (COO)}$ (A^0)**	**$d_{Eu\text{-}O\ (H2O)}$ (A^0)**	**∟O-Eu-O (in ^{0})**
$[Eu\ (H_2O)_9]^{3+}$			2.500	
		Eu (III) - PANO Complexation		
$[Eu(PANO)(H_2O)_7]$	2.355	2.284	2.532	71.35
$[Eu(PANO)_2(H2O)_5]$	2.404	2.332	2.545	70.29
$[Eu(PANO)_3(H2O)_3]$	2.439	2.322	2.874	69.73
$[Eu(PANO)_4(H2O)]$	2.439	2.471	2.475	63.16

Eu (III) - NANO Complexation			
[Eu (H2O)$_9$] (NANO)	4.278	2.602	29.67
[Eu(NANO)(H2O)$_8$]	2.519	2.709	51.89
[Eu (H2O)$_9$] (NANO)$_2$	4.031	2.534	32.21
[Eu(NANO)(H2O)$_8$] (NANO)	2.484 (Inner) 4.183 (Outer)	2.671	52.60 (Inner) 30.82 (Outer)
[Eu(NANO)$_2$(H2O)$_7$]	2.739	2.707	44.85
Eu (III) - IANO Complexation			
[Eu (H2O)$_9$] (IANO)	4.171	2.674	30.86
[Eu(IANO)(H2O)$_8$]	2.527	2.693	51.57
[Eu (H2O)$_9$] (IANO)$_2$	4.060	2.607	31.67, 31.74
[Eu(IANO)(H2O)$_8$] (IANO)	2.531 (Inner) 4.295 (Outer)	2.625	51.63 (Inner) 29.91 (Outer)
[Eu(IANO)$_2$(H2O)$_7$]	2.726)	2.702	37.62, 54.04

*within square brackets indicates innersphere nature while outside of it indicates outersphere complexation.

The optimized geometries for all the possible 1:1 and 1:2 complexes of Eu-NANO and Eu-IANO are shown in figure 4.18 and 4.19 respectively. In the case of Eu-NANO complexes, two inner $[Eu(NANO)(H_2O)_8]^{2+}$ (for 1:1) and $[Eu(NANO)_2(H_2O)_7]^+$ (for 1:2), two outer $[Eu(H_2O)_9](NANO)^{2+}$ (for 1:1), $[Eu\ (H_2O)_9](NANO)_2^+$ (for 1:2) and one inner-outer sphere complex $[Eu(NANO)(H_2O)_8](NANO)^+$ (for 1:2) are considered for the geometry optimization process. Similar scheme of complexation was employed for Eu-IANO as well. The Eu-O (O of H_2O) bond was elongated in outer sphere mode of complexation in case of both Eu-NANO and Eu-IANO complexes. Further, the elongation is higher in case of 1:1 complex than that in 1:2 complexes. Higher elongation in innersphere complexes is due to the higher charge neutralization of Eu(III), which decreases its affinity for coordinated water molecules. This effect gets reduced for coordination by second ligand, which reflects in nearly same Eu-O (H_2O) bond distance in 1:1 and 1:2 complexes for $[Eu(NANO)(H_2O)_8]^{2+}$ and $[Eu(NANO)_2(H_2O)_7]^+$. Due to higher basicity of IANO, the difference in Eu-O (H_2O) bond for $[Eu(IANO)(H_2O)_8]^{2+}$ and $[Eu(IANO)_2(H_2O)_7]^+$ was observed to a small extent. For both Eu-NANO and Eu-IANO inner sphere complexes, the elongation of Eu-O (O of H_2O) bond is higher than the corresponding outer sphere complexes.

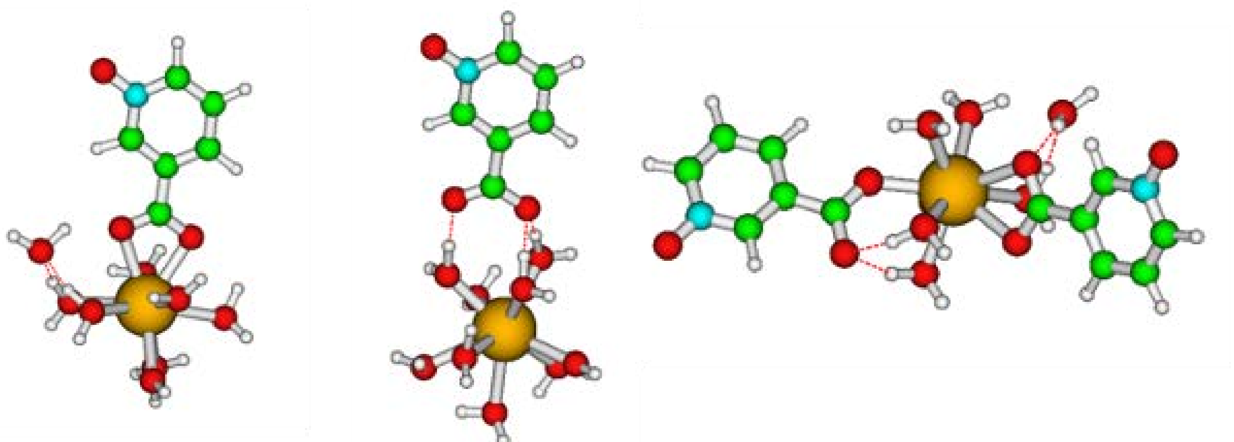

$[Eu(NANO)(H_2O)_8]^{2+}$ $[Eu\ (H_2O)_9](NANO)^{2+}$ $[Eu(NANO)_2(H_2O)_7]^+$

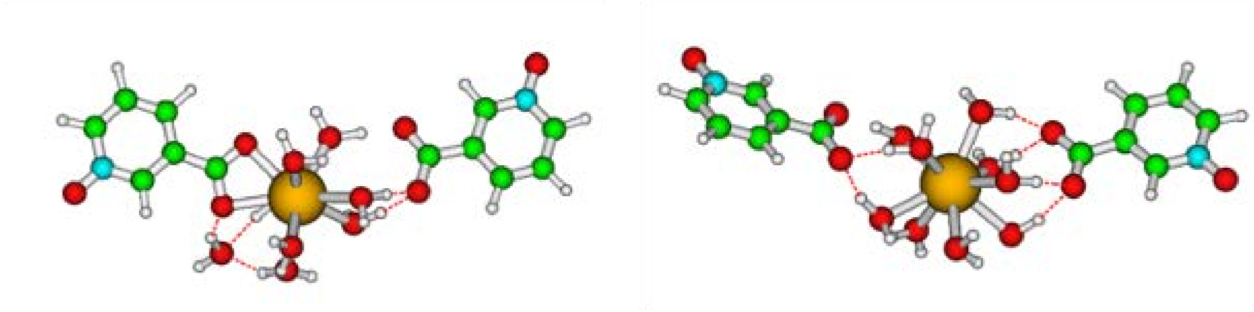

$[Eu(NANO)(H_2O)_8](NANO)^+$ $[Eu\ (H_2O)_9](NANO)_2^+$

Figure 4.18: Optimized geometries for Eu(III)-NANO complexes at B3LYP/SVP level of theory. (Colour code: Yellow - Eu(III), Red - Oxygen, Blue - Nitrogen, Green - Carbon and White - Hydrogen)

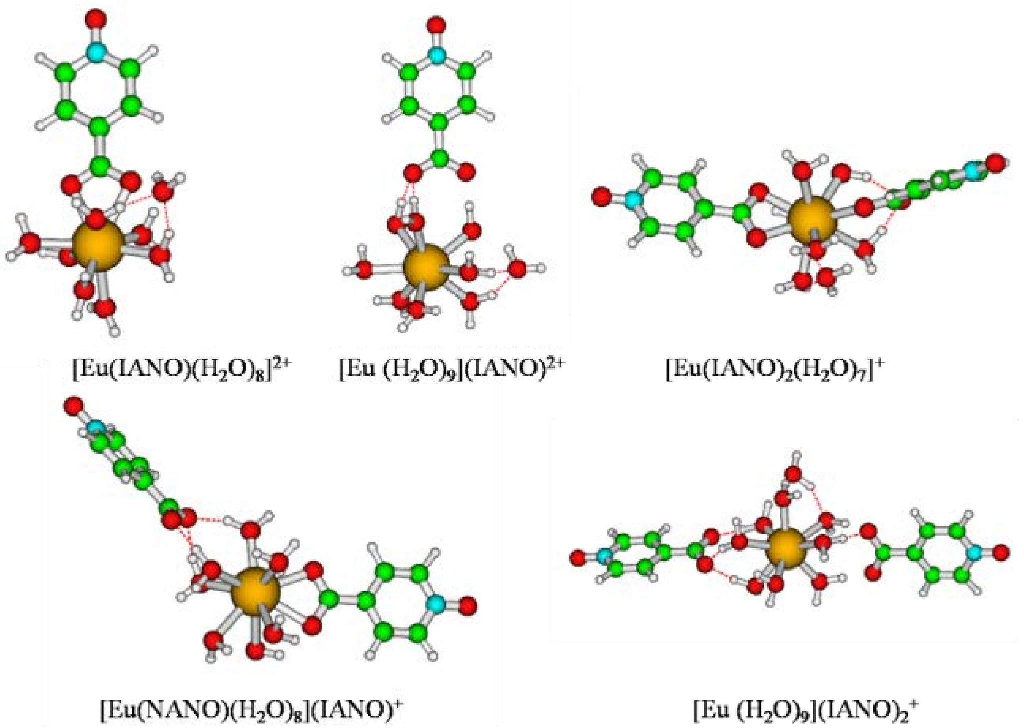

$[Eu(IANO)(H_2O)_8]^{2+}$ $[Eu\ (H_2O)_9](IANO)^{2+}$ $[Eu(IANO)_2(H_2O)_7]^{+}$

$[Eu(NANO)(H_2O)_8](IANO)^{+}$ $[Eu\ (H_2O)_9](IANO)_2^{+}$

Figure 4.19: Optimized geometries for Eu(III)-NANO complexes at B3LYP/SVP level of theory. (Colour code: Yellow - Eu(III), Red - Oxygen, Blue - Nitrogen, Green - Carbon and White - Hydrogen)

The Eu-O (O of COO) bond distance for outer sphere complexes of Eu-NANO are higher than that in respective Eu-IANO complexes indicating the stronger interaction of the latter than the former with the metal ion. The identical inner sphere complexes have nearly equal Eu-O (O of COO) bond distance indicating the same extent of interaction with the metal ion. In case of 1:2 complexes wherein one ligand is in inner sphere while the other is in outer sphere, the ligand in inner sphere is nearly at same distance to metal atom in both the cases while outer ligand is farthest in Eu-IANO than Eu-NANO indicating the higher probability of formation of this complex in case of Eu-NANO than in case of Eu-IANO.

4.4.2.4.2. Binding Energy and Free Energy of Complexation

The calculated binding energy and free energies of different complexes of Eu(III) with all the three PCNOs are presented in Table 4.9. Both the binding energy and free energy of formation in gas phase for the Eu-PANO complexation show a descending order from ML to ML_4, which is in good agreement to the experimental stability constants (table 4.2). The trend is in line with the increase in entropy on successive addition of PANO to $[Eu(H_2O)_9]^{3+}$ during the complex formation. The aqueous phase energetics also shows the formation of inner sphere Eu-PANO complexes to be more favorable with similar trend as in gas phase with exception to the formation of ML_2. The higher interaction and free energies of formation for ML_2 can be attributed to the additional symmetry attained on formation of ML_2 from unsymmetrical ML complex.

Table 4.9: Gas phase and aqueous phase stepwise energetics for the Eu(III)-PCNO complexes (IC - innersphere complex and OC - outersphere complex and ΔE and ΔG are in kJ/mol).

	Gas Phase		**Aqueous Phase**	
Complex	**ΔE**	**ΔG**	**ΔE**	**ΔG**
		Eu (III) - PANO Complexation		
ML	-1170	-1206	-83	-119
ML_2	-744	-791	-89	-136
ML_3	-412	-450	-80	-118
ML_4	-66	-103	-18	-56
		Eu (III) - NANO Complexation		
ML	-1143 (IC) / -1173 (OC)	-1134 (IC) / -1115 (OC)	-55 (IC) / -27 (OC)	-46 (IC) / 30 (OC)
ML_2 (OC)	-736 (from OC)	-668 (from OC)	-102 (from OC)	-34 (from OC)
ML_2 (OC)	-683 (from IC) -654 (from OC)	-664 (from IC) -682 (from OC)	-56 (from IC) 17 (from OC)	-37 (from IC) -79 (from OC)
ML_2 (IC & OC)	-753 (from IC) -724 (from OC)	-683 (from IC) -701 (from OC)	-95 (from IC) -124 (from OC)	-25 (from IC) -100 (from OC)

	Eu (III) - IANO Complexation			
ML	-1152 (IC) / -1204 (OC)	-1142 (IC) / -2143 (OC)	-67 (IC) / -58 (OC)	-57 (IC) / 2 (OC)
ML$_2$ (OC)	-720 (from OC)	-653 (from OC)	-90 (from OC)	-23 (from OC)
ML$_2$ (OC)	-690 (from IC) -638 (from OC)	-668 (from IC) -667 (from OC)	-55 (from IC) -64 (from OC)	-33 (from IC) -92 (from OC)
ML$_2$ (IC & OC)	-696 (from IC) -644 (from OC)	-631 (from IC) -630 (from OC)	-25 (from IC) -34 (from OC)	40 (from IC) -20 (from OC)

In case of Eu-NANO complexes in gas phase, the 1:1 complex interaction energy is more negative in outersphere configuration than in innersphere, while the free energies have opposite trend. Further, the ΔE and ΔG for 1:2 inner, outer and inner-outer complexes were computed for the addition of NANO to the 1:1 inner and outer complexes. The computed values are presented in the table 4.9. The formation of ML$_2$ as outersphere or a mix of inner and outer sphere complex have higher interaction and free energies than that for innersphere ML$_2$. The formation of inner and outer ML$_2$ complex has more negative free energy (-701 kJ/mol) among all the possible reaction schemes indicating the formation of ML$_2$ from the outer sphere ML complex. Thus the calculations suggest the formation of 1:1 outersphere leading to 1:2 inner-outer complex as more favorable reaction path, which is in line with the experimental observation. The aqueous phase calculations also show that the formation of inner-outer ML$_2$ complex from outersphere ML complex has the highest ΔE (-124 kJ/mol) and ΔG (-100 kJ/mol) values thereby further confirming this route as the most probable path of complex formation.

The Eu-IANO complexes have very small difference in both the interaction and free energies of formation for all the possible routes. However, the Gibb's free energy of formation suggests the formation of innersphere ML$_2$ complex from the innersphere ML complex as the most probable scheme. The results of aqueous phase calculation is also in agreement with in gas phase. Thus unlike in case of NANO, IANO forms innersphere complexes in both 1:1 and 1:2 stoichiometry with Eu(III) and has similar trends as with Eu-PANO.

4.4.2.4.3. Partial Charges of Individual Atoms

Considering the hard acid character of the f-block ions, the charges on individual atoms, which directly decide the extent of electrostatic interaction, could be a good measure of the strength of the metal-ligand bonds. With this in view the natural population analysis (NPA) for these complexes in both the gas phase and aqueous phase were carried out at the same level of theory used for calculating the energetics and bond distances. The partial charges on the key atoms which participate directly or are affected by complexation process in aqueous phase are presented in table 4.10. The partial charges on the same atoms in bare ligands are given in table 4.11.

Table 4.10: Charges on all atoms of Eu(III)-PCNO complexes in aqueous phase

Complex	**Eu**	**O (N-O)**	**N (N-O)**	**O (COO)**
[Eu (H2O)$_9$]	1.997			
		Eu (III) - PANO Complexation		
[Eu(PANO)(H2O)$_7$]	1.889	-0.620	0.0725	-0.782, -0.646
[Eu(PANO)$_2$(H2O)$_5$]	1.806	-0.580, -0.610	0.0787, 0.0858	-0.787, -0.653, -0.809, -0.642
[Eu(PANO)$_3$(H2O)$_3$]	1.851	-0.606, -0.568, -0.595	0.0863, 0.0864, 0.0861	-0.770, -0.672, -0.770, -0.664, -0.770, -0.669
[Eu(PANO)$_4$(H2O)]	1.837	-0.580, -0.567, -0.579, -0. 580	0.0789, .0904, 0.0793, 0.0848	-0.754, -0.689, -0.741, -0.693, -0.749, -0.686,

				-0.757, -0.730
Eu (III) - NANO Complexation				
[Eu (H2O)$_9$] (NANO)	1.867	-0.470	0.0797	-0.782, -0.687
[Eu(NANO)(H2O)$_8$]	1.944	-0.555	0.0919	-0.762, -0.708
[Eu (H2O)$_9$] (NANO)$_2$	1.931	-0.588, -0.581	0.0920, 0.0946	-0.779, -0.698, -0.764, -0.768
[Eu(NANO)(H2O)$_8$] (NANO)	1.904	-0.587, -0.573	0.0928, 0.0971	-0.781, -0.693, -0.770, -0.694
[Eu(NANO)$_2$(H2O)$_7$]	1.910	-0.579, -0.572	0.0979, 0.0952	-0.740, -0.740, -0.758, -0.710
Eu (III) - IANO Complexation				
[Eu (H2O)$_9$] (IANO)	1.994	-0.485	0.101	-0.782, -0.690
[Eu(IANO)(H2O)$_8$]	1.966	-0.530	0.118	-0.780, -0.717
[Eu (H2O)$_9$] (IANO)$_2$	2.006	-0.541, -0.551	0.115, 0.111	-0.780, -0.690, -0.791, -0.696
[Eu(IANO)(H2O)$_8$] (IANO)	1.873	-0.533, -0.552	0.118, 0.111	-0.782, -0.710, -0.786, -0.693
[Eu(IANO)$_2$(H2O)$_7$]	1.851	-0.538, -0.537	0.117, 0.117	-0.752, -0.749, -0.744, -0.727

Table 4.11: Charges on bare PCNO molecules in aqueous phase

Ligand	**O (N-O)**	**N (N-O)**	**O (COO)**	**C (COO)**
PANO	-0.571	0.0982	-0.740, -0.780	0.716
NANO	-0.614	0.0820	-0.770, -0.772	0.723

IANO	-0.607	0.0847	-0.775, -0.775	0.716

The charge on Eu(III) ion in aqueous phase was reduced on complexation at all stoichiometry in case of Eu-PANO complexes. Further, the charge on bonding oxygen atom of N-oxide moiety is more negative while the positive charge on the nitrogen atom of N-oxide moiety get reduced on complexation with respect to that in bare ligand. Similar increase in negative charge on the oxygen of carboxylate that binds the metal atom with respect to that on non bonding oxygen atom can be seen in table 4.10. The charge on oxygen and nitrogen of N-oxide are -0.620 and 0.0725 respectively in ML complex of Eu-PANO while the same are -0.571 and 0.0982 in the un-complexed PANO. Similarly, the charges on oxygen atoms of carboxylate moiety in PANO are -0.740 and -0.780 while same on complexation are -0.782 and -0.646 respectively. These two changes on the charge of binding atoms and those neighboring to them can be attributed to the charge polarization during complex formation. Similar effect was observed for all Eu(III)-PANO complexes.

The nitrogen and oxygen atoms of N-oxide moiety in Eu(III)-NANO and Eu(III)-IANO complexes follow an opposite trend on complexation with respect to that of Eu-PANO complexes. In these complexes, the charge on oxygen of N-oxide moiety is reduced while that of nitrogen is enhanced on complexation. While the changes in charge on oxygen atoms of the carboxylate have a similar trend as in Eu-PANO complexes. The oxygen of N-oxide moiety doesn't participate in complexation in case of Eu-NANO and Eu-IANO while it participates in chelate formation in Eu-PANO complexes. The reduction of charge on Eu(III) ion is more for outersphere complex of Eu-NANO and innersphere complex of Eu-IANO for ML and inner-outer complex of Eu-NANO and innersphere complex of Eu-IANO for ML_2. This further supports the reaction scheme of formation of inner-outer complex ML_2 via outersphere ML complex in case of Eu-NANO complexation and the formation of innersphere complexes for both ML and ML_2 for Eu-IANO complexation.

4.5. Conclusion

Eu(III) forms more stable and multiple complexes with picolinate and PANO than that with nicotinate/NANO and isonicotinate/IANO. The ΔH_C of Eu(III) picolinates were found to be negative which are attributed to formation of a stable five membered ring by chelation through pyridyl nitrogen atom, while similar chelate Eu-PANO complexes have positive ΔH_C due to higher dehydration energy for the deprotonated PANO than that for deprotonated picolinate. Significant increase in the life time (in TRLS) of Eu(III) $^5D_0$ state upon complexation by picolinate as well as PANO, indicates formation of 1:4 complex at the end of titration in these complexes. The complexes of Eu(III) isonicotinate/IANO are found to be more stable than Eu(III) nicotinate/NANO complexes which appears to be facilitated by the charge transfer from the nitrogen (N-oxide) in the pyridine ring to the binding carboxylate in case of IANO due to the N and carboxylate being in para positions. The change in position of N-oxide plays a key role in deciding the mode of complexation with the metal ion with pyridine monocarboxylate-N-oxides. PANO and IANO favors the innersphere complexation while NANO favors an outer sphere complexation for ML followed by a mix of inner-outer sphere complex for ML_2. The life time data in conjunction with the isothermal calorimetric titration data support the above conclusions. The detailed theoretical calculations for all the possible reaction schemes to optimize the geometries; and to determine the bond lengths, bond angles and charges on individual atoms on complexation gave a fruitful insight into the studies. The theoretical prediction were found to corroborate the inferences drawn from experimental results.

Chapter 5

Thermodynamic and Density Functional Theory Studies on Complexation of Th(IV) by Pyridine Monocarboxylates and Their N-Oxides

5.1. Introduction

In the present chapter, the results of the thermodynamic and computational studies on the complexation of Th(IV) by pyridine monocarboxylates and their N-oxides have been described. Most of the thermodynamic studies on complexation of pyridine monocarboxylic acids in solution are concerned with transition metals [304-309], with a few reports on rare earths complexes with picolinate [154-157, 280] and nicotinate [158]. To the best of our knowledge no thermodynamic studies have been reported on the complexation of any of the tetravalent actinides with pyridine monocarboxylates in the solution, although a few thermo-gravimetric and crystallographic studies were reported on the complexes of pyridine carboxylates and its derivatives with thorium [183-186].

Complexes of transition metals and lanthanides with pyridine monocarboxylate-N-oxides (PCNOs) in both solid state and in solution have been extensively studied to explore their applications in luminescence, catalysis and many other fields [155, 170, 320-326, 352-355] but only a few studies on actinide complexes with pyridine monocarboxylates were available in literature [128, 130, 159, 160-164, 356]. Many studies have reported the solid state characterization of uranyl [171-172, 357-359] and thorium complexes with different aromatic-N-oxides [173, 360-366] but the studies on actinide complexes with pyridine monocarboxylic acid-N-oxides in particular are very limited. Rickard et al. investigated thorium tetranitrate complexes with N-oxides of pyridine, lutidine, collidine, quinoline, 2-picolinate and 4-picoline in solid state [183]. Nimai has synthesized uranyl and thorium complexes of various pyridine and quinoline carboxylic acids to study their magnetic and spectral properties [367-368]. Complexation of U(VI) with isonicotinic acid-N-oxide by

Stefan Lis et al. and that of trivalent actinides with ligands containing pyridine ring by Al Rifai are the only available data in the literature on actinide complexes with these ligands in aqueous medium [167, 370]. There were no studies on aqueous phase complexation of thorium with the three isomeric pyridine monocarboxylic acid-N-oxides. In the present work thermodynamic investigations on the complexation of thorium with these ligands in aqueous phase has been carried out for the first time.

The objective of the present study includes, (i) bridging the gap in the chemical thermodynamic database for tetravalent actinides complexes with pyridine monocarboxylic acids and their N-oxides in aqueous solution, (ii) to interpret the isomeric effect with respect to position of carboxylate to N- or N-oxide moiety on complexation process, and (iii) comparison of present data on Th(IV) complexes with above mentioned ligands with similar data available in literature on complexes of transition metals and lanthanides. DFT calculations were also carried out for optimized structures of the complexes to estimate the interaction energies, free energies of formation, bond lengths, bond angles and charges on individual atoms to support the experimental studies. The potentiometry and isothermal calorimetric titrations were carried out to determine the stability constants (log β) and enthalpies of formation (ΔH) respectively.

5.2. Experimental

5.2.1. Reagents

$Th(NO_3)_4.4H_2O$ was dissolved in water and $Th(OH)_4$ (s) was precipitated by adding NaOH. The precipitate was centrifuged, washed with water and re-dissolved with an excess of perchloric acid. The precipitation and dissolution were repeated three times. The Th(IV) concentration in the stock solution was determined by EDTA titration using xylenol orange as an indicator. All the other chemicals are of same grade as described in the chapter 4 (under section 4.2.1).

5.2.2 Potentiometric Titrations

The details of the methodology for potentiometric titrations are given in chapter-2. The acid concentration of the Th(IV) stock solution was determined by its titration with standard (~0.1M) NaOH solution and following Gran's method [218]. For all the potentiometric titrations, 25 mL of metal solution was taken in the beaker and was titrated against nearly half neutralized ligand solutions. In case of nicotinate and isonicotinate, the data was considered up to the point of first appearance of turbidity in the titrand solution. The concentrations of the metal and ligand solutions used for titrations were given in table 5.1.

The potentiometric titration data was analyzed using the computer program Hyperquad [217] to obtain the best model containing a set of stability constants of the individual complexes. For all the calculations the ionic product of water (pK_W) was taken as 13.77. Several chemically possible species including the hydrolysis products of the metal ion were submitted as input to Hyperquad [217]. However, the software program consistently converged with the specific set of metal complex species only. Other species were ignored or rejected during the refinement process. As a result, the hydrolysis reactions of Th(IV) were not included in the final data analysis.

Table 5.1: Titration conditions for the Th(IV) complexation with pyridine monocarboxylates and their N-oxides at I = 1.0 M $NaClO_4$, T=298 K.(Potentiometric titration: cup volume 25 mL for Th(IV)-PMC titrations and 10.00 mL for Th(IV)-PCNO titrations, Calorimetric titration: cup volume 2.7 mL for all complexation studies).

S.No.	**Cup Solution**		**Titrant Solution**	
	C_M /M	**C_H /M**	**C_L /M**	**C_H /M**
Th(IV) - picolinate	0.003	0.0373	0.3999	0.2106
	0.005	0.0432	0.1991	0.0992
Th(IV) - nicotinate	0.003	0.0373	0.1993	0.1057
	0.005	0.0432	0.1993	0.1057

Th(IV) - isonicotinate	0.003	0.0373	0.1998	0.1059
	0.005	0.0432	0.1998	0.1059
Th(IV) - PANO	0.003	0.0251	0.2000	0.1009
Th(IV) - NANO	0.003	0.0163	0.0999	0.0481
Th(IV) - IANO	0.003	0.0202	0.1021	0.0485

5.2.3. Calorimetric Titrations

The calorimetric experiments were conducted with an isothermal titration calorimeter system (Nanocalorimeter TAM-III, Thermometric AB, Sweden). The details of the instrumentation are given in section 2.6.1.1 as well a in literature [368]. For the calorimetric titration of Th(IV) with the pyridine monocarboxylates and its N-oxides, the metal ion solution at the desired pH and ionic strength was taken in the reaction vessel and was titrated with the ligand solution (Table 5.1). The heat of dilution of titrant was determined in a separate calorimetric titration of the blank electrolyte solution (I = 1.0 M $NaClO_4$) with the titrant solution. The dilution corrected calorimetric titration data were analyzed to obtain the enthalpy changes in the reaction (detailed in section 2.6.1.2).

5.3. Computational Protocol

All the calculations were carried out using TURBOMOLE program package [263]. For the heavy atom Th, 60 electron core pseudo potentials (ECP) along with corresponding (14s13p10d8f1g) / [10s9p5d4f1g] basis set were selected [370-374]. All other lighter atoms were treated at the all electron (AE) level using the standard def-SV(P) basis sets as implemented in the TURBOMOLE program. Geometries of the bare ligands and their complexes with Th^{4+} ion were optimized at the DFT level using Becke's exchange functional [264] in conjunction with Perdew's correlation functional [265] (BP86) with generalized gradient approximation (GGA). Stability parameter (complexation energy), geometrical parameter (bond lengths) and the charge distribution values were calculated for the complexes of all the possible geometries in both gas phase and in presence of solvent. The atomic charges on bare ligands in gas phase and in presence of solvent were also calculated. The geometries of the bare ligands and all the complexes have also been optimized in presence of solvent. COSMO [340] approach has been adopted to consider the solvent effect using water (ε = 78.4) as solvent in TURBOMOLE.

5.4. Results and Discussion

5.4.1. Complexation of Th(IV) by Pyridine Monocarboxylates

5.4.1.1. Potentiometry

The data obtained from potentiometric titrations along with the fitted curve and speciation diagram generated by the software Hyperquad for complexation of Th(IV) with picolinic acid, nicotinic acid and isonicotinic acid are shown in the figure 5.1. The speciation diagram for the complexation of thorium with picolinate (Fig. 5.1a) shows the formation of four complexes, ML_i (i= 1-4) whereas only ML complexes are formed in case of nicotinate (Fig. 5.1b) and isonicotinate (Fig. 5.1c) under the experimental conditions.

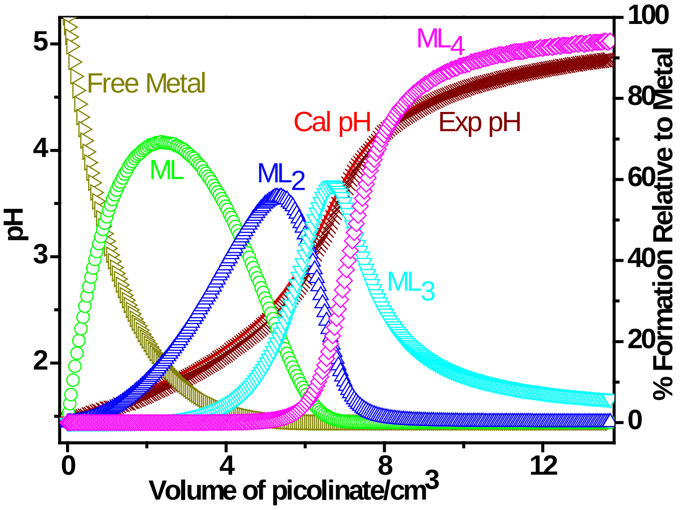

(a)

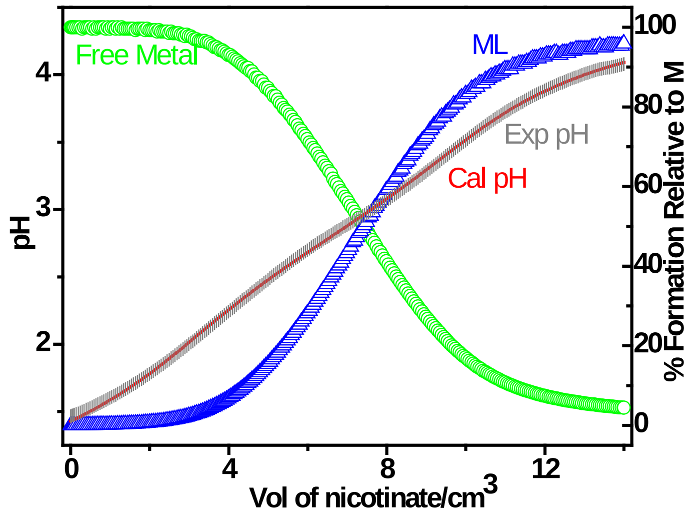

(b)

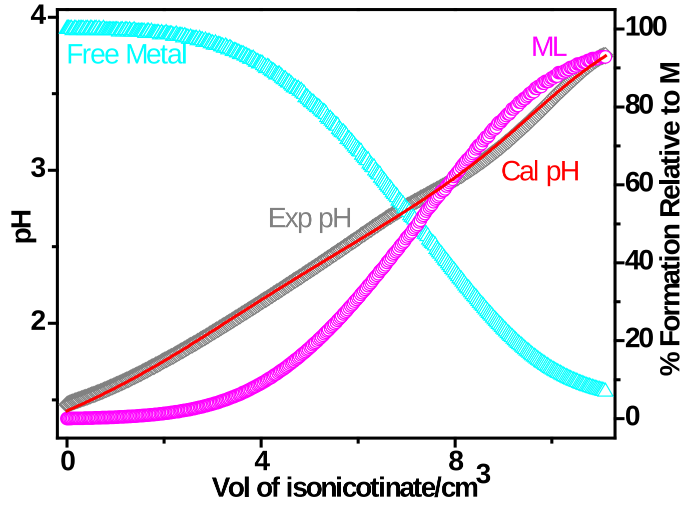

(c)

Figure 5.1: Experimental and fitted potentiometric data along with speciation for titration of Th(IV) with buffered ligand solution: a) Th(IV)-picolinate, b) Th(IV)-nicotinate and c) Th(IV)-isonicotinate. (All the metal ligand concentrations are given in table 5.1)

The deduced stability constants and Gibbs free energy of formation for the complexes are given in table 5.2. The stability constant for the complex, ML is larger in case of Th(IV)-picolinate than the other two isomers. This can be attributed to the chelate formation as the pyridine nitrogen in a sterically favored position to the carboxylate oxygen favors the formation of a five membered ring in case of Th(IV)-picolinate complexes, which is not possible in case of the other two due to far away position of nitrogen from the carboxylate.

Table 5.2: Thermodynamic data for complexation of Th(IV) with pyridine monocarboxylates at 298 K and I = 1.0 M $NaClO_4$. ΔG, ΔH and TΔS are given in kJ/mol.

Reaction	**log K_{MLi}**	**ΔG_{MLi}**	**ΔH_{MLi}**	**$T\Delta S_{MLi}$**
Picolinic acid (Pyridine-2-carboxylic acid)				
$Th^{4+} + L^- \rightarrow ThL^{3+}$	5.90 ± 0.03	-33.7	-11.5 ± 0.2	22.2
$ThL^{3+} + L^- \rightarrow ThL_2^{2+}$	4.38 ± 0.02	-25.0	- 5.4 ± 0.2	19.6
$ThL_2^{2+} + L^- \rightarrow ThL_3^+$	3.74 ± 0.08	-21.3	- 2.6 ± 0.3	18.7
$ThL_3^+ + L^- \rightarrow ThL_4$	2.49 ± 0.10	-14.2	- 1.9 ± 0.4	12.3
Nicotinic acid (Pyridine-3-carboxylic acid)				
$Th^{4+} + L^- \rightarrow ThL^{3+}$	3.35 ± 0.08	-19.1	8.6 ± 0.5	27.7
Isonicotinic acid (Pyridine-4-carboxylic acid)				
$Th^{4+} + L^- \rightarrow ThL^{3+}$	3.52 ± 0.05	-20.0	4.4 ± 0.2	24.4

The actinide elements being hard acids are considered to follow the linear free energy relationship (LFER), according to which log K_{ML} varies linearly with the basicity of the ligand (log K_P). However the data for Th(IV)-picolinate are well above that predicted from the correlation when compared with monodentate ligands such as simple carboxylates and fall in line on comparison with similar kind of bidentate ligands like amino acids (figure 5.2) . This is attributed to chelate formation via pyridyl nitrogen atom in the Th(IV)-picolinate complexes. Log K_{ML} for Th(IV)-nicotinate and Th(IV)-isonicotinate were found to be similar to that of simple monocarboxylates indicating that in neither of these the pyridyl nitrogen is participating in bond formation with the metal ion and the complexation involves the binding of the metal ion to carboxylate group of the ligand as in case of pure carboxylate ligands.. The higher stability of Th(IV)-isonicotinate complex than Th(IV)-nicotinate is due to higher charge transfer from pyridyl nitrogen to carboxylate oxygen, thereby leading to the stronger binding of isonicotinate to metal ion than nicotinate. The electron density on carboxylate with protonated nitrogen (log K_{P2}) is low enough to form stable complex and hence MLH complexes are not observed under the experimental conditions. The absence of MLH species further confirms the deprotonation of nitrogen atom and charge polarization during complexation. The higher value of log K_P of isonicotinate (4.96) than nicotinate (4.86) is also reflected in stability constants of the complexes.

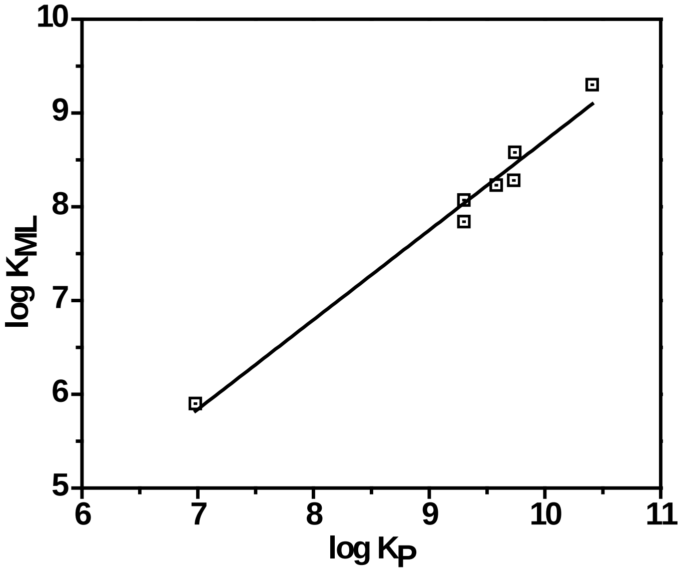

Figure 5.2: Linear Free Energy Relationship for Th(IV) – aminocarboxylates (in increasing order of log K_P - picolinic acid, phenylalanine, serine, hydroxyproline, aspargine, valine, proline). (all the values are taken from the SC database, Academic Software)

5.4.1.2. Isothermal Titration Calorimetry

Figure 5.3 show the data presented in the form of h_{vi} vs. n_{avg} for complexation of Th(IV) with picolinate and isonicotinate respectively. Similar plots were obtained for complexation of Th(IV) with nicotinate also. The enthalpy of complexation obtained are given in table 5.2.

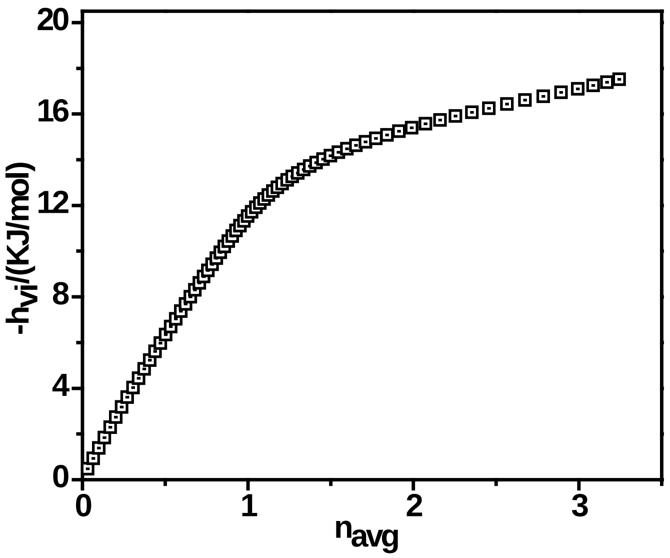

(a)

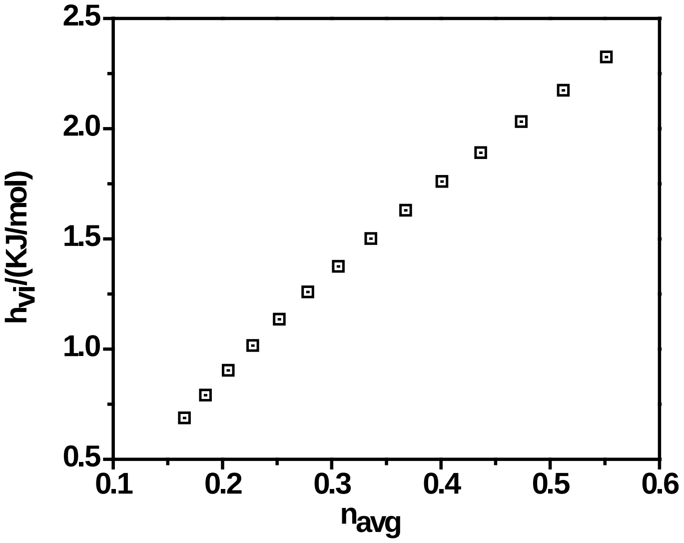

(b)

Figure 5.3: Plot of Δh_{vi} vs n_{avg} for complexation of a) Th(IV)-picolinate and b) Th(IV)-isonicotinate (All the metal ligand concentrations are given in table 5.1).

In general, the complexation process between actinides and simple carboxylates are endothermic and are mainly entropy driven processes which is typical of hard acid hard base reactions. The energy required for dehydrating the metal ion and ligand is more than that released in metal ligand bond formation thus making the overall reactions endothermic. The water molecules released during complexation increase the entropy of complexation. ΔH_C is the resultant of enthalpy change of metal – ligand bond formation ($\Delta H_{M\text{-}L}$) and metal-water bond breaking (dehydration of hydrated metal ion $\Delta H_{M\text{-}H2O}$).

$$\Delta H_C = \Delta H_{M-L} - \Delta H_{M-H_2O} \tag{5.3}$$

However, in case of ligands containing the other functional groups like hydroxyl and amino groups, where there is a possibility of chelate formation, increase Th(IV)-ligand interaction releases more energy in bond formation than the energy required to break the hydration spheres. Thus, the overall reaction becomes exothermic. In case of Th(IV)-picolinate complexes, the metal ion binds with the ligand through both carboxylic oxygen and nitrogen atom and thus forms chelates. Therefore, higher exothermicity of Th(IV)-picolinate indicates the role of nitrogen atom as well as rigid structure of ligand which sterically favors the complexation process. The complexation of Th(IV) with picolinate was found to be highly exothermic and exothermicity decreased with successive complexation. The negative ΔH_C suggests that it is determined mainly by metal ligand bond formation. The decreasing magnitude of ΔH_c on successive complexation is the result of decreased metal ligand interaction due to reduced charge on metal ion and limited availability of coordination space around the metal ion to facilitate further ligand participation.

In the case of nicotinate and isonicotinate, there is no possibility of chelation via pyridyl nitrogen due to far away position of the nitrogen from the oxygen, and hence the complexation of Th(IV) by these ligands are found to be endothermic and entropy driven. This indicates that the complexation is similar to that in case of carboxylates in which the metal ion binds through carboxylate. The difference in endothermicity between the complexes of nicotinate and isonicotinate is due to significant movement of charge from nitrogen in case of isonicotinate than that in case of nicotinate, which is further corroborated by theoretical calculations as discussed below.

5.4.1.3. Theoretical Calculations

Following equations have been used for the calculation of the complexation energy (ΔE_C) values of the various complexes considered in the present work.

$$M^{4+} (aq) + n\, \overline{L} (aq) \rightarrow [ML_n]^{n-4} (aq) \qquad (5.4)$$

$$\Delta E_C = E\,(ML_n)^{n-4} - n \times E\,(L^-) - E\,(M^{4+}) \qquad (5.5)$$

where $E\,(ML_n)^{n-4}$, $E\,(L^-)$ and $E(M^{4+})$ denote the energy of the complex, ligand and the metal ion, respectively. Here 'n' denote the number of ligands considered in the complex, $(ML_n)^{n-4}$. The calculated metal-ligand bond length for various possible geometries of all the complexes are shown in the table 5.3. Trends of solvent phase results are quite consistent with that of the gas phase results. Form the table 5.3, it is clear that, in case of all the Th(IV)-picolinate complexes, the Th-O bond length are lower in the complexes, where the metal ion binds the ligand through both oxygen and nitrogen via chelation than simple carboxylate binding in which the metal atom binds the ligand through both the oxygen atoms of the carboxylate group. In the case of nicotinate and isonicotinate, even though one of the bond lengths is still shorter than picolinate complexes, the other bond lengths are higher resulting in lower stability than picolinate complexes (chelate formation). Further, in case of thorium-nicotinate and thorium-isonicotinate complexes, the bond length values are lower for the simple carboxylate binding than binding the ligand through nitrogen atom alone.

Table 5.3: Calculated metal-ligand bond lengths for various Th(IV)-PMC Complexes ('OO' indicates that both the oxygen atoms of the carboxylate group act as donors; 'ON' indicates that one oxygen atom of the carboxylate group and the ring nitrogen act as donors)

Composition	$\mathbf{d_{Th\text{-}O}}$	$\mathbf{d_{Th\text{-}O(SOLV)}}$	$\mathbf{d_{Th\text{-}N}}$	$\mathbf{d_{Th\text{-}N(SOLV)}}$
Th(IV)-Picolinate Complexation				
ML (OO)	2.105	2.184	-------	-------
ML (ON)	deforming	2.025	deforming	2.419
ML2 $(ON)_2$	2.087	2.158	2.488	2.508

ML21	2.062(ON)	2.135	2.488	2.510
(ON)(OO)	2.240(OO)	2.289		
ML22 (OO)$_2$	2.220	2.288	-------	-------
ML3 (ON)$_3$	2.201	2.238	2.661	2.642
ML31	2.186	2.220	2.625	2.605
(ON)$_2$(OO)	2.375	2.387		
ML32	2.174	2.207	2.594	2.580
(ON)(OO)$_2$	2.360	2.374		
ML33 (OO)$_3$	2.345	2.360	-------	-------
ML4 (ON)$_4$	2.292	2.313	2.753	2.717
ML41	2.286	2.305	2.718	2.694
(ON)$_3$(OO)	2.486	2.485		
ML42	2.258	2.280	2.716	2.691
(ON)$_2$(OO)$_2$	2.476	2.471		
ML43	2.256	2.279	2.713	2.670
(ON)(OO)$_3$	2.457	2.454		
ML44 (OO)$_4$	2.444	-------	2.440	-------
Th(IV)-Nicotinate Complexation				
ML (OO)	2.120	2.189	-------	-------
ML (N)	-------	-------	2.401	2.461
ML2 (OO)$_2$	2.220	2.270	-------	-------
ML3 (OO)$_3$	2.344	2.358	-------	-------
Th(IV)-Isonicotinate Complexation				
ML (OO)	2.144	2.187	-------	-------
ML (N)	-------	-------	2.339	2.413
ML2 (OO)$_2$	2.221	2.280	-------	-------
ML3 (OO)$_3$	2.340	2.356	-------	-------

The charges on each atom in the complex for all the geometries are tabulated in the table 5.4. Further, to investigate the extent of charge neutralization during complexation, the charges on each atom in bare ligand were also calculated and are given in the table 5.5.

Table 5.4: Calculated atomic charges for various Th(IV)- pyridine monocarboxylate Complexes

Composition	q_{Th}	$q_{Th(Solv)}$	q_O	$q_{O(Solv)}$	q_N	$q_{N(Solv)}$
Th(IV)-Picolinate Complexation						
ML (OO)	2.926	3.444	-0.759	-0.770	-0.321	-0.436
ML (ON)	2.826	3.404	-0.945, -0.114	-0.932, -0.462	-0.685	-0.717
ML2 (ON)$_2$	2.639	2.990	-0.874, -0.409	-0.878, -0.546	-0.668	-0.650
ML21 (ON)(OO)	2.667	3.041	-0.866, -0.394 -0.737	-0.882, -0.537 -0.750	-0.675	-0.657
ML22 (OO)$_2$	2.678	3.076	-0.743, -0.717	-0.760, -0.741	-0.406	-0.457
ML3 (ON)$_3$	2.432	2.547	-0.832, -0.499	-0.827, -0.588	-0.599	-0.602
ML31 (ON)$_2$(OO)	2.456	2.580	-0.840, -0.728 -0.700, -0.495	-0.835, -0.728 -0.708, -0.583	-0.608 -0.430	-0.599 -0.469
ML32 (ON)(OO)$_2$	2.477	2.608	-0.841, -0.730 -0.696, -0.489	-0.708, -0.728 - 0.837, -0.580	-0.612 -0.425	-0.604 -0.469
ML33 (OO)$_3$	2.512	2.637	-0.715	-0.725	-0.423	-0.467
ML4(ON)$_4$	2.008	1.991	-0.772, -0.755 -0.567	-0.775, -0.761 -0.620	-0.536 -0.527 -0.507	-0.548 -0.542 -0.526
ML41(ON)$_3$ (OO)	2.021	2.009	-0.768, -0.693 -0.648, -0.563	-0.773,-0.694 -0.667,-0.616	-0.530 -0.438	-0.545 -0.479
ML42(ON)$_2$ (OO)$_2$	2.081	2.065	-0.785, -0.698 -0.677, -0.661 -0.636, -0.556	-0.786, -0.699 -0.688,-0.666 -0.609	-0.530 -0.437	-0.547 -0.476
ML43(ON) (OO)$_3$	2.121	2.087	-0.785, -0.707 -0.649, -0.554 -0.539	-0.792, -0.701 -0.699, -0.676 -0.602	-0.430 -0.539	-0.563 -0.474
ML44(OO)$_4$	2.156	2.126	-0.703,-0.672 -0.649	-0.707,-0.692 -0.680	-0.428	-0.473
Th(IV)-Nicotinate Complexation						
ML (OO)	2.903	3.447	-0.779	-0.780	-0.280	-0.484
ML (N)	2.828	3.307	-0.807,-0.462	-0.828,-0.537	-0.508	-0.481

ML2 (OO)$_2$	2.684	2.813	-0.746	-0.751	- 0.428	-0.431
ML3 (OO)$_3$	2.519	2.638	-0.728	-0.730	-0.452	-0.502
Th(IV)-Isonicotinate Complexation						
ML (OO)	2.876	3.466	-0.776	-0.769	-0.149	-0.437
ML (N)	2.796	3.439	-0.201	-0.800	-0.837	-0.597
ML2 (OO)$_2$	2.616	3.041	-0.748,-0.730	-0.768, -0.746	-0.477	-0.462
ML3 (OO)$_3$	2.527	2.634	-0.731, -0.718	-0.722	-0.414	-0.477

The table 5.4 shows that for the Th(IV)-picolinate complexes, the charge on both the oxygen and nitrogen are higher in chelate complexes than that in bare ligand (table 5.5) as well as in all other complexes of Th(IV)-picolinate which reflected in the lower values of residual charge on metal ion in these chelate complexes.

Table 5.5: Calculated atomic charges for the bare pyridine monocarboxylates in solvent phase.

Ligand	q_O	$q_{O(SOLV)}$	q_N	$q_{N(SOLV)}$
Picolinate	-0.727	-0.773	-0.466	-0.512
Nicolinate	-0.733	-0.773	-0.509	-0.528
Isonicolinate	-0.729	-0.768	-0.517	-0.526

The solvent phase calculations in case of Th(IV)-nicotinate and Th(IV)-isonicotinate complexes show the Th-O bond length to be very close. Also the charges on individual atoms in the complex differ marginally. This can be attributed to the closed shell configuration of Th(IV) ion (having no f-electron) which has little tendency to cause charge polarization in the ligands. This explains the similar binding energy of Th(IV) with nicotinate and isonicotinate.

The overall stability of a complex can be best described based on the energy released during the complex formation. The complexation energies for all the possible geometries were calculated are presented in the table 5.6. The higher negative value of complexation energy than the other possible geometries further confirms the extra stability of chelate complexes over the other geometries. From the table, it can be concluded that the chelate complexes are more stable in case of Th(IV)-picolinates whereas the simple carboxylate bound complexes are more stable in case of Th(IV)-nicotinate and Th(IV)-isonicotinate complexes.

Table 5.6: Calculated complexation energies for various Th(IV)-pyridine monocarboxylate complexes.

Composition	**Complexation Energy (ΔE_g in eV)**	**Complexation Energy (ΔE_s in eV)**
	Th(IV)-Picolinate Complexation	
ML (OO)	-38.73	-6.76
ML (ON)	-39.89	-7.37
ML2 $(ON)_2$	-59.70	-12.06
ML21 (ON)(OO)	-59.16	-11.60
ML22 $(OO)_2$	-58.62	-11.10
ML3 $(ON)_3$	-71.68	-15.12
ML31 $(ON)_2(OO)$	-71.70	-14.84
ML32 $(ON)(OO)_2$	-71.42	-14.56
ML33 $(OO)_3$	-71.08	-13.95
ML4$(ON)_4$	-78.50	-17.49
ML41$(ON)_3(OO)$	-78.51	-17.34
ML42$(ON)_2(OO)_2$	-78.35	-17.12
ML43$(ON)(OO)_3$	-78.09	-16.90
ML44$(OO)_4$	-77.80	-16.55
	Th(IV)-Nicotinate Complexation	
ML (OO)	-38.27	-6.65
ML (N)	-37.79	-5.17
ML2 $(OO)_2$	-57.69	-9.23
ML3 $(OO)_3$	-67.00	-13.64
	Th(IV)-Isonicotinate Complexation	
ML (OO)	-37.88	-8.82

ML (N)	-32.94	-5.95
ML2 (OO)$_2$	-54.04	-11.52
ML3 (OO)$_3$	-69.38	-20.25

The similar bond lengths and the small difference in charge on the each atom are in agreement with the small difference in their complexation energies. These results are consistent with the experimentally observed results which show that the Th(IV)-isonicotinate complex (log K_{ML} = 3.52, ΔG = -19.1 kJ/mol) is more stable than Th(IV)-nicotinate complex (log K_{ML} = 3.35, ΔG = -20.0 kJ/mol), with a very small difference in the free energy formation of the two complexes.

5.4.1.4. Conclusion

The exothermicity and higher values of formation constants of the Th(IV)-picolinates over the other two ligand complexes with thorium is due to the extra stability from the chelating nature of picolinate. The Th(IV)-isonicotinate complex was more stable than Th(IV)-nicotinate complex and both the complexation processes were found to endothermic indicating the similarity of these complexes with the simple carboxylate complexes which are in general are entropy driven and endothermic in nature. The bond lengths, complexation energies and atomic charges on each atom in the complex calculated theoretically by Turbomole are consistent with the experimentally observed results.

5.4.2. Complexation of Thorium with Pyridine Monocarboxylate-N-Oxides

5.4.2.1. Potentiometry

The complexation of thorium with pyridine monocarboxylic acid-N-oxides (represented as L) can be defined by the following reaction schemes

$$Th^{4+} + nL^{-} \rightarrow ThL_n^{(4-n)+} \qquad (5.6)$$

$$Th^{4+} + nLH \rightarrow ThL_n^{(4-n)+} + nH^{+} \qquad (5.7)$$

The equation (5.6) represents the complexation of thorium with deprotonated ligand while the equation (5.7) represents the complexation of thorium with protonated ligand in which the complex formation is accompanied by the release of proton. Thus, the complexation of metal ion with acidic ligands like carboxylates and aminocarboxylates, is always accompanied by deprotonation of ligand, and hence necessitates the determination of thermodynamic parameters for ligand protonation. The protonation constants of all the three pyridine monocarboxylates under present experimental conditions were taken from our previous work [129] as inputs during analysis of the potentiometric data of Th(IV)-PCNO complexation. The potentiometric titration data was analysed by using Hyperquad suit of programming [217]. The software involves the treatment of data by a non-linear least square fitting of experimental data with a modelled data in which the approximate species that can form during the complexation reaction along with their stability constants was given as input. When the species expected with the given stability constants are reasonably well predicted, the modelled data matches with experimental data indicating the validity of predicted species with corresponding stability constants. Different stoichiometry of Th(IV)-PCNO complexes including the polynuclear and ternary Th(IV)-PCNO-OH complexes are considered during the treatment of data by Hyperquad [217] but consideration of only mononuclear binary Th(IV)-PCNO complexes resulted in the best fit of the data. The potentiometric data analysis by Hyperquad [217] indicated the formation of ML_i (i=1-4) for Th(IV)-PANO complexes and ML_i (i=1-3) for Th(IV)-NANO and Th(IV)-IANO complexes. The variation in the percentage of formation of the different stoichiometric complexes with respect to free metal concentration and pH can be well represented as speciation diagrams (Figure 5.4), which helps in predicting the concentrations of various complexes present under any experimental condition (pH, Ligand to Metal ratio). The stability constants along with the other thermodynamic parameters (ΔG, ΔH and ΔS) are given in table 5.7.

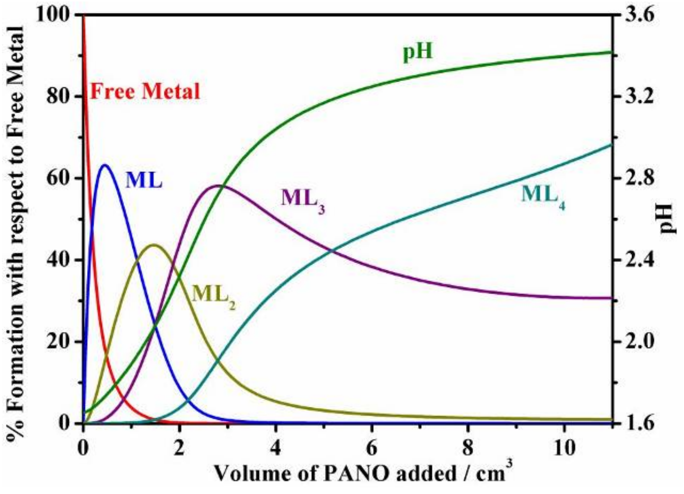
% Formation with respect to Free Metal
pH
Volume of PANO added / cm^3
Free Metal
ML
ML_2
ML_3
ML_4
pH
0
20
40
60
80
100
0
2
4
6
8
10
1.6
2.0
2.4
2.8
3.2
3.6

(a)

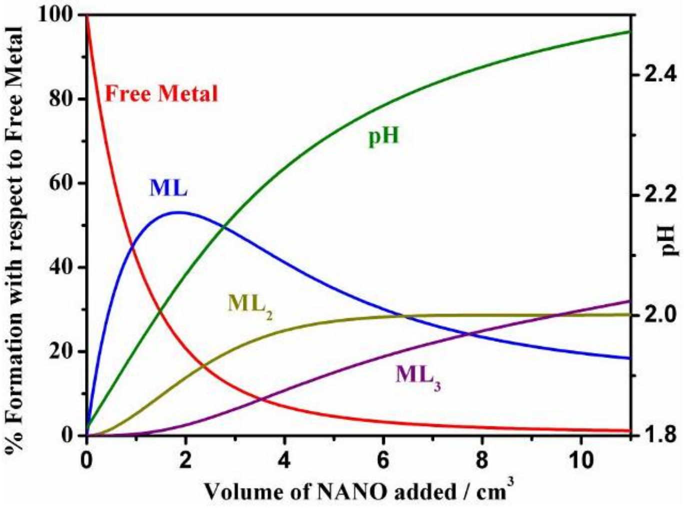
% Formation with respect to Free Metal
pH
Volume of NANO added / cm^3
Free Metal
ML
ML_2
ML_3
pH
0
20
40
60
80
100
0
2
4
6
8
10
1.8
2.0
2.2
2.4

(b)

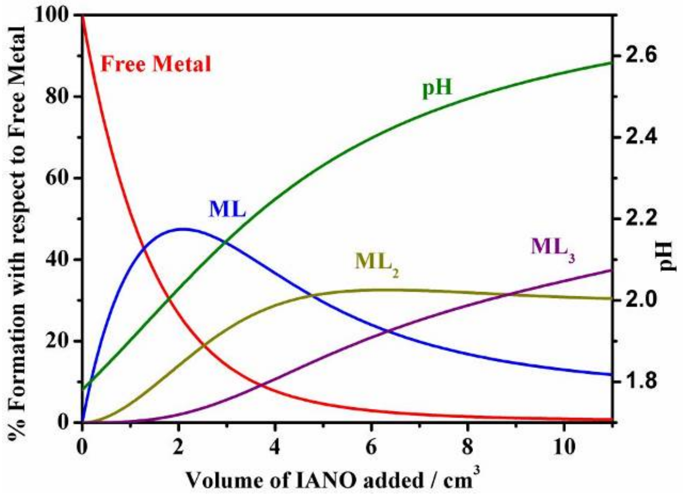
% Formation with respect to Free Metal
pH
Volume of IANO added / cm^3
Free Metal
ML
ML_2
ML_3
pH
0
20
40
60
80
100
0
2
4
6
8
10
1.8
2.0
2.2
2.4
2.6

(c)

Figure 5.4: Speciation diagram for complexation by Th(IV) with PCNOs (a: Th(IV)-PANO, b: Th(IV)-NANO and c: Th(IV)-IANO) in aqueous medium at T = 298 K and I = 1.0 M $NaClO_4$. (All the metal ligand concentrations are given in table 5.1)

Table 5.7: Thermodynamic parameters for the complexation of Th(IV) with pyridine monocarboxylate-N-oxides in aqueous medium at T = 298 K and I = 1.0 M $NaClO_4$. (All the metal ligand concentrations are given in table 5.1). ΔG, ΔH and TΔS are given in kJ/mol while ΔS is in J/K/mol.

Complex	**log β**	**ΔG**	**ΔH**	**T ΔS**	**ΔS**
		Th(IV)-PANO Complexation			
ML	4.44 ± 0.02	-25.38	14.0 ± 0.6	39.40	132.14
ML_2	3.29 ± 0.02	-18.80	29.7 ± 2.0	48.48	162.62
ML_3	2.77 ± 0.03	-15.83	20.6 ± 1.3	36.48	122.36
ML_4	1.62 ± 0.01	-9.26	5.0 ± 0.3	14.22	47.69
		Th(IV)-NANO Complexation			
ML	2.83 ± 0.01	-16.16	15.07 ± 1.1	31.23	104.73
ML_2	1.85 ± 0.01	-10.56	7.5 ± 0.4	18.02	60.44
ML_3	1.69 ± 0.02	-9.65	1.2 ± 0.2	10.83	36.32
		Th(IV)-IANO Complexation			
ML	2.90 ± 0.02	-16.56	12.9 ± 0.7	29.45	98.76
ML_2	2.12 ± 0.03	-12.10	5.7 ± 0.6	17.74	59.51
ML_3	1.80 ± 0.01	-10.28	0.5 ± 0.1	10.75	36.04

The table shows that log β of complexes follow the order Th(IV)-PANO > Th(IV)-IANO > Th(IV)-NANO. The higher log β values of the Th(IV)-PANO complexes cab be attributed to the formation of six membered chelate ring involving the oxygen of N-oxide and that of carboxylate. The favourable position of N-oxide (at ortho position) to carboxylate group facilitates the chelate formation while the same cannot take place in Th(IV)-NANO and Th(IV)-IANO complexes due to higher separation of N-oxide with respect to carboxylate. Th(IV)-IANO forms stronger complexes than corresponding Th(IV)-NANO complexes as the carboxylate group in the former is in electron donating position (para) to N-oxide moiety for charge polarization where the same in NANO is at electron withdrawing position (meta) to N-oxide moiety. The actinides at higher oxidation state behaves as hard acids and prefer binding with hard donors like fluorine, oxygen, etc., in which the major force of attraction is coulombic in nature. The linear free energy relationships for the complexation of thorium with simple monocarboxylates are shown in figure 5.8, which shows the data for Th(IV)-PANO complex much above the linearity indicating the chelation nature of Th(IV)-PANO complexes, while the other two ligands follow binding only through carboxylate in Th(IV)-NANO/IANO complexes.

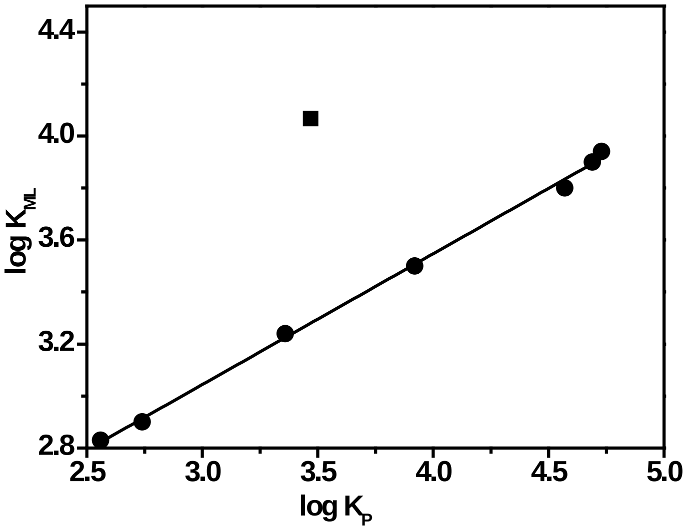

Figure 5.5: Linear free energy relationship for Th(IV) monocarboxylate complexes (● - increasing order: NANO, IANO, Thenoic acid, ß-chloropropionate, γ-hydroxybutyrate, acetate and propionate; ■ - PANO) (all the values are taken from the SC database, Academic Software)

5.4.2.2. Isothermal Titration calorimetry

The enthalpy of formation for the complexes could be obtained directly from the plots h_{vi} vs n_{avg}, where h_{vi} is the heat released per mole of metal ion and n_{avg} is the number of ligand atoms bound per metal atom (as shown in figure 5.6).

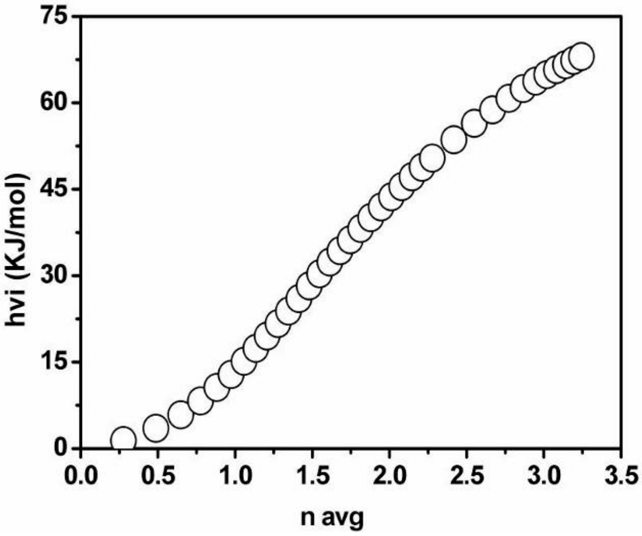
75
60
45
30
15
0
hvi (KJ/mol)
0.0
0.5
1.0
1.5
2.0
2.5
3.0
3.5
n avg

(a)

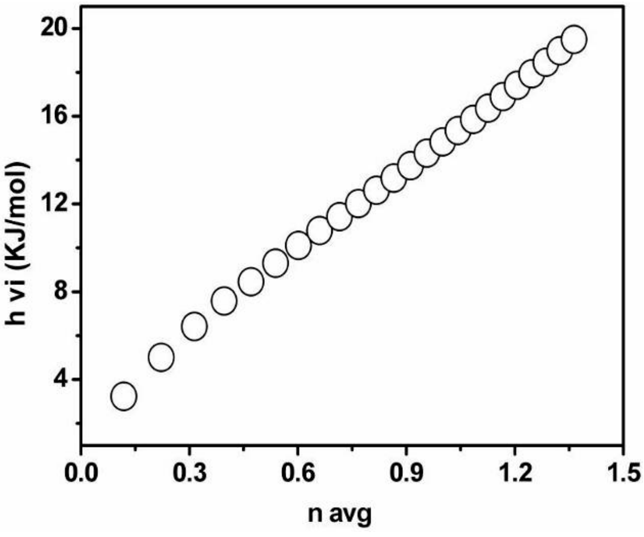
20
16
12
8
4
h vi (KJ/mol)
0.0
0.3
0.6
0.9
1.2
1.5
n avg

(b)

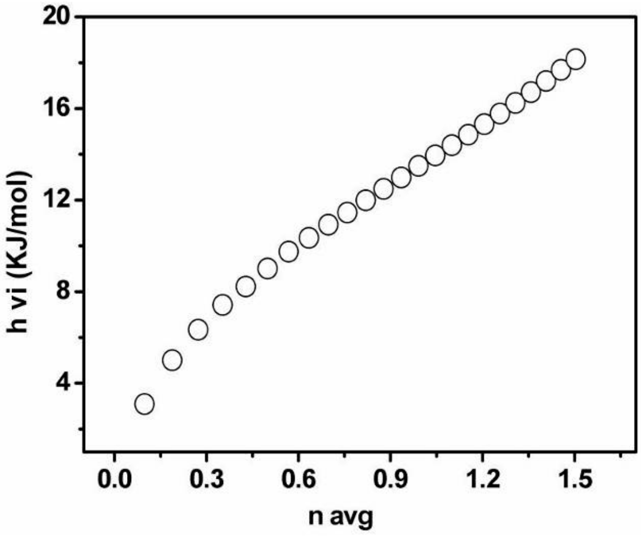
20
16
12
8
4
h vi (KJ/mol)
0.0
0.3
0.6
0.9
1.2
1.5
n avg

(c)

Figure 5.6: Calorimetric plots (h_{vi} vs. n_{avg}) for complexation by Th(IV) with PCNOs (a: Th(IV)-PANO, b: Th(IV)-NANO and c: Th(IV)-IANO) in aqueous medium at T = 298 K and I = 1.0 M $NaClO_4$. (All the metal ligand concentrations are given in table 5.1)

The enthalpy and entropy of formation for all the Th(IV)-PCNO complexes are summarized in Table 5.7. From the table, it's clear that formation of all the Th(IV)-PCNO complexation are endothermic in nature and are strongly entropy driven. The hard acid–hard base interactions involved in actinide complexation by PCNOs constitute positive enthalpy reflecting the energy required for dehydration of both the metal ion and the ligands and a favourable entropy due to increase in disorder caused by the release of solvent molecules in both the primary as well as secondary solvation spheres, the bulk solvent and their reorganization around the resulting species. Furthermore, the similarity in enthalpy and entropy of formation between Th(IV)-NANO and Th(IV)-IANO complexation implies that the oxygen of N-oxide of NANO/IANO does not participate in the complexation process for coordination with Th(IV).

The trends in enthalpy of formation for complexes can be explained in terms of the perturbation of hydration sphere in the primary coordination sphere as well as in bulk structure of solvent. In general the stepwise enthalpy of formation follows a descending order as the charge neutralization becomes more prominent in the stepwise complexation process. Similar trends in enthalpy of formation were observed in case of Th(IV)-NANO and Th(IV)-IANO complexes but in case of Th(IV)-PANO complexes, the enthalpy of formation follow a different trend $\Delta H_{ML2} > \Delta H_{ML3} > \Delta H_{ML} > \Delta H_{ML4}$. This anomaly in the enthalpy of formation could be explained on the basis of dehydration of both the metal ion and ligand molecules on complex formation. In general, ligand dehydration plays minor role in determining the enthalpy of formation as in case of simple monocarboxylates and neutral ligands, which have near zero enthalpies of protonation as in case of NANO and IANO for which the enthalpy of protonation for are -1.83 and 0.40 kJ/mol respectively [129], typical of carboxylic acids ($\Delta H_P \approx$ 0–5 kJ/mol at 298 K). But, in case of ligands that do have relatively higher endothermic enthalpies of protonation, ligand dehydration contributes contribute more to the enthalpy as well as entropy of complexation. In our previous studies [129], it was reported that the protonation of PANO is an endothermic process (ΔH_P = 6.76 kJ/mol). Thus, the addition of more and more ligands requires higher energy for dehydration of ligand molecules, which result in higher enthalpies of formation on stepwise complexation. Further, the drastic structural rearrangements of the ligand moieties around the metal ion also contribute to the abrupt increase of stepwise enthalpies of formation as in case of Th(IV) complexation by oxydiacetate complex for which ΔH_C for the formation of ML, ML_2 and ML_3 are 8.37, -11.46 and 35.90 KJ/mol respectively [375]. Thus the anomalous trend in enthalpy of formation for Th(IV)-PANO complexes could be attribute to the cumulative effect of dehydration of both the metal and ligand ions and the structural rearrangement of ligand around the metal ion simultaneously.

Relatively higher entropy of formation for Th(IV)-PANO complexes are due to chelate formation in these complexes which requires replacement of two water molecules from the primary coordination sphere of Th(IV) ion whereas NANO and IANO need to remove single water molecule from Th(IV) aquo ion for complexation. The trends in entropy of formation for Th(IV)-PANO can be explained analogous to enthalpy of formation of these complexes.

5.4.2.3. Theoretical Calculations

Tianxiao Yang et al reported the combined quantum mechanical and molecular dynamical simulations on Th(IV) hydrates in aqueous solution and conclude that $Th(H_2O)_9^{4+}$ with C_{4V} symmetry can form the most stable complex, with 9 water molecules around the Th(IV) ion in the first shell [377]. Tsushima et al. proved that the energy difference between

9- and 10-oordination is very small (~1 kJ/mol) [378]. From these data it can be concluded that the coordination number is either 9 or 10, and that equilibrium might exist between the 9- and 10-coordinated ions. The relative energies of U^{4+} and Np^{4+} ions with 8, 9 and 10 coordinated water indicate that the preferred coordination number for U^{4+} is 9, while there might be an equilibrium between 8 and 9 coordination for Np^{4+} [379]. Thus, in the present studies, $Th(H_2O)_9^{4+}$ is considered as the base moiety for Th(IV) aqua ion and the analogy can be extended to U(IV) and to a less extent to Np(IV).

The geometries for all the Th(IV)-PCNO complexes predicted under present investigations were optimized at DFT level by using Turbomole programme. The optimized geometries for all the complexes of Th(IV)-PANO, Th(IV)-NANO and Th(IV)-IANO are shown in figures 5.7 to 5.9 respectively. The optimized geometries for Th(IV)-PANO complexes involved the chelate formation by Th(IV) through each oxygen atom of carboxylate and N-oxide moieties whereas the Th(IV)-NANO and Th(IV)-IANO complexes are formed by coordination of Th(IV) with carboxylate oxygen atoms.

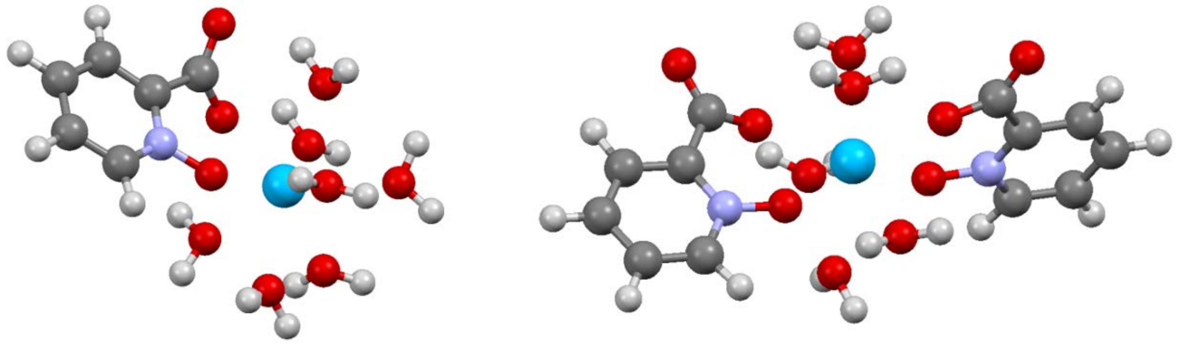

(a) **(b)**

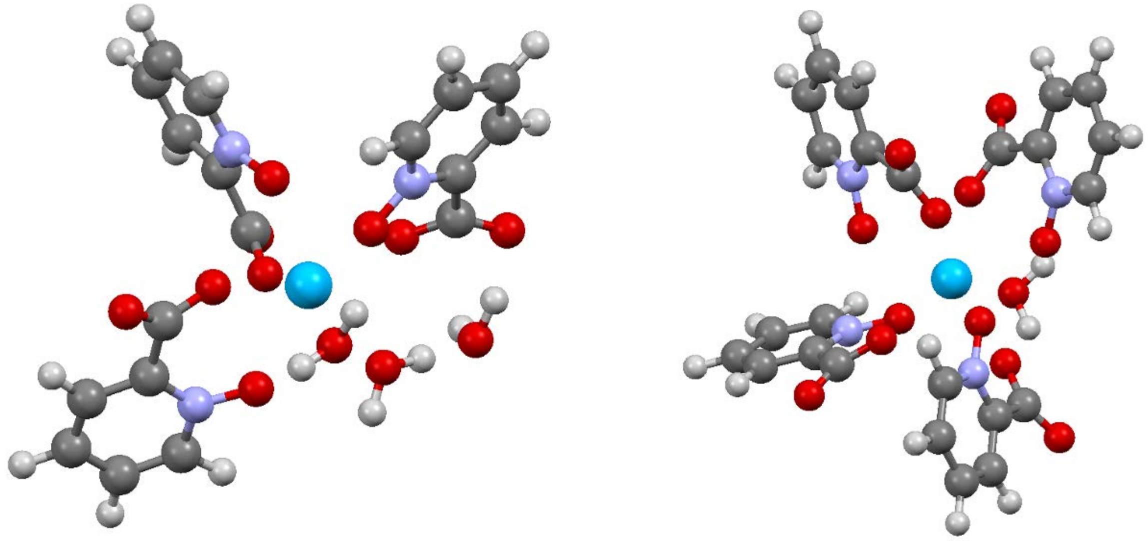

(c) (d)

Figure 5.7: Optimized geometries for Th(IV)-PANO complexes: a) ML, b) ML_2, c) ML_3 and d)ML_4.

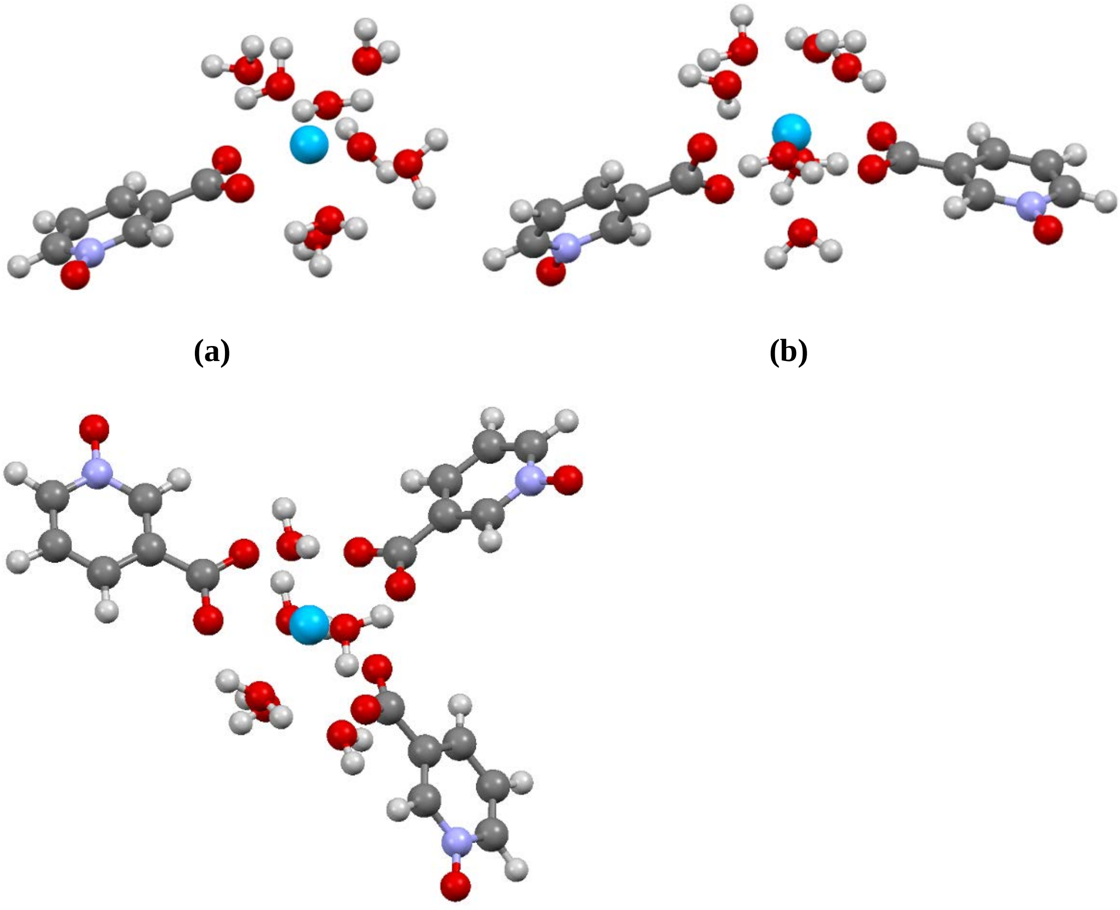

(a) (b)

(c)

Figure 5.8: Optimized geometries for Th(IV)-NANO complexes: a) ML, b) ML_2 and c) ML_3.

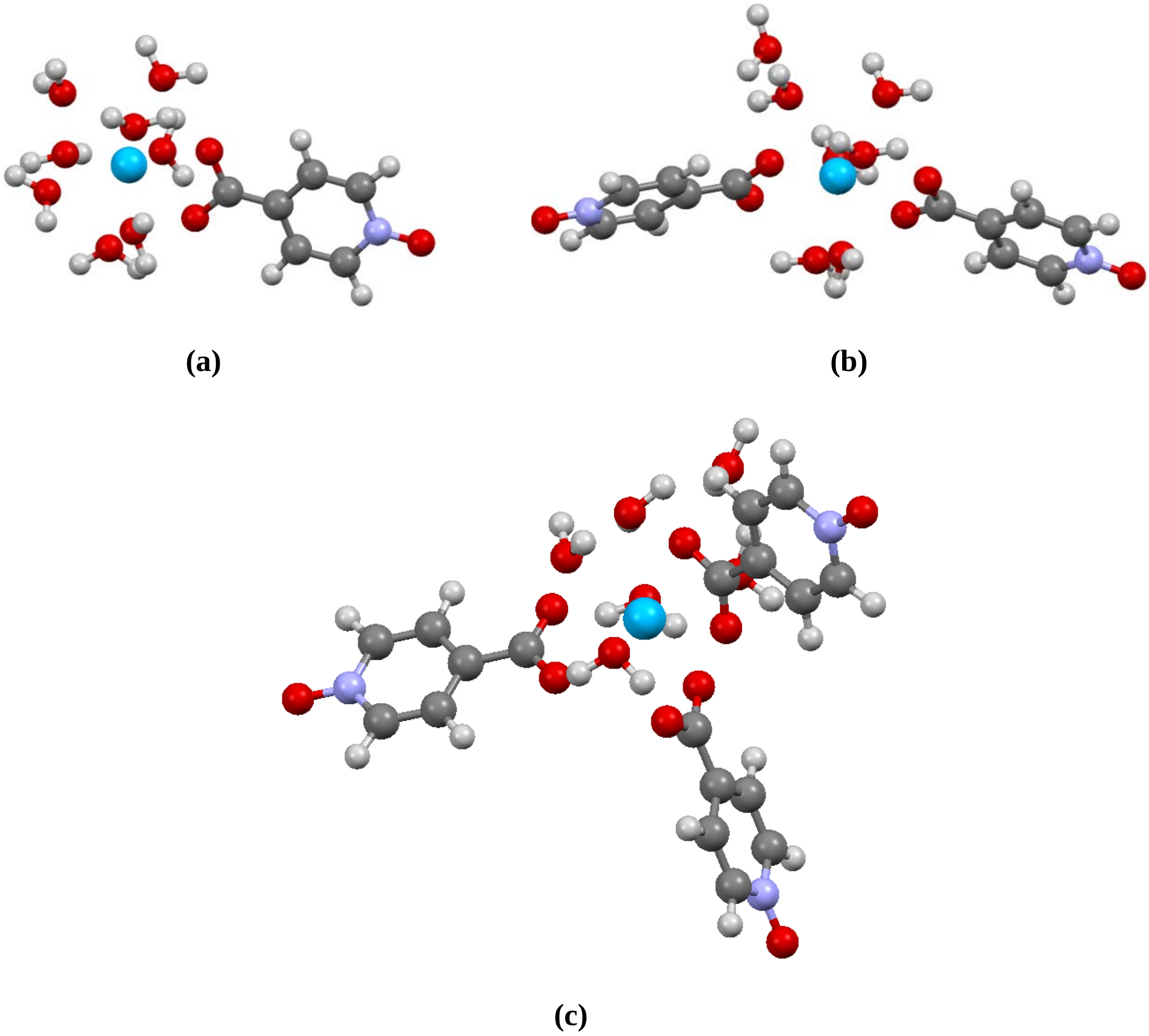

(a) **(b)**

(c)

Figure 5.9: Optimized geometries for Th(IV)-IANO complexes: a) ML, b) ML_2 and c) ML_3.

The metal ion-ligand complexation reaction ($M:L_n$) for all the three Th(IV)-PCNO complexes can be given as below

$$[Th(H_2O)_9]^{4+} + nL \rightarrow [Th(H_2O)_x(L)_m]^{4-n}(L)_{n-m} \quad + \quad (9-x)\ H_2O \qquad (5.8)$$

The strength of a metal ion complex with a particular ligand can be explained using binding energy or free energy. Hence, the gas phase binding energy is computed for the complexation reaction given by equation 5.8 using the following equation.

$$\Delta E = [E_{[[Th(H2O)x(L)m](L)n-m]4-n} + E_{(9-x)H2O}] - [E_{[Th(H2O)9]4+} + n\ E_L] \qquad (5.9)$$

The thermal correction to the electronic energy (E_{el}), enthalpy (H_C) and free energy (G_C) of the optimized complexes has been performed following the earlier reported prescription [380-381]. The energetics (interaction energy (ΔE_C) and Gibbs free energy of formation(ΔG_C)) and the structural parameter (bond distances) for all the three Th(IV)-PCNO complexes were given in table 5.8. The theoretically calculated interaction energies as well as Gibbs formation energies follow the order Th(IV)-PANO > Th(IV)-IANO > Th(IV)-NANO among the three Th(IV)-PCNO complexes and $\Delta E_C/\Delta G_C$ for a particular Th(IV)-PCNO complexes follows the decreasing trend on stepwise complexation analogous to that observed in experimentally stability constants obtained by potentiometric titrations. The shorter bond lengths of Th-O (of COO) in Th(IV)-PANO complexes than the other two further supports the stronger interaction of Th(IV) with PANO than NANO and IANO.

Table 5.8: The calculated interaction energy (ΔE_C), Gibbs free energy of formation(ΔG_C) (in kJ/mol) and bond lengths (in A^0) between Th(IV) and the binding atoms of the ligands for all experimentally predicted Th(IV)-PCNO complexes. O (N-O), O (COO) and O (H_2O) represents the oxygen atoms of N-oxide, carboxylate of ligand molecule and water in Th(IV) aqua ion respectively.

Complex	**Δ E**	**Δ G**	$d_{Th-O(N-O)}$	$d_{Th-O(COO)}$	$d_{Th-O(H2O)}$
			Th(IV)-PANO Complexation		
ML	-189.82	-211.46	2.301	2.218	2.550, 2.556, 2.567, 2.576, 2.584, 2.619, 2.631
ML_2	-145.66	-183.17	2.399, 2.441	2.282, 2.285	2.572, 2.572, 2.574, 2.580, 2.613
ML_3	-130.30	-181.92	2.400, 2.448, 2.489	2.273, 2.309, 2.360	2.464, 2.624, 4.367
ML_4	-60.81	-95.19	2.459, 2.465, 2.486, 2.499	2.356, 2.367, 2.414, 2.450	2.65
			Th(IV)-NANO Complexation		
ML	-99.91	-88.37		2.356, 2.360	2.548, 2.569, 2.573, 2.608, 2.622, 2.623,

				2.645, 2.660
ML$_2$	-91.79	-88.32	2.483, 2.490, 2.492, 2.516	2.548, 2.561, 2.563, 2.592, 2.618, 2.620, 2.798
ML$_3$	-88.97	-67.28	2.479, 2.513, 2.533, 2.535, 2.540, 2.564	2.566, 2.575, 2.624, 2.632, 2.649, 4.055
Th(IV)-IANO Complexation				
ML	-108.07	-105.10	2.461, 2.476	2.546, 2.567, 2.570, 2.587, 2.611, 2.619, 2.645, 2.677
ML$_2$	-105.26	-92.97	2.440, 2.486	2.503, 2.530, 2.553, 2.580, 2.583, 2.602, 4.164
ML$_3$	-61.99	-42.26	2.454, 2.512, 2.506, 2.546, 2.534, 2.601	2.594, 2.606, 2.607, 2.637, 2.700, 4.009

In view of the predominantly Coulombic interaction between actinide and carboxylates, the detailed charge calculations on the individual atoms in each complex and its comparison with the charge on same atoms of the bare ligand would give insight into the charge polarization effects on complex formation of Th(IV) by PCNOs. This further helps in interpreting the trends in stability among all the three structurally isomeric pyridine monocarboxylate-N-oxides. The binding atoms (such as oxygen atoms of N-oxide and carboxylate group) and the atoms directly linked to binding atoms (nitrogen of N-oxide, carbon atoms of the carboxylate and the ring carbon attached to carboxylate group) in ligand are the most effected with respect to charge polarization on complexation with the metal ion. The charges on these key atoms of the complex were given in table 5.9 while the same on the identical atoms in bare ligands are given in table 5.10.

Table 5.9: The charges on key atoms of all experimentally predicted Th(IV)-PCNO complexes. O (N-O), O (COO), N (N-O), O (COO) and O (C-COO) represents the oxygen atoms of N-oxide, carboxylate, nitrogen of N-oxide and carbon atoms of carboxylate and the carbon directly attached to carboxylate carbon of ligand molecule respectively.

Complex	q_{Th}	$q_{O(N\text{-}O)}$	$q_{N(N\text{-}O)}$	$q_{O(COO)}$	$q_{C(COO)}$	$q_{C(C\text{-}COO)}$
Th(IV)-PANO Complexation						
ML	2.230	-0.617	0.072	-0.794, -0.575	0.764	0.087
ML2	2.133	-0.588, -0.581	0.081, 0.084	-0.790, -0.599, -0.788, -0.605	0.759, 0.759	0.066, 0.061
ML3	2.240	-0.565, -0.576, -0.589	0.081, 0.083, 0.087	-0.734, -0.655, -0.769, -0.614, -0.763, -0.625	0.767, 0.764, 0.760	0.074, 0.061, 0.060
ML4	1.979	-0.534, -0.536, -0.536, -0.599	0.086, 0.092, 0.093, 0.095	-0.729, -0.655, -0.752, -0.652, -0.724, -0.661, -0.731, -0.653	0.763, 0.764, 0.754, 0.762	0.063, 0.065, 0.063, 0.058
Th(IV)-NANO Complexation						
ML	2.124	-0.542	0.105	-0.704, -0.708	0.793	-0.193
ML2	1.875	-0.560, -0.561	0.101, 0.101	-0.691, -0.683, -0.680, -0.699	0.778, 0.778	-0.176, -0.174
ML3	1.793	-0.571, -0.569, -0.571	0.097, 0.098, 0.098	-0.705, -0.663, -0.689, -0.661, -0.676, -0.675	0.783, 0.79, 0.778	-0.168, 0.165, -0.168
Th(IV)-IANO Complexation						
ML	2.103	-0.460	0.148	-0.729, -0.719	0.772	-0.204
ML2	2.027	-0.507, -0.507	0.130, 0.129	-0.718, 0.693, -0.706, -0.696	0.767, 0.763	-0.184, -0.184
ML3	1.784	-0.527, -0.527, -0.524	0.121, 0.120, 0.122	-0.694, 0.693, -0.707, -0.657, -0.724, -0.656	0.775, 0.767, 0.774	-0.174, -0.171, -0.179

Table 5.10: The charges on key atoms of bare PCNO molecules. O (N-O), O (COO), N (N-O), O (COO) and O (C-COO) represents the oxygen atoms of N-oxide, carboxylate, nitrogen of N-oxide and carbon atoms of carboxylate and the carbon directly attached to carboxylate carbon of ligand molecule respectively.

Ligand	$q_{O(N\text{-}O)}$	$q_{N(N\text{-}O)}$	$q_{O(COO)}$	$q_{C(COO)}$	$q_{C(C\text{-}COO)}$
PANO	-0.571	0.098	-0.780, -0.740	0.716	0.009
NANO	-0.614	0.082	-0.772, -0.770	0.723	-0.153
IANO	-0.605	0.085	-0.775, -0.775	0.716	-0.137

Comparing the charges on these individual atoms in the complex and on bare ligands, the following observations can be made:

1) During complexation, charge on nitrogen is reduced while of the oxygen was enhanced in N-oxide group. Likewise, the charge on one of the oxygen atoms (bonding to Th(IV)) is enhanced whereas the charge on the other oxygen atom of carboxylate group was decreased as compared to that in bare ligand in case of Th(IV)-PANO complexes.

2) In case of Th(IV)-NANO/IANO complexes, the charge on nitrogen of N-oxide was more than on the bare ligand while the charge on oxygen of N-oxide in complex is lower than on bare ligand. The charges on both the oxygen atoms of the carboxylate group are lower in complex than on bare ligand. This trend in charges on nitrogen and oxygen atoms of N-oxide and oxygen atoms of carboxylate group was opposite to the trend observed in Th(IV)-PANO complexes.

3) The charge on carbon atoms is more in complex form than in bare ligand for all the three Th(IV)-PCNO complexes.

4) In case of Th(IV)-PANO complexes, PANO binds Th(IV) by chelation through the oxygen atom of N-oxide moiety and the oxygen atom of carboxylate. Thus the coulombic interaction with these two atoms would be more resulting in higher charge polarization at

these two atoms during complex formation. Large difference in charge on oxygen atoms of carboxylate also further supports the monodentate nature of carboxylate in complexation process and hence chelate formation in case of PANO binding by Th(IV).

5) In case of Th(IV)-NANO/IANO complexes, the metal ion binds the ligand through both the oxygen atoms of the carboxylate group which is evident from the similar charge on both the oxygen atoms on complex formation also. Both the oxygen of N-oxide and carboxylate functional attached to base pyridine ring in the PCNOs are electron withdrawing groups and can pull the electron density towards them from the base pyridine ring. Further, the electron withdrawing effects in pyridine ring are more pronounced at ortho and para positions which are more favourable positions for charge polarization than meta position. Thus the charge polarization effects would be more prominent in PANO followed by IANO than NANO. The ortho and para positions are considered to be electron donating groups whereas meta position is an electron withdrawing group. Thus the charge reduction on oxygen atoms of carboxylate would be more in NANO (from -0.770 in NANO to -0.704 in Th(IV)-NANO complex) than in IANO (from -0.775 in IANO to -0.719 in Th(IV)-IANO complex). Among Th(IV)-NANO and Th(IV)-IANO complexes, the reduction of charge on oxygen atoms of carboxylate in NANO is more than IANO reflecting higher coulombic interaction of IANO than NANO with Th(IV). Hence the Th(IV)-IANO complexes are more stable than Th(IV)-NANO complexes, which matches with the experimental observation (table 1).

5.4.2.4. Conclusions

The thermodynamic parameters for the complexation by thorium with three structurally isomeric pyridine monocarboxylate-N-oxide were studied by experiment and theory. It was found that the formation of all the complexes are endothermic and entropy driven. The higher stability of Th(IV)-PANO complexes over the other two isomers is due to its chelate nature. The variations in thermodynamic parameters are interpreted in terms of perturbations in hydration spheres of both the metal and ligand ions. Also the theoretical calculation to determine the charges on individual atoms further enhanced the knowledge in interpreting the trends within and among the Th(IV)-PCNO complexes in terms of electrostatic interactions. The linear free energy relationship of log β of the complex with pKa of ligand also showed the chelate and carboxylate kind of binding in Th(IV)-PANO and Th(IV)-NANO/IANO complexes respectively. Overall, the mutual position of the two functional groups, the N-oxide and carboxylate, has a key role on the thermodynamics of complexation process.

Chapter 6

Stability, Speciation and Spectral Properties of Np(V) complexes with Pyridine Monocarboxylates and Hydroxamic acids

6.1. Introduction

The complexation of d-block and 4f elements with the picolinic acid have been studied widely in the past with regard to their applications in analytical chemistry, corrosion effects, luminescence applications [127, 154-158, 304-309]. Limited studies have been reported in the literature on solution chemistry of 5f elements (actinides) with the same series of carboxylates [128, 382-383]. In the recent years, few studies have been reported on the Np(V) carboxylate [147, 161, 384-388] and Np(V) aminocarboxylate complexes [150, 389] including the complexation of Np(V) with picolinic acid [159-163], nicotinic acid [161, 163]. Budantseva et al studied the interaction of Np(V) with all the three ligands and determined the log β values for ML and ML_2 complexes of Np(V)-picolinate and ML complex of Np(V)-nicotinate and Np(V)-isonicotinate complexes [164]. All these studies are limited to determination of stability constant values only and do not report on their speciation and spectral properties. Recently Zhang et al. studied the effect of temperature on thermodynamic and spectroscopic properties of Np(V)-picolinate complex but at I = 1.00 M $NaClO_4$ [356]. Comparison of stability, structures and spectral properties of Np(V) complexes will give an additional insight on the effect of position of nitrogen on the complexation phenomenon.

Hydroxamic acids are reducing chemical agents, and also act as di-oxygen chelating ligand. They have high affinity to hard-acid cations and simulate the hydroxamic acid function of the pyoverdins which have very high affinity for actinides and can cause mobilization and transport of actinides in the geosphere. Complexes of simple hydroxamates with metal ions have been studied both in solution and in solid state [390-398]. Investigations on the complex formation with primary hydroxamate ligands in aqueous solution demonstrated clearly that, depending on pH, two oxygen binding modes of the ligands are accessible to metal ions [397-398]. Acetohydroxamic acid (AHAH) exists in two tautomeric forms as keto and iminol forms (Figure 6.1) which provide a number of sites for chelation [399]. The studies on the interaction of simple hydroxamates with tetra and pentavalent actinides have been reported in the literature on extraction and reduction of actinides [174-180]. It has been reported that stability constants (β) of actinide-hydroxamate complexes increase in the order $\beta_{U(VI)} < \beta_{Np(IV)} < \beta_{Pu(IV)}$ [179-180, 232, 295, 392].

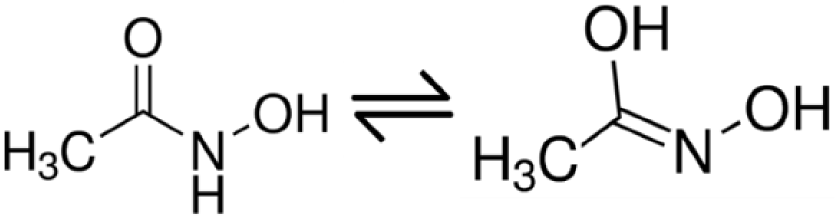

Figure 6.1: Tautomeric forms of acetohydroxamic acid (Left : keto form, Right : iminol form)

Extensive work on binding of actinide ions with HA has been reported in literature but very few studies have focused on coordination modes of structurally varying HA with actinides [181-182, 303]. Moll et al. have reported the stability constants of complexes of benzhydroxamic acid (BHA) and salicylic hydroxamic acid (SHA) with Np(V) using UV-Vis spectrophotometric titration [182]. The formation of 1:1 and 1:2 species for Np-BHA was observed while in case of Np-SHA two 1:1 species ML (1:1) and MLH (1:1:1) were observed. The formation of 1:1 species in Np-AHA and Np-BHA indicate deprotonation of hydroxyl group of hydroxamate during complexation. As SHA is diprotonated ligand, formation of 1:1 species in Np-SHA indicate deprotonartion of phenolic group at ortho position as well as hydroxyl group of hydroxamate whereas in 1:1:1 complex ortho phenolic group remains protonated. However, it is not clear, whether the ortho phenolic group participates directly in bonding with Np(V) or indirectly stabilizes the 1:1:1 complex. Similar species were also observed in U(VI)-HA complexes. U(VI)-SHA complexation studies by time resolved luminescence spectroscopy [181] also showed the presence of protonated 1:1:1 and 1:2:2 complexes of U(VI)-SHA.

Present study is aimed at studying the stability (log β) of the complexes formed, speciation diagrams and spectral properties of Np(V) complexes with three structural isomers viz picolinic acid (pyridine-2-carboxylic acid), nicotinic acid (pyridine-3-carboxylic acid) and isonicotinic acid (pyridine-4-carboxylic acid) (Fig. 1.2) at 298 K in 0.1 M $NaClO_4$ medium using spectrophotometry technique. The DFT calculations were carried out to get the optimized structures and energetics of Np(V)-pyridine monocarboxylate complexes under the specified experimental conditions. The charges on each atom in the complex and free ligand were also calculated to understand the effect of position of nitrogen in the pyridyl ring on the electron density distribution of complexes which in turn helps in rationalizing the energetics of complexation. The DFT calculations are very much helpful in determining the variations in stability due to charge polarization among the Np(V) complexes with all the three isomeric ligands and are compared with the experimental observations.

Studies were also carried out to understand the binding modes and the structural changes in terms of bond distances, bond angles, charge densities on individual atoms on coordination with the ligands in different Np(V)-HA complexes at molecular level. For this purpose, the DFT calculations were carried out for Np(V) complexation with HA ligands of varying substituents viz., AHA, BHA and SHA and the results of theoretical calculations have been correlated with the experimental data available in literature.

6.2. Experimental

6.2.1. Reagents

Neptunium was separated from other actinides and cations using anion exchange (Dowex 1X4) resin in nitrate form [196] and alpha spectrometry was employed to confirm the purity of neptunium in the stock solution. The daughter product Pa-233 was removed from the eluted neptunium solution by solvent extraction with diisobutyl carbinol. Alpha spectrometry and spectrophotometry (981 nm) [197] were used to estimate the concentration of purified neptunium. All the other chemicals were of A.R. grade with purity ≥ 99% (Sigma Aldrich).

6.2.2. Spectrophotometric Titrations

All the spectrophotometric measurements were carried out using a JASCO V530 model spectrophotometer. To minimize the hydrolysis and maximize the dissociation of pyridine monocarboxylates, the pH of all the metal and ligand solutions were adjusted to a final value of 4. The ligand solutions were added in steps (10 to 50 μL) to a known volume (2.00 mL) of metal solution to determine the stability constants of the complexes. An equilibration time of 5 minutes between the successive additions showed a stable absorbance curve for each point of titration and the absorption spectra were recorded for each addition of ligand over the wavelength range from 900 to 1100 nm with a wavelength interval of 0.1 nm. All the titrations were carried out at a fixed temperature (298 K) and ionic strength (0.1 M $NaClO_4$). The spectroscopic data was analyzed using Hyperquad [217] to determine the species present and their fraction along with the respective log β values for all the Np(V)-pyridine monocarboxylate and Np(V)-hydroxamate complexes. Further the molar absorptivity of the complexes formed was derived from the deconvolution of the respective absorption spectra of all the Np(V)-pyridine monocarboxylate and hydroxamate complexes.

6.3. Theoretical Calculations

Turbomole programme was utilized for the geometry optimization by DFT [400]. Generalized gradient approximation (GGA) approximation and Becke's exchange functional [264] in conjunction with Perdew's correlation functional [265] was used for calculations. The geometries of actinide complexes have been found to be less sensitive to level of theory. In a large number of reports, authors have used def-SV(P) basis set for structure optimization

[337, 401]. Cao et al. used two basis sets for geometry optimization def-SV(P) and def2-TZVP and showed the very small change in bond distances and angles on changing the basis set [402]. Ali et al. has shown that the calculated structure of lanthanides and actinide complexes with substituted glycol amides obtained at the BP86/SVP level of optimization were found to be in close agreement with the X-ray data and also with the structure obtained at the B3LYP/TZVP level of theory [403]. Despite the fact that the BP86 functional is quite fast and accurate in predicting the geometry and vibrational frequencies, the energetic parameters are not accurate enough compared to the hybrid functional due to non-consideration of the non-local HF part in the exchange functional. Therefore, general approach followed in number of literature reports on actinides is to optimize the structure using BP86 functional with def-SVP basis set and calculate the energies of optimized structure using the B3LYP functional [404] employing the def-TZVP basis set. The same approach has been followed in the present work. The energy calculation was carried out at B3LYP/def-TZVP level of theory. Lighter atoms are treated at all electron level. Theoretical calculations were carried out using triplet spin state for Np. The B3LYP and BP86 have been used by number of authors in high spin states of actinides and lanthanides, thereby justifying the use of DFT [403]. These functionals take care of electron correlation. The charges on individual atoms in bare ligand and in complex were also calculated by the same software using natural bond orbital population analysis to determine the changes in the charge on individual atoms on complexation process. The bond distances between the bonding atoms and neptunium for the optimized geometries were calculated to rationalize the energetics of complexation. In order to access the effect of bulk solvent medium, binding energies for Np(V)-complexes were calculated using COSMO continuum solvation model [340] using dielectric constant of water as 78.4.

6.4. Results and Discussions

6.4.1. Np(V) Pyridine Monocarboxylates Complexes

6.4.1.1. Spectrophotometric Titration

The 5f-5f transition absorption band of Np(V) at 981 nm is usually red shifted on complexation with removal of water molecules in the primary coordination of Np(V). Figures 6.2-6.4 show the absorption spectra recorded during the titration of Np(V) solution with different ligands. The absorption peak decreases with incremental additions of pyridine monocarboxylate solution to Np(V) solution. The red shift in absorption spectra is quite prominent and visible in case of Np(V)-picolinate while in case of Np(V)-nicotinate (Fig. 6.3) and Np(V)-isonicotinate (Fig. 6.4), there is a decrease in absorbance at 981 nm, though the shift in the λ_{max} is negligible. The measured absorbance at any point of titration is a sum of absorbance of all the species present at that particular point of titration and can be expressed as,

$$A = A_{NpO_2^+} + A_{NpO_2L} + A_{[NpO_2L_2]^-} \tag{6.1}$$

These simultaneous equations were solved (cf. section 2.4 and 2.5.2.3) using Hyperquad software [217] to determine the stability constants (log β) and thereby generate the speciation diagram for the complexes formed during the course of reaction.

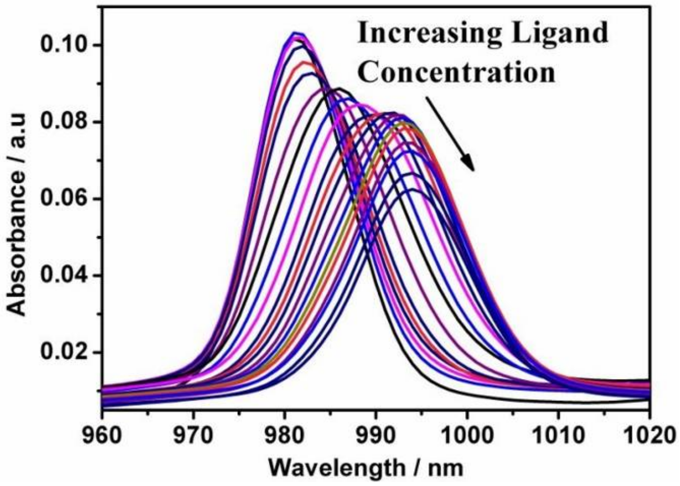

Figure 6.2: Absorption spectra of Np(V)-picolinate complexation ([Np(V)] = 2.5 x 10^{-4} M, [pic] = varied from 0.00 to 0.20 M at pH = 4 and T = 298 K in 0.1 M $NaClO_4$ medium; initial volume of Np(V) in cuvette 2.00 mL)

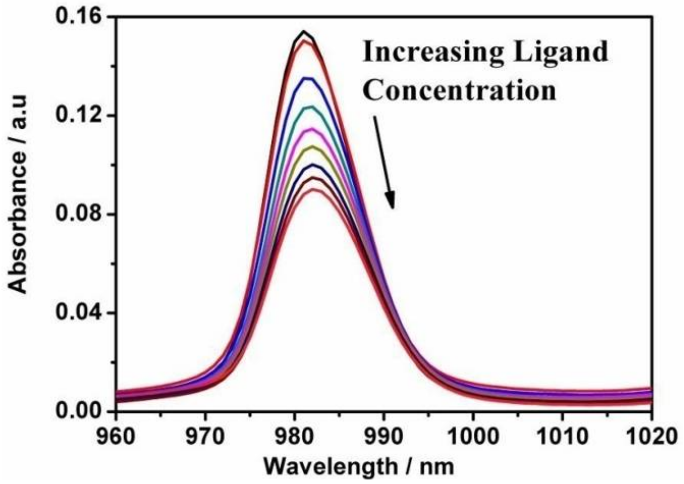

Figure 6.3: Absorption spectra of Np(V)-nicotinate complexation ([Np(V)] = 2.5 x 10^{-4} M, [nic] = varied from 0.00 to 0.17 M at pH = 4 and T = 298 K in 0.1 M $NaClO_4$ medium; initial volume of Np(V) in cuvette 2.00 mL).

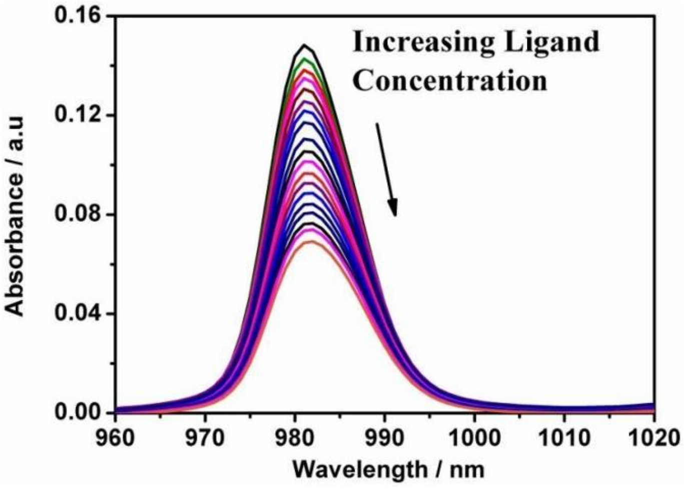

Figure 6.4: Absorption spectra of Np(V)-isonicotinate complexation ([Np(V)] = 2.5 x 10^{-4} M, [isonic] = varied from 0.00 to 0.10 M at pH = 4 and T = 298 K in 0.1 M $NaClO_4$ medium; initial volume of Np(V) in cuvette 2.00 mL).

The speciation diagram for the complexation of Np(V) with picolinate is shown in Fig. 6.5. Np(V) ion forms both 1:1 and 1:2 complexes with all the three ligands with no indication of complexation with protonated form of ligands (MLH or ML_2H). Though the formation of ML_2 complex in case of Np(V)-nicotinate and Np(V)-isonicotinate is less compared to corresponding Np(V)-picolinate complex, the removal of this species from proposed chemical equilibria did not fit the spectrophotometric titration data to obtain log β values and the speciation plots.

The experimentally determined stability constants and the calculated free energy of formation of Np(V) complexes with all the three pyridine monocarboxylates along with those available in literature are given in Table 6.1. The literature reported log β of all the complexes have a wide spread ranging from 3.04 to 3.78 for ML and 5.58 to 6.98 for ML_2 in case of Np(V)-picolinate [159-164, 356], and 0.57 to 2.94 for ML in case of Np(V)-nicotinate complexes [161,163-164]. Only one value for ML_2 of Np(V)-nicotinate [86] and ML of Np(V)-isonicotinate are available in literature [164]. The log β for ML_2 of Np(V)-isonicotinate is not available in the literature and was determined in the present study. The large variations in the log β can be attributed due to the difference in techniques and experimental conditions.

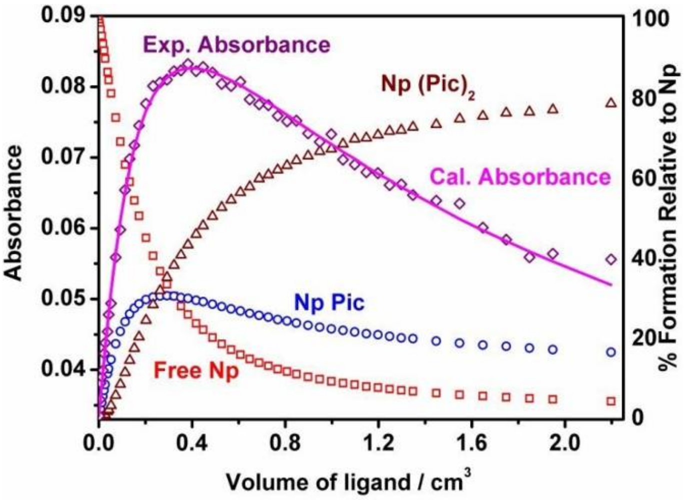

Figure 6.5: Speciation diagram of Np(V)-picolinate complexation ([Np(V)] = 2.5 x 10^{-4} M, [pic] = varied from 0.00 to 0.20 M at pH = 4 and T = 298 K in 0.1 M $NaClO_4$ medium; initial

volume of Np(V) in cuvette 2.00 mL, ◊ - experimentally measured absorbance values, ▬ calculated absorbance values, □ - Free Np(V), ○ - [Np(Pic)], Δ - $[Np(Pic)_2]^-$)

Table 6.1: Stepwise stability constants (log K), ΔG and maximum percentage of Np(V) pyridine monocarboxylates complexes formed during the course of reaction along with the reported values.

Complex	Max. % of Formation	log K	ΔG (kJ mol^{-1})	Reference
		Np(V) - Picolinate Complexes		
ML	40.0	2.96 ± 0.04	-16.9 ± 0.2	Present work
		3.23	-18.4	[160]
		3.45 ± 0.02	-19.7 ± 0.1	[161]
		3.04 ± 0.03	-17.3 ± 0.2	[162]
		3.53 ± 0.03	-20.1 ± 0.2	[163]
		3.59 ± 0.01	-20.5 ± 0.1	[164]
		3.78 ± 0.01	-21.6 ± 0.1	[356]
ML_2	80.9	2.31 ± 0.04	-13.2 ± 0.2	[164]
		2.35	-13.4	[160]
		2.48 ± 0.02	-14.2 ± 0.1	[163]
		2.58 ± 0.02	-14.7 ± 0.2	[161]
		2.71 ± 0.04	-15.5 ± 0.2	Present work
		2.80 ± 0.02	-16.0 ± 0.1	[356]
		Np(V) - Nicotinate Complexes		
ML	61.7	0.57 ± 0.03	-3.2 ± 0.2	[161]
		0.74 ± 0.03	-4.2 ± 0.2	[163]
		1.34 ± 0.09	-7.6 ± 0.5	Present work
		2.94 ± 0.05	-16.8 ± 0.3	[164]
ML_2	22.1	0.31 ± 0.05	-1.8 ± 0.3	[163]
		0.57 ± 0.03	-3.2 ± 0.2	Present work

		Np(V) - Isonicotinate Complexes		
ML	51.4	1.52 ± 0.05	-15.5 ± 0.3	[164]
		2.72 ± 0.04	-8.7 ± 0.2	Present work
ML_2	19.7	0.87 ± 0.02	-5.0 ± 0.1	Present work

The log β for Np(V)-picolinate complexes were found to be higher than that for Np(V)-nicotinic and Np(V)-isonicotinate complexes for both 1:1 and 1:2 complexes. The higher log β of Np(V)-picolinate than other two can be explained in terms of the formation five membered chelate ring through nitrogen and oxygen of picolinic acid. Among the nicotinate and isonicotinate complexes, the log K was found to be higher for the latter. The nitrogen at para position in case of isonicotinate enables higher charge transfer from nitrogen to carboxylate group than that at meta position in nicotinate. This results in stronger complexes of Np(V) with isonicotinate than the nicotinate.

6.4.1.2. Linear Free Energy Relationships (LFER)

Hard acid hard base interactions are dominated by electrostatic attractions that directly depend on the magnitude of opposite charges on the binding moieties. Actinide ions (hard acids) prefer binding with hard donors like fluorine and oxygen groups. Thus, for a particular binding geometry of ligand, the variation of log K_{ML} with the effective charge on metal ion should result in a linear relation. Figure 6.6 shows the plot of loh K as a function of the effective charge on actinide ions. The effective charges on NpO_2^{+}, UO_2^{2+}, Eu^{3+} and Pu^{4+} were taken as 2.3, 3.3, 3 and 4 respectively [67]. The data on stability constants of pyridine monocarboxylates with other actinide/lanthanide ions were taken from literature [127-128]. The log K_1 values vary linearly with the effective charge on the metal ions, thereby corroborating the LFER hypothesis. The linear relationship also suggests the similar binding mode of the all the three ligands with different metal ions. The figure clearly brings out the higher stability of picolinate complexes over the nicotinate and isonicotinate. Further, the slope for actinide picolinate complexation line is higher than that for other ligands and is nearly equal in case of nicotinate and isonicotinate complexes. The higher slope for actinide picolinate can be attributed to higher electron density on the picolinate binding atoms which is also supported by theoretical charge calculations (Section 6.5.1.4).

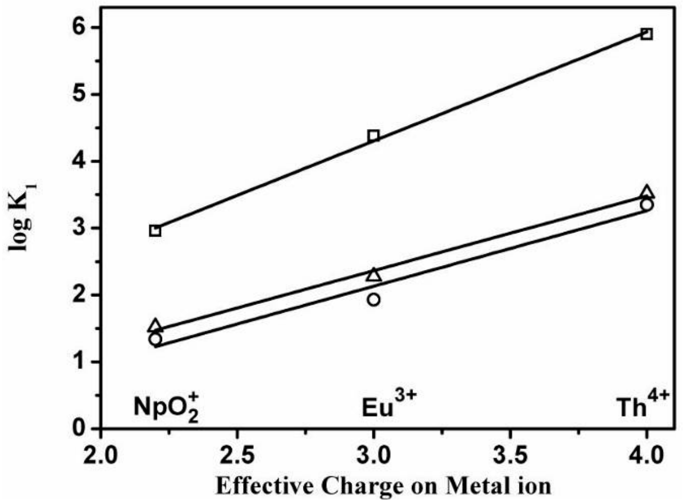

Figure 6.6: LFER of Eu(III), Th(IV) and Np(V) complexes with pyridine monocarboxylates (□ -picolinic acid, Δ - isonicotinic acid and ○ - nicotinic acid).

Fig. 6.7 shows the LFER between log K_1 and log K_P of different Np(V) carboxylate complexes along with the data obtained in the present work. In case of actinide nicotinate and isonicotinate complexation, the binding is solely between metal ion and carboxylate. However, the log K_1 for Np-nicotinate and Np-isonicotinate were found to be higher than that expected from LFER when plotted against log K_P of their carboxylate group (Fig. 5b, symbols ■). Further, the log K_1 data for these ligands fall in line when plotted against sum of log K_{P1} and log K_{P2} (Symbols: ♦ and ▲). This suggests that the electron density from both the donating groups (pyridyl nitrogen and carboxylate) participates in bonding which can be explained by the charge polarization in the ligand during complexation.

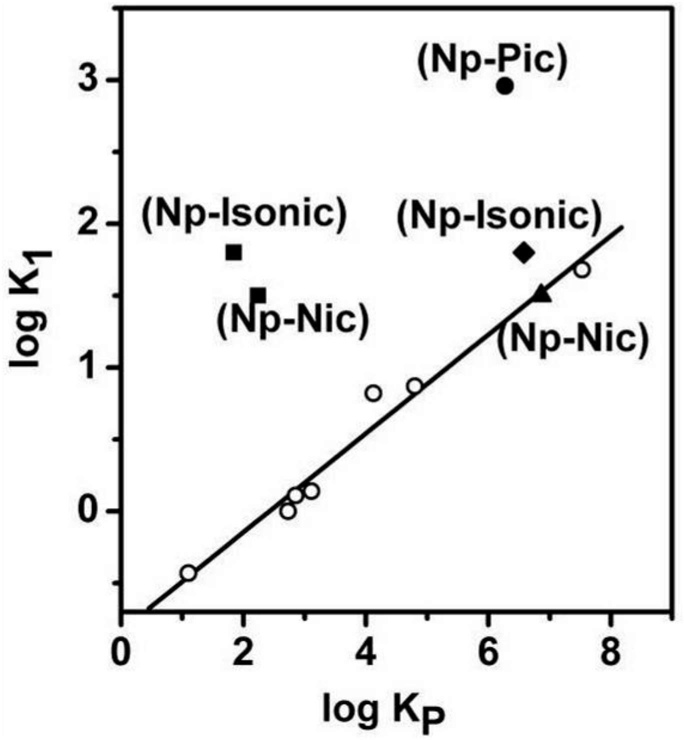

Figure 6.7: LFER of Np(V) complexes with carboxylate based ligand (○ Np-monocarboxylate in the increasing order dichloroacetate, chloroacetate, bromoacetate, iodoacetate, benzoate, acetate and phthalate [162], ■ Np-nicotinate and Np-isonicotinate (vs. log K_{P1}), and ▲ Np-nicotinate ♦ isonicotinate and ● Np-picolinate (Vs log K_{P1}+ log K_{P2}).

The absence of MLH type complexes (protonated) points towards deprotonation of pyridyl nitrogen during complexation. As can be inferred from log K_P of nicotinate and isonicotinate, the electron density on carboxylate groups is too low to form complex under present experimental conditions. However, on complexation with Np(V), the pyridyl nitrogen gets deprotonated and the electron density is transferred from pyridyl nitrogen to carboxylate groups, which in turn enhances its stability. It can be seen that the Np(V) isonicotinate complexes are more stable than corresponding nicotinate complexes which can be attributed to the position of nitrogen in pyridine ring with respect to carboxylate group. In the case of isonicotinate, the electron donating para position of nitrogen can mobilize its charge density to bonding carboxylate more effectively resulting a stronger binding with Np(V)-isonicotinate than in case of Np(V)-nicotinate system.

6.4.1.3. Spectral Properties

The absorption spectra of all the three Np(V) pyridine monocarboxylates were deconvoluted using Hyperquad [217] to determine the individual molar extinction coefficients of all the species formed during the course of reaction under the studied experimental conditions (Fig. 6.8–6.10). The cumulative absorption spectra (Fig. 6.2-6.4) don't show any indication of the shift in wavelength for nicotinate and isonicotinate complexes but the deconvoluted spectra do show a red shift in case of nicotinate and isonicotinate complexes. The extent of shift in λ_{max} for these two ligands is comparatively much lower than that in case of picolinate complexes, which is explained below.

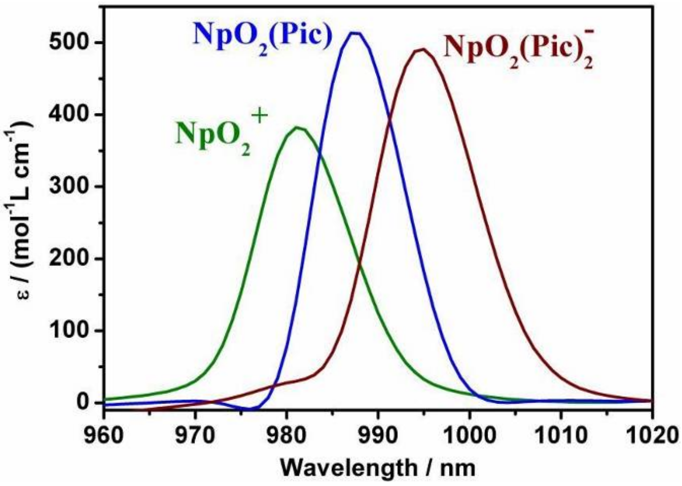

Figure 6.8: Molar absorptivity plots of Np(V)-picolinate complexation. ([Np(V)] = 2.5 × 10^{-4} M, [pic] = varied from 0.00 M to 0.20 M at pH = 4 and T = 298 K in 0.1 M $NaClO_4$ medium; initial volume of Np(V) in cuvette 2.00 mL).

In the uncomplexed Np(V) in aqueous medium, the ligand field include strong axial field due to two axial 'yl' oxygen atoms at close distance of 1.83 A^0 and weaker equatorial field due to oxygen atoms of water molecules at 2.50 A^0 [405]. This ligand field around the $NpO_2(H_2O)_5^+$ leads to shifting as well as splitting of the energy levels. On complexation, the increased ligand field in the equatorial plane changes, leading to further splitting of the energy levels which in turn leads to reduction in the energy gap between ground state ($^3H_4$) and excited state ($^1G_4$) of free ions. Thus, the red shift in the absorption spectrum depends on the ligand field around the metal ion (Nephelaxetic effect). As the ligand field can be directly related to the strength of the complex (log K), the ligand field splitting and thence the red shift in absorption band can be related to log K of complex as shown by Yang et al [406].

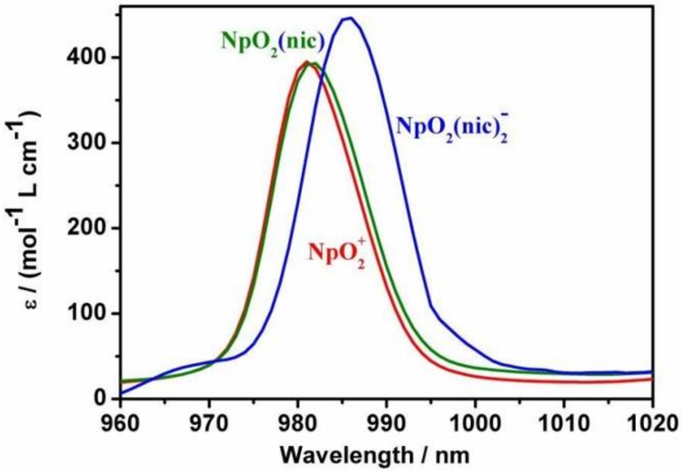

Figure 6.9: Molar absorptivity plots of Np(V)-nicotinate complexation. ([Np(V)] = 2.5 × 10^{-4} M, [nic] = varied from 0.00 M to 0.17 M at pH = 4 and T = 298 K in 0.1 M $NaClO_4$ medium; initial volume of Np(V) in cuvette 2.00 mL).

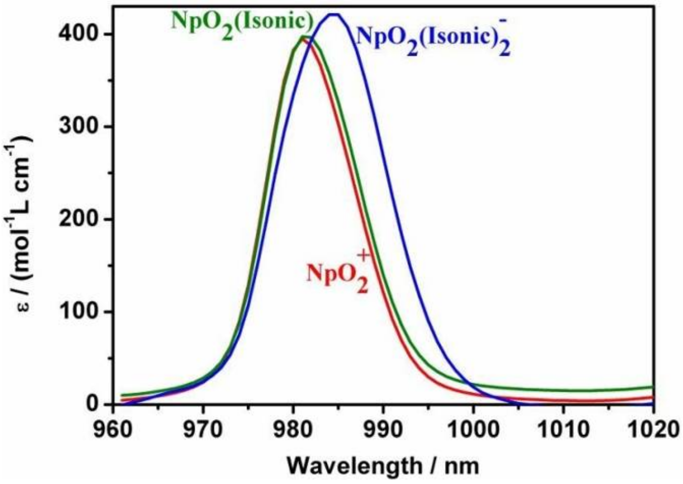

Figure 6.10: Molar absorptivity plots of Np(V)-isonicotinate complexation. ([Np(V)] = 2.5 × 10^{-4} M, [isonic] = varied from 0.00 M to 0.10 M at pH = 4 and T = 298 K in 0.1 M $NaClO_4$ medium; initial volume of Np(V) in cuvette 2.00 mL).

Yang et al. [406] have shown the linear relationship between shift in λ_{max} ($\Delta\lambda_{max}$ / λ_{max}) and log K. The variations in the λ_{max} for the three Np(V) pyridine monocarboxylates can be attributed to the variation in their complexation strength. In case of Np(V) picolinate complexes, nitrogen atom is directly bonded to Np(V) and hence can influence the λ_{max} to the maximum extent (from 981 nm of free Np(V) to 995 nm in ML_2 complex) than in other two cases where there is no nitrogen involvement. Relatively lower shift in λ_{max} for Np(V) nicotinate (from 981 nm of free Np(V) to 986 nm in ML_2 complex) and Np(V) isonicotinate complexes (from 981 nm of free Np(V) to 985 nm in ML_2 complex) than Np(V) picolinate complexes, indicating indirect involvement of nitrogen in bonding process, which could be by the charge transfer from nitrogen to bonding carboxylate oxygen atoms. The λ_{max} with corresponding molar extinction coefficients of all the three Np(V) pyridine monocarboxylates are given in Table 6.2.

Table 6.2: The λ_{max} with corresponding molar extinction coefficients of the Np(V)-pyridine monocarboxylates complexes ([Np(V)] = 2.5 × 10−4 M, [pic] = varied from 0.00 M to 0.20 M, [nic] = varied from 0.00 M to 0.17 M and [isonic] = varied from 0.00 M to 0.10 M at pH=4 and T= 298 K in 0.1 M NaClO4 medium; initial volume of Np(V) in cuvette 2.00 mL).

Ligand	Complex	λ_{max} (nm)	Molar Absorptivity Constant (ε = M^{-1} cm^{-1})
Picolinic acid	ML	987	513.5
	ML_2	995	490.9
Nicotinic acid	ML	982	393.2
	ML_2	986	446.3
Isonicotinic acid	ML	981	397.5
	ML_2	985	421.1

6.4.1.3. Theoretical Calculations

Figures 6.11 and 6.12, show the charges on all individual atoms in free pyridine monocarboxylates and their 1:1 complexes with neptunyl ion respectively. Based on the lowest complex formation energy, the optimized geometries for the predicted complexes were obtained (Fig. 6.12).

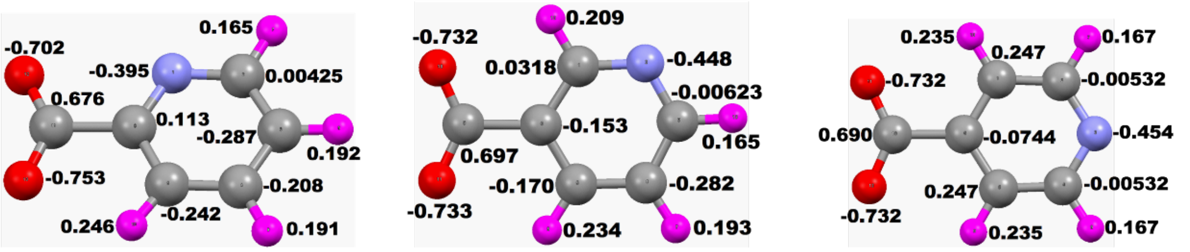

Figure 6.11: Charges on individual atoms of (from top to bottom) picolinate, nicotinate and isonicotinate molecules (colour variation: pink-nitrogen atom, yellow-carbon atom, blue-hydrogen atom, red-oxygen atom).

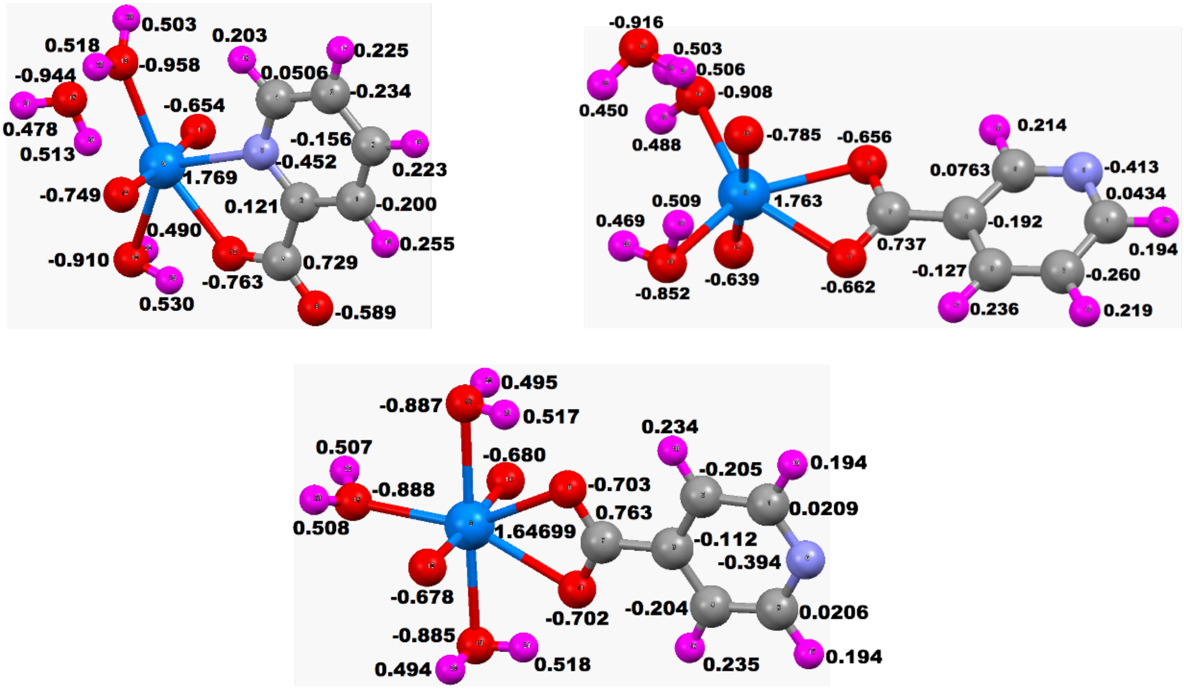

Figure 6.12: Charges on individual atoms of Np(V) – picolinate, nicotinate and isonicotinate complexes (colour variation: violet - nitrogen atom, grey - carbon atom, blue -neptunium, pink - hydrogen atom, red- oxygen atom).

The theoretical calculations were carried out for the reaction,

$$[NpO_2(H_2O)_5]^+ + L^- \overset{\Delta E}{\Leftrightarrow} [NpO_2(H_2O)_5L] + 2\,H_2O \tag{6.2}$$

$$\Delta E = E_{[NpO_2(H_2O)_5L} + 2\,E_{H_2O} - E_{[NpO_2(H_2O)_5]^+} - E_{L^-} \tag{6.3}$$

where E_X is the energy of species 'X'. The ΔE for Np-picolinate is most negative among all the three complexes studied. The trend in ΔE was found to be in line with the experimentally obtained log K values. The calculations corroborate the binding of Np(V) ion with pyridyl nitrogen and carboxylate oxygen in case of Np(V) picolinate complexes, while bonding only with carboxylate oxygen in nicotinate and isonicotinate complexes, which is evident from the charges and bond lengths of bonding atoms in the complexes (Tables 6.3 and 6.4).

Table 6.3: Charges on carboxylate oxygen atoms and pyridyl nitrogen of pyridine monocarboxylate anions.

Complex	**q_O**	**q_N**
Picolinate	-0.753 -0.702	-0.395
Nicotinate	-0.732 -0.733	-0.448
Isonicotinate	-0.732 -0.732	-0.453

Table 6.4: Binding energy, charge on individual atoms and bond distances of Np(V)-pyridine monocarboxylate complexes (1:1 ratio).

Complex	**ΔE (10^{-2} eV)**	**$q_{Np(V)}$**	**q_O**	**q_N**	**d_{Np-O} (A^0)**	**d_{Np-N} (A^0)**
Np(V) - picolinate	-16.40	+1.760	-0.769 -0.589	-0.452	2.360	2.551
Np(V) - nicotinate	-11.46	+1.762	-0.656 -0.656	-0.413	2.457 2.471	No Np(V)-N bond

Np(V) - isonicotinate	-14.90	+1.650	-0.689 -0.691	-0.395	2.510 2.526	No Np(V)-N bond

In the case of Np(V)-picolinate complexes, there is a significant charge transfer from nonbonding carboxylic oxygen (−0.702 to −0.589) to bonding carboxylic oxygen (−0.753 to −0.769) as well as to nitrogen atom (−0.395 to −0.452). The length of Np-O (carboxylate oxygen) bond (2.360 A^0) is the shortest of all the Np(V)-pyridine monocarboxylate complexes. This enhances the strong electrostatic attraction of picolinate towards Np(V) ion resulting in higher values of stability constants. In case of nicotinate and isonicotinate, chelation is not favored due to far away position of nitrogen with respect to carboxylate oxygen, which is well reflected in the higher lengths of Np-O (carboxylate oxygen) bonds in case of Np(V)-nicotinate (2.457 A^0 and 2.471 A^0) and Np(V)-isonicotinate (2.510 A^0 and 2.526 A^0) complexes. In both nicotinate and isonicotinate, the binding to Np(V) leads to transfer of charge from nonbonding pyridyl nitrogen to binding carboxylate which supports the experimental observation of higher log K than that expected from LFER. Further, the reduction on charge density on pyridyl nitrogen atom from free ligand to complex is more for isonicotinate (from −0.453 to −0.395) than that for nicotinate complexation (from −0.448 to −0.413). The higher charge transfer reflects in higher log β values for Np(V)-isonicotinate complex than Np(V)-nicotinate complex. It is interesting to note that, in Np(V)-picolinate, the charge on carbon atoms involved in the chelate ring changed from negative to positive (carboxylate carbon −0.676 to +0.729) and alpha carbon 0.112 to 0.122 on complexation with Np(V). However in case of Np(V)-nicotinate and Np(V)-isonicotinate, the negative charge on alpha carbon became more negative on complexation. On complexation, the charge on alpha carbon changed from −0.152 to −0.192 and −0.0053 to −0.120 in nicotinate and isonicotinate respectively. The increased charge on alpha carbon is also a signature of charge polarization from nonbonding groups.

Thermodynamic study of complexation of lanthanides by various dimethoxybenzoates in aqueous solution reveals the enhanced stability of these complexes due to charge polarization. The shift in ^{13}C NMR which is related to electron density on alpha carbon atom has been used as experimental evidence for charge polarization [293].

6.4.2. Np(V) Hydroxamates Complexes

In order to understand the complexation at molecular level, DFT calculations were carried out to obtain the minimum energy (most stable) structure for the complexes, free ligands and metal ion. To include the effect of solvent, water molecules are explicitly added to coordination shell of metal ion and as well as in complex. In the guess structure of complexes for optimization, considering their bidentate nature, each ligand was assumed to replace two water molecules from coordination shell of Np. The complexation of Np(V) with HA can be written as:

$$NpO_2\,(H_2O)_5^{+} + x\ \ HA^{n-} \quad \rightarrow \quad NpO_2(HA)_x\,(H_2O)_3^{-(xn-1)} + 2x\ H_2O \qquad (6.4)$$

The complexation energy (in eV) for binding of ‘x’ ligand is given by

$$\Delta E_{Cx} = E_{complex} + 2x\ E_{H2O} - E_{Metal\ ion} - x\ E_{Ligand} \qquad (6.5)$$

Table 6.5 gives the geometrical parameters (bond lengths and bond angle) for Np(V)-hydroxamate complexes, obtained for the optimized structure of Np(V), $NpO_2(H_2O)_5^{+}$ and 1:1:1 complexes of Np-HA. The complexation energy for all the hydroxamates with $NpO_2(H_2O)_5^{+}$ was found to be negative, suggesting that Np(V) would prefer to interact with HA ligands or ligands containing HA moiety rather than remain hydrated in aqueous solution. The binding atoms in hydroxamates to Np(V) ion are the oxygen atoms (hard bases) whose interaction with actinides (hard acids) is predominantly electrostatic in nature. Thus, the information about charges on individual atoms in the hydroxamates and in the complexes can also help in rationalizing the strength of complexes.

Table 6.5: Selected bond distances (Å) and bond angles in optimized geometry of Np(V), $NpO_2(H_2O)_5^+$ and 1:1:1 complexes of Np-HA and their interaction energies (ΔE_{C1})

Geometry	d Np-O_{ax}	O_{ax}-Np-O_{ax}	$d_{Np-O(Ligand)}$ *	$d_{Np-O(Water)}$ *	ΔE_{C1} (eV)
Np(V)	1.734, 1.734	180.00	-		-
$NpO_2 (H_2O)_5^+$	1.805, 1.805	176.64	-	2.566	-
Np-AHA	1.822, 1.802	174.75	2.441	2.587	-5.10
Np-BHA	1.800, 1.800	177.66	2.452	2.611	-4.60
Np-SX	1.847, 1.805	175.76	2.450	2.610	-4.01
Np-SY	1.847, 1.805	175.76	2.422	2.899	-4.45
Np-SZ	1.823, 1.802	172.81	2.502	2.583	-3.00

* *average bond distances values*

6.4.2.1. Structure of $NpO_2(H_2O)_5^+$

In the gas phase structure of Np(V), axial oxygen atoms are found to be symmetrically located at 1.734 A^0 (Np-O_{ax}) from Np atom and the charge on Np was calculated as +2.23. On coordinating with five water molecules, $NpO_2(H_2O)_5^+$, the negative charge on O atoms of water molecules neutralizes the effective charge on Np atom thereby reducing it from +2.23 to +1.68 . Reduction in the Np charge decreases its interaction with axial O atoms in Np(V) which in turn results in increase in Np-O_{ax} distance from 1.734 A^0 to 1.803 A^0. Addition of water molecules introduces asymmetry in the equatorial plane resulting in decrease in O_{ax}-Np-O_{ax} bond angle from 180^0 to 176.64^0. The calculated bond distances for $NpO_2(H_2O)_5^+$, are close to the experimental values [405] of Np-O_{ax} bond distance (1.83 A^0) and Np-O_W (distance between Np and 'O' atom from water at equatorial plane) (2.50 A^0).

6.4.2.2. Complexation of Np(V) with AHA

Figure 6.13 represents the complexation process for Np(V)-AHA and Np(V)-BHA, showing the optimized structure of all the species involved in complexation process and charges on bonding atoms. In Np(V)-AHA complex, the carbonyl and hydroxyl 'oxygen' atoms are at 2.47 and 2.40 Å from Np atom respectively (table 6.5). This closer approach of HA oxygen atoms (compared to water molecules in $NpO_2(H_2O)_5^+$), is attributed to higher negative charge on oxygen atoms of HA favoring the stronger interaction of Np with the same.

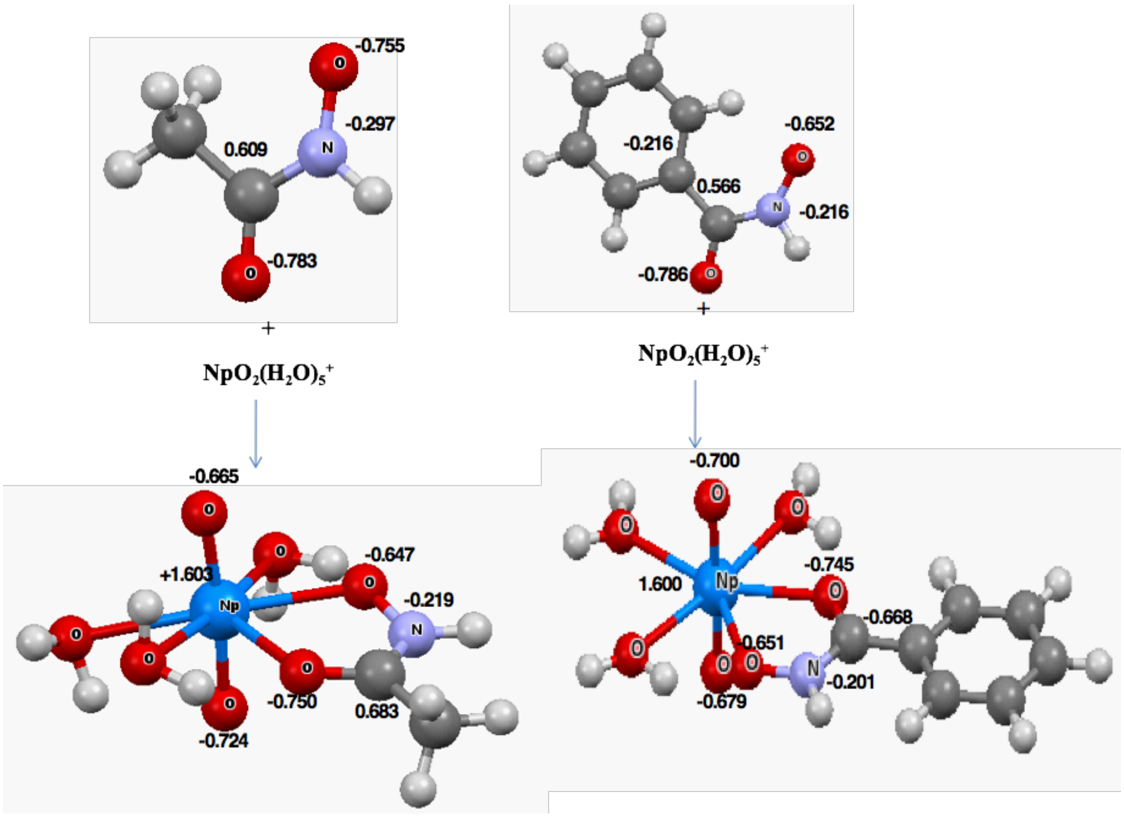

Figure 6.13: Complexation of Np(V)-AHA and Np(V)-BHA (colour variation: violet - nitrogen atom, grey - carbon atom, blue -neptunium, pink - hydrogen atom, red- oxygen atom).

Increased interaction of HA with Np(V) decrease the interaction of the latter with remaining coordinated water molecules. Consequently, on complexation with AHA, the average distance of water molecules from Np also increases from 2.566 to 2.584 Å. On complexation of AHA to Np(V), the negative charge on binding oxygen atoms of AHA decreases to a small extent. However, if we calculate the sum of the charges on all the ligand atoms, it decreases from $-1e^-$ in free ligand to about $-0.5e^-$ in Np-AHA complex. This observation is in contrast to that reported in U(VI)-HA complexation where -0.8e charge is retained by ligand after complexation [182].

6.4.2.3. Comparison of Np-AHA and Np-BHA

Table 6.5 shows that ΔE_{C1} for Np(V) complexation with AHA is more negative than that with BHA. The higher affinity of AHA for Np(V) can be understood in terms of electrostatic binding. Figure 6.13 shows higher negative charge on both the binding oxygen atom of AHA compared to that on BHA. The stronger electrostatic interaction of AHA compared to BHA for Np(V) results in shorter metal ligand bond distances (Np-O_L). The experimental data of log K for Np-AHA is not available in literature for comparison. However, the data on U(VI) complexation with HA shows higher log K for AHA than that for BHA which is in line with trend in calculated ΔE_C for Np-HA complexes. As shown in figure 6.13, the minimum energy structure of BHA molecule is more pre-organized for binding with $NpO_2(H_2O)_5^{+}$. The higher negative energy ΔE for Np-BHA shows the dominant electrostatic effect in determining the ΔE_{C1}. The complexation energies of the Np-AHA and Np-BHA have also been calculated using continuum model, which also corroborates the relative stabilities of the complexes.

6.4.2.4. Coordination Modes of SHA to Np(V) in 1:1:1 Complex

Due to the presence of ortho phenolic group in SHA, there are various possible binding geometries for Np- SHA, such as,

I) Binding of Np(V) to SHA by carbonyl and hydroxyl oxygen atoms of hydroxamate moiety labeled as Np-SX

II) Binding of Np(V) to SHA through hydroxyl oxygen atoms of hydroxamate moiety and ortho-phenolic group, labeled as Np-SY.

III) Binding of Np(V) to SHA through deprotonated nitrogen of hydroxamate moiety and oxygen atom of phenolic group, labeled as Np-SZ.

The optimized structure of the free SHAH- molecule and that of different binding modes in 1:1:1 complexes of Np(V) are given in figure 6.14. The complexation energies for all the binding modes are given in table 6.5 and charges on atoms of binding group are given in table 6.6.

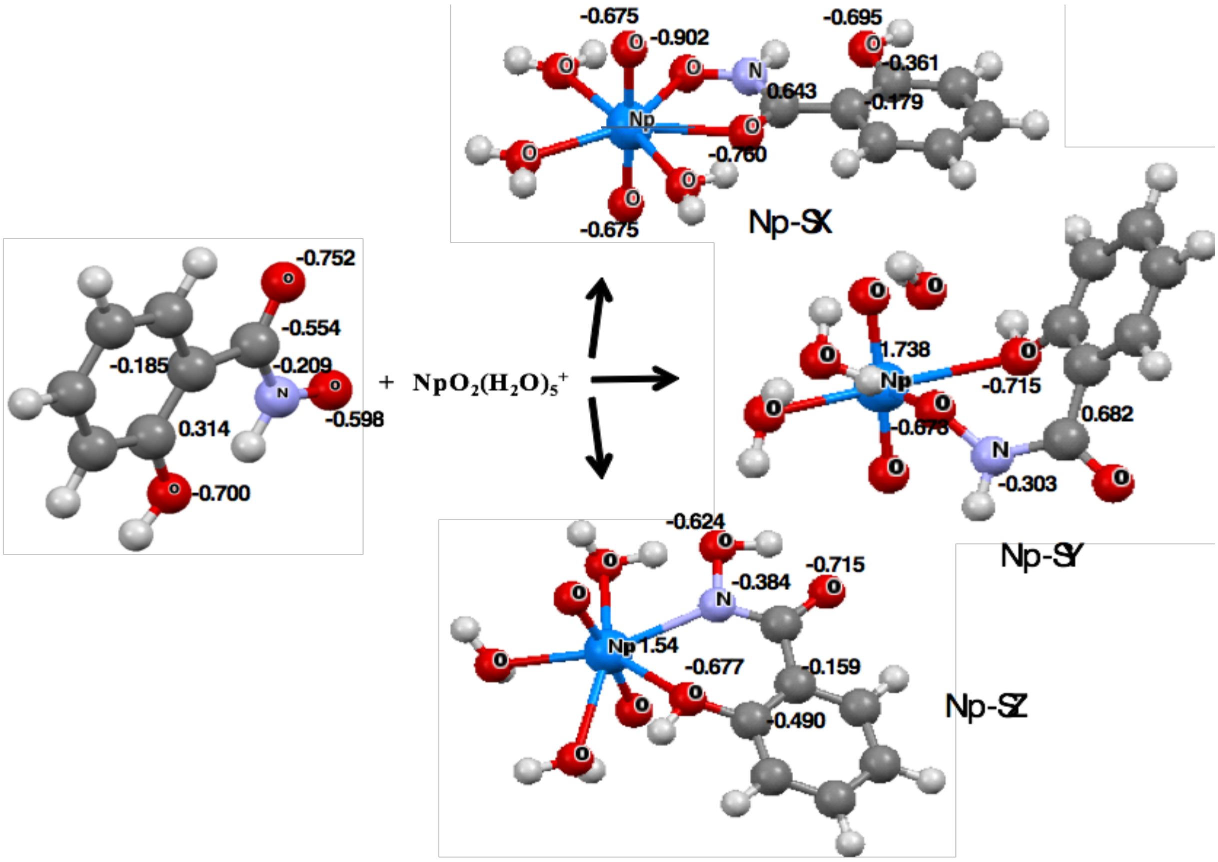

Figure 6.14: Complexation of 1:1:1 complexes of Np-SHA (colour variation: violet - nitrogen atom, grey - carbon atom, blue -neptunium, pink - hydrogen atom, red- oxygen atom).

Table 6.6: Charges on Np atom, axial oxygen atoms, NpO_2 moiety and on total ligand atoms in different geometries

Geometry	**Np**	**O_{ax}**	**NpO_2**	**Ligand Charge**
Np(V)	2.229	-0.115, -0.115	1.999	-------
$NpO_2(H_2O)_5^+$	1.684	-0.666, -0.665	0.353	-------

Np-AHA	1.603	-0.665, -0.724	0.214	-0.540
Np-SX	1.616	-0.674, -0.675	0.266	-0.567
Np-SY	1.728	-0.652, -0.752	0.334	-0.537

6.4.2.5. Comparison of Np-SX and Np-SY Binding Modes

Among the two binding modes involving both O atoms from SHA, Np-SY is the most stable geometry. It is interesting to note that in the optimized structure of Np-SY, two water molecules are directly coordinated to Np at distance 2.785 and 2.449 Å, whereas the third water molecule moves away from first coordination sphere of Np(V). This reduction in coordination number is in contrast to other geometries for 1:1:1 complex optimized in the present work (figure 6.14). Four coordination in equatorial plain have been reported for Np(V) [404]. The removal of a water molecule can be attributed to larger angle (74.31°) exhibited by SHA molecule while forming seven membered ring on Np-SY compared to five membered ring in Np-SX (64.99°). Similar correlation in ring size of chelate and dehydration has also been observed by Kirishima et al [275]. Removal of one water molecule from coordination sphere of Np(V), results in increase in the charge on Np atoms as well as its interaction with ligand atoms which, in turn, leads to decrease in average value of Np-O_L bond. The shorter Np-O distance from ligand increases its interaction with the Np, thereby making it the most stable geometry.

6.4.2.6. Linear Free Energy Relationship

Figure 6.15a shows the linear correlation between theoretically calculated interaction energies for binding with Np(V) ion (ΔE_C) and proton (ΔE_P) which further supports electrostatic binding in Np-HA complexes. Figure 6.15b, shows the linear relationship between log K_1 and Z_{eff} for various actinides and HA reported in literature. The higher log K_1 for SHA than that expected from LFER also supports the different mode binding in Np-SHA from that in simple HA. The extra stability of the complex could be due to formation of more stable binding geometry involving ortho phenolic group. Thus, minimum ΔE for Np-SY geometry for 1:1:1 complex supports the experimental data reported in the literature.

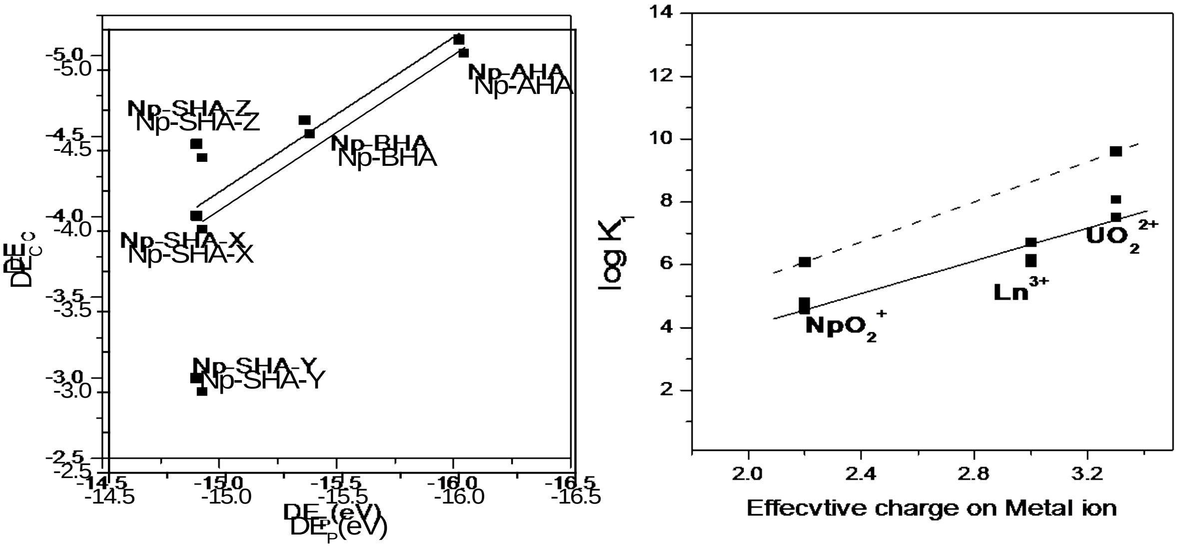

Figure 6.15: Linear free energy relationship between (a) ΔE_P Vs. ΔE_{C1} (left) and (b) Z_{eff} Vs. log K_1 (right) (Dashed line for actinide-SHA complexes).

6.4.2.7. Np-SHA 1:2:2 Complexes

Similar to 1:1:1 complex, the 1:2:2 complex is formed by complexation of Np(V) with two salicylhydroxamate molecules in which the ortho hydroxy group is in protonated form. In the case of 1:1:1 complex, the stability of the different geometries was discussed mainly in terms of electrostatic interactions which depends on bond distance and charges on different atoms. In the case of 1:2:2, other than above factors, the steric constraints are expected to play important role. In order to optimize the structure of 1:2:2 complexes, initially the 1:1:1 complex was assumed to bind in SY mode which has minimum energy and then different binding modes of the second ligand to 1:1:1 complex were evaluated. The coordination by second ligand was investgated in three different modes SX, SY and SZ. Figure 6.16 shows optimized geometries for all the three complex structures.

The stepwise as well as cumulative complexation reactions and respective interaction energies can be given by the following equations

$NpO_2(SHAH)(H_2O)_3 + SHAH^- \rightarrow NpO_2(SHAH)_2(H_2O)^- + 2\ H_2O$ (6.6)

$\Delta E_{S2} = E_{NpO2(SHAH)2(H2O)-} + 2\ E_{H2O} - E_{NpO2(SHAH)(H2O)3} - E_{SHAH-}$ (6.7)

$NpO_2\ (H_2O)_5^+ + 2\ SHAH^- \rightarrow NpO_2(SHAH)_2(H_2O)^- + 4\ H_2O$ (6.8)

$\Delta E_{C2} = E_{NpO2(SHAH)2(H2O)-} + 4\ E_{H2O} - E_{NpO2\ (H2O)5+} - 2\ E_{SHAH-}$ (6.9)

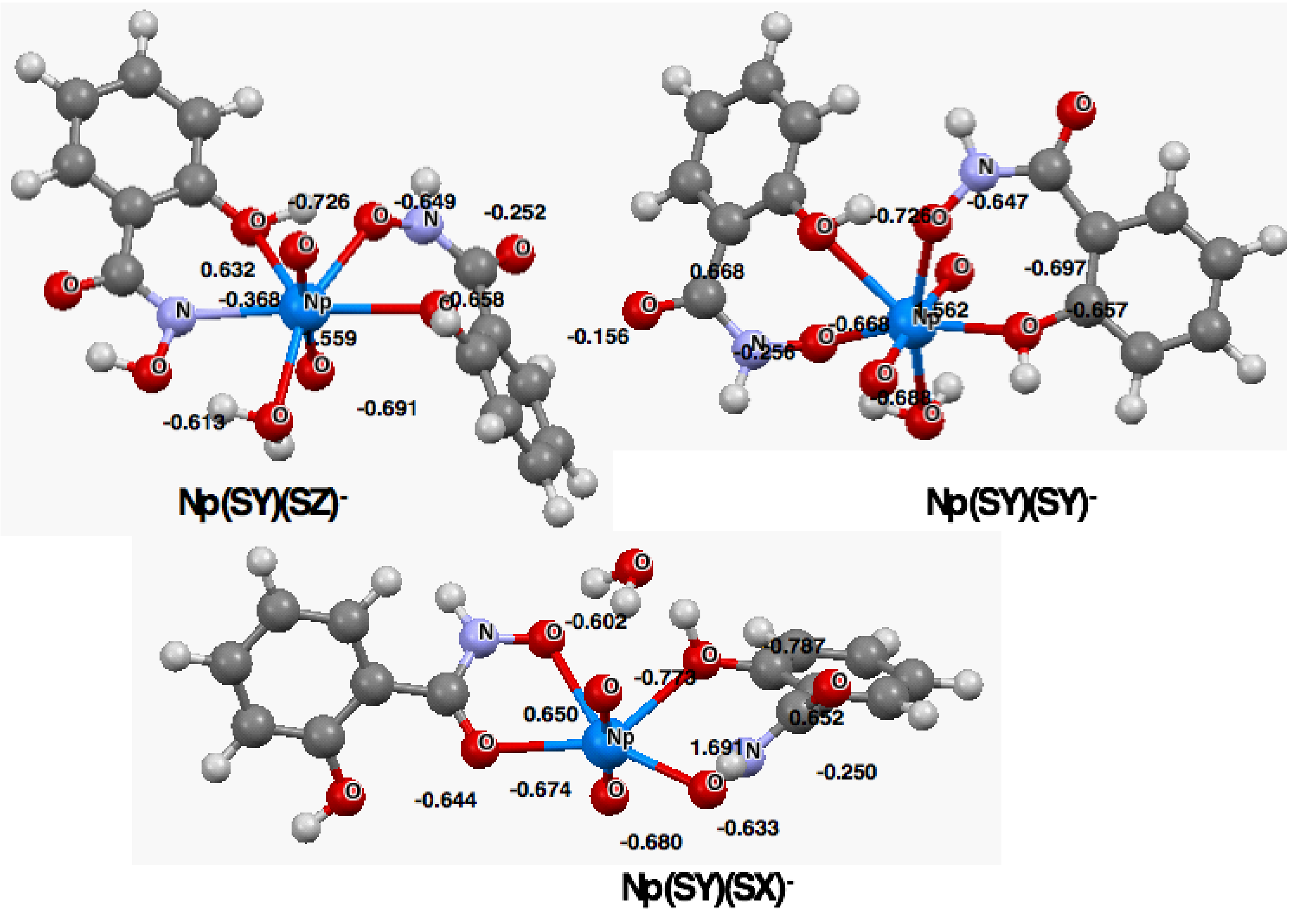

$Np(SY)(SZ)^-$ $Np(SY)(SY)^-$

$Np(SY)(SX)^-$

Figure 6.16: Optimized geometries of 1:2:2 complexes of Np-SHA (colour variation: violet - nitrogen atom, grey - carbon atom, blue -neptunium, pink - hydrogen atom, red- oxygen atom).

The calculated energies and geometrical parameters for 1:2:2 complex are given in table 6.7 and 6.8 respectively. In all the three geometries the stepwise ΔE_{S2} are less negative than ΔE_1 for Np-SY. This suggests the weaker affinity of second ligand in SY mode compared to the first, which can be explained by reduced charge on Np atom. The reduction in charge on Np decreases its affinity for the second ligand. This behavior has been experimentally observed for complexation of lanthanides and actinides [407].

Table 6.7: Interaction energy for overall complexation (ΔE_{C2}) and stepwise complexation (ΔE_C) for 1:2:2 complexes of Np-SHA

Complex Mode	**ΔE_{C2}**	**ΔE_{S2} (Stepwise)**
$NpO_2(SY)(SZ)^-$	-5.72	-1.14
$Np(SY)(SY)^-$	-5.54	-1.09
$Np(SY)(SX)^-$	-5.98	-1.52

Table 6.8: Selected bond distances, d (Å) and bond angles (in degrees) of Np-SHA (1:2:2) complexes

Complex Mode	**Ligand 1**		**Ligand 2**		
	***d*Np-O_L**	**O_L-Np-O_L**	***d*Np-O_L**	**O_L-Np-O_L**	**d_{Np-OW}**
$Np(SY)(SZ)^-$	2.471, 2.655 (2.563) (SY)	64.62 (SY)	2.490, 2.498 (2.494) (SZ)	66.17 (SZ)	2.588
$Np(SY)(SY)^-$	2.574, 2.365 (2.470) (SY)	70.79 (SY)	2.472, 2.586 (2.529) (SY)	59.61 (SY)	2.650
$Np(SY)(SX)^-$	2.519, 2.267 (2.393) (SY)	73.35 (SY)	2.530, 2.489 (2.510) (SX)	65.69 (SX)	

The stability of the different binding geometries for 1:2:2 complexes follows the order $Np(SY)(SX)^-$ > Np(SY)(SZ) > $Np(SY)(SY)^-$. Contrary to the energetics of 1:1:1 complexation where SY binding geometry is the most preferred, the same binding mode is the most unfavorable for 1:2:2 complex formation. The bond angles subtended by two SY^- at the centre are about 70° and 60° that are smaller than the angle (74°) made by SY in 1:1:1

complex resulting an unstable geometry containing the two sterically strained seven membered rings. Also, in presence of ligand coordinated to Np in SY mode, the Np-O_L bond distance for second ligand is maximum for Np(SY)(SY)$^-$ geometry which is responsible for reduced electrostatic interaction between Np and ligand. The ΔE for Np(SY)(SX)$^-$ is marginally more negative than that in Np(SY)(SZ)$^-$ which can be attributed to lower Np-O_L distance (2.393 A^0) and less strained seven membered ring of Np(SY) (O_L-Np-O_L 73.350°) in the former.

6.4.2.8. Np-SHA 1:2:0 complexes

Np(V) forms 1:2:0 complexes with two molecules of completely deprotonated SHA (both ortho hydroxyl and –NH-OH group are deprotonated), which was observed by Moll et al. in spectrophotometric study [303]. The formation of 1:2:0 stoichiometric complex is possible only for complexes involving ortho hydroxyl group in binding. The two modes involving hydroxyl group viz., SY and SZ are considered for second ligand. Similar to 1:2:2 complexes, SY mode is assumed for first ligand and SZ and SY modes of second ligand were evaluated for calculations. Figure 6.17 gives the optimized structure for 1:2:0 complexes. The ΔE_C for 1:2:0 complexes were found to be more negative than 1:2:2 complexes in same mode (table 6.8). This explains the higher tendency for forming complexes having deprotonated hydroxyl group. Interestingly, in the optimized structure of 1:2:0 complexes, the only water molecule coordinated to it moves away from the first coordination sphere of the Np (figure 6.16). Also, the average distance of ligand donor atoms decreases in comparison to that in their corresponding protonated 1:2:2 complexes. The reduction in coordination number of Np atom in 1:2:0 complexes decrease the ring strain in the ligand. This is evident from the O_L-Np-O_L angles of nearly 72°for 1:2:0 complexes.

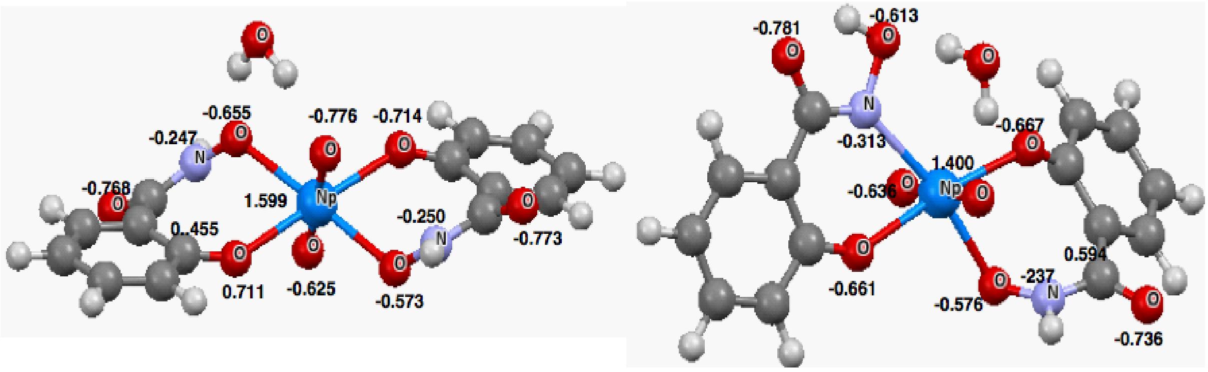

Figure 6.17. Optimized geometry of 1:2:0 complexes of Np-SHA (colour variation: violet - nitrogen atom, grey - carbon atom, blue -neptunium, pink - hydrogen atom, red- oxygen atom).

Despite higher negative charge on deprotonated ligands (-2.0 e), the total charge transferred from ligand atoms is nearly 0.5 e which is nearly same in 1:1:1 as well as 1:2:2 complexes. However, higher negative charge on ligand allows closer approach of donor atoms thus resulting in shorter Np-O_L. The higher stability of 1:2:0 complexes can be attributed to the combined effect of reduced Np-O_L distance and reduced strain on the ring.

6.5. Conclusions

The Np(V) forms ML and ML2 complexes with pyridine monocarboxylates viz. picolinate, nicotinate and isonicotinate, by mainly electrostatic interactions. Among the three geometrical isomers the picolinate forms strongest complex through five membered chelate formation. In case of nicotinate and isonicotinate, the binding is through carboxylate group but enhanced stability than expected from pKa values of carboxylate groups is attributed to the charge transfers from nonbonding nitrogen. The higher charge transfer from nitrogen in para position (isonicotinate) reflects in its higher stability constant and λmax shift compared to nicotinate. The trend in stability constants and charge polarization in ligand molecules on complexation has been supported by theoretically calculated binding energies and the charges on individual atoms.

The present work also gives a detailed theoretical analysis of complexation of Np(V) ion with hydroxamate ligand. The role of substitution in hydroxamate on complexation was understood by carrying out DFT calculations on Np(V)-AHA, Np(V)-BHA and Np(V)-SHA complexes. The charges on atoms and geometrical parameters like bond angles and bond distances are used to rationalize the energetic of complexation reaction. The results revealed the dominant role of electrostatic interaction in determining the complex stability. In Np-AHA, the acetyl group increases the electron density on donating oxygen atoms compared to phenyl group in BHA, thereby making it more stable. Among the various binding modes of Np-SHA on 1:1:1 complexes, the one involving ortho hydroxyl group and hydroxyl group of hydroxamate moiety is most stable whereas in 1:2:2 complex geometries, steric constraints play the dominant role making the geometry involving hydroxamate moiety only (forming five membered ring) as most stable for the second ligand. The calculated results corroborated the experimentally obtained stability constants.

Chapter 7

The Solubility of Th(IV) - The Effect of pH, Ionic Strength and Colloid Formation

7.1. Introduction

In the present chapter, the results of the studies on solubility of Thorium in aqueous solution under varying experimental conditions have been presented. The focus has been mainly on the determination of concentration of metal ion present in the form of colloids, which if not corrected may increase the solubility by several orders of magnitude. Actinide ions with higher oxidations state, particularly tetravalent ions, (pentavalent and hexavalent actinides exist in aqueous solution as actinyl ions and hence are not prone to hydrolysis) undergo hydrolysis, which eventually leads to formation of polymeric species via, -oxo-bridging and ultimately intrinsic colloids. [134]. The size, composition, and structure of actinide intrinsic colloids depend on mode of formation, their source, and history [135-136]. Depending on the size and surface charge present, the actinide colloids can either enhance or retard the migration of actinides in the aquatic environments [137]. Thus, it is essential to take into account the intrinsic colloids for accurate prediction of the migration rates of actinides in geosphere [138]. The literature on the source, formation and interaction of colloids as well as their role in the migration of actinides has been reviewed by Walther and Denecke recently [139].

All the actinides from thorium to californium form tetravalent species in aqueous solution but thorium is found in aqueous solution only in the +4 oxidation state and is often used as analogues for Np(IV) and Pu(IV) behavior [66]. Th(IV) can undergo hydrolysis and polymerization reactions to form colloids depending on metal ion concentration, temperature, and the presence of other ions [59]. The colloidal thorium dioxide is also used as a contrasting agent in vascular radiography in gastroenterology, bronchography and pyelography [408]. Neck and Kim reviewed the literature data on hydrolysis of tetravalent actinides and applied semi-empirical formulations with known stability constants of mononuclear hydrolysis products of these actinides to estimate the solubility products of tetravalent actinide hydroxides and hydrous dioxides and compared with the reported literature values [194]. The literature reported solubility data show considerable discrepancies (log K_{SP} varies from -45.5 to -54.2) for amorphous Th(IV) precipitates either as tetra hydroxides ($Th(OH)_4$) or as hydrous oxides ($ThO_2.xH_2O$) [189-194, 409-411]. This could be attributed to to formation of thorium precipitate with varying chemical composition, which were referred to as hydrated oxyhydroxide $ThO_n(OH)_{4-2n}.xH_2O(am)$ with $0 \leq n \leq 2$ depending on the preparation method, pre-treatment, alteration, and temperature. Furthermore, the presence of colloids can also explain the widely scattered Th(IV) concentrations measured in the various solubility studies [412].

Walther has reviewed different methods and techniques used to characterize the thorium colloids and discussed their suitability in terms of detection limits (for size and concentration of colloids), ease of sample preparation, methodology formulations, in-situ and offline determination, and the nature of analysis (destructive or non-destructive) [413]. The actinide colloids in aquatic media are often detected by absorption spectroscopy, light scattering methods, and by laser-induced breakdown detection (LIBD) [139]. LIBD is a new and the most sensitive method for the quantification of aquatic colloids of lower range nanometre size (<50 nm) in very low concentrations (ppb to ppt), which cannot be detected by conventional light scattering methods [414]. Kim et al have extensively used LIBD technique for characterization of actinide colloids to understand their genesis, formation and migration effects under various geochemical environments [415]. Bitea et al used LIBD in combination with ultra-filtration to investigate the generation of Th(IV) colloids in the concentration range from 10^{-5} to 10^{-2} M thorium nitrate solutions at pH 2.7-4.1 in 0.5 M

NaCl and found that the generated thorium colloids are stable up to 400 days of investigation, without a tendency towards agglomeration or precipitation [416]. Rothe et al characterized the thorium colloids under the similar conditions by X-ray absorption fine structure (XAFS) spectroscopy and LIBD and the solubility data determined was found to be several orders of magnitude lower than the values for amorphous Th(IV) hydroxide or hydrous oxide [411, 416]. Bundschuh et al. applied LIBD to determine the solubility product of Th(IV) in acidic solutions in 0.5 M NaCl at 298 K and concluded that the literature reported data on thorium solubility for amorphous Th(IV) hydroxide or hydrous oxide can be attributed to the exclusion of polynuclear or Th(IV) colloids of very small size in estimating the solubility products [417].

In the present work LIBD was used to study the size and concentration of Thorium colloids in aqueous solutions under varying experimental conditions, viz., pH, ionic strength, presence of complexing anions, etc. To best of our knowledge no reports were available on studies on the colloid determination of Th(IV) solution in aqueous perchlorate media over a range of ionic strength and hydrogen ion concentration over a long period of equilibration (~1080 days). The objective was to investigate the contribution of colloids in the solubility of Th(IV) in perchlorate media under varying conditions of ionic strength (0, 0.1, 0.5 and 1.0 M $NaClO_4$), and pH (5-13). The dynamic light scattering (DLS) for the determination of size of collides formed and LIBD technique was employed for both size and concentrations of the colloid formed in the equilibrated supernatant solutions of the thorium samples. High temperature thermo-gravimetric differential scanning calorimetry (HT-TG-DSC), thermogarvimetric - differential thermal analysis- Evolved gas analysis (TG-DTA-EGA) and X-ray diffraction (XRD) techniques were utilized to characterize the resultant precipitate formed in the equilibrated Th(IV) perchlorate samples.

7.2. Experimental

7.2.1. Reagents

Nuclear grade $Th(NO_3)_4.4H_2O$ (IRE, India) was dissolved in water and $Th(OH)_4$ (s) was precipitated by adding NaOH. The precipitate was centrifuged, washed with water and re-dissolved with an excess of perchloric acid. The precipitation and dissolution were repeated three times. The Th(IV) concentration in the stock solution was determined by EDTA titration using xylenol orange as an indicator. Details of the preparations of other solutions, viz., acid and base for pH adjustment as well as $NaClO_4$ for ionic strength adjustment are given in chapter-2. All the preparations and adjustment of pH and ionic strength were done under inert nitrogen atmosphere.

7.2.2. Sample Preparation

All the samples were prepared in 30 mL Oak Ridge centrifuge tubes. Oversaturation method was employed for the sample preparations in which excess of thorium perchlorate solution was equilibrated with the solution of desired pH and ionic strength. Each tube contains 10 mL of 0.01 M (2320 ppm or μg/mL) thorium perchlorate solution under various pH (5 to 11) and ionic strength (0 to 3 M $NaClO_4$). All the samples were prepared under inert atmosphere (nitrogen purging) at 298 K. All the samples initially kept at various pH and ionic strength were labeled with different labels as (A to D) - (1 to 5) for easier tabulation and analysis of results, where A to D and 1 to 5 represent the ionic strengths and the initial pH of the samples respectively. The details of labels are given in table 7.1.

Table 7.1: Description of sample labels. (within the parenthesis are the labels assigned for the different ionic strengths and pH of the samples).

Initial pH → Ionic Strength ↓	5 (1)	7 (2)	9 (3)	11 (4)	13 (5)
0.0 M $NaClO_4$ (A)	A1	A2	A3	A4	A5

0.1 M $NaClO_4$ (B)	B1	B2	B3	B4	B5
1.0 M $NaClO_4$ (C)	C1	C2	C3	C4	C5
3.0 M $NaClO_4$ (B)	D1	D2	D3	D4	D5

7.3. pH Measurements

As discussed in chapter-2, the adjustment and measurement of pH was done by an autotitrator Metrohm (Model no. 716 DMS Titrino). The ionic strength in all the solutions was maintained by using $NaClO_4$ as an electrolyte. The pH meter was calibrated by standard pH buffers in the range of 4-10. Electrode calibration was done by titration of standard (~0.05M) $HClO_4$ with standard (~0.1M) NaOH solution. Glee software was used to obtain the values of E^0, slope and carbonate impurity in alkali [216].

7.4. Ion Chromatography (IC)

The ion chromatographic system consisted of a Dionex GP50 gradient pump (Dionex, USA), a PEEK made six-port Rheodyne injector (9275i) fitted with a 100 mL PEEK sample loop. The analytical column used was IC-Pak (4.650 mm) cation column (Waters). The post column reagent addition system consisted of a Dionex PC 10 pneumatic controller with reagent reservoir, a zero dead volume PEEK tee and a reaction coil (375 mL). Pyridine-2,6-dicarboxylic acid (PDCA) (5×10^{-4} M) in combination with KNO_3 (0.02 M) in 5% methanol was used as eluent and an UV-VIS absorption detector (model: AD20, Dionex) was used for detecting the peaks at 656 nm after post column addition with arsenazo III. The instrument was calibrated with the standard thorium solutions prepared by dilution of the stock solutions of Th^{4+} (1000 mg L^{-1}, Sigma Aldrich) with 1 M HNO_3.

7.2.5. Inductively Coupled Plasma - Mass Spectrometry (ICP-MS)

A VG Plasma Quad PQ II (V. G. Elemental, Winsford, Cheshire, England) ICP-QMS was used for the determination of thorium concentration. Sample introduction was carried out by pneumatic nebulisation using a Meinhard concentric nebulizer, a double-pass

Scott-type spray chamber cooled to 10^0 C with a locally made recirculating chiller, and a Fessel-type torch. The solution flow rate was controlled by a peristaltic pump (sample uptake rate: 1 mL min-1). The ICP-QMS conditions were optimized for maximum sensitivity and calibrated using a 100 ng mL^{-1} tuning solutions of Li, Be, Al, Ti, C, Sr, In, La, Bi, Th, and U. The mass analysis was carried out using a quadrupole mass analyzer having a mass range of 1-300 amu with a resolution of 0.3 amu. The standard solutions used for the calibration procedures were prepared by dilution of the stock solutions of Th(IV), 1000 mg L^{-1} with 1 M HNO3.

7.2.6. Dynamic Light Scattering (DLS)

Malvern Zetasizer Nano-ZS analyzer which is based on dynamic light scattering (DLS) method was used for the particle size distribution in various supernatants of thorium samples. This device measures the time dependent fluctuations in the scattering intensity of light to determine the rotational diffusion coefficient, and subsequently the hydrodynamic diameter by the Stokes-Einstein equation. Each measurement consisted of 3 subsequent individual runs of which the average result was calculated. Measurements were conducted at 25.0º C and the light scattering was detected at 173 degrees. The data obtained by the Malvern Zetasizer Nano-ZS analyzer was exported into Microsoft Excel for further analyses. The performance of DLS was checked by measuring the size of standard polystyrene particles with mean diameter of 20, 60 and 100 nm (Thermo Scientific™ 3000 Series Nanosphere™ Size Standards) and the results were found to be in good agreement with the certified values.

7.2.7. Laser Induced Breakdown Detection (LIBD)

The present studies used an LIBD system called MAGELLAN developed by Cordouan Technologies (France) in collaboration with the Karlsruhe Institute of Technology (KIT), Germany. The plasma events are detected in the cell by acoustic method where an acoustic sensor (piezoelectric transducer) is connected to the sample cell and the plasma is detected by the acoustic wave emitted during the plasma expansion into the liquid [260]. Preliminary calibration made with standards colloids (latex) of known size and concentrations to determine the size and concentration of colloids in the unknown sample. The details of calibration procedures were given in chapter 2.

7.2.8. High Temperature Thermogravimetric Differential Scanning Calorimetry (HT--TG-DSC)

Thermo-Gravimetric Analyses (TGA) and Differential Thermal Analyses (DSC) of the precipitate were carried out in DSC-2, supplied by M/s Mettler Toledo Pvt Ltd, Switzerland. The TGA profiles of precipitates were recorded from 25^{o} C to 1200^{o} C with heating rate of 10 K min^{-1}. High purity argon with a flow rate of 20 mL min^{-1} was used as ambient. To compare the precipitate of equilibrated thorium samples, a blank was also run in TG-DSC with the freshly prepared amorphous thorium hydroxide by addition of ammonia to thorium nitrate solution.

7.3. Results and Discussion

The long equilibrated thorium samples were centrifuged at 16,500 rpm for one hour and the supernatant was separated to analyze the dissolved thorium species. The supernatant solutions were subjected to pH measurements, DLS measurements for size of colloids and LIBD for both the size and concentration of the colloid particles. The fractionation of supernatant to ionic part (determined by ion chromatography - Th_{IC}), Colloidal thorium (determined by LIBD - Th_{LIBD}) and polynuclear species (Th_{Total} - Th_{IC} - Th_{LIBD}) was done to categorize the soluble thorium into various speciation forms.

7.3.1. pH Measurements

The measured pH for all the samples kept at various initial pH and ionic strengths after an equilibration of ~1080 days are given in table 7.1. The formation of polynuclear species through condensation of smaller hydrolyzed species can occur according to two mechanisms, olation where hydroxyl bridges are formed, and oxolation where oxo bridges are formed [418]. Hydroxide-bridged polynuclear complexes have been observed for actinide cations and the tendency toward polymer formation is a function of the charge density of the actinide cation [66]. The initially formed hydroxo-bridged thorium polynuclear hydroxides would proceed through formation of either single or double oxygen bridged thorium polynuclear species, the latter evicts a H^+ ion from each of hydroxyl bridge (figure 7.1). This would subsequently result in the formation of colloids or precipitate depending on the initial conditions of equilibration like pH and ionic strength. The colloid formation through double oxygen bridged thorium networking would result in an increase in hydrogen ion concentration (or decrease in pH) at the end of equilibration period.

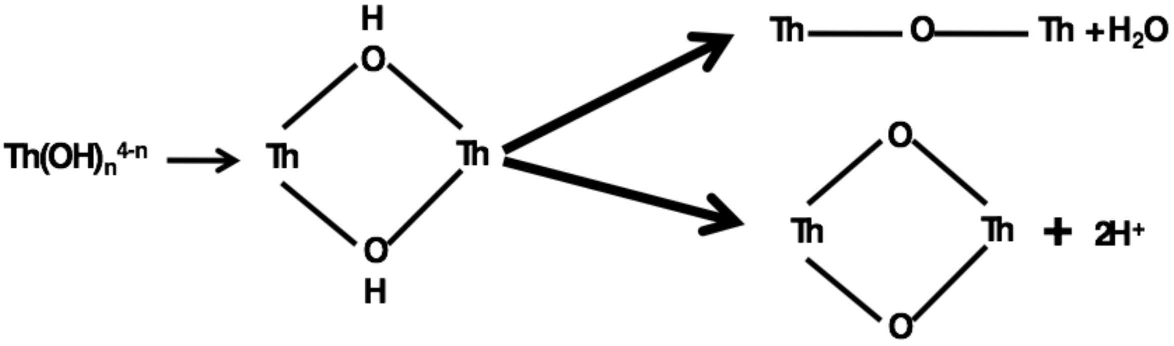

Figure 7.1: Schematic representation for the mechanism of polynucleation of Th(IV) in aqueous perchlorate solutions.

The measured pH of all the thorium samples after equilibration period are given in table 7.2. In the present studies, the pH of all the samples initially kept at pH 5, 7 and 9 at all ionic strengths were found to have decreased to a range of 2.69 to 3.66 indicating the release of H^+ ion. This can be possible only when thorium forms double oxo-bridging polynuclear chains leading to the formation of colloids by release of H^+ ions.. Further, the drop in pH is more for the samples at high ionic strength than at lower ionic strengths. The samples initially kept at pH 11 except the sample at I = 3.0 M $NaClO_4$ showed relatively less change in pH after equilibration than those samples which are initially kept at pH 5, 7 and 9. The samples at an initial pH of 13 kept at I = 0 and 0.1 M $NaClO_4$ showed a small variation in pH after equilibration, while the samples at initial pH of 11 at I = 3.0 M $NaClO_4$ and samples at initial pH of 13 kept at I = 1.0 and 3.0 M $NaClO_4$ showed no change in pH after equilibration. This small or no variation in pH after equilibration period could be attributed to the formation of stable $Th(OH)_4$ precipitate during the time of initial pH adjustment of these samples.

Table 7.2: The measured pH values of different Th(IV)-perchlorate samples after an equilibration period of ~1080 days.

Initial pH → Ionic Strength ↓	5	7	9	11	13
0.0 M $NaClO_4$	2.87	2.98	3.30	6.18	12.17
0.1 M $NaClO_4$	2.88	3.04	3.33	6.84	12.46
1.0 M $NaClO_4$	2.86	2.90	3.66	8.48	13.00
3.0 M $NaClO_4$	2.69	2.85	3.09	11.00	13.00

7.3.2. Fractionation of Soluble Thorium Present in Supernatant Solutions

The soluble thorium in supernatant may be present either as (i) Th^{4+} aqua ion, (ii) as polymeric thorium hydroxide species or (iii) as dissolved eigen colloids. The concentration of ionic thorium as Th^{4+} ion was determined by ion chromatography analysis using arsenazo (III) as chromogenic reagent. For the determination of total thorium concentration in the sample, ICP-MS technique was used. Typical chromatograms showing the thorium peaks for standard and sample solutions are given in figure 7.2, which unambiguously detects Th^{4+} in the supernatant.

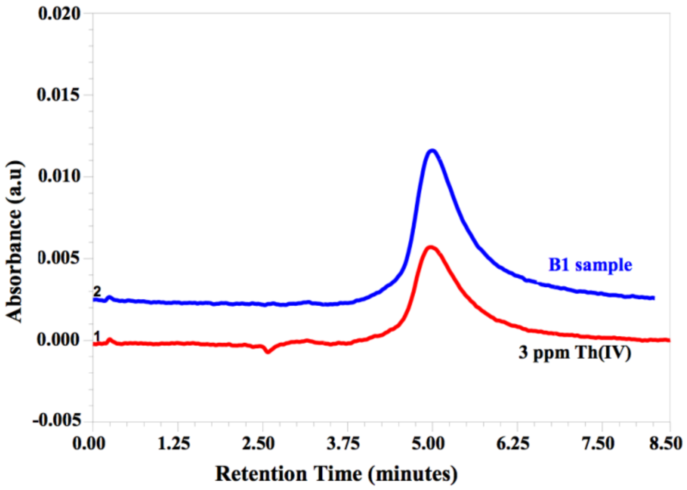

Figure 7.2: Typical chromatograms showing Th(IV) peaks for standard (3 µg/mL) and sample (B1) solutions. (Conditions : Column : NS-1, Eluent: 0.5mM PDCA + 0.02 M KNO_3 in 5%, MeOH, pH-4, Flow Rate: 1mL/min, Detection: Absorbance at 656 nm, PCR: 4.5 × 10^{-4} M arsenazo-III)

Table 7.3 shows the results of IC and ICP-MS analysis for the supernatant of all the thorium samples after equilibration period. The total content of thorium and as Th^{4+} in supernatant follow a descending order with the increase in initial pH of the sample, due to enhancement in precipitation process with increasing pH. The overall thorium content present in supernatant of the samples kept at an initial pH of 11 and 13 at I = 1.0 and 3.0 M $NaClO_4$ was below detection limits for both the IC and ICP-MS analysis indicating a complete precipitation of the entire thorium kept for equilibration. The samples kept at zero ionic strength (A4 and A5) showed very low amount of thorium as Th^{4+} (1.5 and 0.3 µg/mL respectively at an initial thorium of 2320 µg/mL in the sample). The difference in the thorium concentrations determined by ICP-MS and starting concentration of thorium (2320 µg/mL) is equal to precipitated Thorium, while the difference in thorium content determined by ICP-MS and IC would give the amount of thorium (ICP MS - IC) present in a form other than precipitate or as Th^{4+} in the supernatant, and hance may be attributed to polymeric and colloidal form.

Table 7.3: The amount of thorium present in supernatant determined by IC and ICP-MS. All concentrations are in ppm (µg/mL).

Sample	**ICP MS**	**IC**	**ICP MS - IC**
A1	224.30	56.4	167.9
A2	181.80	38.1	143.7
A3	111.60	26.1	85.5
A4	2.00	1.5	0.5
A5	0.90	0.3	0.6
B1	181.24	80. 8	100.4
B2	114.45	8.3	106.1
B3	100.28	2.9	97.4
B4	26.13	0	26.1
B5	1.033	0	1.0
C1	182.99	78.8	104.2
C2	170.48	43.0	127.5
C3	25.43	0	25.4
C4	0	0	0
C5	0	0	0
D1	124.11	96.8	27.3
D2	100.80	8.9	91.9
D3	52.31	3.1	49.2
D4	0	0	0
D5	0	0	0

Walther et al used electro-spray ionization mass-spectrometry (ESI-MS), to determine the contribution of various mononuclear, dimeric and polynuclear thorium hydroxide species present in various solutions of thorium (6 x 10^{-6} to 10^{-1} M at pH of 1-4) kept for equilibration for time period varying from a week to 48 days [419]. They found more than 30 different polymeric complexes with the general trend of increasing number of hydroxide ligands with increasing pH. In the present studies the samples were in equilibrium at higher pH than that in their study and further the equilibrium time was also much longer (1080 days). Under such circumstances, the polynuclear species would dominate and which later covert to colloids. So, the difference of ICP-MS to IC can be attributed to the formation of polynuclear species and detectable colloid particles. If the concentration of the colloid particles can be determined, the content of thorium bearing polymeric species that didn't form colloids can be known. For this, LIBD technique was employed to determine both the size and concentrations of the colloid particles present in the samples. Preliminary studies with DLS were carried out to determine the size and polydispersity in the particle size distributions in the supernatants of the samples.

7.3.3. Dynamic Light Scattering Measurements

The samples which are initially kept at pH = 5 (labeled as A1, B1, C1 and D1) irrespective of the ionic strength and all the samples at I = 1.0 M $NaClO_4$ showed a mono dispersed colloid formation whereas all other samples initially kept at pH of 7 and 9 showed two peaks with higher PDI values (0.27-0.58). The thorium samples initially kept at pH 11 and 13 showed no measurable colloid formation after equilibration period when measured by DLS.

Table 7.4: The average diameter (Z_{avg}) along with PDI for the colloids formed in the thorium samples.

Sample	Size (nm)	PDI
20 nm	22	0.08
60 nm	67	0.02
100 nm	102	0.03
B6	20	0.14
B7	12	0.44
B8	12,	0.58
B21	19	0.18
B22	16	0.39
B23	14	0.55
C1	20	0.27
C2	19	0.12
C3	87	0.27
D1	29	0.12
D2	20	0.41
D3	17	0.36

The average diameter along with the corresponding PDI values for the colloids formed in all the samples are given in table 7.4. Though the particle size distribution (PSD) showed a single intense peak in few samples (labeled as A1, B1, C1, C2, C3 and D1), the PDI values (0.12 to 0.27) showa moderately polydisperse distribution type (PDI = 0.1 to 0.4) for the colloids formed. PSD is usually described by overall average (z-average) of particle diameter (size). The Z-average size will only be comparable with the size measured by other techniques if the sample is monomodal but in case of polydisperse solutions (figure 7.3), interpretation of PSD results using z-average might be insufficient and the details of mean intensity size, area intensity percentage of each peak and polydispersity index (PDI) of the thorium samples (labeled as A2, A3, B2, B2, D2 and D3) would be more appropriate to describe the polydispersity of the PSD in z-average (table 7.5).

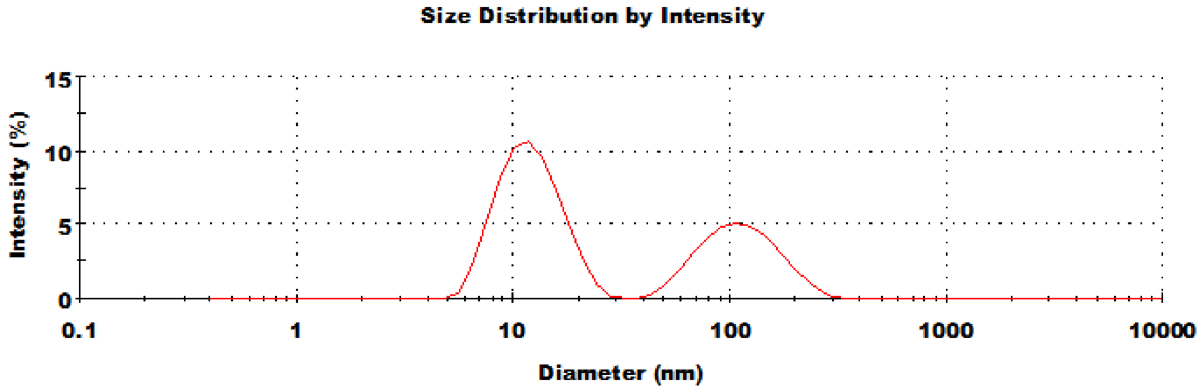

Figure 7.3: Particles size distribution (PSD) graph with two peaks of A2 sample.

Table 7.5: Polydisperse colloid particle size distribution for the equilibrated thorium samples measured by DLS method. (PDI: polydispersity index, mean intensity corresponds to mode of the peak and area intensity corresponds to partial area under the peak of the total distribution)

Sample	**Z_{avg} (nm)**	**PDI**	**Mean Intensity (nm)**		**Area Intensity**	
			Peak 1	**Peak 2**	**Peak 1**	**Peak 2**
B7	17.56	0.44	12.19	118.43	63.00	37.00
B8	24.22	0.58	115.50	11.83	56.00	44.00
B22	18.50	0.39	16.20	102.09	68.30	31.70
B23	45.65	0.55	156.23	13.78	51.66	48.33
D2	24.77	0.42	19.71	125.93	63.33	36.66
D3	134.9	0.52	113.2	16.41	51.00	49.00

DLS technique works without exact knowledge of the sample concentration and the only requirement is that enough light must be scattered to achieve correlation function with significant statistics [420]. The DLS measurements give an insight into the average size and the poly dispersity in particle size distribution for the colloids formed in the thorium samples but not the number of colloid particles present in the supernatants of these samples. The quantitative determination of colloid particles is necessary for fractionating the dissolved thorium content to ionic, polymeric and colloid species which was achieved using LIBD.

7.3.4. Laser Induced Breakdown Detection (LIBD)

The principle of LIBD is described in detail in chapter-2. In short the plot of breakdown probability (BDP) versus pulse energy gives a typical S shape (Figure 2.11) which is characterized by two parameters: breakdown threshold that depends on the particle size only: the bigger the particle size, the lower the threshold (Figure 2.12) and the slope that is related to the colloidal concentration: the higher the particle concentration, the higher the slope (Figure 2.13). Fitting the S curve with calibration data allows to determine the size distribution and the absolute concentration of the colloids in the solution [258].

Bundschuh et al studied the breakdown probabilities of various inorganic reference colloids (alumina, silica and polystyrene) and showed that the thorium colloids can be characterized by calibration of LIBD data with polystyrene reference particles to derive a mean particle diameter and concentration of thorium colloids [417]. The particle size distribution cannot be determined with the present equipment. In this work, polystyrene reference colloids (Thermo Scientific™ 3000 Series Nanosphere™ Size Standards) were used for standard calibration, with mean diameters of (20 to 707 nm). For each reference particle, the concentration are varied over seven orders of magnitude for concentration calibration.

7.3.5. Size and Concentrations of Thorium Colloids

The variation of BDP with laser energy (S-curves) for all the thorium samples which showed the tendency to form colloids are shown in figure 7.4. The closeness of the curves indicates small variation in size and concentrations of the colloids formed in the long equilibrated thorium samples. The breakdown threshold value for colloid formation is defined as the laser energy at which BDP reaches a value 0.01 (Figure 7.5). As the threshold in LIBD is dependent on the diameter of the colloid formed, the comparison of the sample threshold values with those of polystyrene reference standards would give the size of colloids formed in the thorium samples.

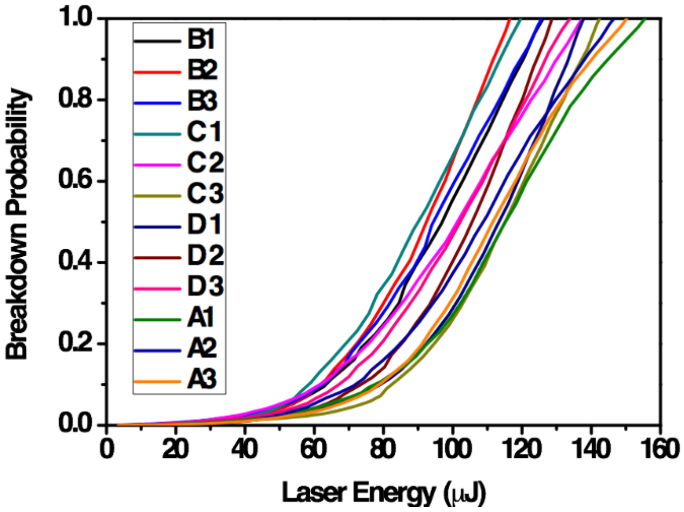

Figure 7.4: The breakdown probabilities of Th(IV) colloids formed in the thorium perchlorate samples kept at various initial pH and ionic strengths for an equilibration of 1080 days.

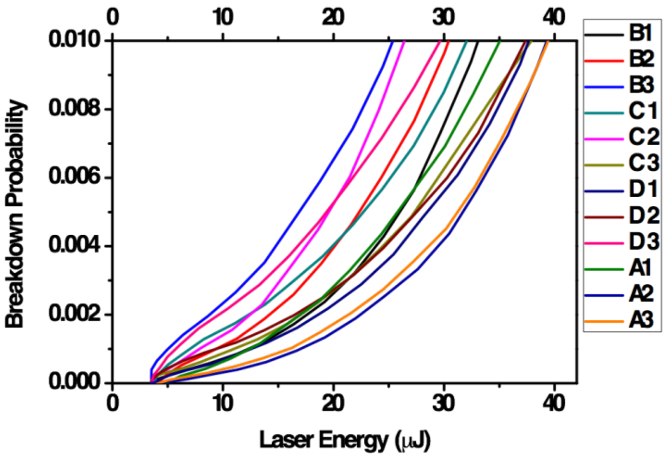

Figure 7.5: The breakdown threshold (0.01 BDP) energies of Th(IV) colloids formed in the thorium perchlorate samples kept at various initial pH and ionic strengths for an equilibration of 1080 days.

The threshold values for all the samples are spread over a range of 25-40 μJ which corresponds to a particle diameter range of 14-37 nm. The average size (diameter) determined by LIBD for the colloid particles formed by thorium under present experimental conditions are given in table 7.6 along with the respective concentrations The table shows that the colloids formed were very small in size (< 40 nm) and low in concentration (at ppb level).

Table 7.6: Size (diameter) and concentration (particles per mL and in ppb - ng/mL) of Th(IV) colloids formed by Th(IV) samples under various pH and ionic strengths.

Sample	Size (nm)	Concentratio (particles/mL)	Concentration (in ppb)	N_{Th} (per particle)	N_{Th} (Total colloids)
A1	21.5 ± 1.6	1.47E+11	56.54	746	1.10E+14
A2	14.9 ± 1.8	1.47E+11	56.54	359	5.26E+13
A3	14.8 ± 1.8	2.15E+11	82.99	351	7.56E+13
B1	24.4 ± 2.2	4.64E+11	178.79	963	4.47E+14
B2	28.7 ± 2.0	2.61E+10	10.05	1327	3.46E+13
B3	36.6 ± 1.8	5.18E+09	2.00	2163	1.12E+13
C1	26.2 ± 2.1	2.15E+10	8.30	1103	2.38E+13
C2	34.9 ± 1.7	1.21E+10	4.67	1963	2.38E+13
C3	17.3 ± 2.5	6.81E+11	262.43	485	3.30E+14
D1	17.6 ± 2.5	1.00E+12	385.19	497	4.97E+14
D2	18.0 ± 2.4	1.00E+12	385.19	523	5.23E+14
D3	29.9 ± 2.0	1.78E+10	6.85	1442	2.56E+13

7.3.6. Fractionation of Soluble Thorium Content

All hydrolyzed solutions contain polymeric species and the weighted average degree of polymerization increases with the degree of hydrolysis. $Th_6(OH)_{15}^{9+}$ is a predominant polynuclear species in the Th(IV)/H2O system, at total Th(IV) concentration exceeding 10^{-3} M (and up to at least 1 M) and for a pH range centered around 4.5–5 [421]. Recently Knope et al studied Th(IV) molecular clusters with a hexa-nuclear Th-Core and found that the distances between adjacent Th atoms range from 3.90 to 3.94 A^0 [59, 422] which is comparable with the typical Th−Th distance (3.94 A^0) in polymers determined by Johansson [423]. In the present studies, total number of Th^{4+} ions (N_{Th}) present in each colloid was calculated by considering the Th-Th atomic distance as 3.94 A^0 [422-423]. The number of Th^{4+} ions present in each colloid particle formed and the total number of Th^{4+} ions towards the total colloid contributions were also given in the table 7.6. From the data on number of Th^{4+} ions as colloids, the total number of Th^{4+} ions as polymeric form can be calculated with the results obtained from IC and ICP-MS analysis of the samples. As IC, ICP-MS and LIBD give thorium content present in the supernatants of the samples as Th^{4+} aqua ions, the total thorium content and colloid contributions, respectively, the subtraction of IC (table 7.3) and LIBD (table 7.6) concentrations from ICP-MS (table 7.3) would give the thorium content, present in a form other than colloidal or Th^{4+} aqua ion form (table 7.7). This amount of thorium, which excludes the colloid contribution, is present as soluble species either in the form of Th^{4+} aqua ions or as polymeric species in the supernatant and contribute to the solubility of thorium.

Table 7.7: The fractionation of total thorium content present in the supernatants as colloidal and non-colloidal forms (ionic and polymeric form of thorium).

Sample	**ICP MS - IC (part/mL)**	**N_{Th} (Total colloids)**	**Non Colloidal (part/mL)**
A1	4.36E+17	1.10E+14	4.36E+17
A2	3.73E+17	5.26E+13	3.73E+17
A3	2.22E+17	7.56E+13	2.22E+17
B1	2.61E+17	4.47E+14	2.60E+17
B2	2.76E+17	3.46E+13	2.75E+17
B3	2.53E+17	1.12E+13	2.53E+17
C1	2.71E+17	2.38E+13	2.71E+17
C2	3.31E+17	2.38E+13	3.31E+17
C3	6.6E+16	3.30E+14	6.57E+16
D1	7.09E+16	4.97E+14	7.04E+16
D2	2.39E+17	5.23E+14	2.38E+17
D3	1.28E+17	2.56E+13	1.28E+17

7.3.7. Solubility of Thorium Hydrous Oxide

There are numerous solubility studies performed with crystalline, microcrystalline or X-ray amorphous thorium oxides and hydroxides or hydrous oxides. Most of these studies have been carried out by adding an appropriate amount of the solid to a test solution and achieving equilibrium starting from under saturation [189-94, 409-411, 416]. The solubility products reported for the thorium oxide and hydroxide species show considerable discrepancies. The reasons can be found in: (1) the characteristics of the solid phase (degree of crystallization, morphology, etc.), which depend on the history of its preparation (hydrolysis, pretreatment, aging); (2) the composition of the solution (pH, ionic strength); (3) method of evaluating the total concentration of thorium in solution (4) use of simplified chemical model used to derive the solubility product; and (5) the set of hydrolysis constants used in the data treatment [424].

The pH-independent solubility of $Th(OH)_4$(am) or ThO_2(am, hyd) in neutral to alkaline solutions is usually ascribed to the reaction:

$$Th(OH)_4\ (am)\ \text{or}\ ThO_2\ (am, hyd) \leftrightarrow Th(OH)_4\ (aq)$$

The present studies involved the calculation of total thorium content present in the supernatant and then its fractionation to separate out the colloid contribution. This methodology allows the soluble non-colloidal thorium present in the supernatants directly, thus enabling deduction of the solubility and solubility products of the species. Further, the characterization of precipitate provides information about the solubility limiting phase. The variations in the solubility products calculated in the present study and in the literature reported data can also be explained on the basis of the precipitation under oversaturated solutions. The determined solubility and solubility products for the thorium under various initial pH and ionic strengths are given in table 7.8, which shows a range of solubility products spanning over four orders of magnitude. This can be explained on the basis of fraction of thorium present as amorphous $Th(OH)_4$ and as crystalline/microcrystalline ThO_2 in precipitate formed under the present experimental conditions.

Table 7.8: The solubility and solubility products of thorium oxy(hydroxide) at different pH and ionic strengths.

Sample	**S (in moles/L)**	**K_{SP}**	**log K_{SP}**
A1	7.24E-10	5.08E-44	-43.29
A2	6.19E-10	2.33E-44	-43.63
A3	3.68E-10	1.74E-45	-44.76

B1	4.32E-10	3.86E-45	-44.41
B2	4.57E-10	5.12E-45	-44.29
B3	4.20E-10	3.33E-45	-44.48
C1	4.49E-10	4.68E-45	-44.33
C2	5.49E-10	1.28E-44	-43.89
C3	1.09E-10	3.95E-48	-47.40
D1	1.17E-10	5.57E-48	-47.25
D2	3.95E-10	2.47E-45	-44.61
D3	2.12E-10	1.10E-46	-45.96

7.3.8. Characterization of Thorium (Oxy) Hydroxide Precipitate

The differences among reported solubility data up to 3-4 orders of magnitude can be attributed to the varying chemical composition, water content and particle size of amorphous thorium oxyhydroxides. Th(IV) oxide or oxyhydroxide solids used in solubility studies are usually not perfectly homogeneous with regard to their particle or crystallite size, but have a certain size distribution. The thermograms for all the samples (Fig.7.7) show three weight loss processes observed at 200^0 C, $370\text{-}400^0$ C and around 900^0 C. Thorium hydroxide is formed as a gelatinous precipitate when alkali or ammonium hydroxide is added to a solution of a thorium salt. Two forms of $ThO_2 \cdot 2H_2O$ (¼$Th(OH)_4$), from precipitation in basic aqueous solution, have been distinguished, one of which is amorphous [425]. $Th(OH)_4$ is reported to be stable in the temperature range $260\text{-}450^o$ C and gets converted to ThO_2 at higher temperature [426].

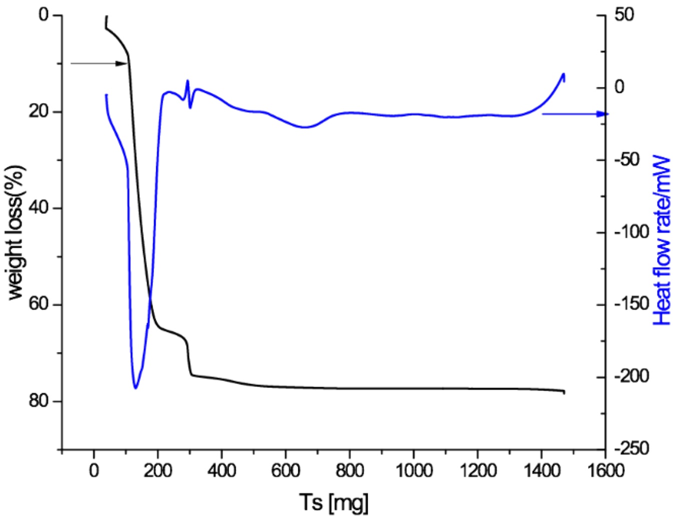

Figure 7.6: TG-DSC pattern of $ThO_2.xH_2O$ + $Th(OH)_4$ synthesized by precipitating Th(IV)-perchlorate using NH_4OH

The thermogram of gelatinous precipitate ThO_2. xH_2O [= $Th(OH)_4$] is given in Figure 7.6. This shows loss of occluded water around 100-200^o C with a corresponding endothermic peak in heat flow rate curve. At around 295^o C, due to kinetic factor, a part of them dried ThO_2. xH_2O, gets converted to $Th(OH)_4$ and then decomposed to ThO_2 which appears as a tail. The weight loss of ~12% is similar to that calculated for the formation of oxide from oxyhydroxide. The exothermic peak in DSC around 295^o C, could outweigh effect of exothermicity (more stronger bond formation on conversion of ThO_2. xH_2O to $Th(OH)_4$) than the endothermicity of decomposition of ThO_2. xH_2O to ThO_2.

The thermogram of A5, B5, C5 and D5, shown in Figure 7.7 are quite different from figure 7.6. The figure shows three weight loss steps. The first step around 200^o C is due to loss of occluded water as the precipitates were not completely dried. The second mass loss at ~370-400^o C which has a corresponding exothermic peak in heat flow curve similar to synthesized oxyhydroxide (Figure 7.6) could be explained as above. Absence of an exothermic peak in the case of B5 could be due to its very small sample size. Thus it is possible that part of $ThO_2.xH_2O$ could have decomposed to ThO_2 and remaining part to $Th(OH)_4$. The third mass loss at ~900^o C is assigned to the decomposition of $Th(OH)_4$ to

ThO_2. The second step corresponds to the loss of water of crystallization and formation of $Th(OH)_4$ and the third step, is due to the loss of water from thorium hydroxide to form ThO_2. The third step in heat flow curve is a broad endothermic peak. The residues obtained after the thermal study were analyzed by XRD and found to be ThO_2. The exact percentage loss, corresponding temperature and the type of reaction (endo /exo) are given in table 7.9.

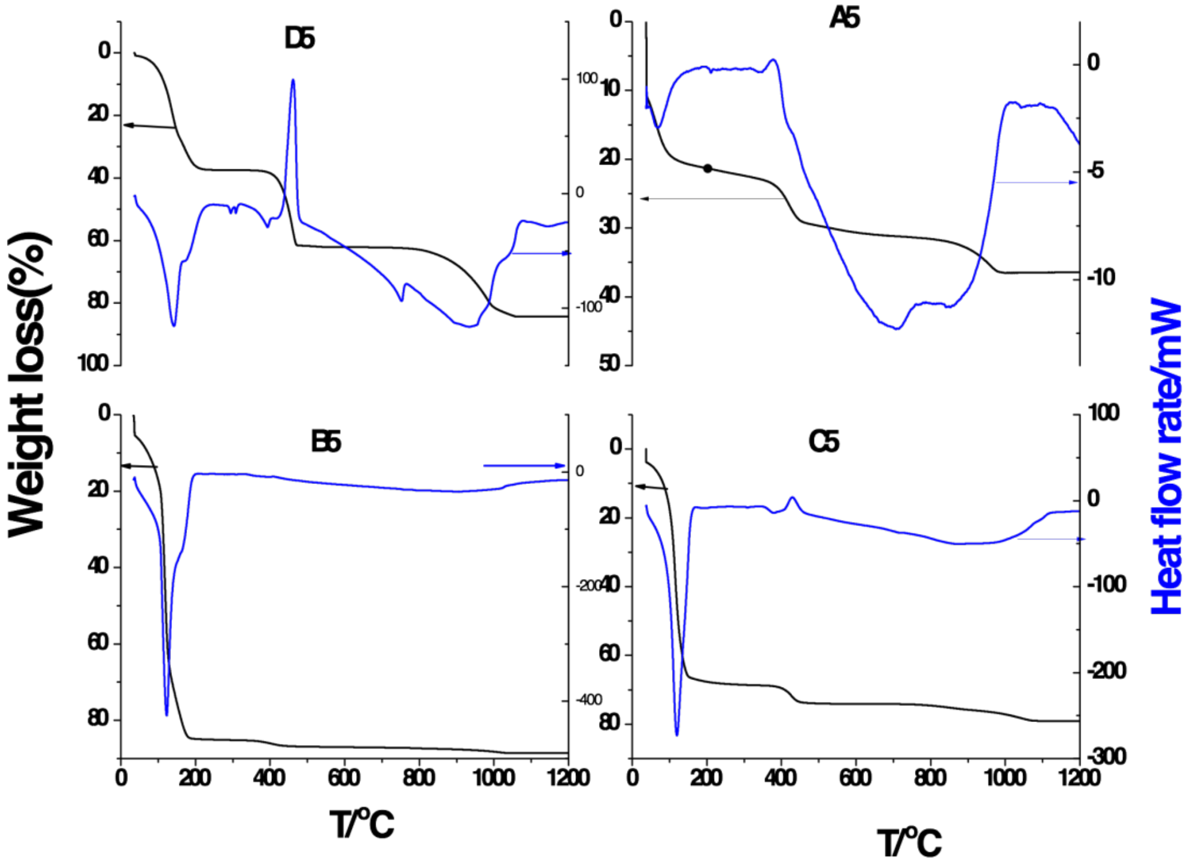

Figure 7.7: TG-DSC pattern of precipitates resulted from the equilibrated samples at pH=13 under different ionic strengths (A5, B5, C5 and D5 samples). (Black: Weigh loss and Blue: Heat flow)

Table 7.9: The percentage of weight loss, temperature and the type of thermal event (endo /exo) of the equilibrated samples at pH=13 under different ionic strengths (A5, B5, C5 and D5 samples).

Sample	**T (in ^{o}C)**	**% Wt. loss**	**Type of thermal event**
A5	100-150	20	endo
	386.6	8.9	exo
	901.0	5.1	endo
B5	120	83	endo
	371	1.9	not visible due to small sample size
	960	1.4	endo
C5	98	67	endo
	400.7	5.4	exo
	899.5	4.9	endo
D5	100-200	37	endo
	425	24.7	exo
	897.3	22.0	endo

The table shows slight variation in percentage loss and the temperature at which the loss occurs. The evolved gas was also analyzed for B5 and C5 using FTIR and the spectrum showed two peaks corresponding to the stretching of O-H bonding (Figure 7.8) which further supports the TG-DSC results. Absence of the peak due to carbonyl group stretching, indicates absence of any carbonate species of thorium as impurities.

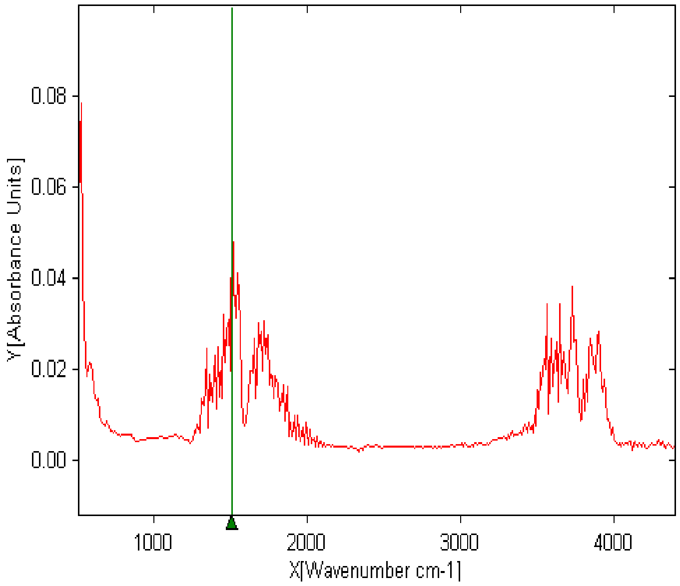

Figure 7.8: FTIR analysis of precipitates resulted from the equilibrated samples at pH=13 under different ionic strengths.

The residues obtained at the end of each peak position of the thermal study were also analyzed by XRD. The diffraction patterns of the sample B-5 at three different temperatures (100^0, 550^0 and 1200^0 C) along with the diffractogram of a freshly prepared $Th(OH)_4$ was shown in figure 7.9. The XRD of the precipitate formed in aged thorium solution (B-5 at 100^0 C in figure 7.9) was typical of an amorphous solid negating the formation of pure $Th(OH)_4$ or ThO_2. Instead the solid may consist mainly of a hydrated oxyhydroxide $ThO_n(OH)_4\text{-}2n{\cdot}xH_2O$ (am) with $0 < n < 2$ rather than ThO_2(s). Further the species at 550^0 C, which corresponds to the residue obtained after a peak around 371^0 C in thermogram (table 7.9 and Figure 7.7) also shows an amorphous pattern similar to the species at 100^0 C, but the XRD peaks are narrower than the later indicating more crystalline configuration of the species at 550^0 C than at 100^0 C. The XRD pattern of residue at the end of thermogram (B-5 at 1200^0 C) corresponds to crystalline ThO_2. Thus the TG-DSC data combined with XRD analysis shows that the precipitate formed in aged Thorium solution was initially an XRD amorphous, which transformed to crystalline ThO_2 with the ageing of the solution.

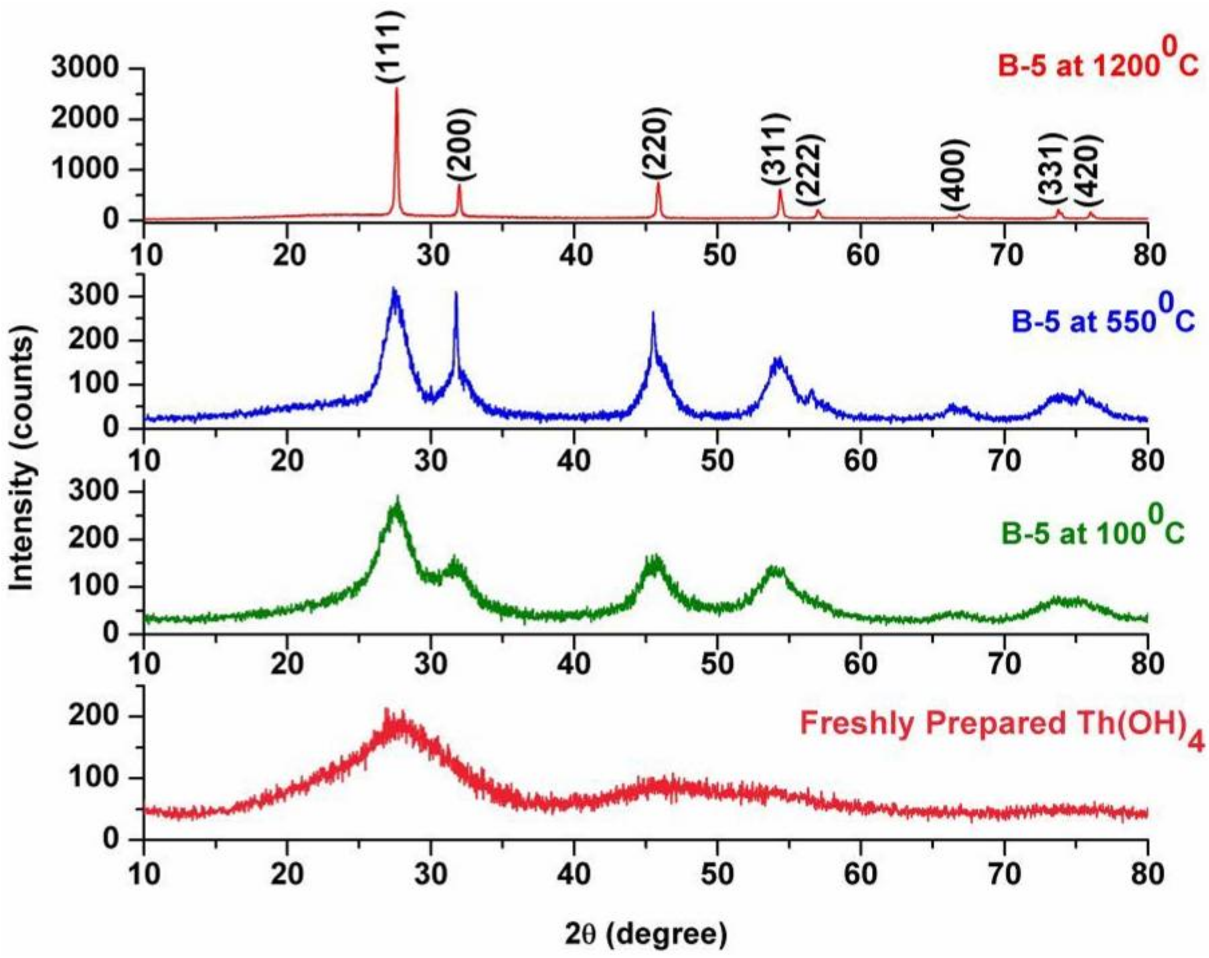

Figure 7.9: XRD patterns of the residues obtained at the end of each peak in thermogram for the aged thorium sample (B-5) along with a freshly prepared Th(OH)$_4$.

7.4. Conclusion

The colloids formed by thorium perchlorate solutions kept for an equilibration period of ~1080 days at various pH and ionic strengths were characterized by LIBD to determine the size and concentration of the colloids. Further, with the available data on Th-Th internuclear distance in polymeric species, the total number of thorium ions present in each particle and hence the total content of thorium as colloids was determined. The LIBD results showed the presence of colloids of size lower than 50 nm at ppb level concentration. This helped in fractionating the soluble thorium species to Th(IV) aqua ion, polynuclear and colloidal form. From the experimentally determined thorium concentrations in each species, the solubility of thorium at different pH and ionic strengths was calculated by considering the thorium content that contributes to non-colloidal form only, that is, ionic or polymeric species. The estimated solubility limits were found to be in agreement to the literature reported data. The precipitate formed at pH=13 under all ionic strengths was also characterized by XRD, TG-DSC and TG-EGA-FTIR, which showed that the precipitate formed is neither completely $Th(OH)_4$ nor ThO_2 but intermediate between the two forms.

Summary

The present work pertains to the thermodynamic studies on complexation of Eu(III), Th(IV) and Np(V) with the anthropogenic ligands like pyridine monocarboxylates, their N-oxides and hydroxamates. The thermodynamic parameters (log K, ΔG, ΔH and ΔS) of complexation have been studied by potentiometry, luminescence spectroscopy and isothermal titration calorimetry. The experimental observations on the stability and binding mode of the complexes are corroborated by theoretical calculations. Stability parameter (complexation energy), geometrical parameter (bond lengths) and the charge distribution are calculated for all the complexes using TURBOMOLE. The geometries of the bare ligands and all the complexes have also been optimized in presence of solvent.

Modeling the behavior of actinides under environmental conditions is very challenging as it requires complete information about the thermodynamic properties of the metal ions involved with a multitude of potential ligands that can regulate the environmental transport of metal ions through formation of complexes. Thermodynamic stability constants can be used to predict speciation. In multi-component systems, such as natural waters, the stability constants of all the known complexes and the concentrations of each component are used to predict the resultant species. Therefore, the inclusion of all relevant species is crucial for obtaining accurate predictions, and experimental speciation data are required as input in these models.

In the case of complexation of metal ion with acidic ligands like carboxylates, the complexation process is accompanied by deprotonation of ligand. Thus, thermodynamic parameters for ligand protonation are required during analysis of complexation data. The protonation constants are obtained by potentiometric titrations whereas enthalpy change of protonation (ΔH_P) is determined by calorimetric titration.

The protonation constants revealed the presence of monoprotonated (protonated carboxylate group) as well as diprotonated pyridine monocarboxylate (protonated carboxylate and nitrogen atom). The more basic nature of pyridyl nitrogen of picolinic acid (log Kp1) compared to other two isomers can be attributed to formation of intra molecular hydrogen bond between proton attached to carboxylate anion and pyridyl nitrogen. The protonation of nitrogen atoms in pyridyl monocarboxylates is found to be highly exothermic whereas enthalpy of protonation of carboxylate is nearly zero. The protonation of carboxylate groups is mainly driven by entropy whereas protonation of pyridyl nitrogen atoms are driven by entropy as well as enthalpy. The less dehydration energy required for nitrogen results in negative enthalpy of protonation and is determined by electron density on nitrogen atom. The lower electron density on pyridyl nitrogen of picolinate compared to isonicotinate and nicotinate can be explained by effective delocalization of electron density by resonance as well as negative inductive effect (-I). The theoretically calculated electron density on pyridyl nitrogen is reflected in similar thermodynamic parameters for protonation of nicotinate and isonicotinate.

The pKa determined for pyridine monocarboxylate-N-oxides by potentiometry follow the order: PANO > IANO > NANO at all ionic strengths. The calorimetric results revealed that the protonation of PANO is endothermic while that of IANO and NANO is exothermic, indicating the entropy driven protonation of PANO while the other two have minor contribution of enthalpy as well in addition to entropy contribution. The ion interaction parameters for PCNOs are obtained by determining the pKa for the same at various ionic strengths (I=0.1-3.0 M $NaClO_4$) and the data is extrapolated to find pKa0 (pKa at I=0) by specific ion interaction theory (SIT). The pKa / pKa0 determined by absorption spectra are also in line with potentiometric results. The energetics and variations in charge densities on individual atoms on protonation were calculated theoretically. PCNOs protonation are compared with their base moieties: pyridine monocarboxylates to interpret the effect of the N-oxide moiety on the protonation thermodynamics.

The analysis of potentiometric and spectrophotometric data by Hyperquad indicated the presence of monoprotonated species for AHA and BHA and mono- and di-protonated species for SHA. Among the three hydroxamic acids, the log K_P value, which is a measure of basicity, follows the order, SHA > AHA > BHA. DFT calculations were carried out for protonation of all the three hydroxamic acids. The trend in proton binding energy of hydroxamate ligand ($-\Delta E_{P1}$) is in good agreement with the experimental log K_{P1} values. The charges on the protonating site are also useful to understand their affinity for proton. The electron density on oxygen atom -NHO group of AHA (-0.755 e) is higher than that of BHA (-0.652) which explains the higher log K_P of AHA compared to that of BHA. This can be attributed to positive inductive effect of acetyl group in AHA and negative inductive effect of phenyl group in BHA. The effect of hydroxyl group on protonation of SHA^{2-} can be understood by comparing protonation of $-NHO^-$ in BHA ($-\Delta E_{P1}$ = -15.36 eV) and SHA ($-\Delta E_{P2}$= -14.90 eV). The negative charge on $-NHO^-$ group is higher in case of BHA^- (-0.655e) compared to that in case of $SHA\text{-}H^-$ (-0.598e) (Figure 5). Thus, decrease in electron density on $-NHO^-$ oxygen atom in $SHA\text{-}H^-$ due to presence ortho hydroxyl group leads to decrease in its basicity and hence protonation constant.

Eu(III) forms more stable and multiple complexes with picolinate than nicotinate and isonicotinate which form only 1:1 complex in the concentration range studied. The ΔH_C of Eu(III)-picolinates were found to be negative which are attributed to formation of a stable five membered ring by chelation through pyridyl nitrogen atom. The TRLS measurements showed a significant increase in the life time of Eu(III) $^5D_0$ state, which suggests the bidentate nature of picolinate with formation of 1:4 complex at the end of titration. The Eu(III)-isonicotinate is found to be more stable than Eu(III)-nicotinate as the charge transferred from the nitrogen in the pyridine ring to the binding carboxylate is higher in former which enhances the electrostatic binding of the ligand to metal. The experimental result are also in good agreement with the theoretically calculated results for the complexes for various geometries.

The thermodynamic data on complexation show that picolinate can be a potential complexing ligand which can facilitate the migration of tetravalent actinides in the geosphere. The exothermicity and higher values of formation constants of the Th(IV)-picolinates over that for other two ligands is due to the extra stability from the chelating nature of picolinate. The Th(IV)-isonicotinate complex is more stable than the Th(IV)-nicotinate complex and both the complexation processes were found to endothermic indicating the similarity of these complexes with the simple carboxylate complexes which are, in general, entropy driven and endothermic in nature. The bond lengths, complexation energies and atomic charges on each atom in the complex calculated theoretically by TURBOMOLE are consistent with the experimentally observed results.

The complexation of Eu(III) ion by three structurally isomeric pyridine monocarboxylate-N-oxides was studied by experiment and theory. The change in position of N-oxide plays a key role in deciding the mode of complexation with the metal ion. Eu(III)-PANO complexes were found to be more stable than Eu(III)-NANO/IANO complexes which is attributed to the additional strength gained in PANO complexes by chelate formation. Among Eu(III)-NANO and Eu(III)-IANO complexes, the later forms more stable complexes than the former, which is attributed to the charge polarization being more favorable in IANO owing to para position of carboxylate to N-oxide. The exothermic nature of the complexation reaction and the constant lifetime of $^5D_0$ excited state of Eu(III) with varying ligand to metal ratio indicates the outer sphere complexation of Eu(III) by NANO whereas the endothermic nature and increase in lifetime of $^5D_0$ excited state of Eu(III) in case of Eu(III)-PANO and

Eu(III)-IANO complexes supported the inner sphere complexation in these complexes. The elaborated theoretical calculation for all the possible reaction schemes to optimize the geometries; and to determine the bond lengths, bond angles and charges on individual atoms on complexation provided useful insight useful into the mechanism of the complexation reaction. The change in energetics for the 1:2 complex formation from 1:1 complexes for all the possible combinations of inner and outersphere complex formation corroborated the experimental observations that Eu(III)-PANO/IANO complexes are innersphere while Eu(III)-NANO forms 1:1 outersphere but at 1:2, it forms a mix of both inner and outersphere complex. The theoretical prediction are found to be in good agreement with the experimental results.

The formation of complexes by thorium with pyridine monocarboxylate-N-oxides was found to be endothermic and entropy driven. The higher stability of Th(IV)-PANO compared to the other two isomers is explained in terms of the chelate formation. The variations in thermodynamic parameters are interpreted in terms of perturbation in hydration spheres of metal and ligand ions. Further, the theoretical calculation of charges on individual atoms helped in interpreting the trends within and among the Th(IV)-PCNO complexes in terms of electrostatic interactions. The linear free energy relationship (log β ovs. pKa) showed the chelate and carboxylate kind of binding in Th(IV)-PANO and Th(IV)-NANO/IANO complexes respectively. Overall, the mutual position of the two functional groups, the N-oxide and carboxylate, was found to play a key role on the thermodynamics of complexation process.

The Np(V) forms ML and ML_2 type of complexes with pyridine monocarboxylates viz. picolinate, nicotinate and isonicotinate, by mainly electrostatic interactions. Among the three geometrical isomers, the picolinate forms strongest complex through five membered chelate formation. In case of nicotinate and isonicotinate, the binding is through carboxylate group but higher stability than expected from pKa values of carboxylate groups is attributed to the charge transfers from nonbonding nitrogen. The higher charge transfer from nitrogen in para position (isonicotinate) reflects in its higher stability constant and the shift in λ_{max} compared to nicotinate. The trend in stability constants and charge polarization in ligand molecules on complexation has been supported by theoretically calculated binding energies and the charges on individual atoms.

The role of substitution in hydroxamate on complexation was understood by carrying out DFT calculations on Np(V)-AHA, Np(V)-BHA and Np(V)-SHA complexes. The charges on atoms and geometrical parameters like bond angles and bond distances are used to rationalize the energetic of complexation reaction. The results revealed the dominant role of electrostatic interaction in determining the complex stability. In Np(V)-AHA, the acetyl group increases the electron density on donating oxygen atoms compared to phenyl group in BHA, thereby enhancing its stability. Among the various binding modes of Np-SHA in 1:1:1 complexes, the one involving ortho hydroxyl group and hydroxyl group of hydroxamate moiety is most stable whereas in 1:2:2 complex geometries, steric constraints result in stabilization of five membered ring (involving hydroxamate moiety) for the second ligand. The calculated results corroborated the trends in experimentally obtained stability constants.

The extensive hydrolysis of tetravalent leads to polynuclear formations through oxygen bridging facilitating the formation of colloids as end products. The concentration of metal ion, hydrogen ion concentration, ionic strength, ageing period of solutions, and presence of complexing agents have phenomenal effects on formation of the colloids. Depending on the size and surface charge present, the actinide colloids can either facilitate the migration or retard the transportation of actinides in the aquatic environments. Thus, the accountancy for colloids is also essential in estimating the pathway for migration of a radionuclide from the source. Furthermore, the presence of colloids can also explain the widely scattered Th(IV) concentrations measured in the various solubility studies.

Thorium perchlorate solution (0.01 M) under various pH (5 to 11) and ionic strength (0 to 3 M $NaClO_4$) were kept for equilibration for 3 years and the supernatants were analyzed by ICP-MS and ion chromatography to determine the total and ionic thorium content present in the same. Dynamic Light scattering (DLS) and Laser Induced breakdown detection (LIBD) were the two techniques employed for the determination of size of colloid particles and the later technique was also used to determine the concentration in addition to size of colloid particles present in the supernatant. The results of pH, IC, ICP-MS, DLS and LIBD measurements on the aged thorium samples were discussed in relation to mechanism of their formation and determination of thorium colloids. The present studies revealed the formation of colloids of range 14-37 nm at concentrations 2.00 to 385 ppb. The solubility products were found to be lower than the reported values upon taking into consideration of the colloids formation.

The solution kept at pH 11 and 13 resulted in the formation of an amorphous precipitate, which was analyzed by TG-DSC and then XRD to know the composition of precipitate formed. The formation of amorphous precipitate indicates that it is neither completely $Th(OH)_4$ nor ThO_2 but consists mainly of a hydrated oxyhydroxide $ThO_n(OH)_{4-2n} \cdot xH_2O$ (am) with $0 < n < 2$ rather than $ThO_2(s)$. The HT-TG-DSC analysis showed three weight loss processes observed at 200^0, $370\text{-}400^0$ and around 900^0 C. The first step around 200^o C was assigned to loss of occluded water as the precipitates were not completely dried. The second step corresponds to the loss of water of crystallization while the third step as due to loss of water from thorium hydroxide to form ThO_2. The residue obtained after the thermal study was analyzed by XRD and found to be crystalline ThO_2.

To summarize, the present thesis presents a detail discussion on the speciation of actinides or their lighter homologues (lanthanides) under different aquatic environments and in presence of the important anthropogenic ligands that are co-disposed in the actinide waste and have significant presence in the waste confinements and near disposal facilities. The thermodynamic parameters reported in the present studies showed that these ligands form very strong and multiple complexes (MLi, i = 1-4) with the actinides and hence can be potential agents for migration of actinides from their source of origin. Further, the actinide colloid formation is a key factor in deciding the solubility limits and the limiting solid phases. The accountancy of colloids helps in re-estimation the solubility products for accurate measurement of actinide concentration in aquatic conditions. The thesis also presents detailed study on colloid characterization in thorium samples kept for prolonged equilibration (~1080 days) at various pH and ionic strengths. The quantitative determination of colloid contribution helps not only in predicting accurate solubility products but also to fractionate the dissolved thorium content to ionic, polymeric and colloid fractions.

References

1. Energy Statistics 2017 by Central Statistics Office, Ministry of Statistics and Programme Implementation, Government Of India
2. Nuclear power in India, World Nuclear association.
3. R Spence, Brit. J. Appl. Phys. 7 (1956) 88-91.
4. H. J. Bhabha, N. B. Prasad, A study of the contribution of atomic energy to a power programme in India. In: Proceedings of 2nd UN International Conference on ‘Peaceful Uses of Atomic Energy’ Geneva, September 1-13, 1958, vol. 1, pp. 89-101.
5. The nuclear fuel cycle by IAEA Division of Nuclear Fuel Cycle and Waste Technology, August 2011, 11-2522
6. Treatment and recycling of spent nuclear fuel: Actinide partitioning – Application to waste management (Editor: Jean-François Parisot) CEA Saclay and GroupeMoniteur (Éditions du Moniteur), Paris, 2008
7. P. K. Dey, N. K. Bansal, Nucl. Eng. Des. 236 (206) 723-729.
8. World nuclear association, 2016, http://www.world-nuclear.org/informationlibrary/ current-and-future-generation/fast-neutron-reactors.aspx
9. K. Balu, D. S. C. Purushotham, A. Kakodkar, Closing Fuel Cycle- a Superior Option for India, Paper Presented at Conf. On‘Fuel Cycle Options for Light Water Reactors and Heavy Water Reactors’, Victoria Canada, April 28- May 1998, vol. 1, pp. 25-34.
10. Trends towards Sustainability in the Nuclear Fuel Cycle, OECD 2011, NEA No. 6980
11. Amit Rajora, et al., Generating One Group Cross-section for Isotope Depletion and Generation Calculation for Thorium, a Paper Presented in International Thorium Energy Conference (ThEC-2015), Held in Anushakti Nagar, Mumbai, India, October 12-15, 2015.

12. P. K. Wattal, Back end of Indian nuclear fuel cycle-A road to sustainability, Prog. Nucl. Energy. 101 (2017) 133-145.
13. Classification of radioactive waste - General Safety guide, IAEA 2009
14. Application of the Concepts of Exclusion, Exemption and Clearance, IAEA Safety Standards Series No. RS-G-1.7, IAEA, Vienna (2004)
15. Sangeeta Deokattey, K. Bhanumurthy, P.K. Wattal, Prog. Nucl. Energy. 62 (2013) 37-45.
16. Radiation in Everyday Life, Fact sheet by IAEA, https://www.iaea.org/Publications/Factsheets/English/radlife
17. A. P. Novikov, B. F. Myasoedov, Radiochemical Procedures For Speciation Of Actinides In The Environment. Methodology And Data Obtained In Contaminated Regions Of Russia By Radionuclides, Environmental Protection Against Radioactive Pollution pp 147-154.
18. G. R. Choppin, J. O. Liljensen, J. Rydberg, Radiochemistry and Nuclear Chemistry, Butterworth-Heinemann, Oxford (1996)
19. J. Lelieveld, D. Kunkel and M. G. Lawrence, Atmos. Chem. Phys., 12 (2012) 4245–4258.
20. Remus Prăvălie, Ambio. 43 (2014) 729–744.
21. R. J. Pentreath, Radioactive Materials - The Aquatic Environment in Food Chains and Human Nutrition (Eds: Blaxter, Kenneth), 1980, Springer, Netherlands
22. Peter H.Santschi, Bruce D.Honeyman, Int. J. Rad. Appl. Instr. Part C. Rad. Phy. Chem. 34 (1989) 213-240.
23. H12: Project to Establish the Scientific and Technical Basis for HLW Disposal in Japan, Supporting Report 2, Japan Nuclear Cycle Development Institute, 2000.

24. Kate Maher, John R. Bargar and Gordon E. Brown Jr., Inorg. Chem. 52 (2013) 3510 - 3532.

25. W. J. F. Standring, Review of the current status and operations at Mayak Production Association, Strålevern Rapport 2006:19. Østerås: Norwegian Radiation Protection Authority, 2006.

26. Radiation Dose Estimates from Hanford Radioactive Material Releases to the Air and the Columbia River, Report by The Technical Steering Panel of the Hanford - Environmental Dose Reconstruction Project, April 21,1994.

27. Fukushima Nuclear Accident Update, International Atomic Energy Agency (IAEA) press release, March 12, 2011.

28. H. R. von Gunten and P. Benes, Speciation of Radionuclides in the Environment, PSI Bericht Nr. 94-03, February 1994, ISSN: 1019-0643

29. Colin R. Phillips and H. Lin Pai, Water, Air, Soil Pollut. 8 (1977) 145-163.

30. C. N. Murray, H. Kautsky, M. Hoppenheit and M. Domian, Nature 276 (1978) 225 - 230.

31. P. J. Coughtrey, D. Jackson, C. H. Jones, P. Kane, M. C. Thorne, Radionuclide Distribution and Transport in Terrestrial and Aquatic Ecosystems: A Critical Review of Data, Volume Four, (1984) A. A. Balkema Publishers, Rotterdam, Boston.

32. G. R. Choppin, J. Radioanal. Nucl. Chem. 273 (2007) 695–703.

33. R. J. Silva and H. Nitsche, Radiochim. Acta. 70/71 (1995) 377-396.

34. H. Nitsche, Radiochim. Acta 52/53 (1991) 3-8.

35. T. Rabung, T. Stumpf,H. Geckeis, R. Klenze, J. I. Kim, Radiochim. Acta 88 (2000) 711-716.

36. A. Kowal-Fouchard, R. Drot, E. Simoni, J. J. Ehrhardt, Environ. Sci. Technol. 38 (2004) 1399-1407.

37. Horst Geckeis, Johannes Lutzenkirchen, Robert Polly, Thomas Rabung, and Moritz Schmidt, Chem. Rev. 113 (2013) 1016-1062.
38. M. Borkowski, R. C. Moore, M. G. Bronikowski, Jianfeng Chen, O. S. Pokrovsky, Yuanxian Xia, G. R. Choppin, J. Radioanal. Nucl. Chem. 248 (2001) 467-471.
39. Satoru Tanaka and Shinya Nagasaki, Nucl. Techn. 118 (1997) 58-68.
40. Christophe Poinssot, Horst Geckeis, Radionuclide Behaviour in the Natural Environment: Science, Implications and Lessons for the Nuclear industry, Elsevier, 2012.
41. Zhongbo Yu, Yuyu Lin, Karen Johannesson, Amy J. Smiecinski, Klaus J. Stetzenbach, Geochemical modelling of solubility and speciation of uranium, neptunium, and plutonium (2007) Available at: http://digitalscholarship.unlv.edu/yucca_mtn_pubs/66, report no: MOD-06-001.
42. M. Dozol1 and R. Hagemann, Pure & Appl. Chem. 65 (1993) 1081-1102.
43. Marcus Altmaier, Xavier Gaona, Thomas Fanghänel, Chem. Rev. 113 (2013)901- 943.
44. Neil A Chapman, Ian G McKinley, John A T Smellie, The Potential of Natural Analogues in Assessing Systems for Deep Disposal of High-Level Radioactive Waste, KBS TR 84-16, Stockholm, Sweden August 1984.
45. W. M. Miller, N. Chapman, I. McKinley, R. Alexander, J.A.T. Smellie, Natural Analogue Studies in the Geological Disposal of Radioactive Wastes, Elsevier, 2011.
46. Simon Cotton, Lanthanide and Actinide Chemistry, John Wiley & Sons, Ltd, 2006.
47. W. D. Loveland, D. J. Morrissey and G. T. Seaborg, Nuclear Reactor Chemistry, in Modern Nuclear Chemistry, John Wiley & Sons, Inc., Hoboken, NJ, USA, (2017)
48. Lanthanides/Actinides: Chemistry, Volume 18, 1st Edition, (Editors: G.R. Choppin, G.H. Lander, L. Eyring, K.A. Gschneidner) in Series: Handbook on the Physics and Chemistry of Rare Earths, Elsevier, North Holland (1994).

49. A. F. Wells, Structural Inorganic Chemistry, Oxford University Press, London, 1975.
50. Kenneth G. Dyall, Chem. Phys. 311 (2005) 19-24.
51. Werner Stumm, James J. Morgan, Aquatic Chemistry: Chemical Equilibria and Rates in Natural Waters, 3rd Edition, John Wiley & Sons, New York, 1995.
52. G. R. Choppin, J. Less-Common Met., 100 (1984) 141-151.
53. J. E. Enderby, Chem. Soc. Rev., 1995, 24, 159–168.
54. G. Johansson and H. Wakita, Inorg. Chem., 1985, 24, 3047–3052.
55. I. Persson, P. D’Angelo, S. D. Panfilis, M. Sandstrorm and L. Eriksson, Chem.–Eur. J., 14 (2008) 3056–3066.
56. Jan Ciupka, Xiaoyan Cao-Dolg, Jonas Wiebke and Michael Dolg, Phys.Chem.Chem.Phys. 12 (2010) 13215–13223.
57. S. L. Bertha and G. R. Choppin, Inorg. Chem. 8 (1969) 613-617.
58. E. N. Rizkalla, Gregory R. Choppin, J. Alloy. Compd. 180 (1992) 325-336
59. Karah E. Knope and L. Soderholm, Chem. Rev. 113 (2013) 944-994.
60. S. Tsushima, A. Suzuki, J. Mol. Struct. (Theochem) 529 (2000) 21–25.
61. G. R. Choppin, Pure & Appl. Chem. 27 (1971) 23-42.
62. C. F. Baes Jr. and R. E. Mesmer, The Hydrolysis of Cations, Krieger Publishing Company, Malabar, Florida, 1976.
63. Greta D. Klungness, Robert H. Byrne, Polyhedron 19 (2000) 99–107.
64. Paul L. Brown, Christian Ekberg, Scandium Yttrium and the Lanthanide Metals in Hydrolysis of Metal Ions, Volume 1, John Wiley & Sons, Germany, 2016, pp 225-324.
65. L. Pettit, G. Pettit, K. J. Powell, IUPAC Stability Constants Database, IUPAC and Academic Software, Otley, UK, 1999.
66. Gregory R. Choppin and Mark P. Jensen, Chapter Twenty Three Actinides in Solution: Complexation and Kinetics in The Chemistry of The Actinide and Transactinide

Elements Fourth Edition Volumes 4 (Eds: Lester R. Morss, Norman M. Edelstein, Jean Fuger), 2010, Springer, Netherlands.

67. Gregory R. Choppin, Radiochim. Acta, 32 (1983) 43-53.
68. M. Rand, J. Fuger, I. Grenthe, V. Neck and D. Rai, Chemical Thermodynamics of Thorium, Elsevier, North Holland, Amsterdam, 2009, vol. 11.
69. W. Stumm, J. J. Morgan, Aquatic Chemistry, John Wiley & Sons, (1981)
70. Helen C. Aspinall, Chemistry of the f-Block Elements, Volume 5, CRC Press, 2001.
71. M. Dozol1 and R. Hagemann, Radionuclide Migration in Groundwaters: Review Of The Behaviour Of Actinides (Technical Report), Pure & Appl. Chem., Vol. 65, No. 5, pp. 1081-1102, 1993.
72. J. I. Drever, The Geochemistry of Natural Waters. Prentice-Hall, Inc., Englewood Cliffs, NJ, 1982.
73. Joseph A. Rard, Chem. Rev. 85 (1985) 555-582.
74. Vinny R. Sastri, J.R. Perumareddi, V. RamachandraRao, G.V.S. Rayudu, J.-C. G. Bünzli, Modern Aspects of Rare Earths and their Complexes, Elsevier, 2003
75. Stephen J. Lippard, Progress in Inorganic Chemistry, Volume 31, John Wiley & Sons, 2009.
76. Thomas Vercouter, BadiaAmekraz, Christophe Moulin, Pierre Vitorg, Lanthanide and actinide inorganic complexes in natural waters: TRLFS and ESI-MS studies, Communication O22-02, ATALANTE 2004, Nîmes (France), June 21-25, 2004.
77. David L. Clark, David E. Hobart and Mary P. Neu, Chem. Rev. 95 (1995) 25-48.
78. M. Eigen and K. Z. Tamm, Elektrochem., 66 (1962) 107-121.
79. G. R. Choppin and S. L. Bertha, J. Inorg. Nucl. Chem. 35 (1973) 1309-1312.
80. Gregory R. Choppin and Rilliax F. Strazik, Inorg. chem. 8 (1965) 1250-1254.
81. Gregory R. Choppin, J. Alloy. Compd. 249 (1997) 9-13.

82. Gregory R. Choppin, Anthony J. Graffeo, Inorg. Chem. 4 (1965) 1254–1257.

83. Chemistry of the f-Block Elements, Helen C. Aspinall, CRC Press, 15-May-2001.

84. I. Grenthe, J. Fuger, , R. J. M. Konings, R. J. Lemire, A. B. Muller, C. Nguyen-Trung and H. Wanner, Chemical Thermodynamics of Uranium, North Holland, Amsterdam, 1992.

85. Silvia Berto, Francesco Crea, Pier Giuseppe Daniele, Antonio Gianguzza, Alberto Pettignano, Silvio Sammartano, Coord. Chem. Rev. 256 (2012) 63−81.

86. G. R. Choppin and L. F. Rao, Radiochim. Acta 37 (1984) 143–146.

87. N. K. Chaudhuri, R. M. Sawant and D. D. Sood, J. Radioanal. Nucl. Chem. 240 (1999) 993–1011.

88. Colin A. Stedmon, StiigMarkager, Rasmus Bro, Mar. Chem. 82 (2003) 239-254.

89. E. M. Thurman, Organic Geochemistry of Natural Waters, Springer: Dordrecht, The Netherlands, 1985.

90. Y. K. Kharaka, J. S. Hanor, Deep Fluids in the Continents: I - Sedimentary Basins; Elsevier: Amsterdam, The Netherlands, 2003; Vol. 5, pp 1−48.

91. David L. Jones, Plant and Soil 205 (1998) 25–44.

92. S. Jr. Boggs, D. Livermore, M. G. Seitz, Humics substances in natural waters and their Complexation with trace metals and radionuclides : a review, ANL - 84/78 (1985)

93. Valerie Moulin, Appl. Geochem. 10 (1995) 573-580.

94. Olivier Pourret, Melanie Davranche, Gerard Gruau, Aline Dia, Chem. Geol. 243 (2007) 128-141.

95. Jennifer C. Stern, Jeroen E. Sonke, Vincent J.M. Salters, Chemical Geol. 246 (2007) 170-180.

96. Jianwu Tang, Karen H. Johannesson, Geochim. Cosmochim. Acta 67 (2003) 2321-2339.

97. Takayuki Sasaki, Hatsumi Yoshida, Taishi Kobayashi, Ikuji Takagi, Hirotake Moriyama, Am. J. Anal. Chem. 3 (2012) 462-469.

98. Jeroen E. Sonke, Environ. Sci. Technol. 40 (2006) 7481-7487.

99. Jeroen E. Sonke, Vincent J.M. Salters, Geochim. Cosmochim. Acta 70 (2006) 1495–1506.

100. J. C. Dobbs, W. Susetyo, F. E. Knight, M. A. Castles, L. A. Carreira, L. V. Azarraga, Anal. Chem. 61 (1989) 483-488.

101. J. W. Thomason, W. Susetyo and L. A. Carreira, Appl. Spectr. 50 (1996) 401-408.

102. Valerir Moulin, Jan Tits and Gerald Ouzounian, Radiochim. Acta, 58/59 (1992) 179-190.

103. Sam Boggs, Jr., David Livermore, and Martin G. Seltz, Humic Substances in Natural Waters and Their Complexation with Trace Metals and Radionuclides: A Review, ANL 84-78, 1985

104. Luca Righetto, Giovanni Bidoglio, Giovanna Azimonti, Ignazio R. Bellobono, Environ. Sci. Technol. 25 (1991) 1913–1919.

105. Kenneth. Nash, Sherman. Fried, Arnold M. Friedman, James C. Sullivan, Environ. Sci. Technol. 15 (1981) 834–837.

106. Pascal E. Reiller, Nick Evans, Gyula Szabo, Radiochim. Acta. 96 (2008).345-358.

107. Kenneth L. Nash And Gregory R. Choppin, J. Inorg. Nucl. Chem. 42 (1980) 1045-1050.

108. E. Tipping, Radiochim. Acta 62 (1993) 141-152.

109. U Olofsson, B Allard, Complexes of Actinides with Naturally Occurring Organic Substances - Literature Survey, SKBF-KBS-TR-85-09, 1983.

110. R.J. Serne, K.J. Cantrell, C.W. Lindenmeier, A.T. Owen, I.V. Kutnyakov, R.D. Orr, Radionuclide-chelating agent complexes in low-level radioactive decontamination

waste: stability, adsorption, and transport potential (NUREG/CR-6758). Pacific Northwest National Laboratory, 2002.

111. P.R. Silverwood, D. Collison, F.R. Livens, R.L. Beddoes, R.J. Taylor, J. Alloys Compd. 271 (1998) 180–183.

112. G.S. Sanyal, R. Ganguly, P.K. Nath, S. Das, J. Indian Chem, Soc. 78 (2001) 444–447.

113. D. Bradbury, M. G. Segal, R. M. Sellers, T. Swan, C. J. Wood, ‘‘Development of LOMI Chemical Decontamination Technology’’, EPRI, Report NP-3177, July 1983.

114. M.S. Davis, P.L. Piciulo, B.S. Bowerman, L. Milian, and L. Nicolosi, ‘‘The Impact of LWR Decontaminations on Solidification, Waste Disposal, and Associated Occupational Exposure, Annual Report’’, FY 1984, NUREG/CR-3444, Vol. 2, 1985.

115. N. Evans, T. Heath, The development of a strategy for the investigation of detriments to radionuclide sorption in the geosphere. SA/ENV-0611. Nirex (2003).

116. K. Andersson, Possible complex formation of actinides with organic matter and phosphate in deep groundwaters: Speciation calculations and data evaluation, Mater. Res. Soc. Smp. Proc.. 127 (Sci. Basis Nucl. Waste Manag. 12) 693-700.

117. Gregory R.Choppin, J. Less Common Met. 112 (1985) 193-205.

118. Donald T. Reed, Sue B. Clark, LinfengRao, Actinide Speciation in High Ionic Strength Media: Experimental and Modelling Approaches to Predicting Actinide Speciation and Migration in the Subsurface, Springer Science & Business Media, 2011.

119. W. Hummel The influence of organic ligands on trace metal speciation, Goldschmidt Conference, Toulouse 1998, pp 671-672.

120. Gregory R. Choppin, J. Alloy. Compd. 249 (1997) 1-8.

121. Christopher Duncan Devine, The stability constants of some carboxylate complexes of the trivalent lanthanons " (1969). Retrospective Theses and Dissertations. Paper 3641.

122. Gregory R. Choppin, Dean R. Peterman, Coord. Chem. Rev. 174 (1998) 283–299.

123. G. R. Choppin , E. N. Rizkalla , T. A. Elansi and A. Dadgar, J. Coord. Chem. 31 (1994) 297-304.

124. G. R. Choppin, P. A. Bertrand, Y. Hasegawa and E. N. Rizkalla, Inorg. Chem. 21 (1982) 3122-3124.

125. G. Tian, L. R. Martin, Z. Zhang, L. Rao, Inorg Chem. 50 (2011) 3087-3096.

126. P. Thakur, J.L. Conca, C. J. Dodge, A. J. Francis, G. R. Choppin, Radiochim. Acta 101 (2013) 221–232.

127. D. Rama Mohana Rao, Neetika Rawat, R. M. Sawant, D. Manna, T. K. Ghanty, B. S. Tomar, J. Chem. Thermodyn. 55 (2012) 67–74.

128. D. Rama Mohana Rao, Neetika Rawat, D. Manna, R. M .Sawant, T. K. Ghanty, B. S. Tomar, J. Chem. Thermodyn. 58 (2013) 432-439.

129. D. Rama Mohana Rao, NeetikaRawat, B. S. Tomar, ChemSlct. 2(2017), 820-829.

130. D. Rama MohanaRao, NeetikaRawat, B. S. Tomar, Spectrochim. Acta A: Mol. Biomol. Spectr., 181 (2017) 13-22.

131. Rama Mohana Rao Dumpala, Neetika Rawat, Arunasis Bhattacharya, and Bhupendra Singh Tomar, ChemSlect, 2 (2017) 2725-2734.

132. J.I. Kim, in Handbook on the Physics and Chemistry of the Actinides (Eds: A. J. Freeman and C. Keller), Elsevier, Amsterdam, 1988

133. J.I. Kim, in Scientific Basis for Nuclear Waste Management XVI (Eds: C. G. Interrante and R. T. Pabalan), Mater. Res. Soc. Symp. Proc. 294, Pittsburgh, PA (1993) p. 3.

134. J. I. Kim, MRS Bulletin, 19 (1994) 47-53.

135. Actinide Nanoparticle Research (Editors: Stepan N. Kalmykov, Melissa A. Denecke), Springer-Verlag Berlin Heidelberg (2011).

136. J. F. Mc Carthy and J. M. Zachara, Environ. Sci. Technol. 23 (1989) 496-502.

137. Bruce D. Honeyman, Nature 397 (1999) 23–24

138. J. K. Bates, J. P. Bradley, A. Teetsov, C. R. Bradley and M. Buchholtz ten Brink, Science 256 (1992) 649-651.

139. Clemens Walther and Melissa A. Denecke, Chem. Rev. 113 (2013) 995−1015.

140. EFSA Panel on Dietetic Products, Nutrition and Allergies (NDA), EFSA J. 13 (2015) 4180

141. P. Tomasik, Z. Ratajewicz, G.R. Newkome, L. Strekowski (Eds.), Chemistry of Heterocyclic Compounds: Pyridine Metal Complexes, 1985, JohnWiley& Sons, Inc., Hoboken, NJ, USA, 1985.

142. Meiji Arai, Yasmene I.H. Alavi, Jacqueline Mendoza, Oliver Billker, Robert E. Sinden, Exp. Parasitol. 106 (2004) 30–36.

143. H.V. Morton, R. Nyfeler, Utilizing derivatives of microbial metabolites and plant defences to control diseases, in: Stephen O. Duke, Julius J. Menn, Jack R. Plimmer, H.V. Morton, R. Nyfeler (Eds.), Pest Control with Enhanced Environmental Safety. CS Symposium Series, 1993.

144. M. H. Bickel, Pharmacol. Rev. 21 (1969) 325-355.

145. Yiling Chen and Huichun Zhang, Environ. Sci. Technol. 47 (2013) 11023−11031.

146. O. D. Fox, C. J. Jones, J. E. Birkett, M. J. Carrott, C. J. Maher, C. V. Roube, R. J. Taylor, Advanced PUREX flow sheets for future Np and Pu fuel cycle demands. in: G. J. Lumetta, K. L. Nash, S. B. Clark, J. I. Friese (Eds.), Separations for the Nuclear Fuel Cycle in the 21st Century, ACS Symposium Series 933, ACS, Washington, 2006, pp. 89-102.

147. U. Casellato, P.A. Vigato, M. Vidali, Coord. Chem. Rev. 26 (1978) 85-159.

148. Linfeng Rao, Chem. Soc. Rev. 36 (2007) 881-892.

149. Jonathan L. Sessler, Patricia J. Melfi, G. Dan Pantos, Coord. Chem. Rev. 250 (2006) 816-843.

150. G.R. Choppin, P. Thakur, J.N. Mathur, Coord. Chem. Rev. 250 (2006) 936-947.

151. ZoltanSzabó, Takashi Toraishi, Valerie Vallet, Ingmar Grenthe, Coord. Chem. Rev. 250 (2006) 784-815.

152. U. Casellato, M. Vidali, P.A. Vigato, Coord. Chem. Rev. 250 (1979) 231-277.

153. Polly L. Arnold, Jason B. Love, Dipti Patel, Coord. Chem. Rev. 250 (2009) 1973-1978.

154. Larry.C. Thompson, Inorg. Chem. 3 (1964) 1319–1321.

155. H. Yoneda, G.R. Choppin, J.L. Bear, A.J. Graffeo, Inorg. Chem. 4 (1965) 244–246.

156. T.F. Gritmon, M.P. Geodken, G.R. Choppin, J. Inorg. Nucl. Chem. 39 (1977) 2021-2023.

157. J.E. Powell, J.W. Ingbmanson, Inorg. Chem. 7 (1968) 2459–2461.

158. Y. Fridman, N. Dolgashova, D. Sarbaev, Zh. Neorg, Khim. 18 (1973) 176–181.

159. A. Yusov, A. Bessonov, M.S. Grigor'ev, A.M. Fedoseev, and G. V. Sidorenko, Radiochemistry 55 (2013) 147–154.

160. Yasushi Inoue, Osamu Tochiyama, T. Takahashi, Radiochim. Acta 31 (1982) 197–199.

161. Yasushi Inoue, Osamu Tochiyama, Polyhedron 2 (1983) 627–630.

162. E.N. Rizkalla, F. Nectoux, S. Dabos-Seignon, M. Pages, Radiochim. Acta 51 (1990) 151–155.

163. O. Tochiyama, Y. Inoue, S. Narita, Radiochim. Acta 58 (59) (1992) 129–136.

164. Nina A. Budantseva, Grigory B. Andreev, Alexander M. Fedoseev, Michail Yu Antipin, Jean-Claude Krupa, Radiochim. Acta 94 (2006) 69–74.

165. A. S. G. Mohamed and A. M. Franz, J. Mol. Struct., 846 (2007) 153-156.

166. Z. He, Z.-M. Wang, C.-H. Yan, Cryst. Engg. Comm., 7 (2005) 143-150.

167. S. Lis, G. Meinrath, Z. Glatty, M. Kubicki, Inorg. Chim. Acta., 363 (2010) 3847-3855.

168. Z. He, E.-Q. Gao, Z.-M. Wang, C.-H. Yan, M. Kurmoo, Inorg. Chem., 44 (2005) 862-874.

169. M. Indrani, R. Ramasubramanian, F.R. Fronczek, D. Braga, N.Y. Vasanthacharya, S. Kumaresan, J. Chem. Sci., 121 (2009) 413-420.

170. Stefan Lis, Zbigniew Piskula, Maciej Kubicki, Mat. Chem. Phys., 114 (2009) 134–138.

171. P. Rama Murthy and C. C. Patel, Can. J. Chem. 42 (1864) 856-860.

172. R. K. Agarwal, H. K. Rawat, Synt. React. Inorg. Metal-Org. Chem. **16**:6, 801-819.

173. C.E.F. Rickard and D.C. Woollard, Inorg. Nucl. Chem. Lett. 14 (1978) 207-210.

174. P. W. Durbin, N. Jeung, S. J. Rodgers, P. N. Turowski, F. L. Wetl, D. L. White, K. N. Raymond, Radiat. Prot. Dosim. 26 (1989) 351–358.

175. R. H. Al-Jarrah, A. R. Al-Karaghouli, S. A. Al-Assaf, N. H. Shamon, J. Inorg. Nucl. Chem. 43 (1981) 2971–2973.

176. S. Baghdadi, C. Bouvier-Capely, A. Ritt, A. Peroux, L. Fevrier, F. Rebiere, M. Agarande, G. Cote, Talanta. 144 (2015) 875–882.

177. I. Maya, R. J. Taylor, I. S. Denniss, G. Brown, A. L. Wallwork, N. J. Hill, J. M. Rawson, R. Less, J. Alloy. and Compd. 275–277 (1998) 769–772.

178. B. Chatterjee, Coord. Chem. Rev. 26 (1978) 281–303.

179. A. Barocas, F. Barconelli, G. B. Biondi, G. Grossi, J. Inorg. Nucl. Chem. 28 (1966) 2961–2967.

180. F. Barconelli, G. Grossi, J. Inorg. Nucl. Chem. 27 (1965) 1085–1092.

181. M. Glorius, Radiochim. Acta 95 (2007) 151–157.

182. H. Moll, M. Glorius, A. Johnsson, M. Sch_fer, H. Budzikiewicz, K. Pedersen, G. Bernhar, Radiochim. Acta 98 (2010) 571–576.

183. N.C. Ta, Transit. Met. Chem. 9 (1984) 29–31.

184. Sandro. Degetto, Livio. Baracco, Transit. Met. Chem. 3 (1978) 351–354.

185. Xu. Jide, W. Donald Jr., Alan C. Veeck, Linda C. Uhlir, Kenneth N. Raymond, Inorg. Chem. 42 (2003) 2665–2674.

186. N.E. Dean, R.D. Hancock, C.L. Cahill, Mark Frisch, Inorg. Chem. 47 (2008) 2000-2010.

187. S. Lis, Z. Hnatejko, P. Barczynski, M. Elbanowski, J. Alloys Compd. 344 (20020 70–74.

188. A. N. Kost, P. B. Terentiev, L. A. Golovleva, A. A. Stolyarchuk, J. Pharm. Chem. 1 (1967) 235–240.

189. J. L. Ryan, D. Rai, Inorg. Chem. 26 (1987) 4140-4142.

190. A. R. Felmy, D. Rai, M. J. Mason, Radiochim. Acta 55 (1991) 177-185.

191. D. Rai, A. R. Felmy, S. M. Sterner, D. A. Moore, M. J. Mason, C. F. Novak, Radiochim. Acta 79 (1997) 239-247.

192. D. Rai, D. A. Moore, C. S. Oakes, M. Yui, Radiochim. Acta 88 (2000) 297-306.

193. H.-D. Greiling, K. H. Lieser, Radiochim. Acta 35 (1984) 79-89.

194. V. Neck, J. I. Kim, Radiochim. Acta 89 (2001) 1-16.

195. A. I. Vogel, A Textbook of Quantitative Inorganic Analysis, Longman Publishers (1966).

196. D. Cvjeticanin, S. Ratkovic, J. Chromatogr. A 46 (1970) 326–328.

197. Atsushi Ikeda-Ohno, Christoph Hennig, André Rossberg, Harald Funke, Andreas C. Scheinost, Gert Bernhard, Tsuyoshi Yaita, Inorg. Chem. 47 (2008) 8294–8305.

198. IUPAC, Compendium of Chemical Terminology, 2nd ed. (the "Gold Book") (1997). Online corrected version: (2006) .

199. J. Bjerrum, and M. Calvin, Metal Amine Formation in Aqueous Solutions, P. Hass and Son, Copenhagen, (1941), Reprinted in 1957.

200. Diss. Leden, Lund, 1943.

201. Sture Fronæus, Acta Chem. Scand. 5 (1951) 859-871.

202. H. M. Irving and S. Rossoti, J. Chem. Soc, 76 (1954) 2904-2910.

203. Edward L. King, Patrick K. Gallagher, J. Phys. Chem. 63 (1959) 1073–1076.

204. F. J. C. Rossotti, H. Rossotti, Acta Chem. Scand. 9 (1955) 1166-1176.

205. J. C. Sullivan, J. C. Hindman, J. Am. Chem. Soc. 74 (1952) 6091–6096.

206. W. C. Hamilton, Statistics in Physical Sciences, The Roland Press Company, New York, 1964, p. 160.

207. D.J. Leggett (Ed.), Computational Methods for the Determination of Formation Constants, Plenum Press, New York, 1985.

208. M. Meloun, J. Have1 and E. Hogfeldt, Computation of Solution Equilibria. Ellis Horwood. Chichester, 1994.

209. P. Gans, Data Fitting in the Chemical Sciences, Wiley, Chichester, 1992.

210. A. Braibant, G. Ostacoli, P. Paoletlti, L. D. Pettit and S. Sammartano, Pure & App. Chem. 59 (1987) 1721—1728.

211. K. B. Yatsimirskii and V. P. Vasil’ev, Instability Constants of Complex Compounds, D. Van. Nostrand Company, Inc. Princeton, New York, 15 (1960).

212. R. K. Murmann, Inorganic Complex Compounds, Chapman & Hall Ltd.London, 30 (1964).

213. Tamás Kiss, Éva A. Enyedy, Tamás Jakusch, Coord. Chem. Rev. (2017), DOI: 10.1016/ j.ccr.2016.12.016.

214. F. J. C. Rossotti, H. Rossotti, The Determination of Stability Constants. McGraw–Hill, 1961.

215. Francisco J. Vidal-Iglesias, José Solla-Gullón, Antonio Rodes, Enrique Herrero, and Antonio Aldaz, J. Chem. Edn. 89 (2012) 936-939.

216. P. Gans and B. O'Sullivan, Talanta 51 (2000) 33-37.

217. P. Gans, A. Sabatini and A. Vacca, Talanta, (1996), 43, 1739-1753.

218. G. Gran, Analyst. 77 (1952) 661-671.

219. B. M. Tissue, Ultraviolet and Visible Absorption Spectroscopy. Characterization of Materials, John Wiley & Sons, New York, 2002.

220. Paul Wormell, Alison Rodger, Absorbance Spectroscopy: Overview in Encyclopaedia of Biophysics (Eds: C. K. Gordon, Roberts), pp 23-25, Springer Berlin Heidelberg, Berlin, Heidelberg, 2013.

221. Suresh Purohit and N Bhojak, Research and Reviews: Journal of Chemistry 2 (2013) 1-3.

222. T. Moeller, The Chemistry of the Lanthanides, Reinhold Publishers, New York, NY, 1963.

223. Sudhindra N. Misra & Shaun O. Sommerer, Appl. Spectr. Rev. 26 (1991) 151-202.

224. D. G. Karraker, Inorg. Chem. 6 (1967) 1863-1868

225. D. E. Henrie, R. L. Fellows and G. R. Choppin, Coord. Chem. Rev. 18 (1976) 199-224.

226. Model V-530/550/560/570 UV/VIS Spectrophotometer Hard ware/Function Manual, P/N:0302-0256B, November 2000, JASCO Corporation, Tokyo, Japan.

227. Paul Job, Annali di Chimica Applicata, 9 (1928), 113–203.

228. J. S. Renny, L. L. Tomasevich, E. H. Tallmadge, D. B. Collum, Ang. Chem. Int. Ed. Eng. 46 (2013) 11998 – 12013.

229. D. A. Skoog, D. M. West, F. J. Holler, Fundamentals of Analytical Chemistry , 5th Ed.; Saunders: New York, 1988.

230. J. S. Coleman, L. P. Varga and S. H. Mastin, Inorg. Chem. 9 (1970) 1015-1020.

231. W. C. Vosburgh and G. R. Cooper, J. Amer. Chem. Soc. 63 (1941) 437-442.

232. Aubrey E. Harvey Jr. and Delmer L. Manning, Inorg. Chem. 72 (1950) 4488-4493.

233. Marian Elbanowski, Stcfan Lis, Barbara Makowska and Jerzy Konarski, Monatshefte fur Chemie, 116 (1985) 901-911.

234. B. Raditzky, K. Schmeide, S. Sachs, G. Geipel, G. Bernhard, Polyhedron 29 (2010) 620–626.

235. Sergei I. Sinkov, Gregory R. Choppin, Robin J. Taylor, J. Sol. Chem. 36 (2007) 815–830.

236. Henry Moll, Gert Bernhard, Polyhedron 31 (2012) 759-766.

237. B. Raditzky, S. Sachs, K. Schmeide, A. Barkleit, G. Geipel, G. Bernhard, Polyhedron 65 (2013) 244-251.

238. Akira Kirishima, Takaumi Kimura, Osamu Tochiyama and Zenko Yoshid, Chem. Commun. (2003) 910-911.

239. Christian M. Marquardt, P. J. Panak , C. Apostolidis, A. Morgenstern, C. Walther, R. Klenze, Thomas Fanghänel, Radiochim. Acta, 92(7), (2009) pp. 445-447.

240. Astrid Barkleit, Gerhard Geipel, Margret Acker, SteffenTaut, Gert Bernhar, Spectrochim. Acta Part A: Mol. Biomol. Spectr. 78 (2011) 549-552.

241. William De W. Horrocks Jr., Daniel R. Sudnick, J. Am. Chem. Soc., 1979, 101 (2), pp 334–340.

242. Takaumi Kimura, Gregory R. Choppin, J. Alloy. Compd. 213–214 (1994) 313-317.

243. Th. Fanghanel, J.-I. Kim, J. Alloy. Compd. 271–273 (1998) 728–737.

244. W.T. Carnall, J. Chem. Phys. 96 (1992) 8713–8726.

245. G. H. Dieke and H.M. Crosswhite, Appl. Opt. 2 (1963) 675–686.

246. Richard N. Collins, Takumi Saito, Noboru Aoyagi, Timothy E. Payne, Takaumi Kimura, and T. David Waite, J. Environ. Qual. 40 (2011) 731-741.

247. J. Heber, Phys. Kondens. Mater. 6 (1967) 381–402.

248. J. L. Kropp, M. W. Windsor, J. Chem. Phys. 39 (1963) 2769–2770.

249. J. L. Kropp, M. W. Windsor, J. Chem. Phys. 42 (1965) 1599–1608.

250. J. L. Kropp, M. W. Windsor, J. Chem. Phys. 45 (1966) 761–762.

251. Y. Haas, G. Stein, J. Phys. Chem. 75 (1971) 3677–3681.

252. J. J. Freeman, D. E. Lawson, G. A. Crosby, J. Mol. Spectrosc. 13 (1964) 399-406.

253. W.D. Horrocks, D.R. Sudnick, Acc. Chem. Res. 14 (1981) 384–392.

254. P.P. Barthelemy, G.R. Choppin, Inorg. Chem. 28 (1989) 3354–3357.

255. Quick Start: Isothermal Titration Calorimetry (ITC), Applications Note (MCAPN-2016-1) by TA instruments, New Castle, USA.

256. Alderighi, P. Gans, A. Ienco, D. Peters, A. Sabatini, A. Vacca, Coord. Chem. Rev. 184 (1999) 311-318.

257. Tobias Bundschuh, Jong-Il Yun, Roger Knopp, Fresenius J Anal Chem (2001) 371 : 1063–1069.

258. Tobias U. Wagner, Tobias Bundschuh, Rainer Köster, Part. Part. Syst. Charact. 22 (2005) 181-191.

259. Jong-Il Yun, Material Dependence of Laser-induced Breakdown of Colloidal Particles in Water, J. Opt. Soc. Korea 11 (2007) 34-39.

260. An insight on LIBD principle and performances, Technical note (NT01-MAGELLAN), Cordouan Technologies, France.

261. M. J. Keith-Roach, Sci Total Environ., 396 (2008) 1-11.

262. Margaret Robson Wright, An Introduction to Aqueous Electrolyte Solutions, chapter 8: Practical Applications of Thermodynamics for Electrolyte Solutions, John Wiley & Sons Ltd, 2007, pp 242-262.

263. R. Ahlrichs, M. Bär, M. Häser, H. Horn, C. Kölmel, Chem. Phys. Lett. 162 (1988: 1989) 165–169.

264. A.D. Becke, Phys. Rev. A, 38 (1988) 3098–3100.

265. J.P. Perdew, Phys. Rev. B, 33 (1986) 8822–8824.

266. M.R. Pâris, Cl. Gregoire, Anal. Chim. Acta 42 (1968) 431–437, 439–441.

267. M. Nair, M. Neelakantan, S. Sunu, Indian J. Chem. 38A (1999) 1307–1309.

268. Lesley. A. Ashton, Joseph. I. Bullock, J. Chem. Soc., Faraday Trans. 1, 78 (1982) 1177–1187.

269. A. Asuero, M. Navas, A. Recamales, M. Herrador, Mikrochim. Acta 88 (1986) 395–406.

270. Jean.-Claude. Hallé, Jacques. Lelievre, François. Terrier, Can. J. Chem. 74 (1996) 613–620.

271. M.A. Zón 1, M. Angulo, J.M. Rodríguez Melladore, J. Electroanal. Chem., 365 (1994) 213-220.

272. Matilde Angulo, José Miguel, Rodríguez Melladore, J. Electroanal. Chem., 403 (1996) 251-255.

273. Plinio Di Bernardo, Pier Luigi Zanonato, Guoxin Tian, Marilena Tolazzic and Linfeng Rao, Dalton Trans., (2009) 4450–4457.

274. Babak Minofar, Martin Mucha, Pavel Jungwirth, Xin Yang, You-Jun Fu, Xue-Bin Wang, Lai-Sheng Wang, J. Am. Chem. Soc., 126 (2004) 11691–11698.

275. A. Kirishima, Y. Onishi, N. Sato and O. Tochiyama, Radiochim. Acta., 96 (2008) 581-589.

276. Astrid Barkleit, Margret Acker, Gert Bernhar, Inorg. Chim. Acta., 394 (2013) 535–541.

277. Paavo Lumme, Esko Kari, Acta Chem. Scand., 29A (1975) 117-124.

278. Akira Kirishima, Yuko Onishi, Nobuaki Sato, Osamu Tochiyam, J. Chem. Thermodyn. 39 (2007) 1432-1438.

279. G. R. Choppin, P. A. Bertrand, Y. Hasegawa and E. N. Rizkalla, Inorg. Chem., 21 (1982) 3722-3724.

280. D. Rama Mohana Rao, Neetika Rawat, R.M. Sawant, D. Manna, T.K. Ghanty, B.S. Tomar, J. Chem. Thermodyn., 55 (2012) 67–74.

281. G. Scatchard, Equilibrium in Solution: Surface and Colloidal Chemistry, Harvard University Press, Cambridge, 1976, pp. 1-208.

282. Stability Constants Database (SC Database), Academic Software www.acadsoft.co.uk.

283. Jernej Stare, Jaroslaw Panek, Juergen Eckert, Joze Grdadolnik, Janez Mavri, and Dusan Hadzi, J. Phys. Chem. A, 112 (2008) 1576-1586.

284. Krystyna Szczepaniak , Willis B. Person and Dusan Hadzi, J. Phys. Chem. A, 109 (2005) 6710–6724.

285. J. Stare, J. Mavri, G. Ambrožič, D. Hadzi, J. Mol. Struct. Theochem., 500 (2000) 429–440.

286. Vytautas Balevicius, Kęstutis Aidas, Ingrid Svoboda, and Hartmut Fuess, J. Phys. Chem. A, 116 (2012) 8753–8761.

287. Jarosław Panek, Jernej Stare, Dusan Hadzi, J. Phys. Chem. A, 108 (2004) 7417-7423.

288. Nadja Došlić, Jernej Stare, Janez Mavr, Chem.Phys., 269 (2001) 59-73.

289. Jernej Stare, Aneta Jezierska, Gabriela Ambrožič, Iztok J. Košir, Jurka Kidrič, Aleksander Koll, Janez Mavri, Dušan Hadži, J. Am. Chem. Soc., 126 (2004) 4437-4443.

290. M. Kumar, R.A. Yadav, Spectrochim. Acta A, 79 (2011) 1316–1325.

291. A. Atac, M. Karabacak, C. Karaca, E. Kose, Spectrochim. Acta A, 85 (2012) 145–154.

292. Caglar Karaca, Ahmet Atac, Mehmet Karabacak, Spectrochimica Acta Part A, 140 (2015) 85–95.

293. Sock Sung Yun, Sung Hee Bae, Sung Won Hong, Sung Kwon Kang, Inn Hoe Kim, Joon Taik.Park, Thermochim. Acta, 246 (1994) 39-47.

294. M. Celina, M. M. Fernandes, E. B Paniago, S. Carvalho, J. Brez. Chem. Soc., 8 (1997) 537-548.

295. N. Dutt, T. Seshadri, J. Inorg. Nucl. Chem., 31 (1969) 2153-2157.

296. P. Das, S. Bhattacharya, R. Banerjee, J. Coord. Chem., 19 (1989) 311-320.

297. O. Erner and R. Kakac, Collect. Czech. Chem. Comm., 28 (1963) 1656-1663.

298. E. Lipczynska-Kochany and H. Iwamura, J. Org. Chem., 47 (1982) 5277-5282.

299. W. M. Wise and W. W. Brant, J. Am. Chem. Soc., 77 (1955) 1058-1059.

300. J. Gerstein and W. P. Jencks, J. Am. Chem. Soc., 86 (1964) 4655-4663.

301. A. R. Fields, B. M. Daye, R. Christian, Talanta, 13 (1966) 929-937.

302. A. Bagno, C. Conuzzi, G. Scorrano, J. Am. Chem. Soc., 116 (1994) 916-924.

303. B. Boulet, L. Joubert, G. Cote, C. Bouvier-Capely, C. Cossonnet, C. Adamo, Inorg. Chem., 47 (2008) 7983-7991.

304. Keith. Bridger, Ramesh.C. Patil, Egon. Matijevic, Polyhedron 1 (1982) 269–275.

305. Ole. Jones, Erik Sylvest Johansen, Inorg. Chim. Acta 151 (1988) 129–132.

306. M. R. Paris, C. L. Gregorie, Anal. Chim. Acta 42 (1968) 439–444.

307. Mary.L. Lugo, Vito.R. Lubes, J. Chem. Eng. Data 52 (2007) 1217–1222.

308. E. Kiss, K. Petrohan, D. Sanna, E. Garribba, G. Micera, T. Kiss, Polyhedron 19 (2000) 55–61.

309. R. W. Green, H. K. Tong, J. Am. Chem. Soc. 78 (1956) 4896–4900.

310. W. Li, X. -L. Wang, X. -Y. Song, L. -C. Li, D. -Z. Liao, Z. -H. Jiang, J. Mol. Struct. 885 (2008) 1–6.

311. H. G. Brittain, Inorg. Chem. 17 (1978) 2762–2766.

312. V. Zolin, L. Puntus, V. Kudryashova, V. Tsaryuk, J. Legendziewicz, P. Gawryszewska, R. Szostak, J. Alloys Compd. 341 (2002) 376–380.

313. B. S. Panigrahi, J. Alloys Compd. 334 (2002) 228–231.

314. V. F. Zolin, L. N. Puntus, V. I. Tsaryuk, V. A. Kudryashova, J. Legendziewicz, P. Gawryszewska, R. Szostak, J. Alloys Compd. 380 (2004) 279–284.

315. S. S. Yun, S. K. Kang, H. R. Suh, H. S. Suh, E. K. Lee, J. K. Kim, C. H. Kim, Bull. Korean Chem. Soc. 26 (2005) 1197–1202.

316. V. F. Zolin, V. I. Tsaryuk, V. A. Kudryashova, K. P. Zhuravlev, P. Gawryszewska, J. Legendziewicz, R. Szostak, J. Alloys Compd. 451 (2008) 149–152.

317. N. Chatterton, Y. Bretonniere, J. Pecaut, M. Mazzanti, Angew. Chem. Int. Ed. 44 (2005) 7595–7598.

318. L. Charbonniere, N. Weibel, C. Estournes, C. Leuvrey, R. Ziessel, New J. Chem. 28 (2004) 777–781.

319. S. M. Lee, S. K. Ryu, C. H. Jung, H. J. Won, W. Z. Oh, Carbon 40 (2002) 329–334.

320. N. S. Navaneetham, S. Soundarajan; Ind. J. Chem. A. (1981) 93-94.

321. P. G. Manning; Can. J. Chem., 44 (1966) 1471-1473.

322. S. A. Boyd, R. E. Kohrman, D. X. West; Inorg. Nucl. Chem. Lett., 12 (1976) 603-608.

323. S. A. Boyd, R. E. Kohrman, D. X. West; Inorg. Nucl. Chem. Lett., 13 (1977) 129-135.

324. G. F. De Sa, F. R. G. e Silva, O. L. Malta; J. Alloys Compd., 207 (1994) 457-460.

325. L. Yan, J. -M. Liu, X. Wang, R. D. Yang, F. -L. Song; Polyhedron., 14 (1995) 3545-3548.

326. M. Sato, M. Yamamoto, K. Imada, N. Katsube, Y. Tanaka, T. Higashi; J. Appl. Cryst., 25 (1992) 348-357.

327. J. G. Mao, H. J. Zhang, J. Z. Ni, S. B. Wang and T. C. W. Mak, Polyhedron., 17 (1998)

328. Lijuan Zhang, Donghua Xu, Yunshan Zhou and Fei Jiang, New J. Chem., 34 (2010) 2470–2478.

329. C. Lee, W. Yang, R. G. Parr, Phys. Rev. B., 37 (1988) 785-789.

330. TurbomoleV6.3. 2009.

331. P. J. Hay, W. R. Wadt, J. Chem. Phys., 82 (1985) 299-310.

332. S. A. Ansari, P. K. Mohapatra, S. M. Ali, A. Sengupta, A. Bhattacharyya and W. Verboom, Dalton. Trans., 45 (2016) 5425-5429.

333. N. K. Gupta, A. Sengupta, A. Boda, V. C. Adya and S. M. Ali, RSC Adv., 6 (2016) 78692-78701.

334. A. Sengupta, S. M. Ali and K. T. Shenoy, Polyhedron., 117 (2017) 612-622.

335. A. Sengupta, J. Sk, A. Boda and S. M. Ali, RSC Adv., 6 (2016) 39553-39562.

336. L. E. Roy, N. J. Bridges, L. R. Martin, Dalton. Trans., 42 (2015) 2636-2642.

337. C. L. Xiao, C. Z. Wang, J. H. Lan, L. Y. Yuan, Y. L. Zhao, Z. F. Chai, W. Q. Shi, Radiochim. Acta., 102 (2014) 875-886.

338. C. L. Xiao, C. Z. Wang, J. H. Lan, L. Y. Yuan, Y. L. Zhao, Z. F. Chai, W. Q. Shi, Inorg. Chem., 53 (2016) 1712-1720.

339. A. Klamt, J. Phys. Chem., 99 (1995) 2224-2235.

340. A. Klamt, G. Schuurmann, J. Chem. Soc. Perkin Trans., 2 (1993) 799-804.

341. J. Ciupka, X. Cao-Dolg, J. Wiebke, M. Dolg, Phys. Chem. Chem. Phys., 12 (2010) 13215-13223.

342. A. Boda and M. A. Sheikh, J. Phys. Chem. A, 116 (2012) 8615-8623.

343. Neetika Rawat, R.S. Sharma, B.S. Tomar, V.K. Manchanda, Thermochimica Acta 501 (2010) 13–18.

344. H. D. Harmon, J. R. Peterson, , W. J. McDowell, C. F. Coleman, J. Inorg. Nucl. Chem., 34 (1972) 1381–1397.

345. H. D. Harmon, J. R. Peterson, , W. J. McDowell, C. F. Coleman, J. Inorg. Nucl. Chem., 34 (1972) 1711–1719.

346. Zhiping Xu, Nature, Sci. Rep., 3 : 2914 (2013) 1-7.

347. X.-B. Wang, X. Yang, J. B. Nicholas and L.-S. Wang, J. Chem. Phys., 119 (2003) 3631–3640.

348. W. C. Nieuwpoort and G. Blasse,Sol. State. Commun., 4 (1966) 227-229,.

349. P. Porcher, P. Caro, J. Lumin., 21 (1980) 207-216.

350. C. Görller-Walrand, L. Fluyt and A. Ceulemans, W. T. Carnall, J. Chem. Phys., 95 (1991) 3099-3106.

351. Koen Binnemans, Coord. Chem. Rev. 295 (2015) 1–45 .

352. L. S. Gelfand, F. J. Iaconianni, L. L. Pytlewski, A. N. Speca, C. M. Mikulski, N. M. Karayannis, J. Inorg. Nucl. chem. 42 (1980) 377-385.

353. Stephen A. boyd, Robert E. Kohrman, Douglas X. West, J. Inorg. Nucl. chem. 38 (1976) 607-608.

354. L. S. Gelfand, F. J. Iaconianni, L. L. Pytlewski, A. N. Speca, C. M. Mikulski, N. M. Karayannis, Inorg. Chim. Acta. 32 (1979) 59-67.

355. F. J. Iaconianni, L. S. Gelfand, L. L. Pytlewski, A. N. Speca, C. M. Mikulski, N. M. Karayannis, Inorg. Chim. Acta. 36 (1979) 97-104.

356. Zhicheng Zhang, Yanqiu Yang, Guokui Liu, Shunzhong Luo, Linfeng Rao, RSC Adv. 5 (2015) 75483–75490.

357. Zbigniew Hnatejko, Stefan Lis, Przemysław Starynowicz, Zdzisław Stryła, *Polyhedron* **30** (2011) 880-885.

358. Zbigniew Hnatejko, Stefan Lis, Zdzisław Stryła, Przemysław Starynowicz, *Polyhedron* **29** (2010) 2081-2086.

359. J. Casellato, P.A. Vigato, S. Tamburini, R. Graziani, M. Vidali, *Inorgan. Chim. Acta* **72** (1983) 141-147.

360. R.K. Agarwal, Gyanendra Singh, S.C. Rastogi, *Thermochim. Acta* **84** (1985) 183-187.

361. R.K. Agarwal, S.C. Rastog, *Thermochim. Acta* **63** (1983) 363-368.

362. R.K. Agarwal, S.C. Rastogi, *Thermochim. Acta* **62** (1983) 379-384.

363. U. Casellato, P.A. Vigato, S. Tamburini, M. Vidali, R. Graziani, *Inorgan. Chim. Acta* **69** (1983) 77-82.

364. A.K. Srivastava, R.K. Agarwal, *Thermochim. Acta* **56** (1982) 247-252.

365. Anant K. Srivastava, Shashi Sharma, Ram K. Agarwal, Inorgan. Chim. Acta 61 (982) 235-239.

366. S.K. Madan, A.M. Donohue, J. Inorg. Nucl. Chem. 28 (1966) 1303-1311.

367. Nimai Chandra Ta, J. Coord. Chem. 7 (1977) 9-11.

368. Nimai Chandra Ta, J. Coord. Chem. 8 (1978) 55-58.

369. S. Al Rifai, Complex Formation between Trivalent Transuranium Elements and Ligand which Contain the Pyridinie or Quinoline Ring. (1970) German Report IRCH-10/70-2.

370. M. Dolg, H. Stoll, H. Preuss, J. Chem. Phys. 90 (1989) 1730-1734.

371. X. Cao, M. Dolg, J. Chem. Phys. 115 (2001) 7348-7355.

372. W. Kuchle, M. Dolg, H. Stoll, H. Preuss, J. Chem. Phys. 100 (1994) 7535- 7542.

373. X. Cao, M. Dolg, H. Stoll, J. Chem. Phys. 118 (2003) 487-496.

374. X. Cao, M. Dolg, J. Molec. Struct. (Theochem) 673 (2004) 203-209

375. Plinio Di Bernado, Albert Cassol, Giuliana Tomat, Arturo Bismondo, Lucian Magon, J. Chem. Soc. Dalton Trans. (1983) 733-735.

376. Linfeng Rao, Pier Luigi Zanonato, Plinio Di Bernardo, J. Nucl. Radiochem. Sci. 6 (2005) 31-37.

377. Tianxiao Yang, Satoru Tsushim, and Atsuyuki Suzuki, J. Phys. Chem. A. 105 (2001) 10439-10445.

378. S. Tsushima, T. Yang, Y. Mochizuki, Y. Okamoto, Chem. Phys. Lett. 375 (2003) 204-212.

379. S. Tsushima, T. Yang, Chem. Phys. Lett. 401 (2005) 68-71.

380. A. Boda, S. M. Ali, M. R. K. Shenoi, H. Rao and S. K. Ghosh, J. Mol. Model., 17 (2011) 1091-1108.

381. A. Boda, S. Musharaf Ali, H. Rao and S. K. Ghosh, J. Mol. Model., 18 (2012) 3507-3522.

382. S. Eberle, W. Robel, Inorg. Nucl. Chem. Lett. 6 (1970) 359–365.

383. B. Raditzky, S. Sachs, K. Schmeide, A. Barkleit, G. Geipel, G. Bernhard, Polyhedron 65 (2013) 244–251.

384. Grigory B. Andreev, Nina A. Budantseva, Alexander M. Fedoseev, Structural Chemistry of Inorganic Actinide Compounds, Elsevier, 2007.

385. Koichiro Takao, Shinobu Takao, Andreas C. Scheinost, Gert Bernhard, Chrisyoph Henning, Inorg. Chem. 48 (2009) 8803–8810.

386. Benoit Brunel, Violaine Philippini, Mickael Mendes, Jean Aupiais, Radiochim. Acta 103 (2015) 27–37.

387. G.R. Choppin, B.E. Stout, M. Pages, J. Alloys Compd. 271-273 (1984) 774–777.

388. M. Saeki, M. Nakada, T. Nakamoto, N.M. Masaki, T. Yamashita, J. Alloys Compd. 271-273 (1998) 176–179.

389. G.R. Choppin, P. Thakur, J.N. Mathur, Coord. Chem. Rev. 250 (2006) 936–947.

390. H. J. Lindner, S. Goettlicher, Acta Crystallogr., Sect. B 25 (1969) 832–842.

391. D. A. Brown, D. McKeith, W. K. Glass, Inorg. Chim. Acta 35 (1979) 5–10.

392. E. C. O’Brien, E. Farkas, M. Jose Gil, D. Fitzgerald, A. Castineras, K. B. Nolan, J. Inorg. Biochem. 79 (2000) 47–51.

393. C. P. Brink, A. L. Crumbliss, Inorg. Chem. 23 (1984) 4708–4718.

394. M. T. Caudle, A. L. Crumbliss, Inorg. Chem. 33 (1994) 4077–4085.

395. A. Evers, R. D. Hancock, A. E. Martell, R. J. Motekaitis, Inorg. Chem. 28 (19890 2189-2195.

396. P. C. Parekh, S. K. Manon, Y. K. Agrawal, J. Chem. Soc., Perkin Trans. II (1989) 1117-1123.

397. E. Farkas, E. Kozma, M. Petho, K. M. Herlihy, G. Micera, Polyhedron 17 (1998) 3331-3342.

398. A. Dess, G. Micera, D. Sanna, L. Strinna-Erre, J. Inorg. Biochem. 48 (1992) 279.

399. W. L. Smith, K. N. Raymond, J. Am. Chem. Soc. 103 (1981) 3341–3349.

400. Turbomole, Filipp Furche, Reinhart Ahirichs, Christof Hattig, Wim Klopper, Marek Sierka, Florian Weigend, WIREs Comput. Mol. Sci. 4 (2013) 91–100.

401. Arunasis Bhattacharyya, Tapan Kumar Ghanty, Prasanta Kumar Mohapatra, Vijay Kumar Manchanda, Inorg. Chem. 50 (2011) 3913–3921.

402. Xiaoyan Cao, Daniel Heidelberg, Jan Ciupka, Michael Dolg, Inorg. Chem. 49 (2010) 10307–10315.

403. Sk M. Ali, S. Pahan, A. Bhattacharyya, P.K. Mohapatra, Phys. Chem. Chem. Phys. 18 (2016) 9816–9828.

404. Mahesh Sundararajan, Vivek Sinha, Tusar Bandyopadhyay, Swapan K. Ghosh, J. Phys. Chem. A 116 (2012) 4388–4395.

405. P.G. Allen, J.J. Bucher, D.K. Shuh, N.M. Edelstein, T. Reich, Inorg. Chem. 36 (1997) 4676–4683.

406. Yanqiu Yang, Zhicheng Zhang, Guokui Liu, Shunzhong Luo, Linfeng Rao, J. Chem. Thermodyn. 80 (2015) 73–78.

407. L. Rao, J. Jiang, P. Zanonato, P. Di Bernardo, A. Bismondo and A. Y. Garnov, Radiochim. Acta 90 (2002) 581-588.

408. J. I. Kim, G. Buckau, R. Klenze, Natural Colloids and Generation of Actinide Pseudocolloids in Groundwater, Springer Netherlands (1987) 289-299.

409. V. Neck, M. Altmaier, R. Müller, A. Bauer, Th. Fanghänel and J. I. Kim, Radiochim. Acta 91 (2003) 253–262.

410. Yuanxian Xia, Andrew R. Felmy, Linfeng Rao, Zheming Wang and Nancy J. Hess, Radiochim. Acta 91 (2003) 751–760.

411. M. Altmaier, V. Neck, R. Müller and Th. Fanghänel, Radiochim. Acta 93 (2005) 83–92.

412. J. Rothe, M. A. Denecke, V. Neck, R. Muller, and J. I. Kim, Inorg. Chem. 41 (2002) 249-258.

413. C. Walther, Colloids and Surfaces A: Physicochem. Eng. Aspects 217 (2003) 81-92.

414. J. I. Kim and C. Walther, Laser-Induced Breakdown Detection (chapter 12), in Environmental Colloids and Particles: Behaviour, Separation and Characterisation, Volume 10 (Eds K. J. Wilkinson and J. R. Lead), John Wiley & Sons, Ltd, Chichester, UK. (2006)

415. C. Bitea, R. Müller, V. Neck, C. Walther, J. I. Kim, Colloids and Surfaces A: Physicochem. Engg. Aspects 217 (2003) 63-70.

416. V. Neck, R. Müller, M. Bouby, M. Altmaier, J. Rothe, M. A. Denecke and J. I. Kim, Radiochim. Acta 90 (2002) 485–494.

417. T. Bundschuh, R. Knopp, R. Müller, J. I. Kim, V. Neck and Th. Fanghänel, Radiochim. Acta 88 (2000) 625–629.

418. M. Henry, J. P. Jolivet and J. Livage, Structure and Bonding" 77 (1992) 153-206.

419. C. Walther, M. Fuss and S. Büchner, Radiochim. Acta 96 (2008) 411–425.

420. Ulf Nobbmann, Malcolm Connah, Brendan Fish, Paul Varley, Chris Gee, Sandrine Mulot, Juntao Chen, Liang Zhou, Yanling Lu, Fei Sheng, Junming Yi & Stephen E. Harding, Biotech. Gen. Engg. Rev. 24 (2007) 117-128.

421. Mathias S. Wickleder, Blandine Fourest, and Peter K. Dorhout, Chapter Three: Thorium in The Chemistry of the Actinide and Transactinide Elements, Fourth Edition (Eds: Lester R. Morss, Norman M. Edelstein, Jean Fuger), Springer, Dordrecht, The Netherlands (2010). pp 117-126.

422. Karah E. Knope, Richard E. Wilson, Monica Vasiliu, David A. Dixon, and L. Soderholm, Inorg. Chem. 50 (2011) 9696–9704.

423. G. Johansson, On the structure of the hydrolysis products of thorium, Acta Chem. Scand. 22 (1968) 399-409.

424. Chemical Thermodynamics of Thorium, Edited by Federico J. Mompean (Series Editor and Project Co-ordinator) Jane Perrone (Volume Editor) and Myriam Illemassène OECD Nuclear Energy Agency, Data Bank Issy-les-Moulineaux, (France), 2007.

425. M. Guymont, C. R. Acad. Sci. Paris C, 285 (1977) 345–348.

426. T. Dupuis, and C. Duval, C. R. Acad. Sci. Paris. 228 (1949) 401–402.